Transactions of the ASME

Transactions of the ASME, The Journal of Fluids Engineering (ISSN 0098-2202) is published quarterly (Mar., June, Sept., Dec.) for $105 per year by The American Society of Mechanical Engineers, 345 East 47th Street, New York, NY 10017. Second class postage paid at New York, NY and additional mailing offices. POSTMASTER: Send address changes to The Journal of Fluids Engineering, c/o THE AMERICAN SOCIETY OF MECHANICAL ENGINEERS, 22 Law Drive, Box 2300, Fairfield, NJ 07007-2300.
CHANGES OF ADDRESS must be received at Society headquarters seven weeks before they are to be effective. Please send old label and new address.
PRICES: To members, $24.00, annually; to nonmembers, $105. Add $6.00 for postage to countries outside the United States and Canada.
STATEMENT from By-Laws. The Society shall not be responsible for statements or opinions advanced in papers or . . . printed in its publications (B7.1, Par. 3).

INDEXED by Engineering Information

Journal of Fluids Engineering

Published Quarterly by The American Society of Mechanical Engineers

VOLUME 109 • NUMBER 2 • JUNE 1987

CONFERENCE REPORT

9th Australasian Fluid Mechanics Conference
8–12 December 1986

J. J. J. Chen[1]

This triennial conference was organized by the University of Auckland School of Engineering and held at the University Conference Centre. Peter Jackson convened the organizing committee during the initial preparatory stages. Three months before the Conference, Ray Meyer took over the task of convener, when Peter left for Perth, Australia, to join the N. Z. America's Cup Challenge team as analyst and subsequent head of the team's "Think Tank."

The Conference was fortunate in having five distiguished researchers as keynote speakers: M. Kiya of Sapporo, Japan, (Vortices and Unsteady Flow in Turbulent Separation Bubbles); A. E. Perry of Melbourne, Australia (A Description of Eddying Motions and Turbulence); D. V. Boger of Melbourne, Australia (Ideal Elastic Liquids and Their Importance in Non-Newtonian Fluid Mechanics); G. F. Hewitt of Imperial College and UKAEA, U.K. (Co-Current and Counter-Current Two-Phase Annular Flow); M. S. Longuet-Higgins of Cambridge, England, (Surface-Wave Interactions). These keynote addresses set the theme for the Conference, highlighting the latest in both theoretical and experimental research in their respective fields of fluid mechanics. The inclusion of David Boger in the program gave an interesting new dimension to the Conference.

The Conference was truly an international one with over 150 delegates representing the following countries: Australia (101 delegates), New Zealand (31), France (2), Japan (5), Canada (2), Hong Kong (1), U.S.A. (4), South Africa (1), Singapore (1), India (1), Qatar (1) and U.K. (3). The range of topics of the papers presented were reflected by the topics covered by the keynote speakers. Papers were presented by applied mathematicians, physicists, civil, mechanical, aeronautical, and chemical engineers, from universities, private and government research establishments, and industry.

The Conference was opened by the Deputy Vice-Chancellor of the University of Auckland, Professor Don I. B. Smith. In his humorous opening address Don, a scholar in English, remarked that he had known a number of fluid mechanics people at Oxford including Bob Bilger from Sydney, and had noticed their interest in a particular fluid. He found several titles in the program intriguing. He wondered what "Flashing Flow in Submerged Orifices" by H. T. A. El Dessouky of Qatar University, was about. The Conference Chairman, Ray Meyer, thanked Don for opening the Conference and introduced the first keynote speaker, M. Kiya, pointing out that Professor Kiya came from Sapporo, the place of origin of a very famous Japanese fluid. The Conference got underway in friendly and lighthearted vein.

Each day of the Conference began with a keynote address. Three concurrent sessions were scheduled for the rest of the day. The sessions covered such wide areas of fluid mechanics as Waves, Industrial Aerodynamics and Wind Engineering, Multiphase Flow, Jets and Nozzles, Separated Flows, Acoustics, Heat Transfer, Stratified Flow, etc. Space does not permit the listing of all the papers but the following reflect the authors impressions.

[1]School of Engineering, University of Auckland, Auckland, New Zealand.

Barry Newman of McGill University, Canada, gave a paper on flow past 2-D battened sail, which was of topical interest as the America's Cup Challenge Series was in progress at that time. Innovative ideas such as the use of fibre-suspension as a transporting medium for solids such as coal or capsules were presented by Geoff Duffy and Mike Walmsley of Auckland University. They pointed out that there was not only the advantage of a reduced drag, but also that during shutdown, the solids will remain in suspensions supported by the fibrous network.

Roger Tanner of Sydney University examined the use of boundary element methods on separation of viscous jets and K. Chiba of Osaka numerically analyzed the flow of viscoelastic fluids around an inclined cylinder. Peter Ulherr of Monash University presented results and a correlation for the creeping motion of a sphere in a non-Newtonian fluid.

In the area of hydraulics, A. J. Sutherland of Canterbury University, Bruce Morton and Jenny Evans-Lopez of Monash University, And Bruce Melville of Auckland University were among those who contributed papers on scouring in river flow situations.

In the areas of separated flow and flow induced acoustics, Ian Gartshore of the University of British Columbia gave an overview of the subject. The research group at the CSIRO Division of Energy Technology comprising P. I. Cooper, K. Hourigan, L. W. Welch, M. C. Welsh and others, also made a strong impression of their presence, complementing the keynote address given by M. Kiya.

A particularly strong contingent of delegates have their interest in Industrial Aerodynamics and Wind Engineering as indicated by the number of sessions under this heading. The high quality of papers presented was indicated by such speakers as Bill Melbourne of Monash University, Cliff Stevenson of Canterbury University, Jonathan Watmuff of Princeton University, and Colin Apelt of Queensland University.

Bob Antonia and his group at Newcastle University contributed papers on various aspects of turbulent flow. M. Lesieur of Grenoble, France, presented his studies on isotopic turbulence, and Ken Bray of Cambridge University described two models of turbulent burning in premixed flames.

In multiphase flow, while Geoff Hewitt of Imperial College and UKAEA presented an up-to-date state-of-the-art account in two-phase flow studies in his keynote address, a strong contingent in this area included David Beattie and Vic Ilic of the Australian Atomic Energy Commission Research Establishment.

Numerical fluid mechanics was also strongly represented. Speakers included Clive Fletcher of Sydney University, Lawrie Doctors of the University of New South Wales, Gordon Mallinson of the University of Auckland.

There were many other topics, including the study of soil-water movement by John Philip of CSIRO Division of environmental Mechanics, deep water waves study by John Hogan of Oxford University, and the study of waves by means of microseism spectrum by Alick Kibblewhite of the Physics Department of Auckland University.

Thus the Conference convered a very wide range of topics in fluid mechanics. A total of over 140 papers were presented and these were published as a bound volume of Proceedings of over 630 pages and were issued to the delegates at the conference. Additional copies of the Proceedings are available, at a cost of NZ$55.00 (payable to University of Auckland), by writing to J. J. J. Chen, School of Engineering, University of Auckland, Auckland, New Zealand.

Apart from the technical sessions, a good time was had by all in the social programs. No technical sessions were scheduled for the afternoon of the third day of the Conference to enable delegates to take part in a Harbour Cruise in the Hauraki Gulf with wine and dinner served on Board. The Conference Dinner took place on Thursday evening and the highlight of the evening was the live performance by a Maori Concert Party which proved highly entertaining and was most appreciated by all, particularly our overseas visitors.

With the success of this 9th Autralasian Fluid Mechanics Conference, we look forward to the next one in three years time, to be held in Melbourne, Australia.

Robert V. Edwards, editor
Case Center for Complex Flow Measurements, Department of Chemical Engineering, Case Western Reserve University, Cleveland, Ohio

Report of the Special Panel on Statistical Particle Bias Problems in Laser Anemometry

This is the report of a special panel that met during the Second International Laser Anemometry Symposium at the 1985 ASME meeting at Miami Beach. The purpose of the panel was to create a consensus document outlining what a group of recognized experts in laser anemometry could agree was known about statistical particle bias in laser anemometry and for that panel to make recommendations for future work in the area. The reason for this extraordinary session was that the area of particle bias statistics tends to be a controversial one and an observer might conclude that there is little agreement on any of the aspects of the topic. Consequently, experimentalists may unnecessarily avoid using techniques that could improve the quality of their work.

We stress that the importance of statistical bias errors lies not in their magnitude, but in the fact that they are systematic. In the limit of zero statistical error, bias errors remain. Further, since the bias errors are a function of the flow velocity and the turbulence intensity, the measured results may contain apparent trends that are artifacts of the measurement process.

This is a consensus document and where disagreements still exist, the panel recommends caution and that further study be made.

The members of the panel were (in alphabetical order:)
Ronald Adrian – University of Illinois at Urbana-Champaign
Alain Boutier – O.N.E.R.A., France
Alexander Dybbs – Case Western Reserve University
John Eaton – Stanford University
Robert V. Edwards, Panel Chairman – Case Western Reserve University
William George – University at Buffalo, SUNY
James Meyers – NASA Langley Research Center
Warren Stevenson – Purdue University
William Yanta – Naval Surface Weapons Center

Terminology

The panel felt that a central cause of some of the confusion regarding particle statistics was the existing, imprecise terminology in the field. Therefore one of its first tasks was to suggest a terminology for future discourse in the area. Unless otherwise noted, the assumption in this paper is that a one-dimensional laser anemometer is being used. The signals from the photodetector are processed by a burst mode detector. In principle, all of the rates referred to below are functions of the velocity.

Rates

$\dot{N}_0$ *Particle Arrival Rate.* This is the rate that measurable particles pass through the measurement volume. It is calculated using the particle number density, the laser power, the optical setup, and particle size distribution. It reflects the number of particles that could be measured by an ideal laser anemometer. This rate does not depend on the processor settings.

$\dot{N}_1$ *Trigger Rate.* Rate of events that trigger the burst processor. This rate depends on the processor threshold setting. Note that every particle that triggers the processor will not result in a successful measurement. The measurement may be rejected by the processor's validation circuit.

$\dot{N}_2$ *Validation Rate.* Rate that a free running burst processor measures particles. This is the number that appears on some counters as the validation rate. The validation rate does depend on the burst processor settings. For instance, when a counter is used the validation rate is influenced by the comparison tolerance and the threshold settings. If only one measurement is made per particle, $\dot{N}_1$ is the upper limit for this rate. For various reasons, it is possible that not all of the successful measurements are stored or used in subsequent algorithms, so that one more rate definition is necessary. In general, $\dot{N}_2$ is a function of velocity.

$\dot{N}_3$ *Stored Data Rate.* Rate that measurements are stored in memory or used by algorithms inside a computer. This rate can differ from $\dot{N}_2$ for many reasons. If the validation rate is higher than the rate that the measurements can be stored for processing, some measurements from the burst processor will be missed. In another case, the system may only store velocity measurements made at regular time intervals; the so-called controlled processor. Such modifications in the measurement rate can be accomplished with either hardware or software. Therefore, in this report we make no distinction between hardware and software rate modifications.

Scales

T_λ *Taylor Time Microscale.* It is a measure of the time that the flow needs to change one standard deviation. In terms of the flow Eulerian flow parameters.

$$T_\lambda = \sigma_v / (< \left(\frac{dv}{dt}\right)^2 >)^{1/2}.$$

The brackets, $< >$, denote the expected value of the enclosed expression. There is an implicit assumption that stationary

Contributed by the Fluids Engineering Division and presented at the Winter Annual Meeting, Miami Beach, Fla., November 17-22, 1985 of THE AMERICAN SOCIETY OF MECHANICAL ENGINEERS. Manuscript received by the Fluids Engineering Division December 1986.

systems are being discussed so that no distinction is made between time averaging and ensemble averaging. The parameter σ_v is the flow r.m.s. variation. The Taylor microscale has also been described as the time scale over which there is no significant change in the energy of an eddy.

T_u Flow Integral Time Scale. Flow Memory Time.
$T_u = \int_0^\infty R_{uu}(\tau)d\tau$, where R_{uu} is the normalized Eulerian fluctuation autocorrelation function.
L_λ Taylor Micro-Length Scale.
L_u Integral Length Scale.

Magnitude of Data Rates

One often finds the terms "high data rate," "low data rate," etc. in the literature. The panel contends that these terms have no objective meaning unless the data rate is compared to one of the relevant flow time scales. The natural flow scale to compare the data rate to is the Taylor microscale, T_λ. Adrian (1983) explains this and defines $\dot{N}_2 T_\lambda$ to be the "data density" as opposed to a dimensional data rate. In the rest of this document, we will define:

High Data Density $\dot{N}_2 T_\lambda > 5$.
Intermediate Data Density $5 \geq \dot{N}_2 T_\lambda \geq .05$.
Low Data Density $.05 \geq \dot{N}_2 T_\lambda$.

Since $\dot{N}_2$ is a function of velocity, the above definitions are referenced to the highest and lowest significant velocities present in the flow. In many systems only the mean value of $\dot{N}_2$ is available. When that is the case, conservative estimates of the upper and lower rates should be made by assuming that the validation rate is proportional to the absolute value of the speed measured. Experience has indicated that when the turbulence intensity is less than 30 percent, it is safe to use the average value of $\dot{N}_2$.

Sources of Statistical Bias

The sources of statistical bias that were considered by the panel were:

Velocity Bias. A succinct statement of the problem is as follows:

A burst mode (or individual realization) laser anemometer operates on the signals generated by single particles passing through the measurement volume and produces a measurement of the velocity of the particle while it is in the volume. There are, however, very few circumstances where those realizations can simply be averaged arithmetically to obtain statistical measures of the velocity. The arrival rate of the measurable particles is, in general, not statistically independent of the flow velocity which brings them to the measurement volume. The result is that the flow statistics are not uniformly sampled and as a consequence, simple averaging of the particle measurements can be, and often is, seriously biased.

The panel believes that for turbulent flow, individual realizations can be properly averaged only if they are used to reconstruct a time series with the same statistics as that of the flow. There are a variety of ways this can be done – all of which avoid bias in given situations. There are two classes of techniques which can be identified. The first class consists of those techniques that are valid only when the average time between samples is small compared to the micro-time scales of the flow, i.e., the data density is intermediate to high. The second class of techniques are valid at all data densities, but are somewhat more difficult to implement. The primary purpose of this document is to detail these various techniques and their regions of validity.

One can estimate whether particle bias is of concern, in a particular instance, by using the McLaughlin and Tiedermann (1973) formula as follows.

$\langle v \rangle_m \simeq \langle v \rangle (1 + \sigma_v^2 / \langle v \rangle^2)$, where the m subscript denotes the measured mean velocity, $\langle v \rangle$ is the true mean velocity and σ_v^2 is the flow variance. The expression states that the bias is on the order of the square of the turbulence intensity. Since $\dot{N}_2$ is not always proportional to the measured velocity component, the bias encountered in practice can be higher or lower than this. This expression thus should only be used to estimate the magnitude of the possible problem.

Filter Bias. This error occurs because of the tendency of real systems to have a measurement efficiency that is dependent on the speed of the measured particle. The two primary causes of this effect are the frequency response of the detection system and the filter settings on the burst processor [Durao and Whitelaw (1979)]. A particle that generates a frequency that is outside the system's optimal response range can fail to exceed the processor's threshold or otherwise fail to be successfully processed. This can distort the measurement statistics over that computed from velocity bias considerations (see above). In fact, the tendency for real systems to have a decreased efficiency at high frequencies can mitigate the tendency of high speed flows to have a higher measurement rate than low speed flows. The filter settings on the processor can have an even more profound effect. A particle with a velocity that generates a frequency outside of the filter setting range can be missed entirely by the processor.

The panel has no specific recommendation for dealing with Filter Bias except to urge that the experimentalist take care that the frequency response of his system is flat in the region of measurement. All velocities present in the flow must be measurable. No correction scheme can reasonably correct for missing velocities.

Angle Bias (sometimes called Fringe Bias). This error is caused by the fact that real processors cannot measure all speeds at all angles. For instance, counters are usually set so that a preset number of fringes must be encountered by a particle before a measurement is considered valid. Even if a Bragg cell is used, there can exist particle trajectories that do not satisfy the processor's present criteria. In a properly configured system, there will be no velocities present that are outside of the measurable range. The flow angle range over which a given system will measure is called the *acceptance angle* of the system.

Gradient Bias. This error occurs in a mean gradient in the flow. The measurement volume is always finite in size and thus several velocities can be present in it at the same time. As before, the measurement rate for a given velocity can be correlated with that velocity and again the arithmetic average of the measurements is not the same as the average in the measurement volume. At this point, Gradient Bias is distinguished only in that the error is not caused by velocity *fluctuations.*

Processing Methods for Elimination of Velocity Bias

Several algorithms or processors are in existence that are used to construct a time series from the measured data and thus to correct for the effect of the particle arrival statistics. Since any of these methods can be implemented either in hardware or in software, we make no distinction between them here. They are all called processors. For instance, the controlled processor described below can be created either by gating a counter at regular intervals or by recording all the measurable particle velocities along with the time of the measurement. A regularly sampled signal can then be constructed in a computer using the recorded velocities and the measurement times.

The processes discussed in this section are for treatment of velocity bias only.

•*The Controlled Processor.* [Erdmann and Tropea (1981), Edwards (1981)]. This processor divides time into equally spaced intervals of T seconds. Only the first particle measured during each time interval is stored and used in the subsequent algorithms. See Fig. 1. When the time interval T is small compared to the flow microscale, ($T << T_\lambda$), and the data density

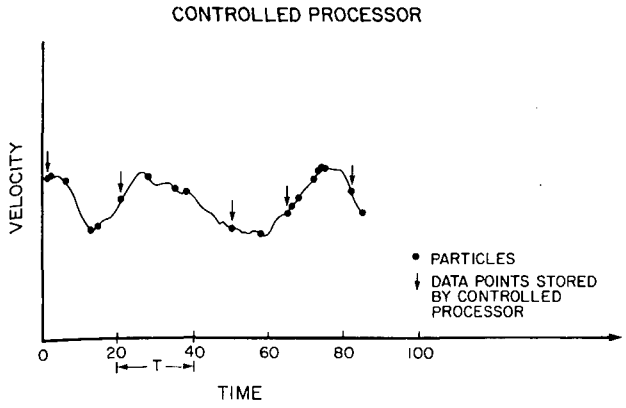

Fig. 1

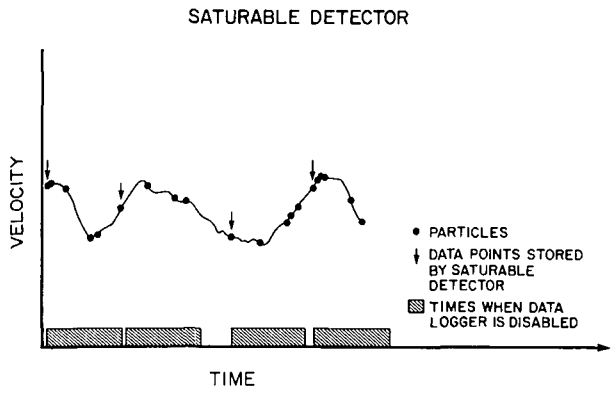

Fig. 2

is high for all velocities of interest, ($\dot{N}_2 T > 5$), the procedure approaches that of uniform sampling a continuous data record with time interval T. Hence, one can construct a time series whose statistics are indistinguishable from those of the flow. Essentially, the rate is high enough that a measurement is obtained for every measurement interval, making the sampling procedure independent of the velocity. Of course, any flow information above a frequency of $1/2T$ is lost because of the sampling procedure. *This processor is recommended for high data densities.* With the proviso that the filters are set so that the data density for all velocities present in the flow exceeds the requirements set above, the processor is also insensitive to the distortions caused by filter bias errors.

•*The Saturable Detector.* The data logger will record no additional measurements for T seconds after a measurement is recorded. See Fig. 2. A finite speed computer buffer behaves this way. It can only record another reading when the buffer is "ready". Under the same conditions as the controlled processor (i.e., high data density. $\dot{N}_2 T > 5$ and $T_\lambda >> T$), this method will generate a time series that has statistics identical to those of the flow [Stevenson et al. (1980), Johnson et al. (1982), Edwards and Jensen (1983)]. *This method is recommended for high data densities.* Again given that all velocities present in the flow are measured at the appropriately high rate, this method is also insensitive to filter bias errors.

•*Sample and Hold.* A continuous analog signal is created by holding the last measurement value until a new measurement is obtained. See Fig. 3. A variation on this scheme is to interpolate between measurement points by a trapezoid or other spline fit. When the data density is high, $\dot{N}_2 T_\lambda > 5$, the statistics of the reconstructed signal are identical to those of the flow up to a frequency of $1/\dot{N}_2$ [Dimotakis (1976), Edwards and Jensen (1983), Adrian and Yao (1987)] *This method is recommended for high data densities.* This method is insensitive to filter bias errors if all velocities present are measured at the above rate.

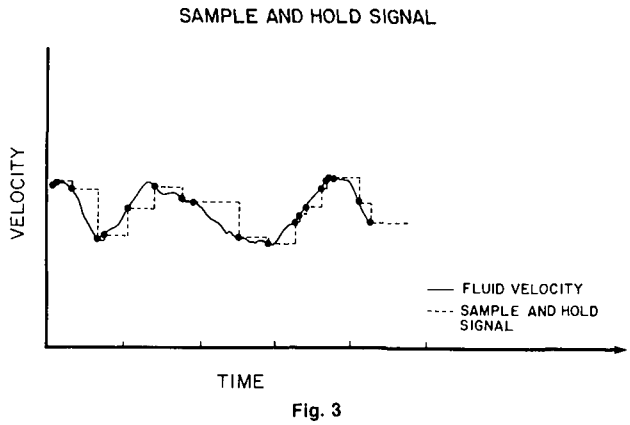

Fig. 3

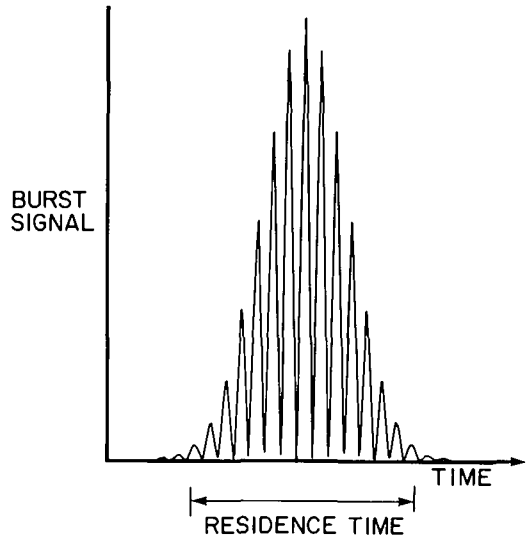

Fig. 4

The following are all methods that attempt to generate correction factors for the individual velocities that are used to compute the mean flow quantities. Define the following.

The particle mean nth moment, $\langle v^n \rangle_m$.

$$\langle v^n \rangle_m = \left(\sum_{k=1}^{N} v_k^n \right) / N \tag{1}$$

The corrected mean nth moment, $\langle v^n \rangle$.

$$\langle v^n \rangle = \left(\sum_k W_k v_k^n \right) / \sum_k W_k \tag{2}$$

where W_k is the appropriate weighting factor for the kth velocity measurement.

•*McLaughlin and Tiedermann Correction.* [McLaughlin and Tiedermann (1973), Buchhave (1976)]. This method uses the inverse of the particle's speed or velocity component as a weighting factor for each measured velocity, $W_k = 1/|v_k|$. The basic assumptions of this method are that the seed number density is spatially uniform, that the effective measurement volume is spherical, and that the acceptance angle is 4π steradians. Since all the velocity components are not always available to the user, so-called one and two dimensional versions of the correction have been used. The one dimensional form uses the absolute value of one velocity component to approximate the speed. The two dimensional method uses two measured components to estimate the speed, i.e., $|(v_{1k}^2 + v_{2k}^2)^{1/2}| \simeq |v_k|$. Since the two dimensional method can sometimes increase the error over that obtained in applying no correction, the panel felt that it is *not recommended.* The

panel could not agree to recommend any version (1-D, 2-D, or 3-D) of this correction method.

•*Residence Time Weighting*. Here, the amount of time that a particle spends in the measurement region is measured in addition to the particle's velocity (See Fig. 4). [Buchhave et al. (1979)] denote the residence time for the kth measured velocity by $T_b(v_k)$. The corrected moments (including the autocorrelation function) of the flow can be computed by setting $T_b(v_k)$ equal to W_k in equation (2).

This Method Has a Qualified Recommendation for All Data Densities. The qualifications are that the user must be sure that the particle seeding density is spatially uniform, that filter bias effects are not present and that the processor used gives an accurate estimate of the residence time. At present, off-the-shelf counters do not always give accurate burst times.

•*Rate Measurement*. Here the measurement rate corresponding to each velocity is either computed or measured. The computational method consists of computing $\dot{N}_0(v_k)$, [Dimotakis (1976)], the expected arrival rate for the kth velocity realization v_k from the theoretical model. One then assumes that the measurement rate for each velocity is proportional to $\dot{N}_0(v_k)$. The correct moments are computed by using equation (2) with $W_k = 1/\dot{N}_0(v_k)$. *This method has the qualified recommendation of the panel*. The qualifications are that the user be assured of uniform spatial particle seeding and that filter bias effects are negligible.

Alternatively, under some circumstances, namely moderate to high data densities, $\dot{N}_2 T_\lambda > .05$, the rate for each velocity can be estimated [Meyers and Edwards (1983), Chen and Lightman (1985)]. The conditional interarrival time distribution for a velocity v_k, $I(\tau;v_k)$ is defined as the probability of another measurement τ seconds (the interarrival time) after a measurement of v_k has been made. The measurement rate for velocity v_k, $\dot{R}(v_k)$, is the limit of the interarrival time distribution as the interarrival time goes to zero. The interarrival time distribution is a measurable quantity, thus the moments can be corrected using equation (2) with $W_k = 1/\dot{R}(v_k)$. See Appendix 1 for details of this method). *This method is recommended for high and intermediate data densities*. Provided all velocities present in the flow are measured with a high enough rate, it is insensitive to filter bias effects.

Angle Bias

The best method to handle angle bias is to ensure that the measurement system is capable of measuring all flow angles that are likely to be encountered in the flow with equal probability. In a fringe anemometer, this often means using a Bragg cell to move the fringes within the measurement volume [Whiffen (1976), Buchhave et al. (1979), Stevenson (1982)]. *The panel recommends that these papers be read and heeded*. The effective fringe velocity should be at least twice the maximum Doppler shift to provide uniform angular response. Fringe biasing can also be ameliorated by reducing the required number of fringes for processing, or by using a variable fringe number mode. At present, there is no Bragg cell equivalent for a two-spot anemometer, thus no specific recommendation can be given for these devices at this time.

Additional Recommendations

1. Given the myriad of processes that can affect the measurement statistics, a given experiment will not be interpretable unless the relevant parameters are known, recorded, and reported.

Seeding Parameters. One should know and report the uniformity of the number density of the seed particles. For instance, in a jet the core and surrounding fluid must be seeded separately and thus the seed number density in the two regions may not necessarily be the same. The mean measurement rates, $\dot{N}_2$ and $\dot{N}_3$, should be recorded and reported along with estimates of T_λ. The effective particle size distribution should also be reported. The panel recognizes that this may be difficult, but suggests that every experimenter at least estimate the size distribution and report his method for forming the estimate.

System Parameters. The properties of the data recorder, such as speed and capacity, should be reported as these can have a profound influence on the results. The processor settings such as the number of fringes required for a successful measurement, the Bragg cell frequency, the filter settings and the deadtime should also be reported. Some estimate of the flow time scales should always be given, since these affect all processing schemes.

The type of processing scheme used should always be reported.

2. The panel was aware of many areas that are of concern where more work is needed. These are listed below.

Gradients. Although gradients are known to be a source of bias errors, there is little in the literature covering this problem. In addition to theoretical work, experiments need to be performed where this effect and the possible cures are clearly demonstrated.

Rapid Procedures for Measuring Estimates of the Flow Time Scales. Many experimenters do not have the facilities to measure correlation functions or spectra and thus need an inexpensive and rapid method of estimating their flow time scales.

Verification of Angle Bias Correction Procedures. Although the panel had confidence in the theoretical results [Whiffen (1976), Buchhave (1979), Stevenson (1982)] on eliminating angle bias, it felt that some careful experimental verification was still needed.

Controlled Processor in Low and Intermediate Seeding Rate Systems. There is a claim that the controlled processor can eliminate velocity bias at any data density, if the sampling time is increased so that the probability of getting a measurement every interval is high [Erdmann and Tropea (1981)]. This claim has never been experimentally verified and some members of the panel questioned its derivation. Given the wide currency of the truth of this claim and its possible value, if true, the panel urges further work on the method.

Reliable Procedures for Measuring Reynolds Stresses. Several panel members report problems in the accurate measurement of Reynolds stresses, particularly in three-dimensional flows [Driver and Hebbar (1985), Bell et al. (1985), Barlow and Johnston (1985)]. In cases in which careful comparisons to hot wire and other measurements have been made, the LDA systems consistently underestimates the shear stress. The measurements appear to depend strongly on the coincidence window and on the validation rate. Both new theory and experiment are needed here.

Seeder. It is clear that all the possible bias mechanisms would be easier to deal with if there existed an inexpensive seeder that was capable of generating monodispersed seed particles fast enough that the measured data density was above one. This is a HIGH PRIORITY.

References

Adrian, R. J., 1983, "Laser Velocimetry," in *Fluids Mechanics Measurements*, ed. R. J. Goldstein, Hemisphere Publishing Corp., pp. 155-244.

Adrian, R. J., and Yao, Y. S., 1987, "Power Spectra of Fluid Velocities Measured by Laser Doppler Velocimetry," in *Experiments in Fluids*, 5, 17-28 (1987).

Barlow, R. S., and Johnston, J. P., 1985, "Structure of Turbulent Boundary layers on a Concave Surface," Rept. MD-47, Dept. of Mech. Engr., Stanford University, August.

Bell, J. H., Rodman, L. C., and Mehta, R. D., 1985, "Aspects of the Design and Performance of a 3-Component LDV System," paper presented at 11th ICIASF Meeting on Instrumentation, Stanford University, August.

Buchhave, P., 1985, "Bias Errors in Individual Particle Measurements With

the Laser LDA-Counter Processor in the Accuracy of Flow Measurements by Laser-Doppler Methods," *Proceedings of LDA Symposium Copenhagen*, pp. 258-278.

Buchhave, P., George, W. K., Lumley, J. L., 1979, "The Measurement of Turbulence with the Laser-Doppler Anemometer," *Annual Review of Fluid Mechanics*, Vol. 11, Annual Reviews Inc., Palo Alto, CA, pp. 443-503.

Chen, T-H., and Lightman, A. J., 1985, "Effects of Particle Arrival Statistics on Laser Anemometer Measurements," in *International Symposium on Laser Anemometry,"* ed A. Dybbs and P. A. Pfund, ASME FED-Vol. 33.

Dimotakis, P. E., 1976, "Single Scattering Particle Laser Doppler Measurements of Turbulence," Applications of Non-Intrusive Instrumentation in Fluid Flow Measurement, AGARD CP-193.

Driver, D. M., and Hebbar, S. K., 1985, "Experimental Study of a Three-Dimensional, Shear-Driven, Turbulent Boundary Layer Using a Three-Dimensional Laser-Doppler Velocimeter," AIAA-85-1610, presented at AIAA 18th Fluid Dynamics and Plasmadynamics and Lasers Conference, Cincinnati, Ohio, July.

Durao, D. F. G., and Whitelaw, J. H., 1979, "Relationship Between Velocity and Signal Quality in Laser Doppler Anemometry," *Journal of Physics E: Scientific Instruments*, Vol. 12, No. 1, pp. 47-50.

Edwards, R. V., and Meyers, J., 1983, "Particle Bias in Perspective," *Proceedings of LADOAN 1983*, Lisbon.

Edwards, R. V., Jensen, A. S., 1983, "Particle Sampling Statistics in Laser Anemometers: Sample-and-Hold Systems and Saturable Systems," *J. Fluid Mech.*, Vol. 133, pp. 397-411.

Edwards, R. V., 1981, "A New Look at Particle Statistics in Laser Anemometer Measurements," *J. Fluid Mech.*, Vol. 105, pp. 317-325.

Erdmann, J. C., and Tropea, C., 1981, "Turbulence Induced Statistical Bias in Laser Anemometry," *Proceedings of the Seventh Symposium on Turbulence*, University of Missouri-Rolla, September.

Johnson, D. A., Moddarress, D., and Owen, F., 1982, "An Experimental Verification of Laser Velocimeter Sampling Bias and Its Correction," *Engineering Applications of Laser Velocimetry*, ASME, New York, pp. 153-162.

McLaughlin, D. K., and Tiedermann, W. G., Jr., 1973, "Biasing Correction for Individual Realization of Laser Anemometer Measurements in Turbulent Flow," *The Physics of Fluids*, Vol. 16, No. 12, pp. 2082-2088.

Stevenson, W. H., Thompson, H. D., Bremmer, R., and Roesler, T., 1980, "Laser Velocimeter Measurements in Turbulent and Mixing Flows-Part II," Air Force Tech Rept. AFAPL-TR-79-2009, Part II.

Stevenson, W. H., Thompson, H. D., and Roesler, T. C., 1982, "Direct Measurement of Laser Velocimeter Bias Errors in a Turbulent Flow," *AIAA Journal*, Vol. 20, December, pp. 1720-1723.

Whiffen, M. C., 1976, "Polar Response of an LV Measurement Volume," in "Minnesota Symposium on Laser Anemometry Proc. -1975," ed. E.R.G. Eckert, University of Minnesota, Dept. of Conferences, Minneapolis.

APPENDIX I

Measurement of the Measurement Rate for Velocity v_k

The conditional interarrival time distribution for velocity v_k, $I(\tau;v_k)$ is defined as the probability of measuring another particle in the time interval τ, $\Delta\tau$ after the velocity v_k has appeared. One practical problem with measuring this function with a laser anemometer is that the chances of getting the same velocity more than once are negligible. Therefore one must compromise and divide the measured velocity range into subranges and then measure the interarrival time distributions for each subrange. The subranges should be smaller than the R.M.S. fluctuation at that point. Ten or fewer divisions are recommended.

1. Denote the mth velocity range R_m.
2. Pick a time $\Delta\tau$ that is small compared to T_u, but larger than the reset time of the data logger. (More on this later.)
3. Measure the number of particles that occur in the time intervals $(\Delta\tau,2\Delta\tau)$, $(2\Delta\tau,3\Delta\tau)$, $(3\Delta\tau,4\Delta\tau)$ . . . after a velocity is recorded in the interval R_m. In general, you will find that if the subinterval R_m is below the mean velocity, the number of measurements will initially increase as the time lag increases, and the number of measurements will decrease if the subrange is above the mean.

The estimated rate for the mth velocity subinterval, $\dot{R}_m$ is obtained by extrapolating the number of measurements in the intervals to zero time. This number divided by $\Delta\tau$ is the rate $\dot{R}_m$. The estimated measurement variance of the rate divided by the square of the rate is the number of times that the subinterval R_m is encountered. i.e., $\sigma^2_{\dot{R}_m}/\dot{R}^2_m \simeq 1/N_m$, where $\sigma^2_{\dot{R}}$ is the measurement variance and N_m is the number of times that a velocity was found in subinterval R_m.

A rough estimate of an appropriate time scale to use for this procedure can be obtained by calculating the average time that the velocity remains in each of the velocity subintervals.

Lateral Fluid Forces on Whirling Centrifugal Impeller (1st Report: Theory)

H. Shoji
Lecturer,
Institute of Engineering Mechanics,
University of Tsukuba,
Ibaraki-ken, 305 Japan

H. Ohashi
Professor,
Department of Mechanical Engineering,
University of Tokyo,
Tokyo, 113 Japan

Lateral fluid forces acting on a rotating centrifugal impeller in whirling motion are analyzed using unsteady potential flow theory. Impellers operating in diffusers with and without vanes are modeled and the fluid forces calculated for different whirl speeds and flow rates. The influences of these parameters are clarified by parametric calculations. The results for whirling impellers operating in vaneless diffusers show that the fluid forces exert a damping effect on the rotor whirling motion at all operating conditions. The results for impellers operating in vaned diffusers or guide vanes show that the time averaged values of fluid forces remain almost unchanged, while there are significant instantaneous fluctuations due to the impeller/guide vane interactions.

Introduction

The rotordynamic stability of the rotating shaft of high performance turbomachines is as important as its fluid dynamic performance. This is especially true for the case of high-speed multistage centrifugal pumps and compressors whose rotors are usually less rigid than in other machines. The rotordynamic behavior of such systems must be studied to enable accurate estimates of their response to unblanced mass and to seismic loads.

It is necessary for the stability analyses of centrifugal rotors to estimate the fluid dynamic forces acting on each element of the vibrating rotor such as journal bearing, wear ring, throttle bushing, balance piston and centrifugal impeller. Among these elements, the fluid forces on journal bearings have been studied most extensively. Bearing data are available for various geometric parameters in the form of stiffness and damping constants (Someya 1987) and solutions are available for instability problems like oil whip such as observed in journal bearings. This has been accompanied by progress in the study of the fluid forces on annular pressure seals such as wear rings and throttle bushings (Black 1969, Iino 1980, Childs 1984).

Many studies have been made on the steady lateral fluid forces which act on the centrifugal impeller caused either by azimuthally asymmetric configuration of volute casing or by misalignment of impeller and guide vanes (Hergt 1969, Domm 1970). When a rotating shaft with a centrifugal impeller whirls as shown in Fig. 1, the impeller motion is the resultant of the shaft center whirl and the shaft rotation. In this case the flow around the impeller becomes unsteady and asymmetric, in spite of the fact that its casing is completely symmetric. This causes unsteady fluid forces acting on the impeller. The force component normal to the shaft is denoted as lateral force. This component plays a predominant role in the shaft vibration in bending mode.

The present study deals with the lateral fluid forces on centrifugal impellers for the case of impeller whirling on a circular orbit with a constant eccentricity. The lateral force component is further divided into normal and parallel components relative to the whirl motion. The influence of impeller geometry, ratio of whirl speed to impeller speed, and flow condition (flow coefficient) etc. are investigated theoretically in this article and experimentally in the following article.

In this study, an unsteady incompressible potential flow theory is introduced to estimate the fluid forces on a two-dimensional centrifugal impeller whirling on a circular orbit with a constant whirl speed. This theory takes into consideration shed vortices from the impeller vanes. In the accompanying article, the 2nd Report, an experimental study of these fluid forces is presented for two-dimensional impellers whirling in vaneless diffusers along with comparisons between theory and experiment.

Previous researchers have modeled the unsteady part of lateral forces, which occur from the whirling motion of a rotating impeller or to the interaction between impeller and

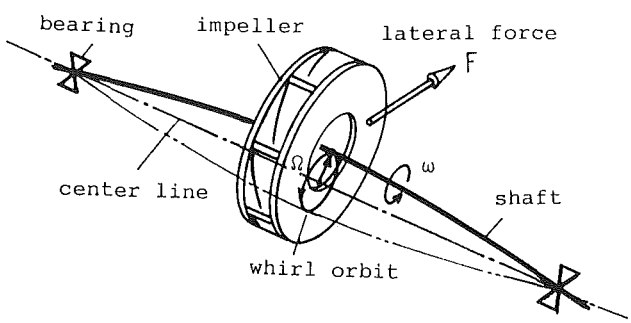

Fig. 1 Centrifugal impeller in whirling motion

Contributed by the Fluids Engineering Division for publication in the JOURNAL OF FLUIDS ENGINEERING. *Manuscript received by the Fluids Engineering Division, January 30, 1986.*

guide vanes. Chamieh (1983) applied an actuator disc model to the calculation of lateral forces on a whirling centrifugal impeller in a volute. The result of this analysis was, however, unable to explain the measured behavior of tangential force properly. This actuator disc model was later improved by Tsujimoto, Acosta and Brennen (1986) and the calculated radial and tangential forces where shown to qualitatively agree with experimental measurements.

Thompson (1978) has treated the case of an unbounded centrifugal impeller under the assumption of quasi-steady flow. The perturbed flow in each impeller passage was solved by the streamline curvature method. This calculation proved that whirl-exciting fluid forces occur for some impeller parameters. Since it is questionable whether a quasi-steady theory is realistic for this kind of highly unsteady problem, no generalizations were given.

Colding-Jorgensen (1980) treated the case of a whirling centrifugal impeller in a spiral volute casing under the assumption of quasi-steady flow. In their analysis the casing was replaced by distributed vortices, and the impeller by a point source with constant circulation. Although the theory succeeded in determining the stiffness and damping coefficients of fluid forces, the results should be carefully checked since the theory is based on a simple flow model. Allaire et al. (1984) has reported a theory using a finite element model of a full impeller.

The authors (1980) earlier treated the case of whirling centrifugal impeller in a vaneless diffuser using the singularity method for the whole flow field including shed vortices. This theory was restricted to the case of shockfree entry to the leading edge of impeller vanes. The theory presented in this paper is not restricted to shockfree entry condition. It is used to treat the case in which the impeller whirls in a vaned diffuser or in an asymmetric volute casing under the assumptions of two-dimensional, inviscid, incompressible flow.

Whirling Motion and Lateral Force

The bending mode vibration of a rotating shaft typically appears as a whirling motion with an elliptical orbit as shown in Fig. 1. If we consider the simple case of a circular orbit, the plane motion of the impeller is illustrated in Fig. 2. The impeller rotates counterclockwise with angular speed ω around its center 0, which revolves with angular speed Ω around its absolute center 0′ along a circular orbit with eccentricity $|\epsilon|$. Positive whirl occurs, when the shaft whirls in the same direction as its rotation, and negative whirl occurs when the shaft whirl is in the opposite direction.

When an impeller rotates without whirl in a vaneless diffuser or in the center of a vaned diffuser, the flow around the impeller becomes azimuthally symmetric and no lateral force acts on the impeller. However once a whirling motion occurs,

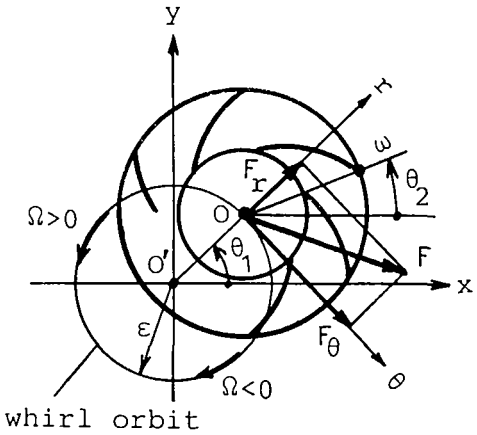

Fig. 2 Fluid forces acting on impeller

the flow becomes asymmetric and causes an unsteady lateral force **F**. This lateral force is further divided into radial and tangential components relative to the orbit as shown in Fig. 2. Here an outward radial force F_r is taken as positive. To avoid confusion the fluid force normal to the shaft is called lateral force instead of the commonly used radial thrust.

The radial force component F_r applies a bending moment to the shaft and influences the shaft's natural frequency in bending. The tangential force component F_θ acts parallel to the motion of shaft center 0, and thus transfers kinetic energy to the whirling rotor. In positive whirl, a positive F_θ acts against the whirl velocity and exerts a stabilizing or damping effect, while a negative F_θ exerts a destablizing or excitatory effect. In negative whirl these effects are reversed. When the tangential force becomes excitatory and feeds more kinetic energy to the whirling shaft than it damps out, a severe impeller-induced self-excitation, or impeller whip occurs which is similar to oil whip.

In the absence of external forces, the bending mode frequency of whirling motion is equal to the natural frequency or critical speed of the shaft. Therefore, the case of whirl speed ratio $|\Omega/\omega|>1$ corresponds to subcritical, while $|\Omega/\omega|<1$ corresponds to supercritical rotational conditions. When the shaft experiences forced vibration due to an external force like a seismic load, the whirling frequency coincides with that of the external force. In this study the range of whirl speed ratio, covering positive to negative ratios, was selected to deal with these possible cases.

Major Assumptions

Since the flow around a real centrifugal impeller in whirling

Nomenclature

b = vane width
$\mathbf{F}$ = fluid force vector
$\mathbf{f}$ = nondimensional fluid force vector
M = mass of the fluid displaced by the projected volume of impeller vanes
M_a = apparent mass of impeller calculated by potential theory
N = number of vanes
Q = flow rate
r_1 = inner radius of impeller
r_2 = outer radius of impeller
r_3 = inner radius of guide vanes
r_4 = outer radius of guide vanes
v = complex expression of velocity
z = complex expression of position
$\bar{z}$ = complex conjugate of z
β = angle between radius and vanes
γ = vortex distribution
ϵ = complex expession of eccentricity
ρ = density of fluid
ϕ = flow coefficient
Ω = angular speed of whirling motion, positive counterclockwise
ω = impeller angular speed of rotation, positive counterclockwise

Subscripts

a = free vortices
G = guidevane
r = radial component
sf = shockfree entry condition
T = trailing edge of vane
θ = tangential component

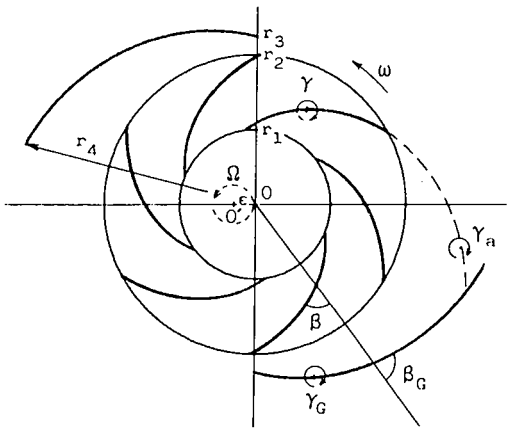

Fig. 3 Impeller surrounded by guide vanes

motion is very complex, in the present theory the following simplifications and assumptions are introduced:

(1) The flow is assumed inviscid, incompressible, two-dimensional and irrotational in the absolute coordinate system.

(2) Flow rate, rotational speed, eccentricity, and whirl speed of orbital motion are assumed to be constant.

(3) The ratio of whirl eccentricity to the radius of the impeller is assumed to be very small.

(4) The geometries of impeller vanes and guide vanes are taken as logarithmic spirals with no thickness.

(5) Interaction of impeller to guide vanes is neglected, so that guide vane circulation is steady and constant.

(6) Each impeller vane wake is replaced by a distributed free vortex which is shed from the trailing edge and carried downstream along the streamlines of steady flow with the local steady flow velocity.

Assumption (5) deserves some comment. In actuality, impeller and guide vanes interact with each other, and the distribution of vortices on the impeller and guide vanes becomes unsteady. But unless the impeller and guide vanes clearance is very small, the contribution of this interaction to the lateral fluid force is considered to be small. In this study, this interaction is neglected and the vortex distribution on the guide vanes is assumed to be steady and constant.

Figure 3 shows the centrifugal impeller considered here. The impeller is surrounded by a vaned diffuser and rotates at a constant angular speed ω, while its center 0 whirls at a constant angular speed Ω along a circular orbit with a fixed center 0′. The vaneless diffuser problem can be treated as a special case of the vaned diffuser problem. A relative coordinate systems fixed to the impeller is used in the impeller flow analysis. The absolute center 0′ and guide vanes rotate around the impeller center 0. All vectorial quantities such as position, velocity, and force are expressed by corresponding complex numbers.

Unsteady Flowfield

Let the position vector of 00′ in the relative coordinate system be ϵ; then ϵ is given by

$$\epsilon = |\epsilon| e^{i(\Omega-\omega)t} \tag{1}$$

An arbitrary point on the guide vanes rotating around 0′ at speed ω, is described by:

$$z_G = \epsilon + z_{G0} e^{-i\omega t} \tag{2}$$

where z_{G0} is the position vector of the same point in the absolute coordinate system.

The singularity method is applied to this problem. The flow rate Q is replaced by source Q/b at 0′ and impeller and guide vanes are replaced by the distribution of vortices, γ and γ_G. When the impeller whirls, free vortices are shed from the trailing edges of the impeller vanes.

The distribution of vortices γ on the impeller has to satisfy the boundary condition that there is no flow through the vanes. This leads to

$$\mathrm{Im}[\{v_Q(z_1)+v_\omega(z_1)+v_\Omega(z_1)+v_\gamma(z_1)+v_a(z_1) + v_G(z_1)\}(\bar{z}_1/|z_1|)e^{i\beta}]=0 \tag{3}$$

where, z_1 is an arbitrary point on the vanes and $v_Q(z_1)$, $v_\omega(z_1)$ and $v_\Omega(z_1)$ represent the complex velocities caused by Q, ω and Ω, respectively.

These velocities are expressed further as

$$v_Q(z_1) = \frac{Q/b}{2\pi(\bar{z}_1-\bar{\epsilon})} \tag{3a}$$

$$v_\omega(z_1) = -iz\omega \tag{3b}$$

$$v_\omega(z_1) = i\epsilon\Omega \tag{3c}$$

$v_\gamma(z_1)$, $v_a(z_1)$, and $v_G(z_1)$ represent the complex velocities induced by the distribution of vortices γ, γ_a, and γ_G. They are expressed as

$$v_\gamma(z_1) = \sum^N \int_S \frac{-i\gamma(s)}{2\pi}\frac{1}{\bar{z}_1-\overline{z(s)}}\,ds \tag{3d}$$

$$v_a(z_1) = \sum^N \int_{S_a} \frac{-i\gamma_a(s)}{2\pi}\frac{1}{\bar{z}_1-\overline{z(s)}}\,ds \tag{3e}$$

$$v_G(z_1) = \sum^N \int_{S_G} \frac{-i\gamma_G(s)}{2\pi}\frac{1}{\bar{z}_1-\overline{z(s)}}\,ds \tag{3f}$$

where the integral path S, S_a, and S_G represent the contour of impeller vanes, shed free vortices and guide vanes, respectively. The unknowns in equation (3) are γ, γ_a, γ_G and the contour of free vortices S_a.

According to assumption (5), the distribution of vortices on guide vanes γ_G is determined from the flowfield, where the impeller vortices are replaced by a time-averaged circulation concentrated at the fixed center 0.

The contour of free vortices S_a can be obtained by integrating their velocities. The strength of shed vortices from a trailing edge of impeller vane $\gamma_a(z_T)$ can be determined from γ and γ_a by applying Helmholz's law on the conservation of vorticity giving:

$$\frac{d\Gamma}{dt} = -\gamma_a(z_T)\,|dz_a/dt|_{z_a=z_T} \tag{4}$$

The above relation shows the amount of shed vortices per unit time is equal to the rate of change of impeller vane circulation.

Then the equation (3) can be considered as an integral equation to determine γ, since γ_a, γ_G, and S_a are known.

Unsteady Fluid Forces

In two-dimensional potential flow theory, the fluid force $\mathbf{F}(F_x, F_y)$ acting on an arbitrary body in an unsteady flow is obtained by applying the conservation law of momentum to a closed loop C enclosing the body,

$$F_x - iF_y = \frac{1}{2} i\rho \oint_C (dW/dz)^2 dz - i\rho \oint_C \bar{z}\overline{dW} \tag{5}$$

where W is the complex potential of the flow field.

Applying the above equation to the whirling impeller with the integration path shown in Fig. 4, the following relation is obtained by partial integration and the Cauchy-theorem (Imaichi 1980);

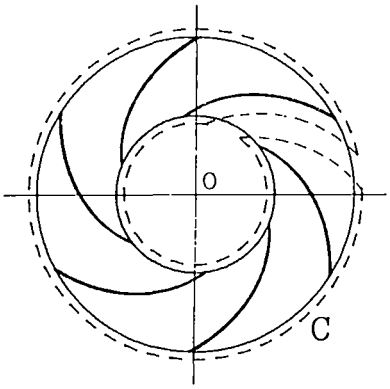

Fig. 4 Integration path

$$F_x - iF_y = -i\rho\Big[\sum^N \int_S \gamma(l)\Big\{\frac{Q}{2\pi}\frac{1}{z(l)-\epsilon} + \frac{i}{2\pi}\sum^N \int_{S_a}\frac{\gamma_a(s)}{z(l)-z(s)}\,ds\Big\}dl\Big] - i\rho\sum^N \int_S \gamma(l)\,(-i\omega\overline{z(l)} + \overline{i\Omega\epsilon})\,dl + i\rho\sum^N \int_S (\overline{z(l)-\epsilon})\,\frac{\partial\gamma(l)}{\partial t}\,dl - i\rho\sum^N (\overline{z_t}-\epsilon)\,\frac{\partial}{\partial t}\int_S \gamma(l)\,dl \qquad (6)$$

The first term represents the forces acting on the impeller vortices from the velocity induced by Q and γ_a, the second term is due to the rotation and whirling motion of the impeller while the third and forth terms represent the forces due to the change of vortex distributions.

The radial and tangential components of the fluid force, F_r and F_θ, can be obtained from F_x and F_y by

$$F_r - iF_\theta = (F_x + iF_y)\,|\epsilon|/(-\epsilon) \qquad (7)$$

The authors (1980) calculated unsteady force by the integration of pressure distribution on the vane surfaces. This method could be applied, only when the shockfree entry condition is satisfied. This restriction is removed by equation (6) which enable the influences of flow rate on fluid forces to be evaluated.

Method of Numerical Calculation

The vortex distributions on vanes and wakes are replaced in the calculations by a finite number of discrete vortices. In this way the integral equations are transferred into simultaneous equations. If γ is known at the time $t = t$, the strength of vortices shed from the impeller vane trailing edges are determined from equation (4). These values are used in the above mentioned simultaneous equations to obtain γ at the time $t = t + \Delta t$, where Δt is an appropriate time interval. Thus, starting from the time $t = 0$ when no free vortex exists, γ can be obtained stepwisely. The integrations are carried out numerically using the trapezoidal method and analytically for the free vortices in the vicinity of the trailing edges.

Results of Whirling Impeller in Vaneless Diffuser

The case of a whirling impellers in vaneless diffuser is first calculated, by neglecting the appropriate terms of equations (3) and (6), respresenting the guide vane influence. The calculations were performed for the conditions listed in Table 1 to understand influences of the impeller geometry and flow rate on the lateral forces.

When the number of vanes exceeds two, the magnitude of

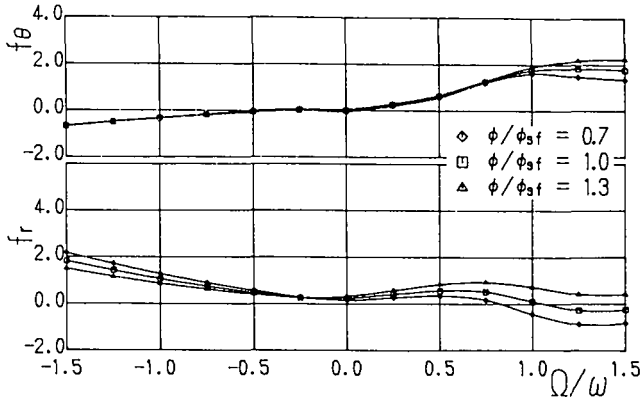

Fig. 5(a) Normalized fluid force of impeller in vaneless diffuser ($N = 6$, $\beta = 45$ deg)

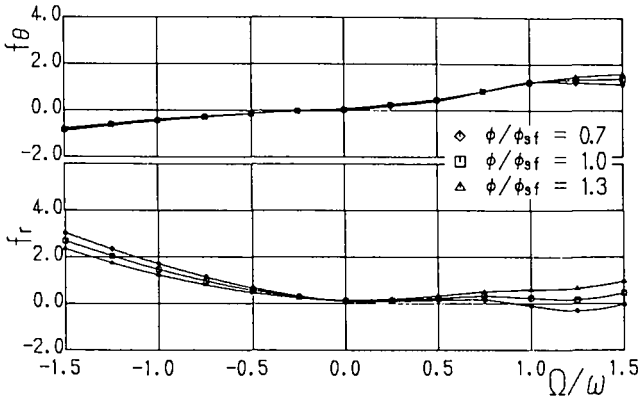

Fig. 5(b) ($N = 6$, $\beta = 60$ deg)

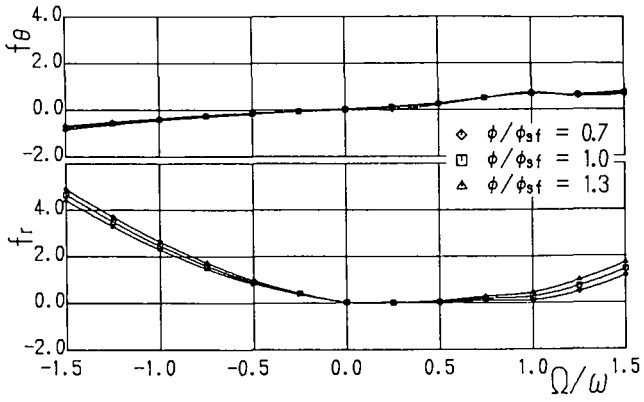

Fig. 5(c) ($N = 6$, $\beta = 75$ deg)

Table 1 Geometry of impellers for sample calculations

vane angle to radius, β (logarithmic spiral)	75°	60°	45°
r_1/r_2	0.5	0.5	0.5
number of vanes, N	6	3, 6, 9	6
shockfree flow coefficient, ϕ_{sf}	0.067	0.144	0.25

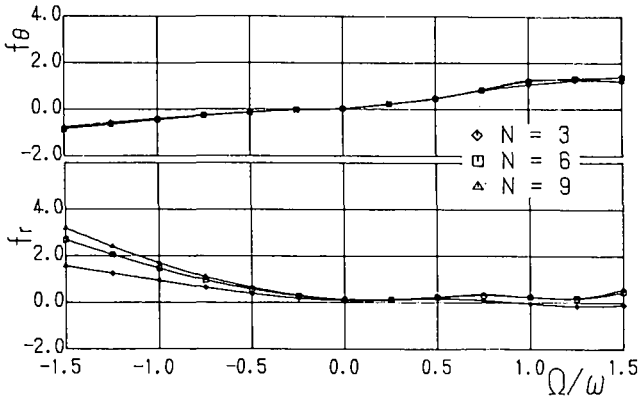

Fig. 6 Normalized fluid force of impeller in vaneless diffuser ($\beta = 60$ deg, $\phi/\phi_{sf} = 1.0$)

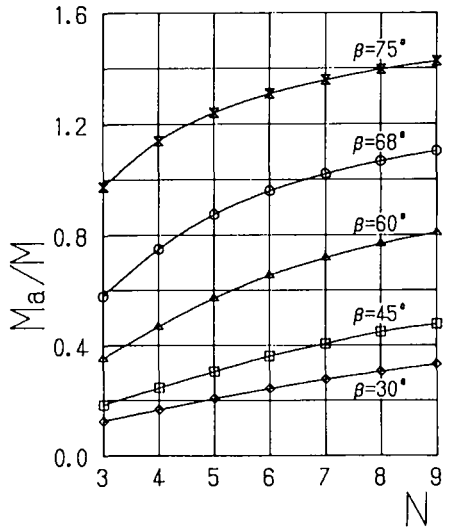

Fig. 7 Apparent mass of two-dimensional centrifugal impeller (logarithmic spiral vanes, $r_1/r_2 = 0.5$)

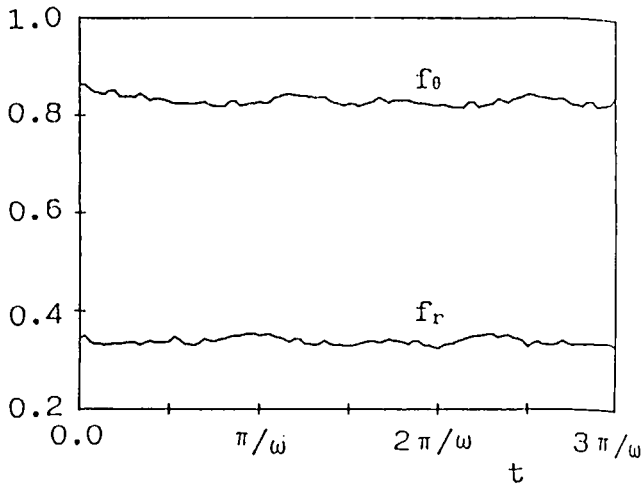

Fig. 8(*a*) Instantaneous values of fluid forces on impeller in vaned diffusser ($\Omega/\omega = 0.75$, $N_G = 2$, $\beta_G = -75$ deg, $|\epsilon|/r_2 = 0.001$, $(r_3 - r_2)/r_2 = 0.114$)

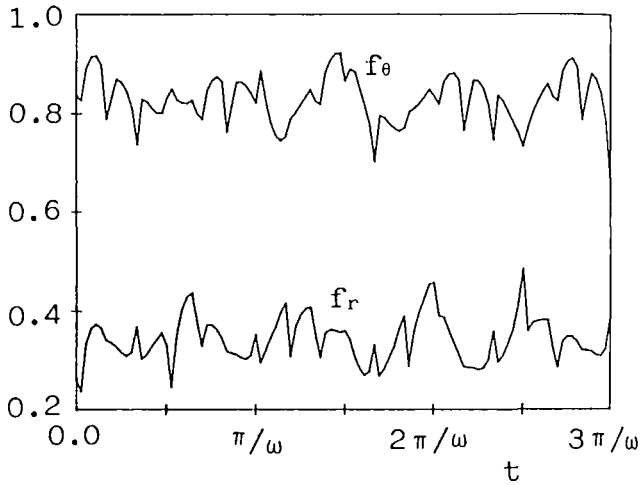

Fig. 8(*b*) ($\Omega/\omega = 0.75$, $N_G = 2$, $\beta_G = -60$ deg, $|\epsilon|/r_2 = 0.001$ $(r_3 - r_2)/r_2 = 0.114$)

resultant force stays constant and its direction rotates with angular speed $\Omega - \omega$ in the relative coordinate system. The force acting on individual vanes varies independently with time. The direction of resultant force in the absolute coordinate system rotates counterclockwise at angular speed Ω, so the angle between the force vector and eccentricity 0′0 remains constant.

The radial force component F_r and tangential force component F_θ, are further normalized as follows:

$$f_r = F_r/(M|\epsilon|\omega^2)$$
$$f_\theta = F_\theta/(M|\epsilon|\omega^2) \quad (8)$$
$$M = \rho\pi r_2^2 b$$

where ρ is the density of the fluid and M is the mass of the fluid displaced by the projected volume of impeller vanes.

Figure 5 shows f_r and f_θ calculated for whirl speed ratio Ω/ω values between -1.5 to 1.5, when the impellers ($\beta = 45$ deg, $\beta = 60$ deg, $\beta = 75$ deg) operate at three different flow rates ($\phi/\phi_{sf} = 0.7$, 1.0, 1.3).

These results show that the radial force f_r increases as the flow rate increases in positive whirl, with a decrease in negative whirl. The calculated tangential force f_θ is positive in positive whirl and negative in negative whirl. This indicates that fluid forces exert a damping effect on the whirling impeller. The influence of flow rate on f_θ is generally small. The influence of number of impeller vanes, N, can be seen in Fig. 6, where as N increases the radial force f_r becomes larger but as N increases the calculated tangential forces f_θ appears almost independent of N. The f_r component is substantially influenced both by β and N since f_r is caused by the centrifugal force on the apparent mass of the impeller. Figure 7 shows the impeller apparent mass M_a calculated by potential theory for translatory oscillation without rotation. The results of Figs. 5 and 6 are consistent with these apparent mass values.

Results of Whirling Impeller in Vaned Diffuser

The fluid forces acting on a whirling impeller surrounded by guide vanes were next calculated. In these calculations the impeller and guide vanes interaction was neglected and the circulation around each guide vane was assumed to be constant for the sake of simplicity.

When the number of guide vanes is equal to two or more, their influences on the impeller without whirling motion cancel each other and cause no lateral force. Once the whirling motion occurs, this cancellation stops and the fluid force varies in a very complicated way.

Figure 8 shows the time variation of f_r and f_θ during whirling motion. In the case of $\beta_G = -75$ deg (low guide vane loading), f_r and f_θ change little as shown in Fig. 8(*a*). In the case of $\beta_G = 60$ deg (high loading), a significant interaction occurs as seen from Fig. 8(*b*). In spite of the fluctuation of the

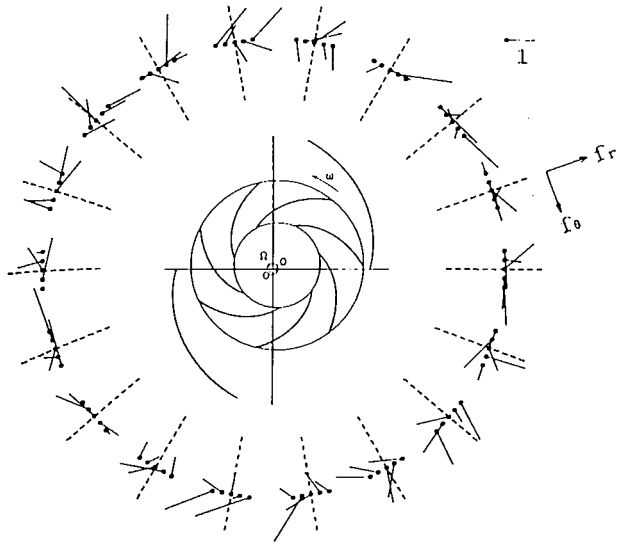

Fig. 9(*a*) Instantaneous fluid force vectors of impeller in vaned diffuser at 18 equally spaced locations on the orbit ($r_1/r_2 = 0.5$, $\beta = 60$ deg, $N = 7$, $\Omega/\omega = 0.57$, $r_3/r_2 = 1.05$, $r_4/r_2 = 1.714$, $\beta_G = -60$ deg, $N_G = 2$, $|\epsilon|/r_2 = 0.025$, $N\omega/N_G\Omega = 6.14$)

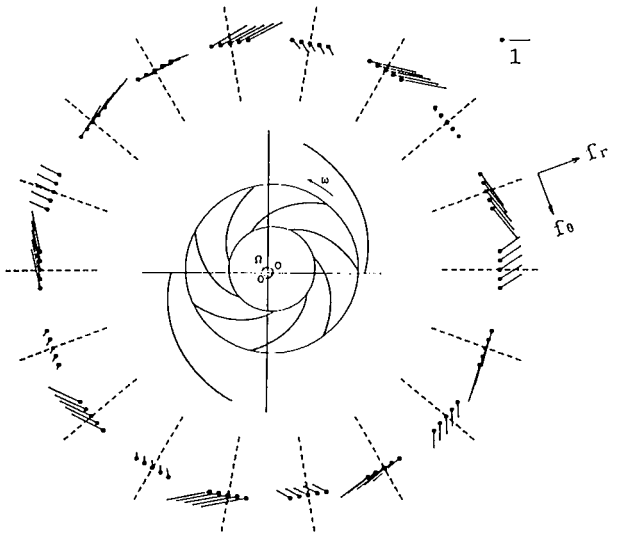

Fig. 9(*b*) $\Omega/\omega = 0.7$, $N\omega/N_G\Omega = 5$ (integer)

instantaneous values of f_r and f_θ, the calculations indicate that their time-averaged values are almost unaffected.

In Fig. 9 instantaneous force vectors in the absolute coordinate system at 18 equally spaced orbit locations are shown. Five successive vectors are plotted at each location from left to right. The force vectors change randomly as shown in Fig. 9(*a*), because the relative position of impeller vanes and guide vanes is different every time the impeller center 0 passes the same location of the orbit. Only in special cases when the value $N\omega/N_G\Omega$ is equal to an integer do the same relative position of impeller and guide vanes occur at an orbital location. In this case the successive force vectors are the same at each location as shown in Fig 9(*b*).

Conclusion

This paper has presented the results of flow calculations for a two-dimensional centrifugal impeller whirling in a vaneless and a vaned diffuser. These calculations illustrate the influences of the impeller goemetry, whirling speed to impeller speed ratio, flow rate, and guide vane geometry, etc. on the unsteady lateral force. The calculated results showed the following:

(I) Whirling impeller in vaneless diffuser:

(1) The magnitude of fluid force stays constant, provided the number of vanes exceeds two, and the angle between force vector and eccentricity 0′0 remains constant, which is a direct consequence of the assumed circular orbit.

(2) Tangential force f_θ is positive in positive whirl and negative in negative whirl. Thus the fluid force exerts a damping effect on whirling impeller.

(3) Radial force f_r increases in positive whirl and decreases in negative whirl as the flow rate increases. The flow rate influence on tangential force f_θ is generally small.

(II) Whirling impeller in vaned diffuser:

(4) The components f_r and f_θ undergo significant fluctuations due to impeller-guidevane interactions while the time-averaged values appear to be unaffected.

(5) The instantaneous force vectors change randomly in general whirling conditions. Only in the special cases that the value $N\omega/N_G\Omega$ is equal to an integer do the successive force vectors at an orbitral location become the same.

Acknowledgment

This study was supported by a Grant-in-Aid for Scientific Research by the Japanese Ministry of Education, Science and Culture. The authors are grateful to Dr. Robert Latorre for his assistance in preparing the final manuscript.

References

Allaire, P. E., et al., 1984, "Hydraulic Forces on a Centrifugal Impeller Undergoing Synchronous Whirl," NASA CP 2338, pp. 123-135.

Black, H. F., 1969, "Effects of Hydraulic Forces in Annular Pressure Seals on the Vibrations of Centrifugal Pump Rotors," *J. Mech. Eng. Sci.*, Vol. 11, No. 2, pp. 206-213.

Chamieh, D., 1983, "Forces on a Whirling Centrifugal Pump Impeller," Ph.D. thesis, California Institute of Technology.

Childs, D., and Kim, C., 1984, "Analysis and Testing for Rotordynamic Coefficients of Turbulent Annular Seals with Different, Directionally Homogeneous Surface-Roughness Treatment for Rotor and Stator Element," NASA CP 2338, 1984, pp. 313-340.

Colding-Jorgensen, J., 1980, "Effect of Fluid Forces on Rotor Stability of Centrifugal Compressors and Pumps," NASA CP 2133, 1980, pp. 249-265.

Domm, V., and Hergt, P., 1970, "Radial Forces on Impellers of Volute Casing Pumps," *Flow Research on Blading*, Elsevier Pub. Co., pp. 305-321.

Hergt, P., and Krieger, P., 1969-1976, "Radial Forces in Centrifugal Pumps with Guide Vanes," *Proc. Inst., Mech. Eng.*, Vol. 184, Part 3N, pp. 101-107.

Iino, T., and Kaneko, H., 1980, "Hydraulic Forces Caused by Annular Pressure Seals in Centrifugal Pumps," NASA CP 2133, pp. 213-225.

Imaichi, K., et al., 1980, "A Two-Dimensional Analysis of the Interaction of Radial Impeller in Vaneless Casing," *Proc. 10th IAHR Symposium*, 1980, pp. 635-647.

Shoji, H., and Ohashi, H., "Fluid Forces on Rotating Centrifugal Impeller with Whirling Motion," NASA CP 2133, 1980, pp. 317-328.

Someya, T., 1987, "*Journal Bearing Databook*, Springer, 1987.

Thompson, W. E., "Fluid Dynamic Excitation of Centrifugal Compressor Rotor Vibrations," ASME Journal Fluids Engineering, Vol. 100, No. 1, 1978, pp. 73-78.

Tsujimoto, Y., Acosta, A. J., and Brennen, C. E., 1986, "Theoretical Study of Fluid Forces on a Centrifugal Impeller Rotating and Whirling in a Volute," *Trans. JSME*, Vol. 52, No. 480, 1986, pp. 3159-3165 (in Japanese).

Lateral Fluid Forces on Whirling Centrifugal Impeller (2nd Report: Experiment in Vaneless Diffuser)

H. Ohashi
Professor,
Department of Mechanical Engineering,
University of Tokyo,
Bunkyo-ku, Tokyo, 113 Japan

H. Shoji
Lecturer,
Institute of Engineering Mechanics,
University of Tsukuba,
Ibaraki-ken, 305 Japan

Fluid forces acting on a rotating centrifugal impeller in whirling motion are studied experimentally. A two-dimensional impeller installed in a parallel walled vaneless diffuser was forced on a circular orbital motion at various positive and negative whirl speeds. The measurements show that the fluid forces exert a damping effect on the rotor at most operating conditions, but excite positive whirl when the impeller operates at a partial discharge and rotates at speeds more than twice the whirl speed. The test results were compared with those calculated by the theory described in the 1st Report. The characteristics of whirling fluid forces are examined from both the measurements and calculations. The measured fluid forces are expressed in terms of mass, damping, and stiffness matrices.

Introduction

The present paper represents the experimental counterpart of the theory described in the 1st Report (Shoji and Ohashi, 1987). The test impellers and casing geometries were chosen as simple as possible to clarify the nature of fluid forces on whirling centrifugal impellers through direct comparison with corresponding calculations.

In these tests, a two-dimensional centrifugal impeller with logarithmic-spiral vanes was installed in a parallel walled vaneless diffuser and forced into a whirling motion with a circular orbit. Only the lateral fluid forces acting on the impeller vanes were measured at various operating conditions. This was accomplished by a special test procedure which excluded all the other forces acting on the shrouds, shaft and seals. This enabled a direct comparison of experimental and theoretical results.

In the data analysis the measured lateral forces were divided into radial and tangential components relative to the orbital motion. The influences of impeller geometry, whirl speed ratio and flow condition (flow coefficient) on these components were then separately investigated. To facilitate the calculation of rotordynamic response to an unbalance mass or to seismic loads, the measured forces were converted to mass, damping and stiffness matrices by assuming that the forces are proportional to the acceleration, velocity and displacement of the impeller center.

The investigation of fluid forces on whirling centrifugal impellers was first approached analytically as described in the introduction of the 1st Report. The corresponding experimental studies on this problem are quite limited. Investigations similar to the present one have been carried out by Acosta et al. (Brennen et al., 1980; Chamieh et al., 1982 and 1985; Jery et al., 1984) for propellant-turbopump impellers and by Bolleter and Wyss (1985) for boiler feed pump impellers. Their measurements were presented using the same expressions adopted in the present study. In the comparison of these results, attention must be paid to the difference of the whirling body of the interest, namely two-dimensional impeller vanes or a complete three-dimensional impeller with shrouds.

Test Setup

For the measurement of lateral fluid forces, a single-stage, vertical-shaft, centrifugal pump is used. As Fig. 1 shows, water is sucked from the tank to the impeller. The test impellers A and B differ only in their vane angles. Their geometries and the test parameters are given in Table 1. Each impeller is installed at the center of a parallel walled vaneless diffuser as illustrated in Fig. 2(*b*). The discharged water is decelerated in the diffuser and returns to the tank via two symmetrically arranged pipes. The flow rate of each pipe is ad-

Table 1 Principal specifications

Impeller	Two-dimensional, closed type
outer diameter $d_2=2r_2$	350 mm
inner diameter	175 mm
vane width b	35 mm
shroud thickness	5 mm × 2
number of vanes	6
vane angle to radius β (logarithmic spiral)	68° for impeller A 60° for impeller B
mass	4.1 kg
Vaneless diffuser	Parallel walled
exit diameter	700 mm
screen	40 mesh per inch, 51% opening
width	70 mm
Test condition	
rotational speed ω	525 rpm
whirl speed Ω	-683 to +683 rpm
eccentricity ε	variable, mainly 1.5 mm
shock-free flow rate	2.25 m³/min for impeller A 3.21 m³/min for impeller B

Contributed by the Fluids Engineering Division for publication in the JOURNAL OF FLUIDS ENGINEERING. Manuscript received by the Fluids Engineering Division, January 30, 1986.

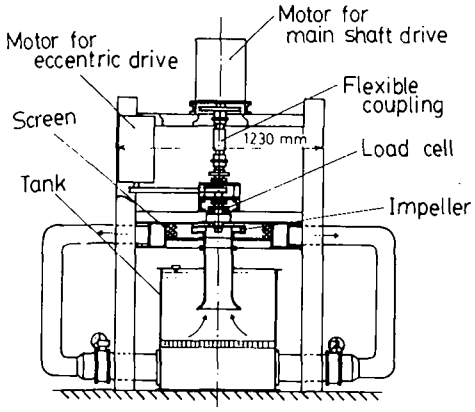

Fig. 1 Layout of test facility

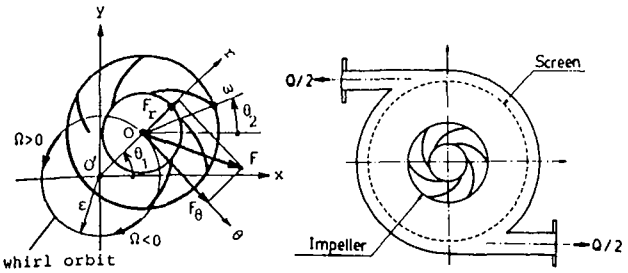

(a) Impeller force (b) Vaneless diffuser

Fig. 2 Fluid forces on whirling impeller

justed to be the same by flow control valves. In order to improve the diffuser flow uniformity, a screen (40 mesh per inch) is installed at the outer periphery of the diffuser. The pump discharge is measured by a flow nozzle at the suction pipe entrance.

The forced whirling motion apparatus is illustrated in Fig. 3. The impeller is supported overhung by two self-aligned spherical roller bearings and driven by an electric motor through a flexible coupling. The upper and lower bearings are supported by two auxiliary crankshafts with the same eccentricity, which are driven synchronously via a cogged belt connected to a variable speed electric motor. The rotating pump shaft can thus be forced into an orbital motion with a given whirl speed and eccentricity, while keeping its axis always parallel. To reduce the whirling motion resistance, a multidisk shaft seal is installed. The wear ring on the front shroud is replaced by a teflon face seal with a narrow axial gap.

Lateral fluid forces on the impeller are evaluated from the

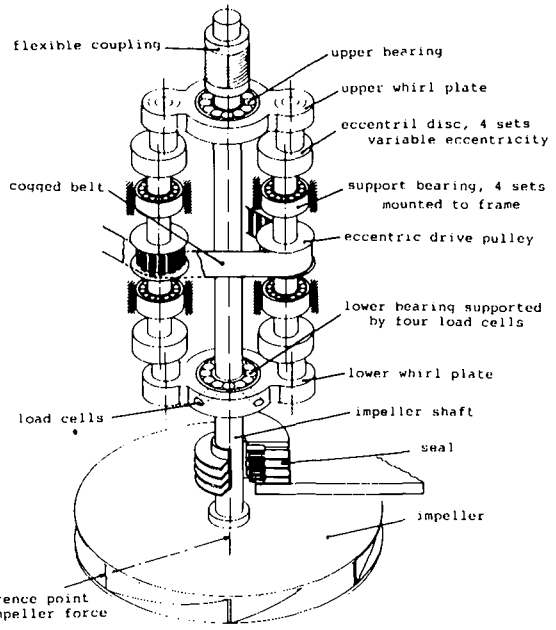

Fig. 3 Forced whirling motion apparatus

lower bearing reaction. As seen from Fig. 3, the outer race of this bearing is attached to the lower whirl plate by four load cells arranged orthogonally (x- and y-direction). The phase angles of whirl and rotation, θ_1 and θ_2 (see Fig. 2(a)), are recorded by rotary encoders attached to the auxiliary and main shafts. The rotational speed of the impeller ω is kept constant (525 rpm), while the whirl speed Ω is varied from negative to positive (-683 to $+683$ rpm) giving a wide range of whirl speed ratios ($-1.3 < \Omega/\omega < 1.3$).

Test Method

Calibration. The relation between load cell outputs and lateral forces working at the center of the vane width was obtained dynamically by rotating a dummy disk with a known unbalance mass. The x- and y-component of the calculated centrifugal force, F_x and F_y, are related to the load cell outputs, E_x and E_y, by the linear equation:

$$\begin{bmatrix} F_x \\ F_y \end{bmatrix} = \begin{bmatrix} a_{xx} & a_{xy} \\ a_{yx} & a_{yy} \end{bmatrix} \cdot \begin{bmatrix} E_x \\ E_y \end{bmatrix} \tag{1}$$

The four elements of the conversion matrix, **a**, are deter-

Nomenclature

$\mathbf{a}(a_{xx}, \ldots)$ = conversion matrix and their elements
b = vane width
$\mathbf{b}$ = damping matrix
$\mathbf{E}(E_x, E_y)$ = load cell output in x- and y-direction
$\mathbf{F}(F_x, F_y)$ = fluid force in x- and y-direction
f = normalized fluid force
$\mathbf{k}$ = stiffness matrix
M = mass of fluid displaced by rotating vanes, $\rho\pi r_2{}^2 b$
M_a = apparent mass of impeller vanes
$\mathbf{m}$ = mass matrix
n = number of data sampling
Q = flow rate
r_2 = outer radius of impeller
S = standard deviation of sampled data
u_2 = peripheral speed
x, y = Cartesian coordinate
Δp_t = total pressure rise
β = vane angle
ϵ = eccentricity
θ_1 = whirl angle
θ_2 = rotational angle
ν = kinematic viscosity
ρ = fluid density
ψ = head coefficient
ϕ = flow coefficient
Ω = whirl speed
ω = rotational speed

Subscripts

r, θ = radial and tangential component to the orbit
sf = shockfree entry condition

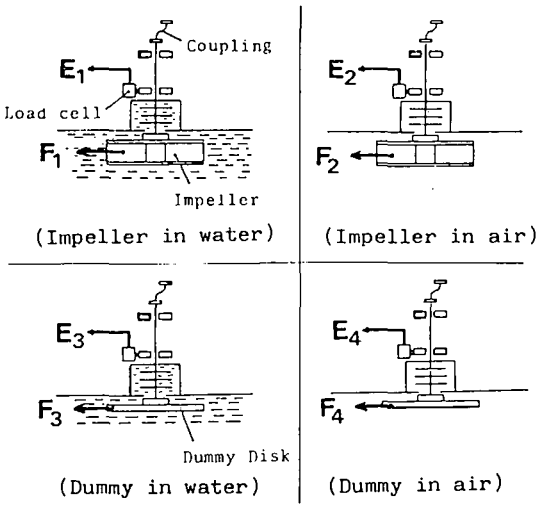

Fig. 4 Four sub-experiments

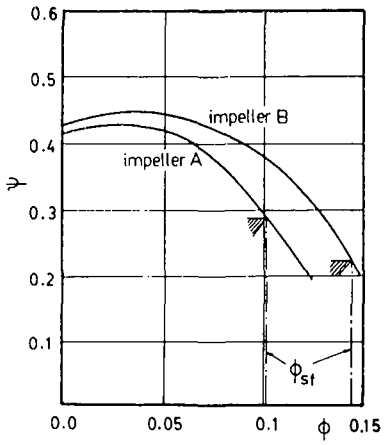

Fig. 5 Characteristics of test pump

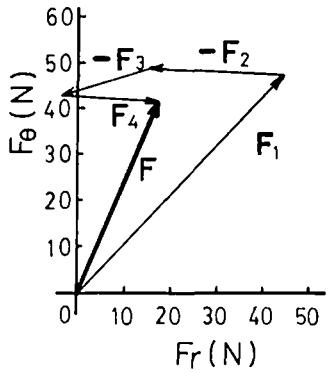

Fig. 6 Relative position of force vectors (impeller A, ϵ = 2.0 mm, $\phi = \phi_{sf}$, Ω/ω = 0.83)

mined from calibration data collected at various rotational speeds using the least squares method. The interaction terms, a_{xy} and a_{yx}, between x- and y-direction were less than 2 percent of the principal terms, a_{xx} and a_{yy}. Therefore the impeller forces were evaluated using $F_x = a_{xx}E_x$ and $F_y = a_{yy}E_y$, neglecting small cross interaction.

Data Sampling. There is no impeller/guidevane interaction in this vaneless diffuser arrangement. Therefore the lateral force on a whirling impeller does not depend on the rotational angle θ_2, as theory predicts for an impeller with 3 or more vanes (Shoji and Ohashi, 1987). If the vaneless diffuser created a perfectly unbounded condition for the impeller as expected, the fluid force on the impeller would also not depend on the whirl angle θ_1. However in reality the fluid force varies with the whirl angle θ_1 due to the nonuniform flow at the diffuser exit as well as the slightly inhomogeneous ridigity of the whirling apparatus. In these tests the load cell outputs were sampled and A-D converted at each 10 degree increment of whirl angle resulting in 36 equally spaced locations on the orbit. At each location $n = 200-300$ sampling data were collected and their ensemble average was evaluated. To check the uncertainty of these ensemble averages, the standard deviation S of 512 sampling data were evaluated for several representative test conditions. A 95 percent confidence interval, $\pm 1.96\ S/\sqrt{n}$, was then estimated. The uncertainty associated with the measuring system itself is negligible compared to the confidence interval caused by the force fluctuation.

Lateral Force on Impeller Vanes. When the impeller whirls in water, the resultant reaction force at the lower bearing is due to the following: the inertial (centrifugal) force acting on whirling body, the fluid force on the submerged parts including the shaft seal, the reaction force from the deformed flexible coupling, as well as the reaction force from the driving torque of non-aligned motor shaft. In order to extract the fluid force acting purely on the impeller vanes from the measured resultant force, four sub-experiments are carried out. They are shown in Fig. 4. First the whirling impeller is tested in water (output $\mathbf{E}_1$) and in air (output $\mathbf{E}_2$). Then the impeller is replaced by a dummy disk made up from the shrouds and hub of the original impeller, and the whirling test is again carried out in water (output $\mathbf{E}_3$) and in air (output $\mathbf{E}_4$).

The fluid forces on the impeller vanes, $\mathbf{F}(F_x, F_y)$, can then be evaluated by the relation,

$$\mathbf{F} = \mathbf{a}(\mathbf{E}_1 - \mathbf{E}_2 - \mathbf{E}_3 + \mathbf{E}_4) \tag{2}$$

where $\mathbf{a}(\mathbf{E}_1 - \mathbf{E}_2)$ represents fluid forces on all the submerged parts and $\mathbf{a}(\mathbf{E}_3 - \mathbf{E}_4)$ those on the submerged parts other than the impeller vanes. The reaction of driving torque on the lower bearing is calculated from the geometrical relation and the influence is corrected to the result obtained by equation (2). Hereafter fluid forces refer only to those on impeller vanes, unless otherwise specified.

Test Condition. Test parameters are listed in Table 1. Most of the tests were carried out for an eccentricity ϵ = 1.5 mm, since preliminary tests showed that fluid forces were proportional to the eccentricity as long as it was sufficiently small compared to the impeller radius. The test flow rate was adjusted from shutoff to the maximum including shockfree entry condition. The machine Reynolds number was $\mathrm{Re} = u_2 d_2/\nu = 3.4 \times 10^6$ at constant rotational speed of 525 rpm.

Test Results

Pump Characteristics. The performance of the test pump was measured at steady operating conditions without whirl and was converted to flow and head coefficients by

$$\phi = Q/2\pi r_2 b u_2, \quad \psi = \Delta p_t/(\rho u_2{}^2/2) \tag{3}$$

The pump characteristics are shown in Fig. 5 for impeller A and B. Impeller A with larger vane angle has correspondingly smaller shockfree flow coefficient ϕ_{sf} and smaller head than those of impeller B. The head of the test pump was generally smaller than that of an industrial pump with the same vane angle. This was due to additional losses at the sharp inlet corner of the two-dimensional test impeller and the presence of the resistance screen which reduced the net pressure rise.

Character of Unsteady Fluid Forces. The fluid forces on impeller vanes were derived from four sub-experiments in Fig. 4. The relative magnitude and direction of these forces are illustrated in Fig. 6 for a typical test condition (impeller A, Ω/ω

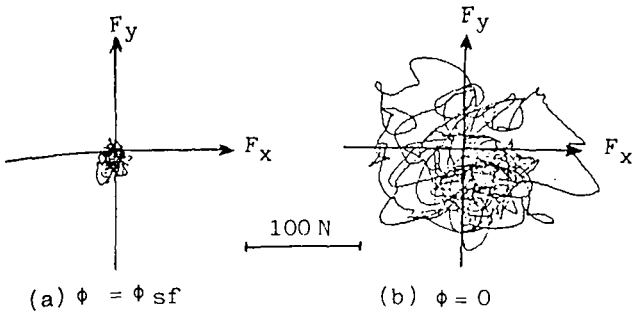

Fig. 7 Lissajous's figure of impeller force without whirling motion (impeller A)

$= 0.83$, $\phi = \phi_{sf}$). The forces $\mathbf{F}_2$ and $\mathbf{F}_4$ measured in air are mostly due to the inertial centrifugal force and thus have a predominant radial component. The reduction of the whirling mass by using aluminum impeller helps to keep the magnitude of the fluid force substantially larger than that of the inertial force.

While the oscillatory output of load cells primarily correlates with the whirl speed Ω, it also contains secondary fluctuations caused by the mass unbalance of rotating impeller (frequency ω), the rolling noise of bearings, the turbulence of flow and so on. From the preliminary tests, it became clear that the largest and predominant source of secondary fluctuation resulted from the separation-induced flow disturbance. Figure 7 illustrates Lissajous's figures of overall impeller force, when impeller A rotates in water without whirling motion. As seen from Fig. 7(*a*) the fluctuation of measured force is rather weak at design condition corresponding to shockfree entry. As the discharge decreases, the fluctuation increases and becomes quite violent at shutoff as seen from Fig. 7(*b*). This strong fluctuation can be obviously attributed to the stall of impeller vanes at partial flow rate, where large eddies grow and mix randomly in the separated zones. From the spectrum analysis of measured data at partial flow rate, no distinct peak frequency was observed, which suggests that no orderly phenomena like propagating stall occurred in the impeller. The power of fluctuation in synchronism with the shaft rotation remained within one tenth of the power related to the whirling motion.

Figure 8 shows the variation of fluid force acting on whirling impeller vanes along the orbit. The vector at each location represents the ensemble average of 512 sampled data taken at that point. The fluctuation from the average is indicated by a circle with its rms value as its radius. Examples are shown for shockfree and shutoff conditions with positive and negative whirl, $\Omega/\omega = \pm 0.83$. Fluid forces are nearly axisymmetric and uniform on the circular orbit as expected. It is worthwhile to note that the rms fluctuation near shutoff can be several fold larger than its average and the fluid forces excite the whirling motion only at such extraordinary flow conditions. This will be treated in detail in the discussion.

Fluid Forces on Whirling Impeller. In spite of the precautions to establish an azimuthally uniform flow, the ensemble averaged force vectors on the orbit were not completely identical as shown in Fig. 8. Since the motion of whirling rotor is due to the impulse of the fluid force, the force components, $F_r(\theta_1)$ and $F_\theta(\theta_1)$, are hereafter averaged over one cycle of whirling motion, $\theta_1 = 0$ to 360 deg, and are denoted by $\bar{F}_r$ and $\bar{F}_\theta$. These forces are further normalized using the following definitions:

$$f_r = \bar{F}_r/M\epsilon\omega^2, \quad f_\theta = \bar{F}_\theta/M\epsilon\omega^2 \tag{4}$$

$$M = \rho\pi r_2{}^2 b$$

where M denotes the mass of fluid displaced by the envelope of rotating vanes.

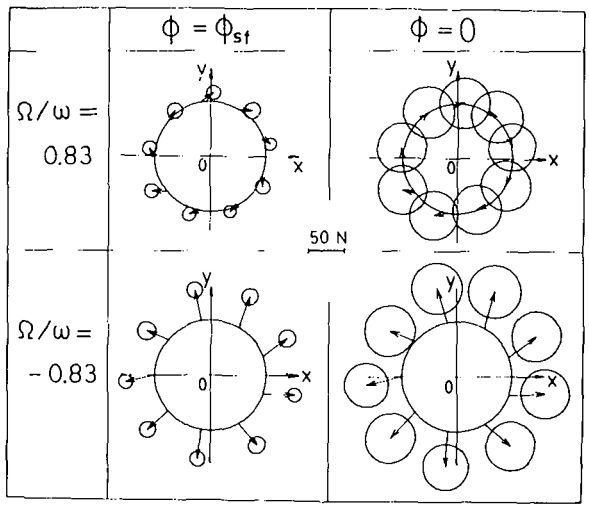

Fig. 8 Ensemble averaged fluid forces and their fluctuations (impeller A, ϵ = 1.5 mm)

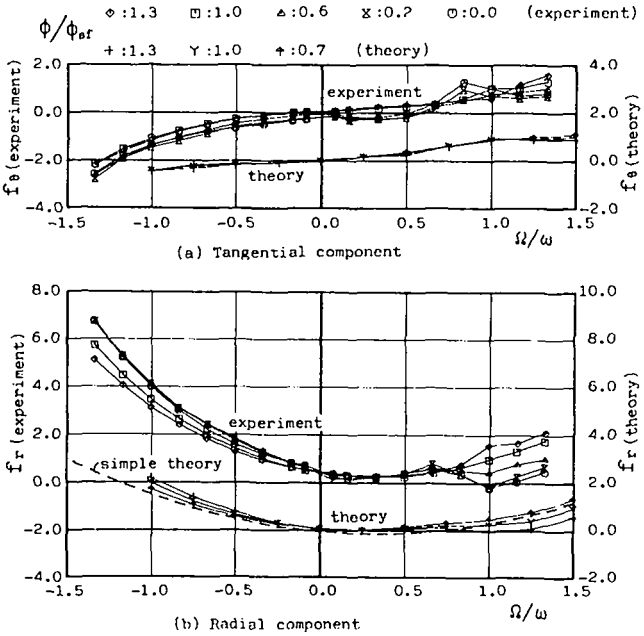

Fig. 9 Normalized fluid forces on impeller A (Uncertainty in f_θ and f_r =; ±0.10 for ◇, ±0.17 for △, ±0.21 for ○. Uncertainty in Ω/ω = ±0.02 for all cases)

Figures 9(*a*) and (*b*) show the dependence of f_θ and f_r on the whirl speed ratio Ω/ω between -1.3 and $+1.3$. These results are for impeller A (β = 68 deg) whirling with eccentricity ϵ = 1.5 mm at five different flow rates; $\phi/\phi_{sf} = 1.3, 1.0, 0.6, 0.2$, and 0. The corresponding calculations are also plotted in the same figures. Figures 10(*a*) and (*b*) show the result for impeller B (β = 60 deg) at $\phi/\phi_{sf} = 1.0, 0.7, 0.4, 0.1$, and 0.

The confidence intervals of measured fluid forces depend primarily on the flow coefficient and are slightly influenced by the whirl speed ratio. The uncertainties of force measurement are substituted in this case by the corresponding 95 percent confidence intervals and are given for representative flow coefficients in Figs. 9 and 10.

Fluid forces on whirling shrouds were determined from two sub-experiments using dummy disk whirling in water and in air. The results are normalized also by equation (3) with reference mass $M = \rho\pi r_2{}^2 t$ (where t is total thickness of front and back shrouds). The results are shown in Fig. 11.

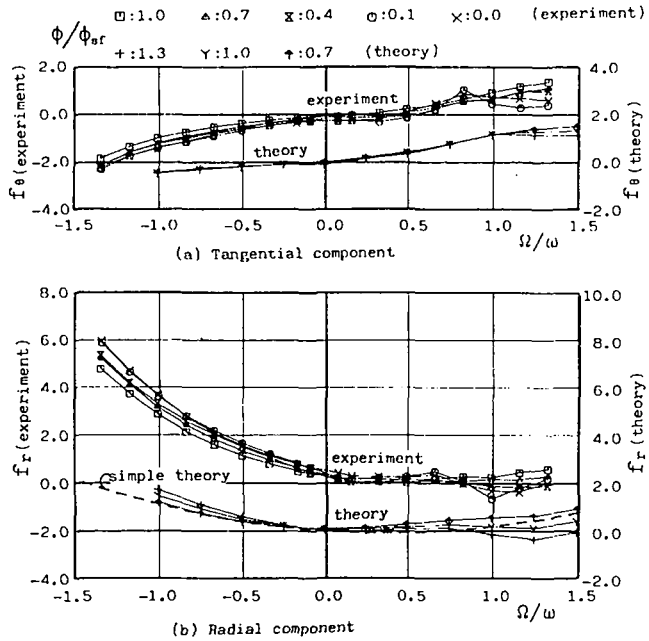

Fig. 10 Normalized fluid forces on impeller B (Uncertainty in f_θ and f_r =; ±0.07 for □, ±0.14 for ⧖, ±0.21 for X. Uncertainty in Ω/ω = ±0.02 for all cases)

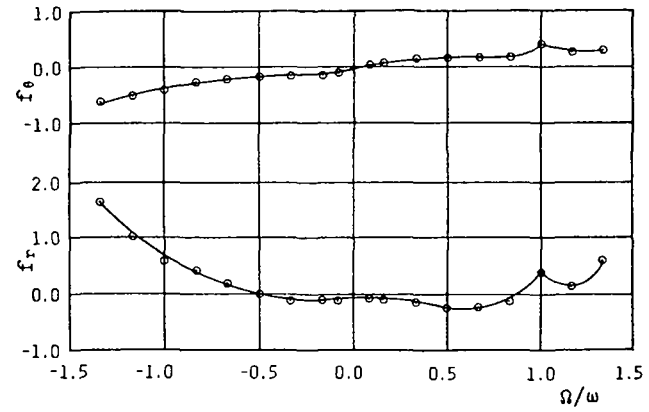

Fig. 11 Normalized fluid forces on shrouds (Uncertainty in f_θ and f_r = ±0.10, in Ω/ω = ±0.02)

Discussion of Results

Comparing the experimental results with the corresponding calculations, the character of whirling fluid forces could be clarified.

Tangential Forces.

(1) Normalized tangential forces f_θ increase on the whole with the increase of whirl speed ratio Ω/ω. Under most operating conditions except those described below, the tangential forces are positive for positive whirl and negative for negative whirl and exert a damping effect to the whirling motion.

The theoretical results show the same tendency. Quantitative agreement with the experiment is fairly good for positive whirl, while for negative whirl calculated damping is approximately half of the measured values.

(2) Tangential forces decrease slightly with the decrease of flow rate. Consequently, they become negative for positive whirl when both flow rate and whirl speed ratio are small, $\phi/\phi_{sf} < 0.6$ and $\Omega/\omega < 0.5$. From the viewpoint of rotordynamics, this indicates that the centrifugal impeller can excite positive whirl of the rotor, only when it is mounted on a flexible shaft rotating faster than twice its critical speed and operates at a partial flow rate near shutoff.

Comparison of impeller A and B indicates that impeller A with smaller head coefficient has a slightly wider excitation zone.

(3) Calculated f_θ is nearly zero at zero whirl speed ratio, $\Omega/\omega = 0$, or for a steady displacement of the impeller center. Therefore, the existence of excitation zone cannot be simulated using potential flow theory. In contrast the damping at most operating conditions can be predicted quantitatively.

(4) The mechanism of whirl-exciting tangential force is not clear. A clue could be found in the strong fluctuation of impeller force at partial flow rate. It is conceivable that the propagation of stall region in the impeller (usually about a half of the rotational speed) becomes synchronized with the whirling motion (also about a half or less) from time to time and this random fluctuation transfers positive energy to the whirling shaft stochastically. It seems that a potential flow theory is essentially powerless to explain the mechanism, since the flow in question is characterized by large separation and turbulence which are phenomena outside inviscid flow theory.

(5) Tangential force on whirling shrouds exerts always damping effect.

Radial Forces.

(1) Normalized radial forces f_r are smaller in positive whirl than in negative whirl. The distribution appears approximately parabolic with the minimum at about $\Omega/\omega = 0.4$–0.5. While there is qualitative agreement between theory and experiment, the measured values are 1.5 to 2 times larger than the calculated ones.

(2) In positive whirl f_r increases with increasing flow rate and in negative whirl an opposite tendency is observed. The same tendency is also observed in the calculation.

(3) Radial forces are positive or outwards acting in most cases. Negative radial forces occur at higher positive whirl speed ratio, $\Omega/\omega > 1$, and partial discharge. These characteristics are also present in the calculated results.

(4) When whirl speed coincides with rotational speed, $\Omega = \omega$, the relative flow in the whirling impeller becomes stationary and the shedding of free vortices from the trailing edges into the discharge flow disappears. Consequently the condition $\Omega/\omega = 1$ represents a singular flow condition and fluid forces, f_r as well as f_θ, exhibit irregular behavior around this point. This can be also seen in the calculated results.

(5) The condition $\Omega/\omega = 0$ corresponds to the case where the center of rotating impeller is statically displaced by eccentricity ϵ from the geometrical center of suction pipe. The radial forces are positive in this condition and act to further increase the displacement (negative spring).

(6) Impeller A with larger vane angle (hence longer vane) generates larger f_r values than impeller B, which agrees with the theoretical predictions.

(7) Radial forces are generated principally by the centrifugal force on the apparent mass of whirling impeller. Apparent mass of an impeller, M_a, in translatory oscillation without rotation can be calculated by potential flow theory. The result is given in Fig. 7 of the 1st Report for two-dimensional impellers with various vane numbers and angles. From this figure the apparent mass of impeller A is read as $M_a/M = 0.95$ and of impeller B as $M_a/M = 0.65$. Normalizing the centrifugal force of apparent mass, $M_a\epsilon\Omega^2$, using the reference force, $M\epsilon\omega^2$, results in a normalized radial force given by $f_r = (M_a/M)\ (\Omega/\omega)^2$. While this parabolic distribution is symmetric both to positive and negative whirl, it is not sufficient to explain the asymmetric distribution of the measured data.

When a body like impeller with circulation Γ travels on the orbit with velocity $\epsilon\Omega$, a lift $L = \rho\Gamma\epsilon\Omega b$ is supposedly generated according to the Kutta-Joukowski's theorem.

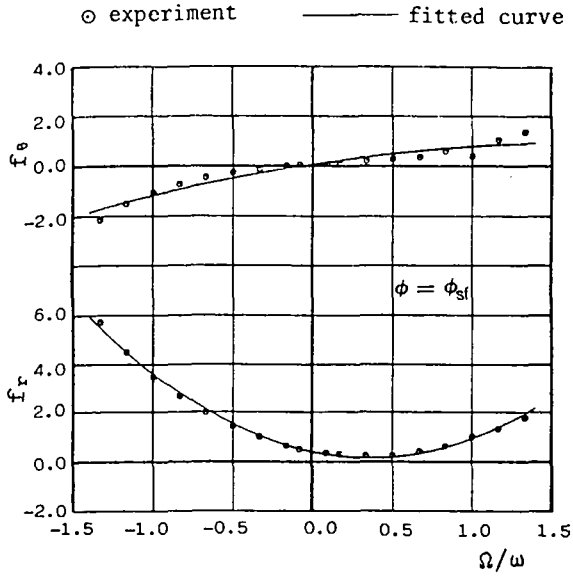

Fig. 12 Measured data and fitted curves of impeller A at shockfree entry condition (Uncertainty in f_θ and $f_r = \pm 0.07$, in $\Omega/\omega = \pm 0.02$)

Defining circulation in counterclockwise direction as positive, the impeller with positive whirl generates lift inwards corresponding to a negative radial force. Taking the absolute tangential velocity at the impeller exit as $v_{\theta 2}$, the circulation is $\Gamma = 2\pi r_2 v_{\theta 2}$ and the total pressure rise is given by $\Delta p_t = \psi(\rho u_2^2/2) = \rho u_2 v_{\theta 2}\eta$ (η is hydraulic efficiency). Normalizing this lift L by the same reference force, a linear relation $f_r = -(\psi/\phi)(\Omega/\omega)$ can be obtained. Combination of the above two forces leads to the following simplified equation for radial force:

$$f_r = (M_a/M)(\Omega/\omega)^2 - (\psi/\phi)(\Omega/\omega) \tag{5}$$

By substituting ϕ and ψ of impeller A and B at shockfree entry condition to the above equation, the impeller radial forces can be estimated and are plotted in Figs. 9 and 10 by broken curves. Since equation (5) does not account for the negative spring effect, the predicted distribution is a little smaller than the one by complete flow analysis. Nevertheless the overall relation between radial force and whirl speed can be adequately represented by equation (5).

(8) The radial force on whirling shrouds shows also the influence of lift. The rotating flow induced by disk friction causes a lift due to so-called Magnus effect.

Conversion to Force Matrices

For the vibration analysis of a rotor with centrifugal impellers, fluid forces must be formulated for an arbitrarily given motion of the shaft center. Although the experiment was carried out only for whirling motion with a circular orbit, the results can be generalized to an arbitrary shaft motion, if the forces are assumed to be proportional to the displacement, velocity and acceleration of the shaft center. Using absolute coordinate system with its origin at the whirl center O' (cf. Fig. 2(*a*)), x- and y-components of fluid forces, F_x and F_y, on impeller at $O(x, y)$ are expressed by the following relation with three linear terms:

$$\begin{bmatrix} F_x \\ F_y \end{bmatrix} = -\underbrace{\begin{bmatrix} m_{xx} & m_{xy} \\ m_{yx} & m_{yy} \end{bmatrix}}_{\text{mass}} \begin{bmatrix} \ddot{x} \\ \ddot{y} \end{bmatrix} - \underbrace{\begin{bmatrix} b_{xx} & b_{xy} \\ b_{yx} & b_{yy} \end{bmatrix}}_{\text{damping}} \begin{bmatrix} \dot{x} \\ \dot{y} \end{bmatrix} - \underbrace{\begin{bmatrix} k_{xx} & k_{xy} \\ k_{yx} & k_{yy} \end{bmatrix}}_{\text{stiffness}} \begin{bmatrix} x \\ y \end{bmatrix} \tag{6}$$

Table 2 Matrix elements of fluid forces on vanes

matrix element		m_{xx}, m_{yy}	$m_{xy}, -m_{yx}$	b_{xx}, b_{yy}	$b_{xy}, -b_{yx}$	k_{xx}, k_{yy}	$k_{xy}, -k_{yx}$
normalized by		$\rho\pi r_2^2 b$		$\rho\pi r_2^2 b\omega$		$\rho\pi r_2^2 b\omega^2$	
impeller A	$\phi/\phi_{sf}=0$	1.64	-0.27	1.14	2.02	-0.55	0.13
	0.2	1.72	-0.35	1.10	2.01	-0.55	0.17
	0.6	1.87	-0.32	1.08	1.88	-0.56	0.10
	1.0	1.86	-0.27	0.98	1.33	-0.42	-0.09
	1.3	1.82	-0.23	1.09	1.01	-0.43	-0.08
impeller B	$\phi/\phi_{sf}=0$	1.30	-0.21	0.98	1.98	-0.58	0.12
	0.1	1.32	-0.33	0.94	1.96	-0.57	0.17
	0.4	1.26	-0.20	1.06	1.80	-0.43	0.13
	0.7	1.34	-0.19	1.01	1.62	-0.39	0.05
	1.0	1.32	-0.05	1.00	1.35	-0.35	-0.01

Table 3 Matrix elements of fluid forces on shrouds

matrix element	m_{xx}, m_{yy}	$m_{xy}, -m_{yx}$	b_{xx}, b_{yy}	$b_{xy}, -b_{yx}$	k_{xx}, k_{yy}	$k_{xy}, -k_{yx}$
normalized by	$\rho\pi r_2^2 t$		$\rho\pi r_2^2 t\omega$		$\rho\pi r_2^2 t\omega^2$	
Q = 0	0.67	-0.07	0.34	0.30	0.20	-0.01

where $x = \epsilon\cos\theta_1$, $y = \epsilon\sin\theta_1$ and $\theta_1 = \Omega t$.

The assumption that the fluid forces are identical at every location of the orbit, in other words, F_r and F_θ are constant and independent of whirl angle θ_1 in an unbounded vaneless diffuser, leads to the relations:

$$\begin{aligned} F_r(\epsilon,\Omega) &= \epsilon(F_{r0} + F_{r1}\Omega + F_{r2}\Omega^2) \\ F_\theta(\epsilon,\Omega) &= \epsilon(F_{\theta 0} + F_{\theta 1}\Omega + F_{\theta 2}\Omega^2) \end{aligned} \tag{7}$$

The six constants in the above equations are related to twelve unknown elements in three force matrices of equation (6) by

$$\begin{aligned} m_{xx} &= m_{yy} = F_{r2}, & m_{xy} &= -m_{yx} = F_{\theta 2} \\ b_{xx} &= b_{yy} = F_{\theta 1}, & b_{xy} &= -b_{yx} = -F_{r1} \\ k_{xx} &= k_{yy} = -F_{r0}, & k_{xy} &= -k_{yx} = -F_{\theta 0} \end{aligned} \tag{8}$$

All measured F_r and F_θ data over the entire whirl speed range, $-1.3 < \Omega/\omega < 1.3$, were fitted to equation (7) and the six constants, F_{r0}, F_{r1}, . . . , determined by the method of least squares. Figure 12 illustrates the good fit of these constants with the measured data for the case of impeller A at shockfree entry condition. As seen from this figure, the whirling fluid forces can be approximated by the linear relation of equation (7) satisfactorily ignoring the previously mentioned irregular behavior near $\Omega/\omega = 1$.

Normalized matrix elements for impeller A and B at various flow rates are summarized in Table 2.

The fitted curves of tangential force f_θ appear nearly linear to the whirl speed ratio. This implies from equation (8) that the cross mass term, $F_{\theta 2} = m_{xy} = -m_{yx}$, is small and has little effect (see Table 2). The radial force f_r, on the other hand, has a parabolic distribution with its minimum at around $\Omega/\omega = 0.4$ to 0.5. This is obviously caused by the existence of a large principal mass term, $F_{r2} = m_{xx} = m_{yy}$, while the minimum is due to a large cross damping term, $F_{r1} = -b_{xy} = b_{yx} < 0$, resulting from the circulation-induced lift on the orbiting impeller.

The influence of tangential force f_θ on the stability of the rotor can be ascertained by the sign of f_θ at small whirl speed ratio, that is, by the sign of $F_{\theta 0} = -k_{xy} = k_{yx}$. If cross stiffness term k_{xy} is positive, the impeller excites positive whirl at higher supercritical rotational speed. From Table 2 it can be clearly seen that k_{xy} turns from negative (damping) to positive (exciting), as the discharge is decreased from design to partial flow rate.

Fluid forces on whirling shrouds can be also converted to matrix elements and they are listed in Table 3, where total thickness of shrouds, t, is used as the reference width instead of vane width b.

The matrix elements of impeller with an arbitrarily given vane width b and shroud thickness t, can be obtained by adding the impeller and shrouds matrix elements from Tables 2 and 3.

Conclusions

Fluid forces acting on two-dimensional centrifugal impeller whirling in a vaneless diffuser were measured and compared with the corresponding theoretical results. The principal results obtained from tests with two impellers are:

(1) Fluid forces have tangential components which damp the whirling motion at most operating conditions.

(2) In the case when impeller rotates faster than twice the critical speed and operates at partial flow rate, the tangential forces excite positive whirl and can induce an impeller-excited oscillation or impeller whip.

(3) The mechanism of radial force generation can be explained as the sum of an equivalent negative spring force acting against eccentricity, the circulation-induced lift on the orbiting impeller, and the centrifugal force on the apparent mass of the impeller.

(4) Calculated results agree with all measured data qualitatively. However, the mechanism of whirl-excitation cannot be explained by the inviscid theory used in the calculations.

(5) By assuming a linear relationship, whirling fluid forces are expressed in terms of mass, damping and stiffness matrices, separately for impeller and shrouds. This enables the formulation of fluid forces on impeller in an arbitrary motion.

In a future investigation, this study will be extended to treat the cases of two-dimensional impellers in a vaned diffuser and in a volute casing. This will be followed by the whirling test of industrial pumps such as a boiler feed pump.

Acknowledgments

This study was supported by the Japanese Ministry of Education through the Grant-in-Aid for Scientific Research. The authors express their deepest appreciation to Messrs. S. Yanagisawa, K. Tomita, J. Hanawa, K. Kawakami, and C. Kato for their assistance in the construction of test apparatus and in performing the measurements. The authors are also indebted to the Mechanical Engineering Research Laboratory of Hitachi, Ltd. for the continuous support and advice in this study. The authors are grateful to Dr. R. Latorre for his assistance in preparing the final manuscript.

References

Bolleter, U., and Wyss, A., 1985, "Measurement of Hydrodynamic Interaction Matrices of Boiler Feed Pump Impellers," Paper 85-DET-148 presented at the ASME Design Engineering Division Conference.

Brennen, C. E., Acosta, A. J., and Caughey, T. K., 1980, "A Test Program to Measure Fluid Mechanical Whirl-Excitation Forces in Centrifugal Pumps," NASA CP 2133, pp. 229–235.

Chamieh, D. S., Acosta, A. J., Brennen, C. E., and Caughey, T. K., 1982, "Experimental Measurements of Hydrodynamic Stiffness Matrices for a Centrifugal Pump Impeller," NASA CP 2250, pp. 382–398.

Chamieh, D. S., Acosta, A. J., Brennen, C. E., and Caughey, T. K., 1985, "Experimental Measurements of Hydrodynamic Radial Forces and Stiffness Matrices for a Centrifugal Pump-Impeller," ASME JOURNAL OF FLUIDS ENGINEERING, Vol. 107, No. 3, pp. 307–315.

Jery, B., Acosta, A. J., Brennen, C. E., and Caughey, T. K., 1984, "Hydrodynamic Impeller Stiffness, Damping and Inertia in the Rotordynamics of Centrifugal Flow Pumps," NASA CP 2338, pp. 137–160.

Shoji, H., and Ohashi, H., 1987, "Lateral Fluid Forces on Whirling Centrifugal Impeller (1st Report: Theory)," ASME JOURNAL OF FLUIDS ENGINEERING, published in this issue pp. 94–99.

M. Tsutahara
Associate Professor.

T. Kimura
Professor.

Department of Mechanical Engineering,
Kobe University, Nada, Kobe 657, Japan

An Application of the Weis-Fogh Mechanism to Ship Propulsion

A mechanism of hovering flight of small insects which is called the Weis-Fogh mechanism is applied to ship propulsion. A model of the propulsion mechanism is proposed, which is based on a two-dimensional model of the Weis-Fogh mechanism and consists of one or two wings in a square channel. The dynamic properties of the model are studied experimentally, and the propulsive efficiency obtained is as high as 75 percent. A model ship equipped with this propulsion mechanism was made, and working tests performed. The model ship sailed very smoothly and the moving speed of the wings was small compared with the advancing speed of the ship.

Introduction

The so-called Weis-Fogh mechanism [1], which was discovered by observing the hovering flight of a small insect called Encarsia formosa, is a novel and very efficient mechanism of lift generation. Lighthill [2] has considered a two-dimensional inviscid-flow model and showed that circulations of opposite directions to each other are generated respectively around the two wings, which is a characteristic of this mechanism. Maxworthy [3] has performed an experimental simulation of this mechanism in a two-dimensional and also in a three-dimensional model. He has found that the circulation in the two-dimensional case is even larger than that obtained by the inviscid model of Lighthill. Edwards and Cheng [4] have obtained a result applying a shed vortex from the leading edge which agrees well with the experiment even though it is based on the assumption of an inviscid fluid. On the other hand, Haussling [5] has solved the Navier-Stokes equation by the finite difference method for the two-dimensional model of this mechanism and showed that a jet is produced between the wings in the closing (clapping) stage. Very recently, Spedding and Maxworthy [6] performed a detailed observation of the flowfield in two-dimensional fling, and measured the lift and the moment on the wing. They reported that the time averaged lift coefficient is as high as 7 to 8. In practical applications of this mechanism, however, there is no example other than a study that Furber and Ffowcs Williams [7] have applied to an axial compressor.

We have applied Lighthill's two-dimensional model to the mechanism of ship propulsion and propose a model of the propulsion mechanism as shown in Fig. 1, in which two wings move in a square channel as shown in (*a*) to (*h*). The detailed wing motion is as follows. A point p located between the leading edge and the trailing edge (closer to the leading edge) of each wing reciprocates in the direction perpendicular to the uniform flow denoted by U. In (*a*) the two wings rotate up to some angle α about the common trailing edge, which slides upstream, as the points p move apart. On the other hand, the wings rotate about the leading edge in (*c*). The opening angle α in this figure does not denote the instantaneous angle but the ultimate angle, and such use of this symbol holds throughout this paper. We call the motion in (*a*) the opening stage, that in (*b*) the translating stage, and that in (*c*) and (*d*) the closing stage. The motions in (*e*) to (*h*) are the same, respectively, as those in (*a*) to (*d*), considering the images due to the wall of the channel. We shall therefore treat all the continuing stages from (*a*) to (*d*) as one cycle.

The uniform flow downward in Fig. 1 corresponds to the advancing speed of a ship. In the opening stage in (*a*), when the angular velocity is large enough, a clockwise circulation is generated around the left wing and a counterclockwise circulation, of equal magnitude, around the right wing. These produce the thrust (the upward force in this figure) when the wings translate in the opposite directions. In the closing stage in (*c*), the fluid between the wing and the wall is pushed downward as a jet, which produces a large thrust.

Tsutahara and Kimura [8] have analyzed the dynamic properties of this model on the assumption of a perfect fluid, and have obtained the following qualitative results:

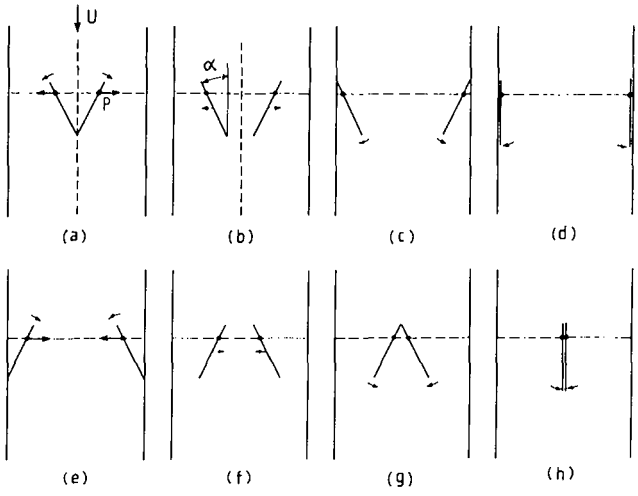

Fig. 1 A model of propulsion mechanism

Contributed by the Fluids Engineering Division of THE AMERICAN SOCIETY OF MECHANICAL ENGINEERS. Manuscript received by the Fluids Engineering Division December 6, 1985.

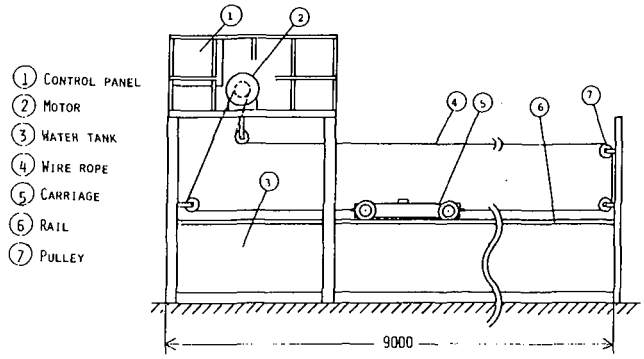

Fig. 2 Water tank

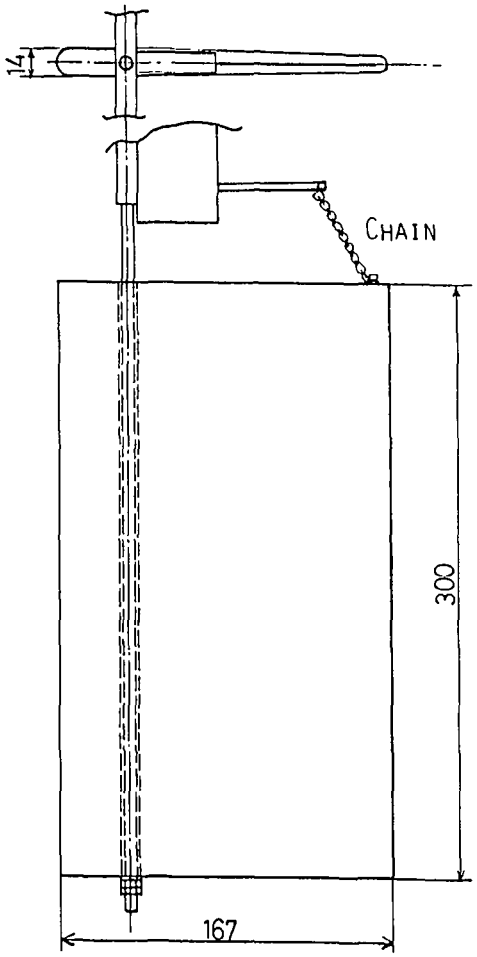

Fig. 3 Structure of wing (unit of length is mm)

1) In the opening stage, when the angular velocity is constant, the trust is negative, and adequate angular acceleration is required in order to produce a positive thrust.

2) In the closing stage, sufficient positive thrust is produced by a constant angular velocity of the wing.

3) In the translating stage, when the wing translates at a constant velocity, the thrust is large when the opening angle is small. On the other hand, when there is acceleration, the thrust is large when the opening angle is large.

In the case where the channel in Fig. 1 is sufficiently long, the flow fields on the left and right sides of the centerline shown in (*a*) and (*b*) of Fig. 1 are symmetrical, and the centerline can be considered as a solid wall. In the analysis in [8] mentioned above, only the flow field on the left side has been considered. In the experiment to be described later, the

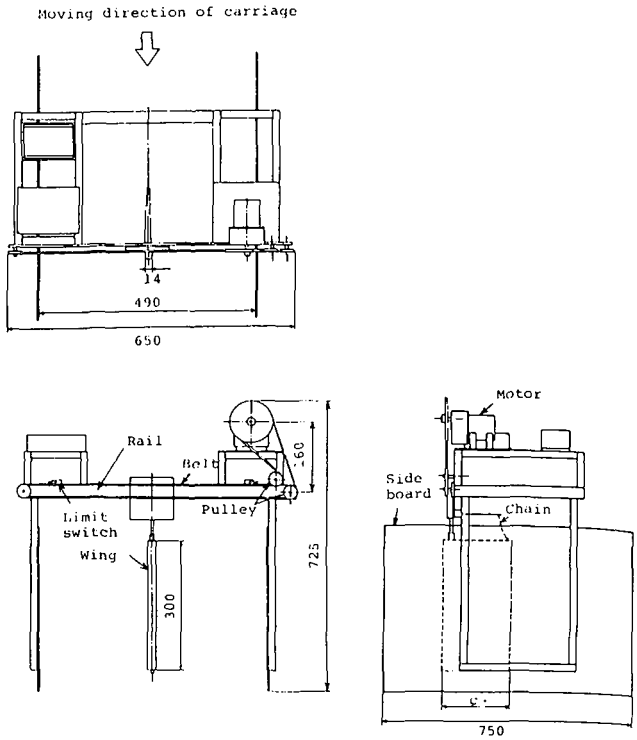

Fig. 4 Equipment for propulsion generation

motion of one wing in a channel is also studied corresponding to the analysis. When the channel is short, however, the momentum fluxes in the right and left directions are not balanced, and the ship will shake as the wing moves. Therefore, the two wings are made to move symmetrically for the model ship presented in this study.

The expected advantages of this propulsion mechanism are as follows:

1) As the flow velocity relative to the wings will not be very large, cavitation will not be generated until the ship reaches a very high speed.

2) Since conventional screw propellers are located at the rear of ships and inside the wake, it is difficult to operate the propellers at their maximum efficiencies. Moreover, as they accelerate the fluid at the rear of ships, the pressure there becomes lower and produces pressure drag. However, in the propulsion mechanism presented above, the propulsion unit can be set in a channel or duct inside the ship's hull or between the two hulls of a catamaran, eliminating the aforementioned defects.

3) In this propulsion mechanism, unsteadiness of the flow is used effectively to generate the thrust.

4) As the flow is two-dimensional in nature, the analysis is relatively simple; therefore it will be relatively easy to opitmize the performance of this propulsion mechanism through analysis.

On the other hand, the expected disadvantages are as follows:

1) The mechanism for moving the wings is complicated.

2) The load on the motor will vary during half a cycle of the wing motion.

3) A periodic acceleration occurs on the ship hull.

Some of these will be considered again in the Discussion section.

Experimental Study

Apparatus and Experimental Method. The experimental apparatus consists of a water tank 0.8m (width) × 0.8m (depth) × 9m (length) and equipment for propulsion genera-

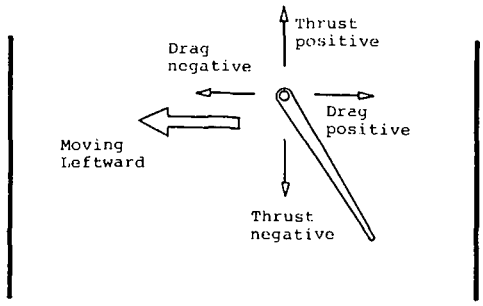

Fig. 5 Definition of thrust and drag

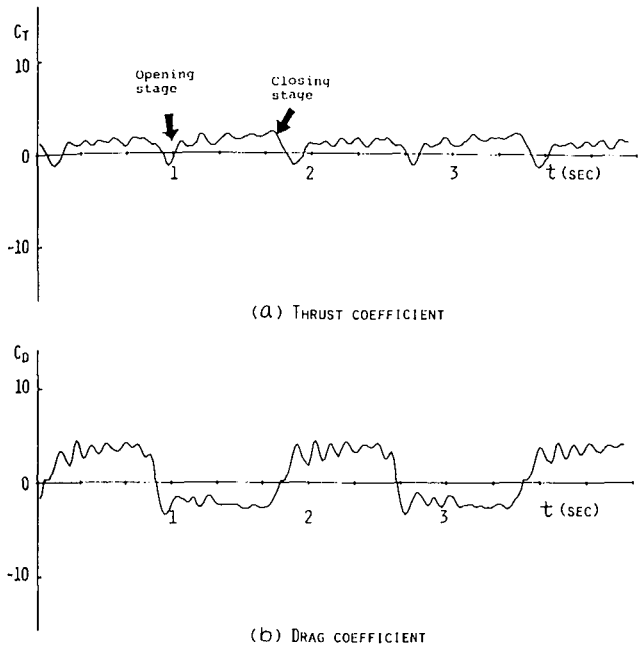

Fig. 6 Time variations for thrust coefficient and drag coefficient

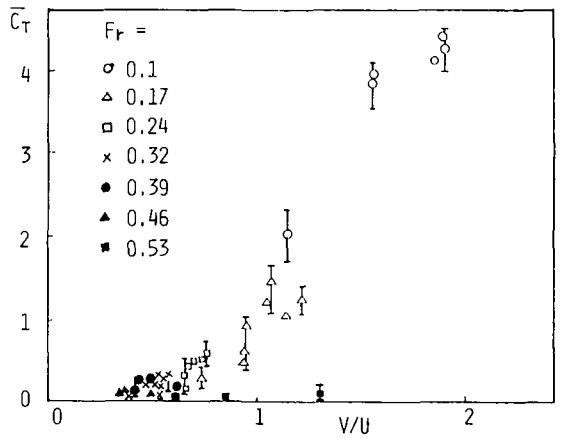

Fig. 7(a)

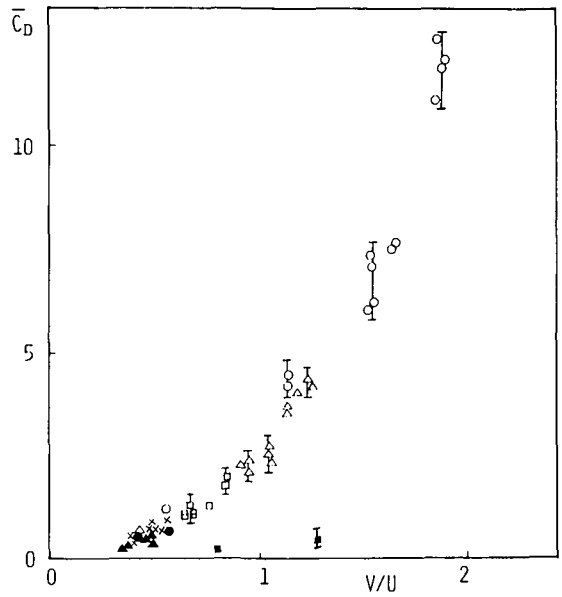

Fig. 7(b)

Fig. 7 Time averages of thrust and drag coefficients for c/h = 0.342 and α = 30 deg

tion attached to the carriage shown in Fig. 2. The carriage is driven through a rope by an AC motor (1.5 kw) placed above the tank. The motor is controlled by an inverter and the carriage is towed initially with constant acceleration and then at constant speeds from 0 m/s to 2.5 m/s.

In order to make the wing move as shown in Fig. 1, the following equipment is used. A thin pipe of aluminum is imbedded at the point 0.1 the chord length from the leading edge of the wing, and a steel rod of 4mm diameter (piano wire) is put through the pipe as shown in Fig. 3; the wing is freely rotatable about the rod. The point where the pipe is imbedded corresponds the point p in Fig. 1. The rod is connected rigidly to a slide (linear bearing) moving back and forth along a rail laid on the carriage perpendicular to the direction of towing. When the slide is moving, the wing opens up to a certain angle by the moment acting on the wing about the rod. The opening angle is fixed by adjusting the length of a chain connecting the slide and a point near the trailing edge of the wing. The wing closes at the wall, and translates after opening to some angle, and at this stage the angle is kept almost constant (although with some fluctuation). The reciprocal motion of the slide is achieved by reversing the current into a DC geared motor (14W) with limit switches located at both ends of the rail. A pulley is attached to the shaft of the gear, and the slide is driven by a belt. In order to make the wing close perfectly, side boards (750mm × 500mm) are located on both sides of the facility as shown in Fig. 4.

Method of Measurement of Thrust and Drag. The thrust and the drag on the wing have been defined in Fig. 5. These forces are obtained by measuring the strain of the rod with strain gages attached on the front, rear, right, and left sides of the rod. As shown in Fig. 5, if the rod is deflected upward, the thrust is positive, while if the rod is deflected downward, the thrust is negative (and the wing is resistant against the forward movement of the ship). When the wing is moving leftward, the drag is positive if the rod is deflected rightward, while it is negative (and the wing receives energy from the flow) if the rod is deflected leftward.

The output from the strain gages is amplified up to 250 times and fed to a computer (NEC PC8001) through an AD converter. The data are taken at 60 points per second for both the thrust and the drag, and for each run of the experiment the data of, at least, three cycles are taken. From the data, the variation of the thrust and the drag with time is plotted and the average values of these forces through one cycle, and the efficiency, are calculated.

Conditions of Experiment. In the experiment, the width h

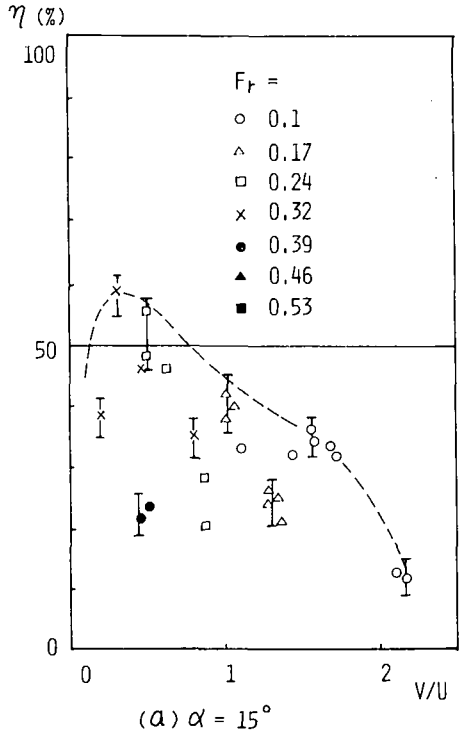

Fig. 8(a)

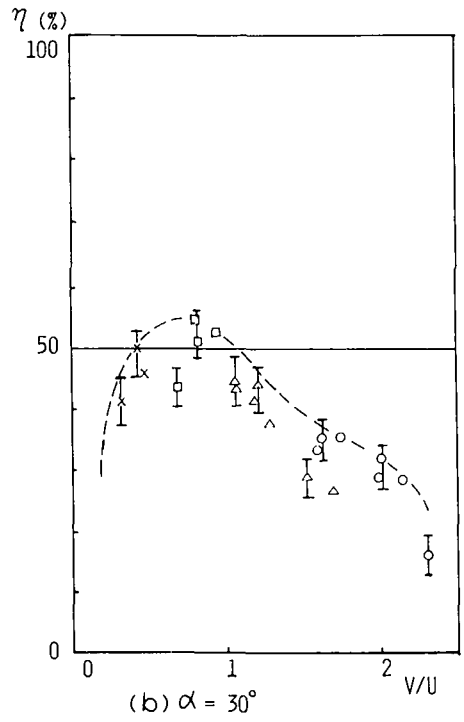

Fig. 8(b)

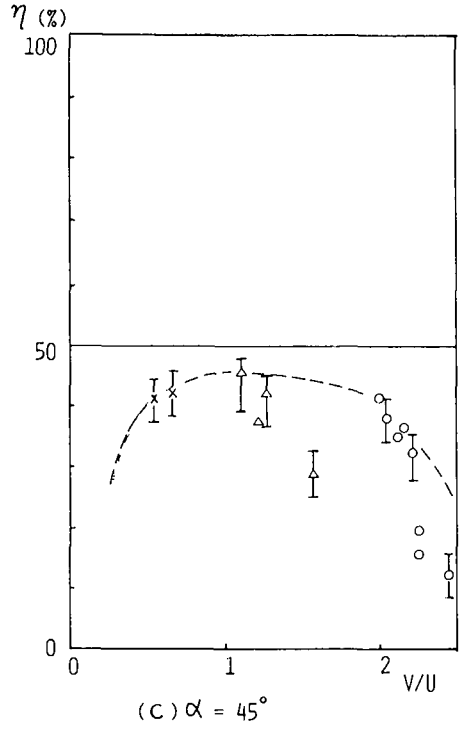

Fig. 8(c)

Fig. 8 Propulsive efficiencies for c/h = 0.256. Dashed lines in figures denote curves connecting high efficiency points for variable values of V/U.

of the channel (the distance between the side boards) is fixed as 0.49m, and to types of wings of different chord length $c=0.167$m and 0.125m but of the same span 0.3m are used. The opening angles α are set at 15, 30, and 45 deg, and the towing speed of the carriage U (corresponding to the speed of the downward flow in Fig. 1) and the moving speed of the slide V are varied, and the thrust and drag are then measured.

As Spedding and Maxworthy [6] mentioned, the flowfield and therefore the force on the wing will vary according to the time-history of the wing motion. Although we did not record the time-history, the slide to which the wing was connected was moving at almost constant speed V. Therefore the point p in Fig. 1 is considered to move at constant speed, and in the opening stage the wing may rotate about the trailing edge with decreasing velocity and translate upstream. In the closing stage, on the other hand, the rotation of the wing may accelerate and the wing may move slightly downstream.

The present study is the first to show that the two-dimensional model of the Weis-Fogh mechanism does work for ship propulsion, although the time-history of the wing motion is not considered. However, it is necessary to consider the detailed wing motion to improve or raise the efficiency of the propulsion mechanism.

Experimental Results. The thrust coefficient and the drag coefficient are defined as

$$C_T = T/\frac{1}{2}\rho V^2 S, \quad C_D = D/\frac{1}{2}\rho V^2 S,$$

where T is the thrust, D is the drag, ρ is the density of water, and S is the area of the wing. The variations of the thrust and drag coefficients with time through five cycles for $U=0.43$ m/s, $V=0.48$ m/s, $c/h=0.342$, and $\alpha=30$ deg are shown in Fig. 6.

Figure 6 shows that when the wing begins to open, the thrust becomes negative. This is in agreement with the potential flow analysis in [8]; if the rotation of the wing is accelerated, then positive thrust may be obtained as long as the flow does not differ from a potential flow. However, the thrust appears to be positive in the later stage of opening, where the flow will differ from the potential solution, and the positive thrust may be due to an increase of the circulation by a separation bubble near the leading edge. For a more definite description, we need more detailed information on the flowfield. When the wing is closing, one might expect a large thrust because the fluid between the wing and the wall is pushed out. However such a

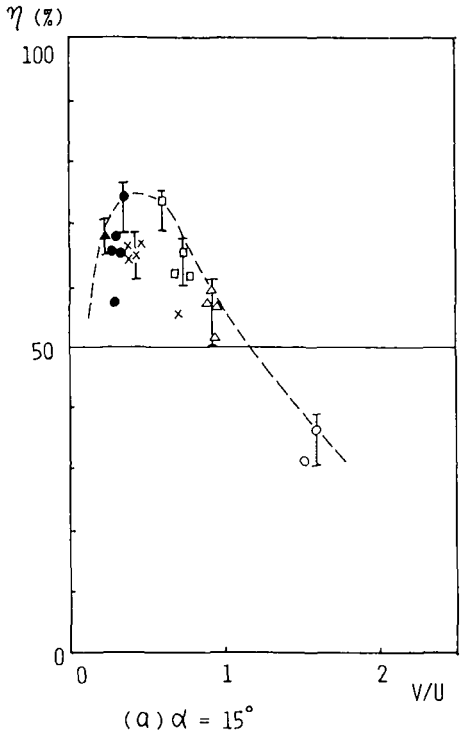

Fig. 9(a)

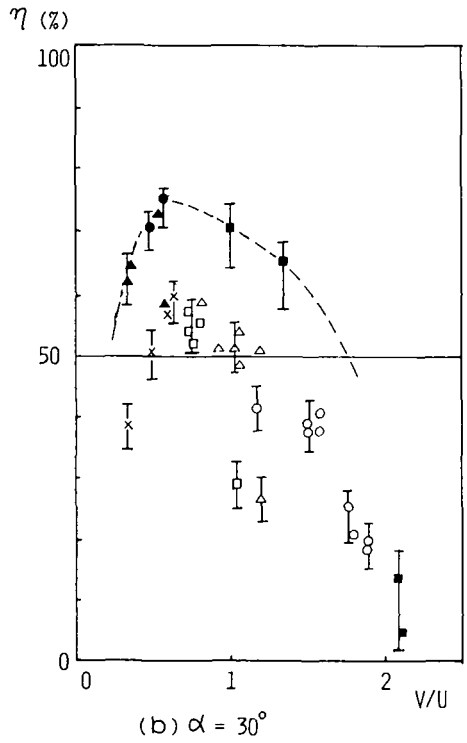

Fig. 9(b)

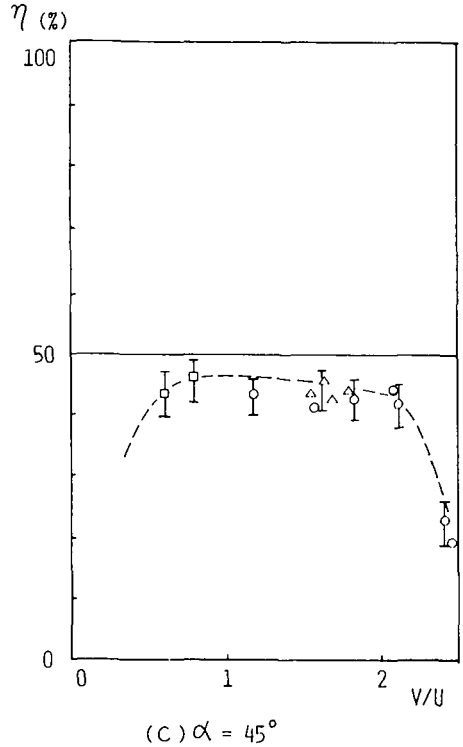

Fig. 9(c)

Fig. 9 Propulsive efficiencies for $c/h = 0.342$

large thrust is not obtained because there is a free surface above the wing, and the fluid will escape to the surface.

Figure 6 also shows that the drag is positive when the wing is moving rightward, and negative when the wing is moving leftward. The absolute values for the two cases are different because the moving speeds of the slide to the right and left are somewhat different. Thus the data for each case should be considered independently (this also applies to the thrust). The fluctuations in the thrust and the drag are due to the shedding of vortices from the wing surface.

The time averages of the thrust and the drag through one cycle are denoted as $\bar{C}_T$ and $\bar{C}_D$, respectively, and are shown in Fig. 7 for $c/h = 0.342$ and $\alpha = 30$ deg. The Froude number

$$\mathrm{Fr} = U/\sqrt{dg},$$

where g is the acceleration of gravity and d is the water depth, is considered a significant parameter because wave resistance acts in this experiment. It is seen that as V/U increases, both $\bar{C}_T$ and $\bar{C}_D$ increases. However, at the largest value of Froude number (.53), $\bar{C}_T$ and $\bar{C}_D$ are too small relative to the experimental uncertainty to draw any conclusions.

We define here the propulsive efficiency of this mechanism as the ratio of the product of the average thrust and the advancing speed of the ship to the external work performed on the wing per unit time,

$$\eta = \bar{C}_T U/\bar{C}_D V.$$

The efficiency is plotted as a function of V/U, with the Froude number as a parameter for $c/h = 0.256$ in Fig. 8 and for $c/h = 0.342$ in Fig. 9. The efficiency is high in the vicinity of the opening angle of 15 deg for $c/h = 0.256$, and of 15 and 30 deg for $c/h = 0.342$. In these cases, the efficiency is high for V/U less than 0.6, indicating that the moving speed of the wing can be smaller than the advancing speed of the ship which is suitable for practical operation. The maximum efficiency is about 75 percent for $c/h = 0.342$, opening angle $\alpha = 30$ deg, and $V/U = 0.5$.

Working Test of a Model Ship

As described above, this mechanism of ship propulsion is efficient and has several advantages which are described in the Introduction. In order to determine how this mechanism works for actual ships, we made a model ship, conducted

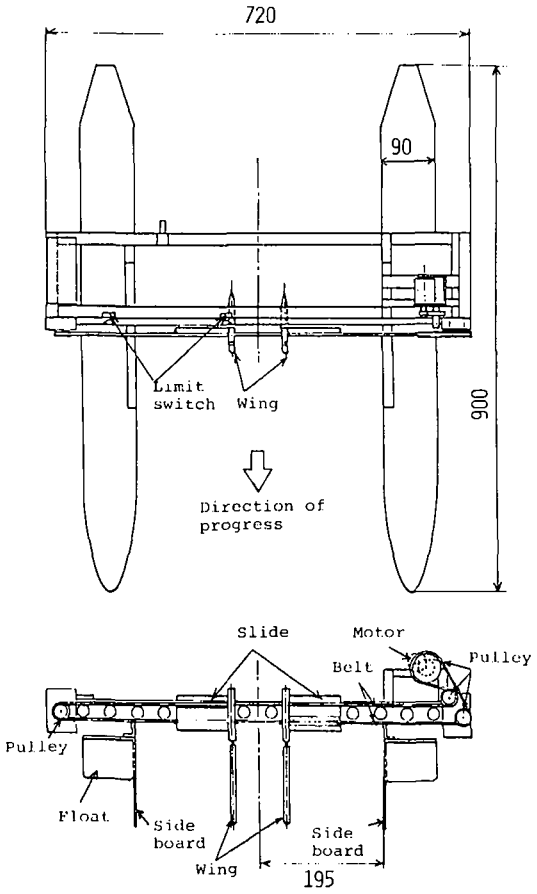

Fig. 10 Model ship (unit length is mm)

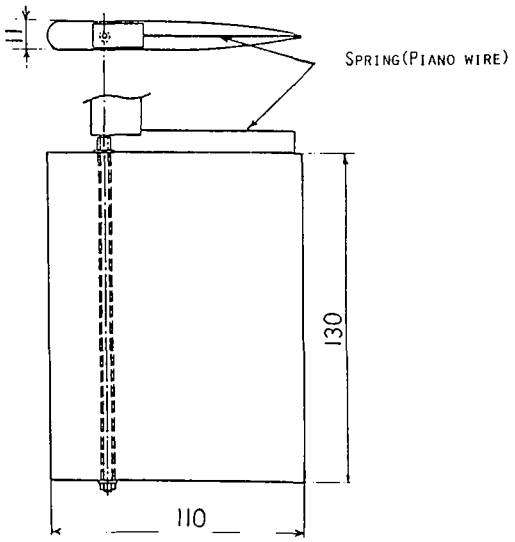

Fig. 11 Structure of wing for model ship

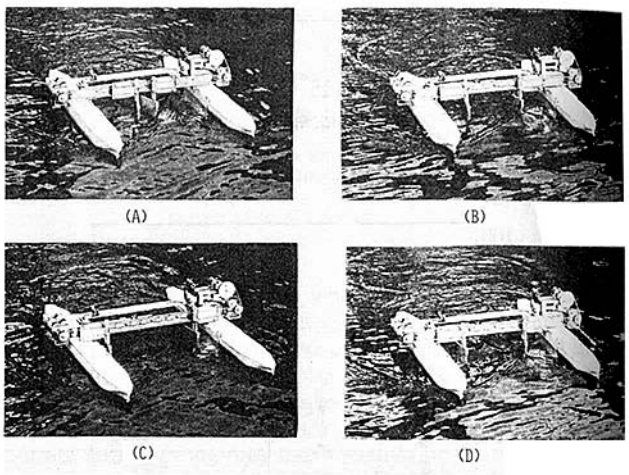

Fig. 12 Sailing model ship

working tests, and obtained results which support the applicability of this mechanism to actual ship propulsion.

The Model Ship. The model used in this test is of catamaran type with two wings which move as shown in Fig. 1 between the two hulls of the ship. The scale of the model is shown in Fig. 10. The mechanism of driving the wings is almost the same as that used in the experiment described in the previous section. The differences are: there are two wings, which move symmetrically, instead of one and the opening angle is controlled by a spring (piano wire) shown in Fig. 11 instead of a chain. The wing opens up to the angle at which the moments due to fluid forces and the spring force balance about the rod. A DC motor (6V, 1.2W) is used and run by four rechargeable dry batteries (Ni-Cd).

The advancing speed of this model is almost constant and about 0.59 m/s, while the moving speed of the wings is 0.19 m/s on the average. The opening angle of the wings is about 40 deg, and is somewhat larger when the ship starts or when the ship is at rest.

The efficiency of propulsion is defined as

$$\eta = \frac{\text{(Drag on the ship's hull)} \times \text{(Advancing speed)}}{\text{External work on the wings (per unit time)}}$$

and is about 0.53. In the equation of efficiency, the drag on the ship's hull is measured directly by towing the model with wings closed. The external work on the wings is obtained by towing the wings in water at the same speed as that in actual runs, measuring the force on the wing and calculating the external work from the force and the moving speed of the wings. We should note here that the drag on the ship and the mean thrust on the wings will coincide when the ship is advancing steadily. However the measured drag is that obtained by stopping the wing motion; therefore the mean thrust and the drag will be slightly different. Accordingly, the above definition of the efficiency is not the same as that presented in the previous section. In this test, we did not alter conditions because of limitation of the model. Since this test had actually been carried out before the experimental study previously described, the data and suggestions for improvement of the efficiency obtained through the experiment were not used in the test. The efficiency of the model ship can therefore be improved by changing the operational conditions.

Discussion

In the Introduction, expected advantages and disadvantages of this propulsion mechanism are presented. The experimental results on the model of the propulsion mechanism and the working test of the model ship confirm that the flow velocities relative to the wing are small (advantage #1 in Introduction) and that unsteadiness in the flow is used effectively to generate thrust (advantage #3).

Considering the disadvantages, the most serious problem may be #1 the complicated mechanism for moving the wings. The mechanism used in this study is just an example; hopefully a more practical mechanism can be used for actual ships. Regarding #2, the load variation of the motor, it was found by

monitoring the current into the motor that the load was almost constant, through one cycle. Therefore, it is beleived that this will not become a serious problem. For #3, the periodic acceleration on the ship hull, the model ship appeared to be sailing very smoothly, although periodic acceleration must have occurred. This acceleration can be reduced considerably by using a series of mechanisms and varying the phases of the wings' motion.

We have so far studied the charcteristics of this propulsion mechanism at rather low ship speeds. As described above, the wings move very slowly compared with the advancing speed of the ship so that cavitation should not appear, even at high speeds of the ship. Thus, the mechanism is expected to have a high efficiency for high-speed ships, as well.

Conclusions

An application of the Weis-Fogh mechanism to ship propulsion was investigated. The conclusions obtained so far are as follows.

1) A working model of the propulsion mechanism based on the Weis-Fogh mechanism is proposed.

2) The characteristics of the above model have been experimentally investigated; in particular, the thrust and the drag on the wing have been measured. The thrust becomes negative in the opening stage as suggested by previous analysis. The maximum efficiency is about 75 percent when the opening angle is about 30 deg and the ratio of the moving speed of the wing to the advancing speed of the ship V/U is about 0.5.

3) A working test of a model ship has been performed and this propulsion model found to work well. The ship advances very smoothly and the wings move much more slowly than the advancing speed of the ship. The efficiency of propulsion for this model is about 53 percent.

4) The applicability of this propulsion mechanism to actual ships is expected to be very good and further study on this subject is of great interest.

Acknowledgments

The authors thank Professor Kosaku Hiroshima for his valuable comments. Thanks are also due to Messrs. Y. Nakamura, M. Ishimaru, Y. Hasegawa, and G. Deki for their assistance in carrying out the experiments.

References

1 Weis-Fogh, T., "Quick Estimates of Flight Fitness in Hovering Animals, Including Novel Mechanism for Lift Production," *Journal Exp. Biol.*, Vol. 59, 1973, pp. 169-231.

2 Lighthill, M. J., "On the Weis-Fogh Mechanism of Lift Generation," *Journal Fluid Mech.*, Vol. 60, 1973, pp. 1-17.

3 Maxworthy, T., "Experiments on the Weis-Fogh Mechanism of Lift Generation by Insects in Hovering Flight. Part 1. Dynamics of the 'Fling'," *Journal of Fluid Mech.*, Vol. 93, 1979, pp. 47-63.

4 Edwards, R. H., and Cheng, H. K., "The Separation Vortex in the Weis-Fogh Circulation-Generation Mechanism," *Journal Fluid Mech.*, Vol. 120, 1982, pp. 463-473.

5 Haussling, H. J., "Boundary-Fitted Coordinates for Accurate Numerical Solution of Multibody Flow Problems," *Journal Comp. Phys.*, Vol. 30, 1979, pp. 107-124.

6 Spedding, G. R., and Maxworthy, T., "The Generation of Circulation and Lift in a Rigid Two-Dimensional Fling," *Journal Fluid Mech.*, Vol. 165, 1986, pp. 247-272.

7 Furber, S. B., and Ffowcs Williams, J. E., "Is the Weis-Fogh Principle Exploitable in Turbomachinery?" *Journal Fluid Mech.*, Vol. 94, 1979, pp. 519-540.

8 Tsutahara, M., and Kimura, T., "A Propulsion Mechanism for a Ship Using the Weis-Fogh Mechanism," *Bulletin JSME*, Vol. 29, No. 252, pp. 1710-1718.

Koji Kikuyama
Professor,
School of Engineering,
Nagoya University,
Furo-cho, Chikusa-ku,
Nagoya, Japan

Mitsukiyo Murakami
Professor,
Aichi Institute of Technology,
Yagusa-cho, Toyota, Aichi, Japan

Shin-ichi Oda
Engineer,
Nippon Denso Co. Ltd,
Showa-cho, Kariya,
Aichi, Japan

Ken-ichi Gomi
Engineer,
Mitsubishi Electric Cooperation,
Wadasaki-cho, Hyogo-ku,
Kobe, Japan

Pressure Recovery of Rotating Diffuser With Distorted Inflows

The pressure recovery and velocity distributions in a two-dimensional rotating curved diffuser have been studied experimentally when even and uneven flows, respectively, were introduced to the diffuser. Two types of uneven flow were adopted; one has a linear velocity gradient on the surface of revolution and the other a linear velocity gradient in the meridian plane. The pressure recovery in the diffuser is improved by the uniformalizing process of the uneven inlet velocities in the downstream sections if larger velocities are in the suction side region, but it is deteriorated if larger velocities are introduced in the pressure side region. When an uneven flow with a velocity gradient in the meridian plane is introduced to the diffuser, increased rotation speed and the gradient of the inlet velocity profile deteriorate the pressure recovery.

1 Introduction

Recently there has been in increased interest in flow patterns inside rotating channels. Many studies have been made on this problem using channels of comparatively simple configurations in order to clarify the fundamental flow nature in centrifugal impellers. It has been experimentally proven that system rotation affects the turbulence inside a channel and that the Monin-Oboukov law about the turbulent mixing length is valid for the rotating channel flow [1]. Koyama et al. also conducted experiments concerning Coliolis effects upon the turbulent boundary-layer developments and turbulence structures inside a rotating rectangular channel with a large aspect ratio [2, 3]. Using two equation model, Howard et al. calculated the velocity profiles in a rotating rectangular channel, the results of which were confirmed with their experiments [4]. Moore [5, 6] have made both theoretical and experimental studies of flow patterns inside a two-dimensional straight diffuser when it was rotated about an axis perpendicular to the channel, and found that the channel rotation suppresses the boundary-layer development on the pressure side wall and thickens the layer in the suction side. The occurrence of a stall inside a rotating diffuser was examined by Rothe et al. [7] for various diffuser angles and rotation rates. It was found that the rotation increased stalling possibilities. In these studies, however, a uniform flow pattern is conditioned at the channel inlet, but in the actual centrifugal impeller passages this uniform flow condition is rarely satisfied. Recently, the effects of the distorted inlet velocity profiles upon the pressure recovery of a rotating straight diffuser, were examined by the present authors [8] and the inlet flow, with higher velocities near the lower pressure side of the channel, was found to improve the pressure recovery of the diffuser.

The present study describes the experimental results on the pressure recovery in a curved diffuser rotating about an axis perpendicular to the channel when uneven flows with shear type velocity distributions were introduced into the diffuser.

2 Equipment and Method of Experiments

Figure 1(*a*) shows the general configuration and measuring sections of the curved diffuser used in this experiment. The aspect ratio of the inlet section is 2:1 and the area ratio of the exit section to the inlet one A_2/A_1 is 1:2.6. The radius of the curvature and length of the diffuser centerline are 14.0 W_1 and 7.6 W_1, respectively, where W_1 denotes the width of the inlet section.

Figure 1(*b*) shows the change in the volumetric mean velocity V_m/V_{m1} along the channel when the diffuser was regarded as an isolated impeller channel having the exit section of S-6. The curves of typical deceleration rates w/w_1 of mixed flow impeller passage obtained by Balje [9] are plotted by broken lines in the same figure where K_e is a numerical constant given in the following equation;

$$w^2 = w_1^2 + (w_2^2 - w_1^2)(l/L)^{K_e} \tag{1}$$

where w_1 and w_2 are the inlet and exit relative velocities, respectively.

The change in the relative velocity V_m/V_{m1} is almost linear, corresponding to the relation for $K_e = 1$.

Contributed by the Fluids Engineering Division for publication in the JOURNAL OF FLUIDS ENGINEERING. Manuscript received by the Fluids Engineering Division October 22, 1985.

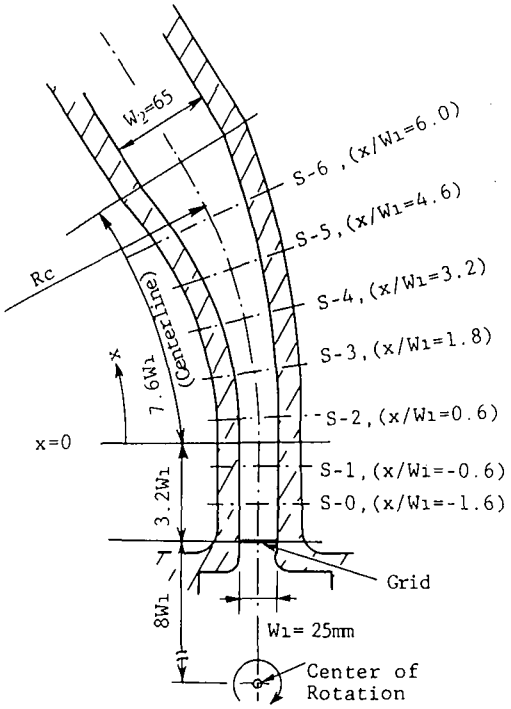

Fig. 1(*a*) Dimensions of curved diffuser and measuring sections

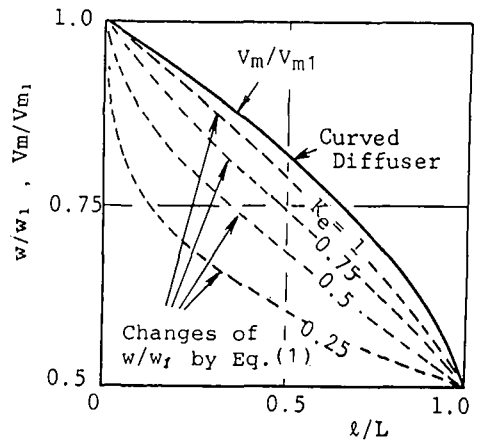

Fig. 1(*b*) Change in longitudinal mean velocity along channel

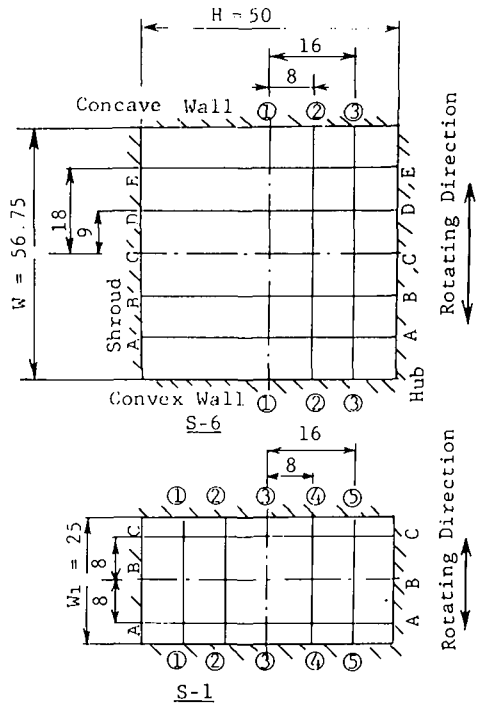

Fig. 1(*c*) Directions of yaw probe traverse (S-1 and S-6) (dimensions in mm)

Static pressures in the rotating diffuser were taken on the convex and concave walls at the measuring sections, respectively, as shown in Fig. 1(*a*), and they were transmitted to manometers in the stationary state by mechanical seals. The velocity profiles inside the diffuser were also measured in these sections by a three-hole cylindrical yaw meter of 2.0 mm diameter. Figure 1(*c*) shows the cross-sectional views of the diffuser both at S-1 and S-6, where the probe was traversed along the lines of A-A, B-B, . . . , and E-E or the lines ①-①, ②-②, . . . , and ⑤-⑤.

Experiments were made at the ranges of Reynolds number of Re ($=V_{m1}W_1/\nu$) = 4.6 to 6.0×10^4 (V_{m1} = 1.8 to 2.4 m/s) and of the rotation rate n = 0 to 150 rpm. The rotation parameter was taken to be $N(=\omega W_1/V_{m1})=0$, ±0.04, ±0.08, and ±0.16, respectively.

In order to clarify the effects of the distorted inlet velocity profile upon pressure recovery, flows with both even and uneven velocity profiles were introduced to the diffuser. Grids were installed just upstream of the diffuser and two kinds of

Nomenclature

A = area of diffuser section, mm²
C_{pw} = pressure recovery coefficient measured by wall pressures (equation (4))
C_{pi} = pressure recovery coefficient for inviscid fluid
C_{pm} = averaged value of *Cpw* at section S-6 (equation (5))
H = height of diffuser channel, mm
K_e = numerical constant in equation (1)
l = axial distance measured from diffuser inlet, mm
L = value of l at S-6($=6.0W_1$), mm
N = rotation parameter (equation (6)) $=\omega W_1/V_{m1}$
N_c = ratio of centrifugal to inertia force (equation (7))
N_t = ratio of resultant to inertia force (equation (8))
P_w = measured wall pressure, Pa
P_w^* = reduced wall pressure $= P_w-\rho(r\omega)^2/2$, Pa
Ri = gradient Richardson number (equation (9))
V_m = mean axial velocity at diffuser section, m/s
V_{m1} = value of V_m at diffuser inlet section, m/s
V_x = longitudinal component of velocity, m/s
V_y, V_z = secondary components of velocity, m/s
W_1 = width of diffuser inlet section, mm
λ = dimensionless velocity gradient at S-1 in a shear flow of Type-1
λ_0 = value of λ behind grid
λ_m = mass average value of λ at S-1
ξ = dimensionless velocity gradient at S-1 in a shear flow of Type-2
ξ_0 = value of ξ behind grid
ω = angular velocity of channel rotation, 1/s

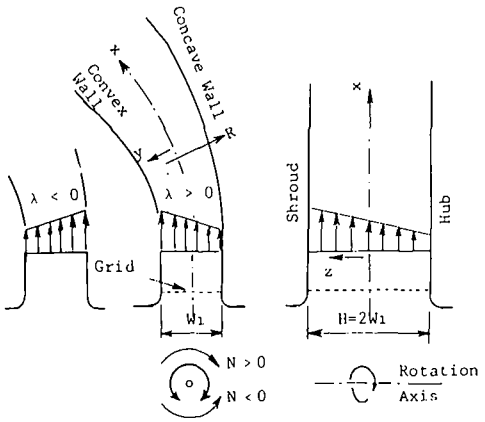

Fig. 2 Two kinds of shear flow at diffuser inlet

uneven velocity profiles, one having a linear velocity gradient in the rotating surface (Type-1) and the other having a velocity gradient in the surface normal to the rotating surface (Type-2) as shown in Fig. 2, were used. The dimensionless gradients of these shear flows were defined as follows:

for the shear flow of Type-1

$$\lambda = (dV_x/dy)/(W_1/V_{m1}) \tag{2}$$

where the positive or negative value correspond to the velocity profile increasing or decreasing toward the convex side of the wall, respectively, and

for the shear flow of Type-2

$$\xi = (dV_x/dz)/(H/V_{m1}) \tag{3}$$

In the experiment, the gradient of the inlet velocity were taken to be $\lambda_0 = \pm 0.35$ and ± 0.65 for Type-1, and $\xi_0 = 0.35$ and 0.65 for Type-2, where λ_0 and ξ_0 denote the gradients of the flow behind the grid provided that the flow is inviscid and the channel is stationary.

3 Equations

3.1 Coefficient of Pressure Recovery. The measured wall pressure P_w was corrected for the increase due to the centrifugal force caused by the system rotation as

$$P_w^* = P_w - \rho(r\omega)^2/2$$

Thus, the pressure recovery coefficient C_{pw} of the diffuser was defined by the following equation using the corrected pressures at the inlet and measuring sections, P_{w1}^* and P_w^*, respectively,

$$C_{pw} = (P_w^* - P_{w1}^*)/(\rho(V_{m1}^2/2) \tag{4}$$

To evaluate the pressure recovery in the diffuser, a mean pressure recovery coefficient was used as defined by

$$C_{pm} = (C_{pw1} + C_{pw2})/2 \tag{5}$$

where C_{pw1} and C_{pw2} are values of C_{pw} at the section of S-6 on the concave and convex walls, respectively.

3.2 Rotation Parameter. The ratio of the Coriolis force to the inertia force in the rotating channel is defined by the following equation, using the values of the diffuser inlet section,

$$N = \omega W_1/V_{m1} \tag{6}$$

where N is taken to be positive when the channel rotates clockwise and negative when it rotates counterclockwise as shown in Fig. 2.

The ratio of the centrifugal force due to the channel curvature to the inertia force is also given by

$$N_c = W_1/2R_c \tag{7}$$

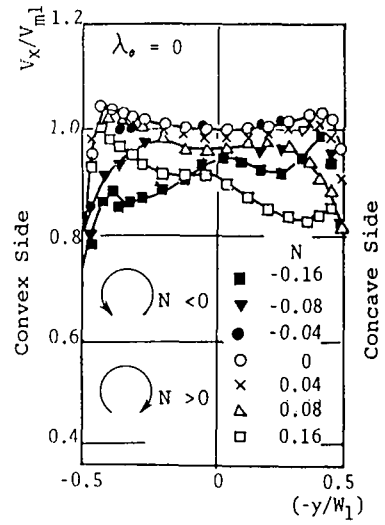

Fig. 3(a) $\lambda_0 = 0$

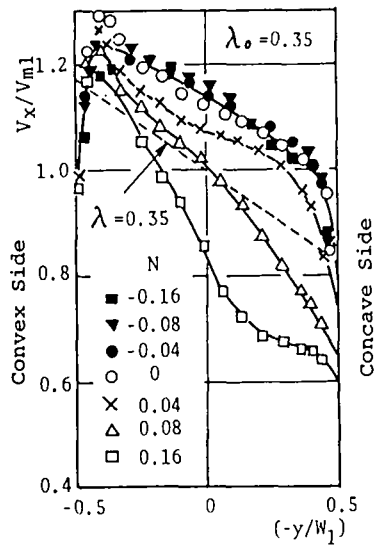

Fig. 3(b) $\lambda_0 = 0.35$

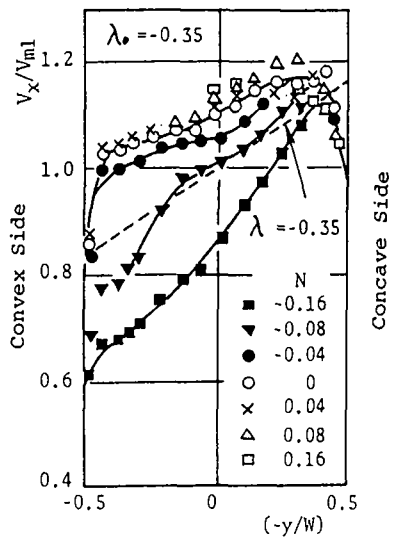

Fig. 3(c) $\lambda_0 = -0.35$

Fig. 3 Velocity profiles at section S-1 for different inlet flow conditions (Uncertainty in $V_x/V_{m1} = \pm 0.05$ at 20:1 odds and $= y/w_1 = \pm 0.04$)

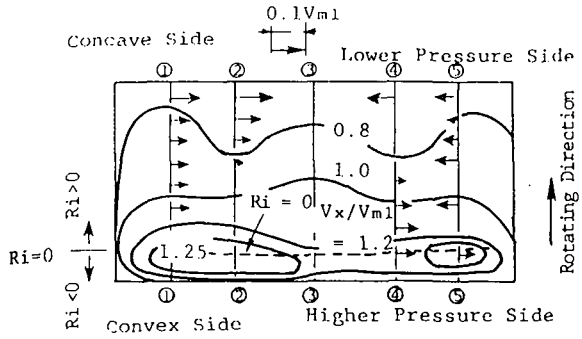

Fig. 4(*a*) $\lambda_0 = 0.35$

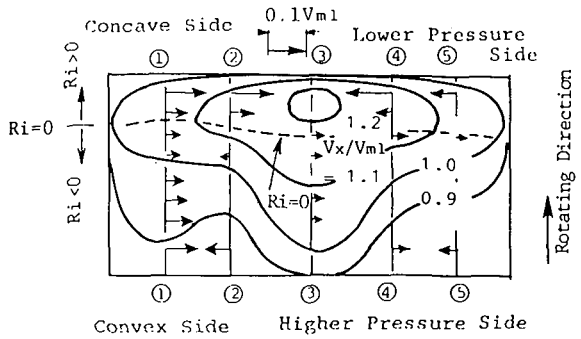

Fig. 4(*b*) $\lambda_0 = -0.35$

Fig. 4 Equi-velocity contours at section S-1 ($N = 0.08$ and $\lambda_0 = \pm 0.35$)

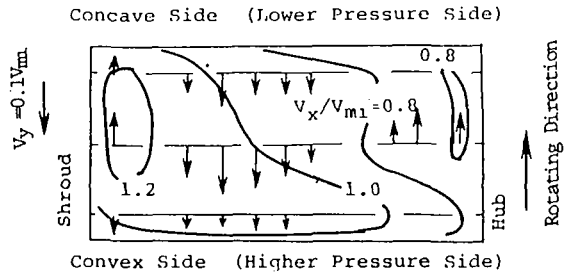

Fig. 5 Equi-velocity contours at section S-1 ($N = 0.16$ and $\xi_0 = 0.65$)

where R_c denotes the radius of curvature of the channel centerline. As the radius of the curved diffusers used in this study are 14.0 W_1, the value of N_c becomes 0.036.

With equations (6) and (7), the ratio of the resultant force to the inertia force N_t, is given as

$$N_t = (2\omega V_{m1} - V_{m1}^2/R_c)/(2V_{m1}^2/W_1)$$
$$= N - 0.036 \quad (8)$$

4 Uncertainties

The uncertainty limits of lengths W_1 and L were ascertained to be 0.1 mm and 0.5 mm, respectively. The mean velocity V_{m1} was determined from the volumetric flow rate divided by the cross-sectional area of the channel inlet. The volumetric flow rate was measured by an orifice within the uncertainty of 1.5 percent and the uncertainty limit of the rotation rate n was 1 rev/min. Thus, the uncertainty limit of the rotation parameter $N(=\omega W_1/V_{m1})$ is calculated to be 2 percent at 20:1 odds.

The uncertainty of the velocity measurement by a yaw probe was 5 percent at 20:1 odds. By integrating the local velocity over a section of the channel, the volumetric flow rate through that section can be calculated. The calculated flow rate for section S-6 was found to agree with those measured by the orifice within the uncertainty of 7 percent.

The pressure recovery coefficient C_{pw} derived by equation (4) would be within the uncertainty of 4 percent at 20:1 odds.

5 Results of Experiments and Discussions

5.1 Inlet Velocity Profiles. Figures 3(*a*), (*b*), and (*c*) show the longitudinal velocity profiles measured along the line ③-③ (shown in Fig. 1(*c*)) in the section S-1, lying 0.6 W_1 upstream from the diffuser inlet. The effects of rotation rates are compared for the cases with a grid ($\lambda_0 = \pm 0.35$), and without it ($\lambda_0 = 0$). For the lower rotation rates ($|N| \leqq 0.04$) the profiles exhibit nearly the same gradients as that prescribed by the grid. But the velocities in the lower pressure region decrease when $|N| > 0.04$. These decreases in velocity gradient are due to the accumulation of low velocity fluids in the suction side, which is caused by the Coriolis force. The inlet velocity profiles for the designated gradient of $\lambda_0 = 0.35$ in Fig. 3(*c*) are seen to agree well with those in Fig. 3(*b*) when the sign of rotation rate and abscissa ($= y/w_1$) are reversed.

The equi-velocity contours and secondary flow component in section S-1 are shown in Figs. 4(*a*) and (*b*) for the inlet conditions of $\lambda_0 = \pm 0.35$ when the channel was rotated at $N = 0.08$. In the case of the shear flow of Type-1 with $\lambda_0 = -0.35$, the region of larger velocities of V_x is seen to be concentrated in a central part of the concave side, which is due to the secondary flow caused by the Coriolis force as shown in the figure. On the other hand, when the shear flow of $\lambda_0 = 0.35$ enters the rotating diffuser, the fluids with larger velocities in the convex side are shifted toward the end surfaces and low velocity fluids dominate in the lower pressure side near the concave wall. This accumulation of low velocity fluids will cause an increase in the velocity gradient on line ③-③ of the section.

Figure 5 shows the velocity contours in section S-1 for $N = 0.16$ when an uneven flow of Type-2 with $\xi_0 = 0.65$ was introduced. In this inlet flow condition, a strong circulating flow was generated by the Coriolis force and the region of larger velocities is seen to dominate both the convex and shroud side regions in the inlet section of S-1.

5.2 Pressure Recovery in Diffuser. The changes in the pressure recovery coefficient C_{pw} of the curved diffuser are shown in Figs. 6(*a*) and (*b*), where the effects of rotation parameter N and the inlet flow condition λ_0 are compared. Due to the centrifugal force from the channel curvature, the wall pressures on the concave surface of the diffuser exhibit larger values than those on the convex surface. When the diffuser was rotated with the speed of $N = 0.04$, C_{pw} for $\lambda_0 = 0$ becomes largest at section S-6, but for the uneven inlet flow condition with $\lambda_0 = 0.35$, the pressure recovery is largely deteriorated. For the inlet condition of $\lambda_0 = -0.35$, the secondary flow caused by the Coriolis force makes the main flow velocities uniform and brings about an increase in the pressure recovery compared with that for $\lambda_0 = 0.35$, as shown in the figure. When the rotating direction is reversed ($N = -0.04$), the pressure recovery is increased for the inlet condition of $\lambda_0 = 0.35$, but not increased for the condition of $\lambda_0 = -0.35$ because of the reversed direction of the Coriolis force.

Figure 6(*b*) shows the pressure distributions for $N = 0.16$. When an uneven flow of $\lambda_0 = -0.35$ is introduced to the diffuser rotating at $N = 0.16$, larger values of C_{pw} are obtained than those with an even inlet flow condition, and they exceed even the value of C_{pi} calculated for the inviscid fluid flow with an even inlet profile. The reversal of the rotating direction, $N = -0.16$, causes an increase in C_{pw} for $\lambda_0 = 0.35$ and a decrease for $\lambda_0 = -0.35$.

Figure 7 shows the pressure recovery along the channel for the inlet flow condition of uneven profiles in the meridian surface (Type 2) and $N = 0.04$. Independent of the rotating direction, the pressure recovery coefficient C_{pw} is decreased with

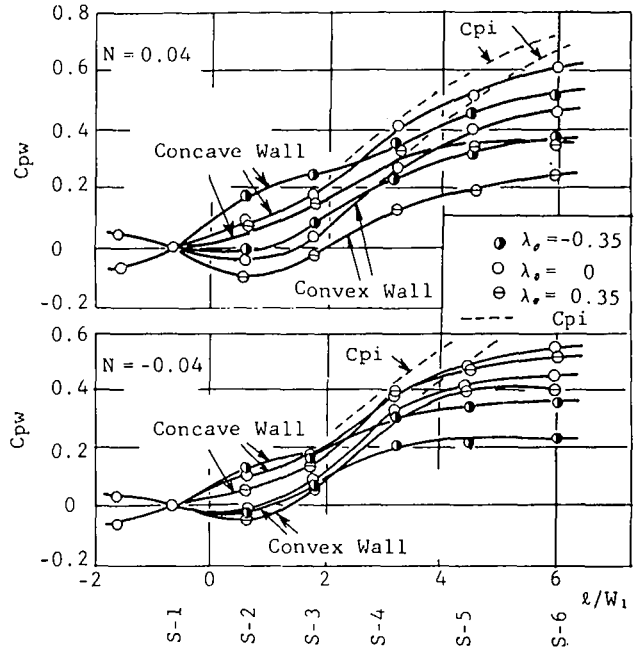

Fig. 6(a) $N = \pm 0.04$

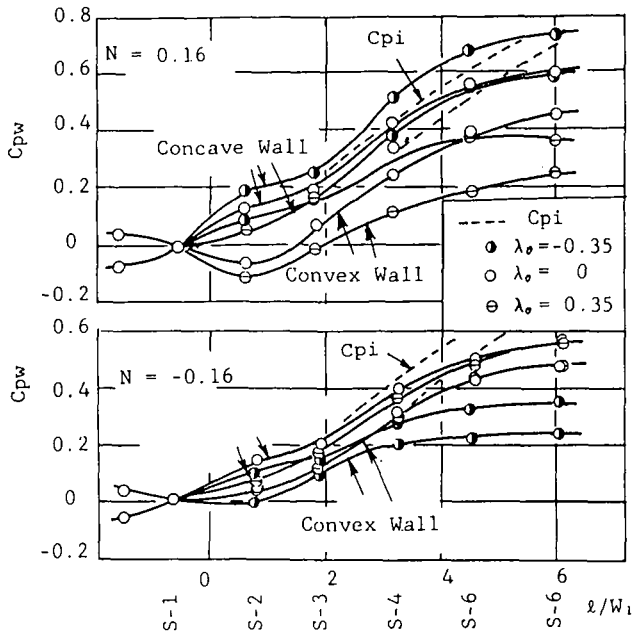

Fig. 6(b) $N = \pm 0.16$

Fig. 6 Wall pressure recoveries for inlet shear flow of Type 1 (Uncertainty in $l/W_1 = \pm 0.03$, and $C_{pw} = \pm 0.02$ at 20:1 odds)

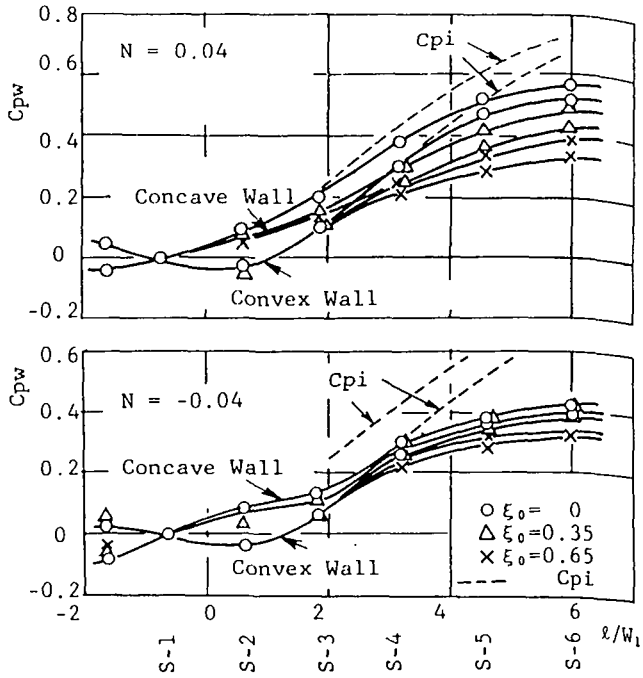

Fig. 7 Wall pressure recoveries for inlet shear flow of Type 2 (Uncertainty in $l/W_1 = \pm 0.03$, and $C_{pw} = \pm 0.02$ at 20:1 odds)

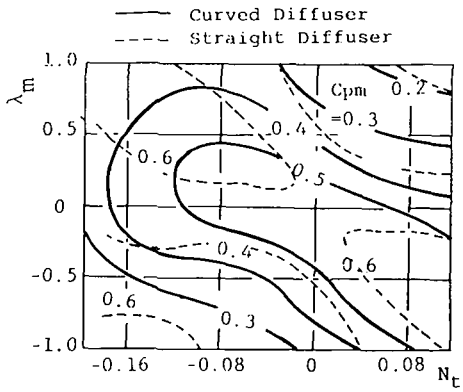

Fig. 8 Equi-pressure recovery contours for inlet shear flow of Type 1

increase in the velocity gradient, which means that the unevenness of inlet flow in the meridian surface deteriorates pressure recovery. In this rotational condition, C_{pw} for $N = 0.04$ exhibits larger values than those for $N = -0.04$. In the former condition, the centrifugal force due to the channel curvature weakens the effect of the Coriolis force and the generation of secondary flow inside the diffuser is prevented.

The effects of the inlet flow profile and rotation rate on the pressure recovery in the diffuser are summarized in Fig. 8 when uneven flows of Type-1 are introduced into the diffuser. In this figure, the value of pressure recovery averaged on the convex and concave surfaces at section S-6, C_{pm}, are plotted against the ratio of the resultant force to the inertia one, N_t, and the mass average velocity gradient, λ_m, calculated from the velocity profile at S-1. Using the parameter of N_t, the distribution of the pressure recovery coefficient for the curved diffuser is seen to be symmetric against the origin, and C_{pm} is increased with N_t approaching zero. In the same figure, the values of C_{pm}, obtained in the straight diffuser at the section of the same area corresponding to the section S-6 of the curved diffuser (8), are plotted for comparison. Due to the absence of the curved effect in the straight diffuser, the curves of equi-pressure recovery become symmetric with respect to the origin ($N_t = 0$, $\lambda_m = 0$), and C_{pm} takes its largest value for the combinations of $\lambda_m > 0$ and $N_t < 0$, and also $\lambda_m < 0$ and $N_t > 0$.

The contours of the equi-pressure recovery coefficient are shown in Fig. 9 when a Type-2 shear flow enters the diffuser. A larger value of C_{pm} appears near the region of $N_t = 0.04$ and $\xi_0 = 0$. As ξ_0 increases, the contours tend to be symmetric to the ordinate ($N = 0$), which means that C_{pm} tends to be independent of the rotational direction.

5.3 Velocity Distributions. Figures 10(*a*) and (*b*) show the velocity distributions at section S-6 when $N = \pm 0.08$ and Type-1 shear flows were introduced to the diffuser. As seen in

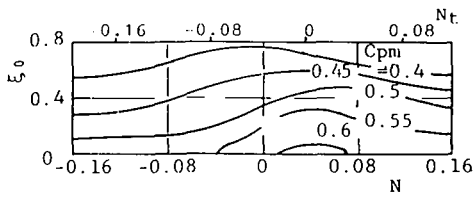

Fig. 9 Equi-pressure recovery contours for inlet shear flow of Type 2

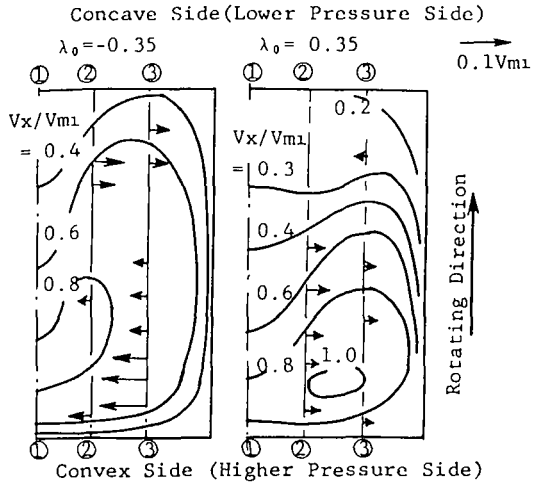

Fig. 10(*a*) $N = 0.08$

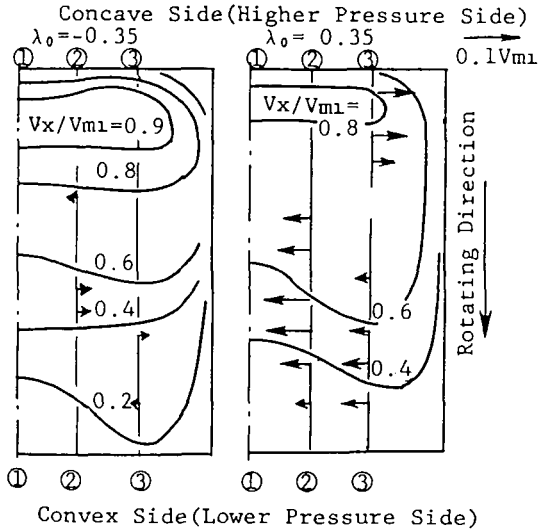

Fig. 10(*b*) $N = -0.08$

Fig. 10 Equi-velocity contours in section S-6 ($N = \pm 0.08$ and $\lambda_0 = \pm 0.035$)

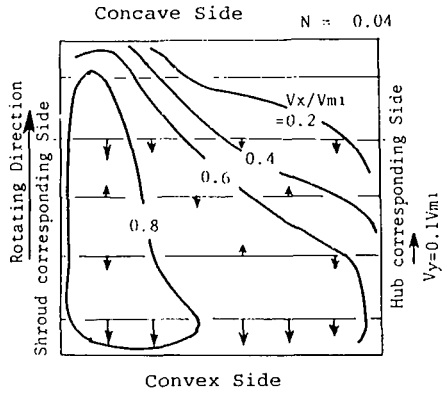

Fig. 11(*a*) $N = 0.04$

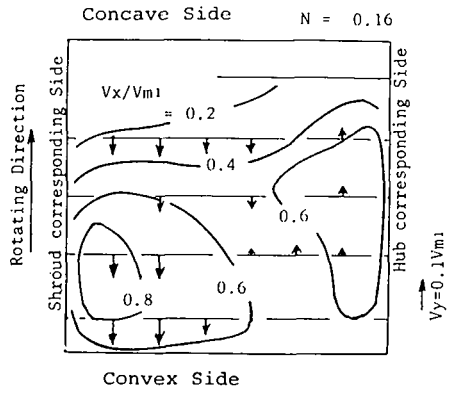

Fig. 11(*b*) $N = 0.0.16$

Fig. 11 Equi-velocity contours in section S-6 for $\xi_0 = 0.035$

Fig. 8, the pressure recovery is found to increase when the values of N and λ_0 have opposite signs and decrease when N and λ_0 have the same sign.

When $N = 0.08$ and $\lambda_0 = -0.35$, the flow having larger velocities near the convex wall at the inlet section, is seen to be largely flattened in section S-6, except for the mid-section, and the same results can be seen when $N = -0.08$ and $\lambda_0 = 0.35$ in Fig. 10(*b*).

On the other hand, when $N = 0.08$ and $\lambda_0 = 0.35$ (Fig. 10(*a*)), and when $N = -0.08$ and $\lambda_0 = -0.35$(Fig. 10(*b*)), the pressure recoveries are largely deteriorated, and uneven velocity distributions at the inlet are kept unchanged to the downstream section of S-6; the velocity being higher near the pressure wall. Distribution of the secondary flow components are plotted in Figs. 10(*a*) and (*b*). It is found that the generation of the secondary flow and the flattening of the velocity profiles are suppressed when N and λ_0 have the same sign.

Thus, the uniforming of flow velocities is considered to depend on the degree of suppression or promotion of turbulence caused by the Coriolis force and centrifugal forces of curved flow. As the criterion of the stability of flow in a rotating system or a curved duct, Bradshaw (10) proposed a gradient Richardson number. The Richardson number for the flow field under the effects of the centrifugal force due to the duct curvature and Coriolis forces of system rotation can be given by

$$R_i = \frac{2V_x/R_c - \omega\{1 - 2\omega/(\partial V_x/\partial R)\}}{(\partial V_x/\partial R)} \tag{9}$$

If the Coriolis force exceeds the centrifugal force and the term (V_x/R_c) in this equation can be neglected, the above equation can be transformed as

$$R_i = 2(N/\lambda)(1 + 2N/\lambda) \tag{10}$$

where it is assumed that the gradient of the inlet flow is linear and $(\partial V_x/\partial R)$ is replaced by $(-\partial V_x/\partial y)$. In the above equation, if (N/λ) is positive, that is, N and λ have the same sign, R_i is positive. This means that the velocity fluctuations in the flow tend to be suppressed and the rate of change in the velocity distribution along the channel is decreased. On the other hand, when $|N/\lambda|$ is small, and N and λ have different signs, the value of R_i becomes negative and fluctuations in the flow are enhanced, which promotes a flattening of velocity distributions in the downstream sections. As an example, the

line of $R_i = 0$ in the inlet section of S-1 is plotted in Figs. 4(*a*) and (*b*) by dotted lines. It is found that a larger part of the inlet section is covered by the region of $R_i > 0$ when $\lambda_0 = 0.35$, and that the inlet section is dominated by the region of $R_i < 0$ when $\lambda_0 = -0.35$.

Figures 11(*a*) and (*b*) show the velocity distributions at the section of S-6 for $N = 0.04$ and 0.16 when shear flows with uneven velocity distributions in the meridian surface ($\xi_0 = 0.35$) were introduced. When $N = 0.04$, both the Coriolis and centrifugal forces are almost counterbalanced, and the unevenness of the velocity profiles at the inlet are seen to be kept almost unchanged to the downstream sections. When the rotational speed was increased to $N = 0.16$, the larger velocity region is shifted toward the pressure side and any velocity uniformalization is visually undetectable. This uneven velocity distribution brings about a decrease in the pressure recovery as shown in Fig. 8.

6 Conclusions

The changes in the pressure recovery coefficient and velocity distributions along the channel were investigated when a curved diffuser was rotated about an axis perpendicular to the flow field and uneven flows were introduced into the channel. The results are summarized as follows;

(1) When a shear type of flow having a velocity gradient in the plane of rotating surface curvature, (Type-1), is introduced, the channel rotation increases pressure recovery of the diffuser where higher velocities prevail in the lower pressure region at the inlet section, but the rotation decreases the pressure recovery in the case where higher velocities prevail in the higher pressure region. These increases/decreases in pressure recovery of the diffuser will be attributable to the uniforming of the uneven inlet velocities and suppression of secondary flow generation in the downstream section of the diffuser.

(2) When a shear flow having a velocity gradient in the meridional surface is introduced, the pressure recovery is decreased with increases in the velocity gradient and rotation speed. This is because the fluids with larger velocities are shifted to the pressure side in the flow course, and the flattening of flow is prevented.

References

1 Johnston, J. P., "The Suppression of Shear Layer Turbulence in Rotating Systems," ASME Journal, Vol. 98, June 1976, pp. 229-236.

2 Koyama, H., Masuda, S., Ariga, I., and Watanabe, I., "Stabilizing and Destabilizing Effects of Coriolis Force on Two-Dimensional Laminar and Turbulent Boundary Layers," ASME *Journal of Engineering for Power*, Vol. 101, No. 1, 1979, pp. 23-31.

3 Koyama, H., Masuda, S., Ariga, I., and Watanabe, I., "Turbulence Structure and Three-Dimensionality of a Rotating Two-Dimensional Turbulent Boundary Layer," *Proceedings of the 2nd Symposium on Turbulent Shear Flows*, 1979, pp. 4.22-4.27.

4 Howard, J. H. G., and Patankar, S. V., and Bordynik, R. M., "Flow Prediction in Rotating Ducts Using Coriolis-Modified Turbulence Models," ASME JOURNAL OF FLUIDS ENGINEERING, Vol. 102, Dec. 1980, pp. 456-461.

5 Moore, J., "A Wake and an Eddy in a Rotating, Radial-Flow Passage, Part 1: Experimental Observations," ASME *Journal of Engineering for Power*, Vol. 95, July 1973, pp. 205-212.

6 Moore, J., "A Wake and an Eddy in a Rotating, Radial-Flow Passage, Part 2: Flow Model," Vol. 95, July 1973, pp. 213-219.

7 Rothe, P. H., and Johnston, J. P., "Effects of System Rotation on the Performance of Two-Dimensional Diffusers," ASME JOURNAL OF FLUIDS ENGINEERING, Vol. 98, Sept. 1976, pp. 422-430.

8 Kikuyama, K., Murakami, M., and Oda, S., "Flows and Pressure Recovery in a Rotating Diffuser," *Bulletine of JSME*, Vol. 26, No. 216, 1983, pp. 970-977.

9 Balje, O. E., "Loss and Flow Path Studies on Centrifugal Compressors: Part 2," ASME *Journal of Engineering for Power*, Vol. 92, July 1970, pp. 287-300.

10 Bradshaw, P., "The Analogy Between Streamline Curvature and Buoyancy in Turbulent Shear Flow," *Journal of Fluid Mechanics*, Vol. 36, Part I, 1969, pp. 177-191.

Response of an Operational Turbofan Engine to a Simulated Nuclear Blast

M. G. Dunn

C. Padova

Physical Sciences Department,
Calspan Advanced Technology Center,
Bufallo, N.Y.

R. M. Adams

Headquarters/SPAS,
Defense Nuclear Agency,
Alexandria, Va.

This paper describes the results of a measurement program designed to determine the transient response of an air-breathing propulsion system to simulated nuclear blast waves. A Ludwieg-tube facility, incorporating a driver technique consisting of an activating chamber and a nonfrangible diaphragm, was used to create the required shock waves. Detailed measurements were performed at incident shock overpressures of approximately 6.9, 10.3, 13.8, and 17.2 kPa (1.0, 1.5, 2.0, and 2.5 psi). For each of these overpressures, data were obtained for engine speeds of 0, 80, 90, and 100 percent of maximum speed. Typical results are presented for distortion patterns at the fan face for both an extended bellmouth and a S-shaped inlet at either 0 or 20 deg yaw angle.

1 Introduction

The response of a given propulsion system to inlet flow distortion and internal blast-wave propagation is governed by many factors. The type of engine is known to be important. As part of the program, two types of engines (a turbojet and a turbofan) have been utilized. The results of the turbojet measurements were previously reported [1]. This paper will describe the results of the turbofan engine measurements program. For a specific engine, the internal gasdynamic response is dependent on the internal engine configuration (the number and type of compressor and turbine stages, and combustor type), the engine operating point (stage pressure and stall-margin ratios, nozzle pressure ratio, turbine inlet temperature, and fuel/air ratio) and the engine control system. The type of inlet (internal, external, or mixed compression; high or low length-to-diameter ratio; boundary-layer bleed and bypass provisions), and type of nozzle (converging or converging-diverging), will modify overpressure waves by changing the effective wave strength and introducing flow distortion. A S-type inlet or an extended bellmouth was mounted on the engine for the measurements reported here. The local blast-wave strength and orientation with respect to the engine inlet strongly affect the resultant internal engine pressures and temperatures.

The purpose of this research was to implement a laboratory experiment in order to obtain fundamental data for the transient response of a turbofan engine when that engine is subjected to a simulated blast-wave environment. A limitation of our previous turbojet experiments [1] was that the engine instrumentation was not sufficiently detailed for the overall objectives because that engine had been specifically instrumented for the purpose of studying rotating stall. Therefore, a prime goal of the current turbofan program was to provide an instrumentation package that was as complete as possible within the constraints of cost and non-interference with engine performance. This goal was met by using a Williams International engine (F107) that was fully instrumented and previously used for engine verification tests.

In the remainder of the paper, the facility in which the measurements were performed, the engine instrumentation, and a discussion of the results obtained for several configurations and overpressure values will be described. A more complete description of the experimental technique and a more extensive presentation of the experimental results is given in [2].

2 Facility

The basic Ludwieg-tube facility around which this program was developed, consists of a supply tube (the driver gas supply) of 1.10-meters (3.5-ft) diameter by 18.3-meters (60-ft) long and the test section (in which the engine was located) which is 2.44-meters (8-ft) diameter by 18.3-meters (60-ft) long. The pressure limitation on the supply tube was 1379 kPa (200 psia) which was a factor of ten greater than necessary to achieve the desired shock wave strength. In order to convert the existing facility to one that could be used to perform blast-wave response measurements of air-breathing propulsion systems, several modifications were necessary and these will be described below.

An important restriction on the generation of shock waves that are to be directed into operating engines is that the flow environment must be free of foreign particles. It was necessary to modify the facility as shown in Fig. 1 so as to incorporate a driver technique [1, 3, 4] consisting of an actuating chamber and a flexible diaphragm in order to create a particle-free shock wave. The sketch shown in Fig. 1 illustrates that two tubes, one of diameter d and the other of diameter D, were added to the existing facility in order to perform the desired ex-

This work was sponsored by the Defense Nuclear Agency under support of Contact No. DNA001-79-C-0155 and Contact No. DNA-001-81-C-0058.

Contributed by the Fluids Engineering Division of THE AMERICAN SOCIETY OF MECHANICAL ENGINEERS and presented at the Fluids Engineering Conference, Atlanta, Ga., May 12-14, 1986. Manuscript received by the Fluids Engineering Division August 26, 1986.

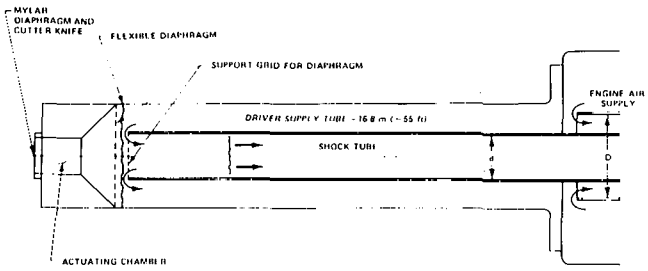

Fig. 1 Sketch of system

periments. The shock wave is initiated in the small diameter tube by rapid removal of the flexible diaphragm from the tube entrance. A shock wave is then formed in the 0.25-meter (10-in.) diameter tube (d) and progresses on to the 0.83-meter (21-in.) diameter tube (D) where it weakens and is eventually directed into the operating engine. The initial pressure in the 0.83-meter diameter tube is always nearly one atmosphere since for steady-state operation of the engine prior to initiation of a shock wave the engine draws its supply air through the annulus bounded by the two tubes of diameters d and D as shown in Fig. 1.

It is illustrated in [2] that when the engine was run in the extended bellmouth configuration, the engine centerline and the shock-tube centerline were coincident. When the S-type inlet was installed on the engine, the engine centerline was inclined at 9 deg to the shock-tube centerline and the inlet face was normal to the shock-tube centerline. In order to utilize the existing shock tubes, it was necessary to design and construct a bypass duct because the weight flow rate of the F107 was signficantly less than the previous J-85 engine. The porosity of the bypass perforated plate was designed so that a shock wave caused by the reflection from this plate would be cancelled by the expansion wave as a result of escaping gas for the incident-shock Mach numbers of interest. There is a unique porosity for a given Mach number for which the expansion wave will exactly cancel the reflected compression. However, over a small range of Mach numbers consistent with those used here, a single porosity plate can be used with minimum reflected disturbance. Sidewall pressure data obtained in the bypass to illustrate this point will be discussed later in this paper. A moveable neoprene flap was lightly taped adjacent to the perforated plate so that shock-processed gas was permitted to exit from the bypass, but ambient air was not permitted to flow in the opposite direction.

2.1 Engine Instrumentation. The F107 engine used here was heavily instrumented with pressure transducers and accelerometers. Total pressure measurements were obtained at 44 locations within the engine: four just downstream of the fan discharge in the bypass duct, six just downstream of the fan discharge in the core flow, ten just upstream of the radial compressor in the core flow, four downstream of the radial compressor, ten at the bypass discharge, and ten in the turbine discharge passage. There were also three static pressure measurements obtained within the engine. In addition, a forty-probe dynamic-pressure rake was located just upstream of the first-stage fan. From these measurements, the fan-face pressure history was determined before, during, and after the shock-wave arrival. The engine had three accelerometers located at the following places: (1) on the rear bearing housing, (2) on the forward bearing housing, and (3) a triaxial accelerometer on the main housing. An electronics package was constructed to appropriately integrate the acceleration in order to determine displacements which were continuously monitored.

Hypodermic tubing, 0.041-in. inside diameter/(0.063-in. outside diameter, was used to transmit the pressure pulse from the internal portion of the engine to the externally mounted pressure transducers. For the fan discharge and the inlet to the high-pressure compressor locations, the maximum length of tubing was on the order of 0.102-meters (4 in.) while the maximum length of tubing for other locations was on the order of 0.152-meters (6 in.). The calculated response time for the indicated pressure to reach 95 percent of the equilibrium pressure level was a maximum of approximately 0.25 milliseconds, which was satisfactory for the purposes of these measurements.

Thge transducers from the high-pressure compressor discharge rearward through the engine were water cooled because of the internal hot-gas environment. The technique for cooling involved sandwiching groups of five transducers within two copper plates (held together with Thermon cement) to which a 3/16-in. diameter copper line was attached.

2.2 Engine Configuration. With the extended bellmouth and the S-type inlet, measurements were obtained with the engine at 0 and 20 deg angle of yaw. The baseline case for verification of satisfactory engine performance in the Calspan facility was the extended bellmouth configuration of 0 deg yaw angle. Williams International provided performance data for this configuration. After installation of the engine in the facility, the stage pressure ratios provided by Williams International were verified.

2.3 Experimental Conditions. Detailed information regarding the experimental conditions and the local steady-state pressure ratios referenced to the fan-face 40-probe rake data is provided in [2] for the measurements discussed here. A discussion of these pressure results, the techniques used to obtain them, and the portion of the experimental test time from which they were deduced will be described later in this paper. In general, measurements were performed for incident shock wave overpressures of approximately 6.9, 10.3, 13.8, and 17.2 kPa (1.0, 1.5, 2.0, and 2.5 psi). At each of these overpressures, the engine was operating at approximately 80 percent (48,750 rmp), 90 percent (55,520 rmp), or 100 percent (61,700 rpm) of maximum core speed. Baseline measurements of pressure response and g-loads with the engine at rest (0 rpm) were also performed over the above pressure range, but will not be discussed here.

2.4 Data Recording System. The digital data acquisition system (DDAS) used here [5] contains 128 channels that can be sampled and digitized with 10-bit resolution at a maximum sampling rate of 50 μs. For the results to be reported, the sampling rate was decreased to either 100 μs or 250 μs in order to increase the total sampling time.

The software system performs two major functions: (1) data reduction and calibration, and (2) data display. The data reduction task generates a sorted, calibrated reduced data file from the DDAS raw data file. This reduced data file contains a digitized time history of each channel calibrated in engineering units. The second task permits the system to plot, list and generate strip-charts for each channel on the reduced data file.

All of the data were recorded on magnetic tape to facilitate permanent storage and the associated advantage of later analysis. The system amplifiers have a bandwidth in excess of 20 kHz. The pressure data were recorded at wideband and the system could then be used at a later time to digitally filter at any desired bandpass for comparison with the wideband results.

3 Discussion of Results

This section of the paper has been divided into several sections that can best be described by referring to Fig. 2, which illustrates a typical pressure history obtained from one of the

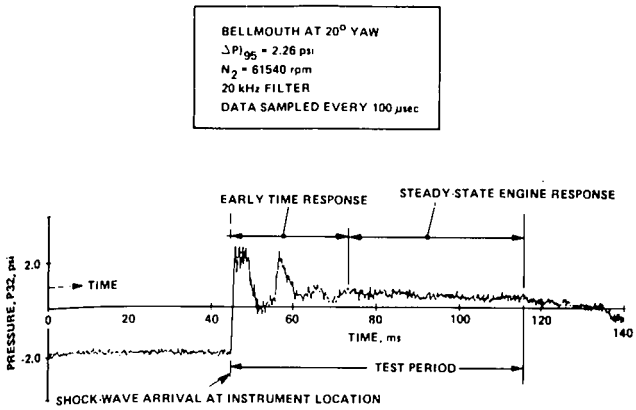

Fig. 2 Typical pressure history

Table 1 Engine Characteristic Times

Core Speed rpm	Time/rev ms	Fan speed rpm	Time/rev ms
61,600	1.0	31,900	1.9
55,500	1.1	28,700	2.1
48,700	1.2	25,900	2.3

40-probe rake transducers (in this case, P_{32}).[1] The 40-probe rake was located just upstream of the fan face. The corresponding shock-wave overpressure just upstream of the bellmouth inlet was 2.26 psi and is given by ΔP_{95}. The engine core speed for this particular case was 61,540 rpm. The result shown in Fig. 2 illustrates the pre-experiment pressure level, the early time engine response to the overpressure immediately after shock arrival, and the succeeding steady-state engine response. The discussion of results will thus be separated into the following subsection: (1) typical wave diagram of the engine/facility response to the shock-processed gas and the early-time inlet data and (2) the steady-state engine response to the shock-processed gas. Note from Fig. 2 that at about 135 ms the pressure begins to fall rapidly from a relatively steady value. It was initially thought that the engine operation might have been more sensitive to the pressure fall associated with an expansion fan than it was to the pressure rise associated with the shock wave. However, the engine handled this pressure decrease without any indication of a problem. Wave diagrams will be used to illustrate the origin of the pressure spikes appearing during the early-time response shown on Fig. 2. The steady-state portion of the record will be used to describe internal stage-by-stage engine response, to obtain a measure of the pressure distortion at inlet, to obtain a comparison between bellmouth and S-type inlet response, to obtain an indication of the influence of yaw angle on the engine/inlet behavior for both the early engine response period and the steady-state response period, and to summarize facility parameters.

A particular engine component responds to a pressure-pulse disturbance within a time period on the order of several revolutions. It is, therefore, helpful to put the time periods shown on Fig. 2 in perspective by comparing the early-time (~28 ms) and the steady-state (~43 ms) durations with typical engine characteristic times. Table 1 presents such a comparison for one revolution of the main core and for one revolution of the fan.

The shock wave system is moving through the engine at an axial rate of approximately a foot per millisecond. Thus, the time/rev given in Table V, correspond to flow distances of

[1]The subscript on P indicates the transducer number and will be used throughout this paper. A detailed description of transducer locations can be found in [2].

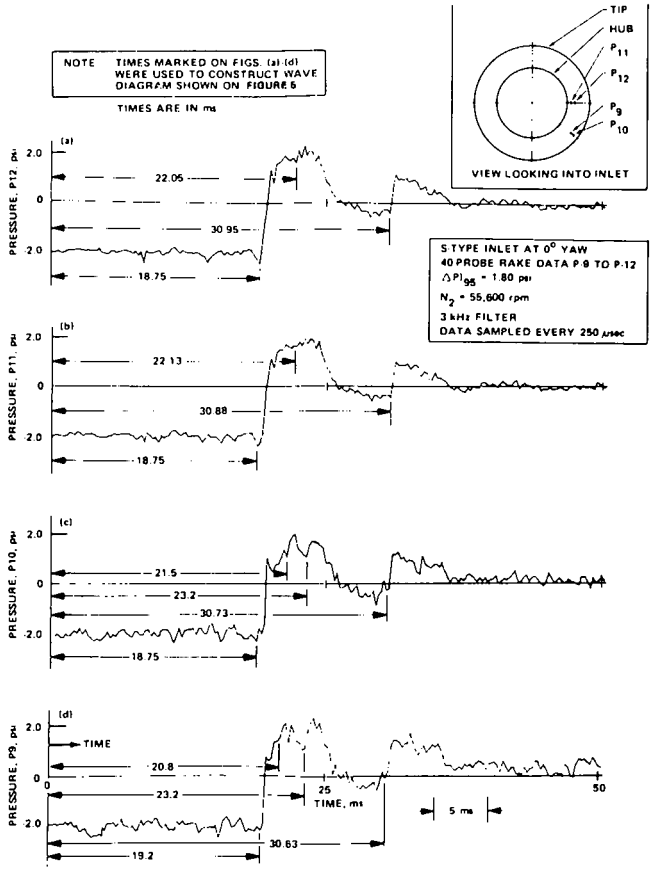

Fig. 3 Typical pressure data history from 40-probe rake in S-type inlet at 0 deg yaw

tens of chord lengths and it would be anticipated that steady-state operation would be achieved.

3.1 Wave Diagrams and Early-Time Inlet Data for 0 Deg Yaw Angle. Since the pressure data were recorded on magnetic tape, it was possible to display them on many different time bases. The initial 50 ms of the record was expanded in order to construct the wave diagram discussed in this section. It is important to note that construction of the wave diagrams was guided by: (1) the unambiguous shock wave arrival at the ten shock-tube pressure transducer locations and the two bypass transducer locations, and (2) the obvious arrival at these locations of the wave system resulting from the presence of the porous plate. The argument is then made that the wave disturbances travel within the facility at velocities given by the local values of $U \pm a$. It will become clear as the wave diagrams are presented that arrival of the weaker wave systems at some locations within the inlet are indicated on the basis of the $U \pm a$ argument. To illustrate the data, only two wave diagrams will be described here, the first obtained using the S-type inlet at 0 deg yaw for an engine speed of 55,600 rpm and the second obtained using the S-type inlet at 20 deg yaw for an engine speed of 61,600 rpm. The wave diagrams internal to the engine beyond the fan face will not be presented here.

Figures 3(*a*) and 3(*d*) illustrate four typical pressure histories obtained from transducers on the 40-probe rake located just upstream of the engine fan face. The engine configuration used for this case was the S-type inlet at 0 deg yaw. The engine speed was 55,600 rpm and the shock wave overpressure was 1.80 psi. The insert illustrates that probes P_{11} and P_{12} are located nearest the hub while probes P_{10} and P_9 are located nearer the outer portion of the inlet. The arrival of the shock wave at approximately 19 ms is noted on the data records as is

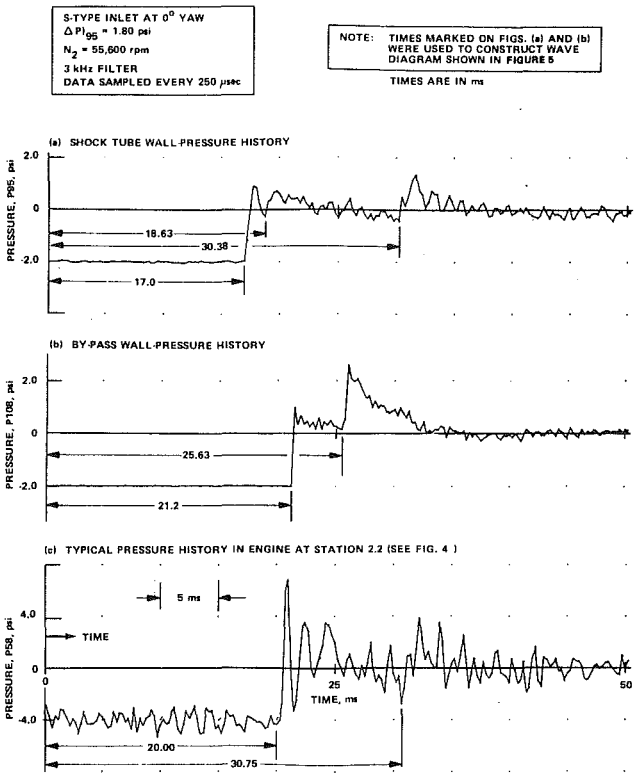

Fig. 4 Typical pressure-history data for shock tube bypass, and internal to engine for S-type inlet at 0 deg yaw

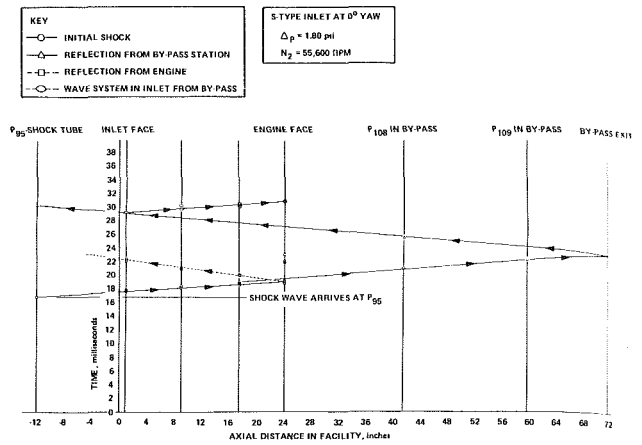

Fig. 5 X-τ diagram with S-type inlet at 0 deg yaw

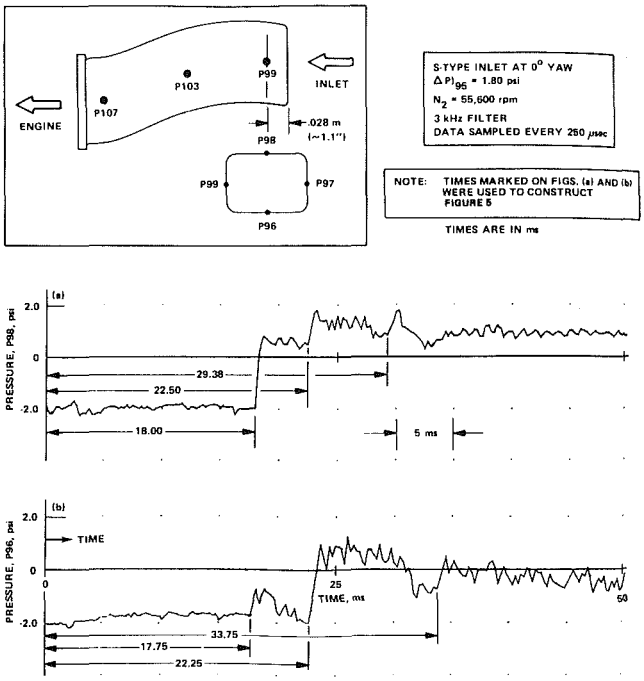

Fig. 6 Typical pressure-data history for station #1 in S-type inlet at 0 deg yaw

the arrival of the wave system reflected from the bypass at approximately 31 ms. The P_9 and P_{10} pressure transducers illustrate a disturbance at approximately 23 ms that could not be explained on the basis of the $U \pm a$ local velocity arguments. This disturbance weakens greatly near the hub as illustrated the P_{11} and P_{12} records. This same pattern was observed for all operating cases. The results suggest that the origin of the disturbance is in the fan bypass.

Figures 4(a) and 4(b) illustrate the shock tube wall-pressure history and the bypass wall-pressure history for the same experimental configuration used to obtain Fig. 3. The reflection from the perforated plate is clearly shown on both Figs. 4(a) and 4(b). However, as was generally the case, as soon as this reflection moves back upstream into the shock tube, the pressure levels return to their pre-reflection values. Figure 4(c) is a pressure history obtained in the engine core flow just ahead of the centrifugal compressor. The noticeable difference in the preshock baseline fluctuations between the shock-tube pressure transducers (4(a) and 4(b)) and the engine transducer (4(c)) is characteristic of the data obtained with the engine operating.

Figure 5 is the wave diagram that was constructed using the pressure data (and some additional) shown in Figs. 3 and 4. The origin of the waves shown on this figure is relatively straightforward and consistent with the results obtained for the engine-off case (see [2]). The origin of the data points plotted at 22 to 23 ms for the engine face was discussed above. It should be noted that this particular disturbance is sufficiently weak so that it does not appear obvious in the inlet pressure histories to be discussed in the following figures.

The early-time pressure histories used to construct the wave diagrams are interesting from the viewpoint of inlet-engine iteractions. Figures 6-8 present several typical data records obtained at three axial locations in the S-type inlet for an engine speed of 55,600 rpm at an overpressure of 1.8 psi. The data obtained from the two pressure transducers (the other two did not function on this run, but P_{97} was subsequently repaired) nearest the inlet lip are shown in Fig. 6. The difference between these pressure histories is striking, with the lower transducer output (P_{96}) decaying to a zero ΔP pressure level immediately after arrival of the shock wave, suggesting a tendency for local flow separation. The respective final steady-state pressure levels for transducers P_{96} and P_{98} will be discussed in a later section. Figure 7 presents the three pressure histories obtained at the inlet mid-station (P_{101} did not operate). The general characteristics of these pressure histories are very similar suggesting that circumferential variations have decreased at this axial location. Figure 8 presents four pressure histories obtained at the inlet location nearest the engine fan face. These results are compatible with the station 2 results (shown in Fig. 7) in that the pressure histories are circumferentially similar as distinct from the results obtained at station #1 (Fig. 6).

3.2 Wave Diagrams and Early Time Inlet Data for 20 Deg Yaw Angle. As noted previously, measurements were performed with the inlet/engine at 0 deg yaw angle and at 20 deg yaw angle. The data presented in this section were obtained at

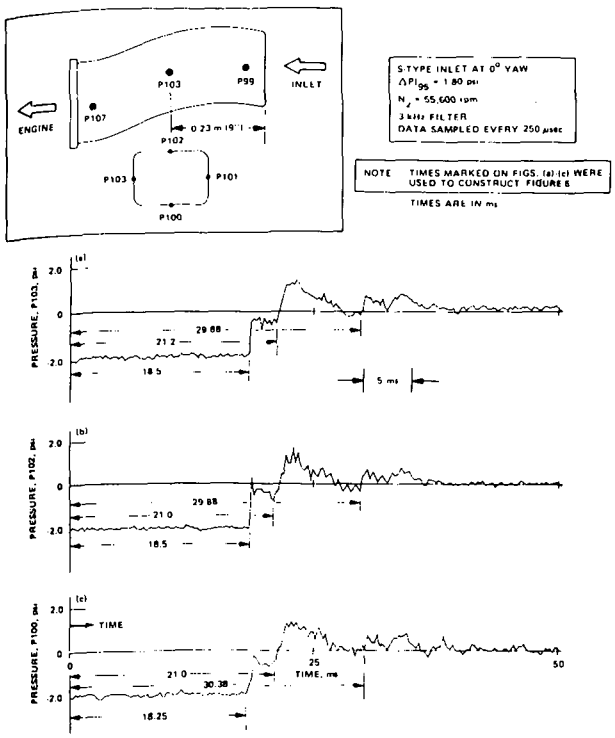

Fig. 7 Typical pressure-data history for station #2 in S-type inlet at 0 deg yaw

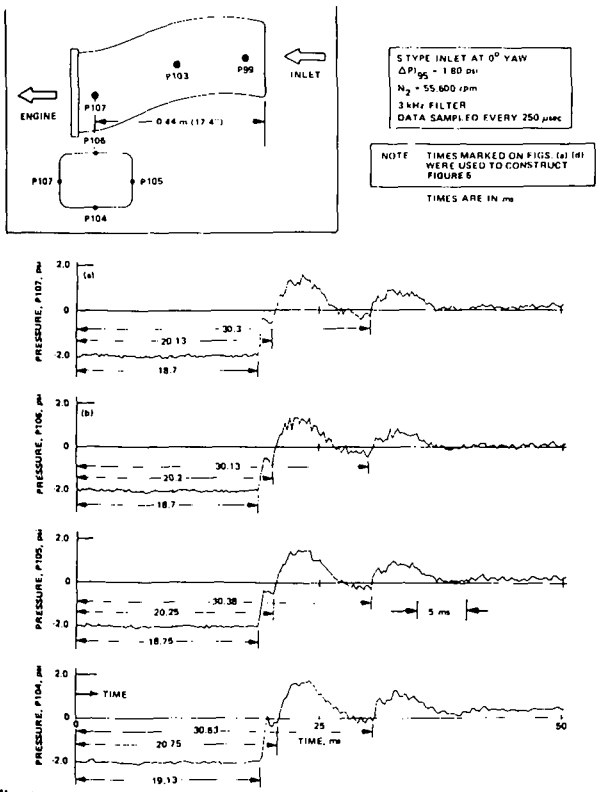

Fig. 8 Typical pressure-data history for station #3 in S-type inlet at 0 deg yaw

an overpressure of approximately 2.4 psi for a core speed of 61,600 rpm at yaw angle of 20 deg.

Pressure-data histories obtained for rake transducers P_1 to P_4 are shown in Fig. 9. The insert on this figure illustrates the location of these probes relative to the hub and the tip. For presentation of these data, the pre-shock baseline has been

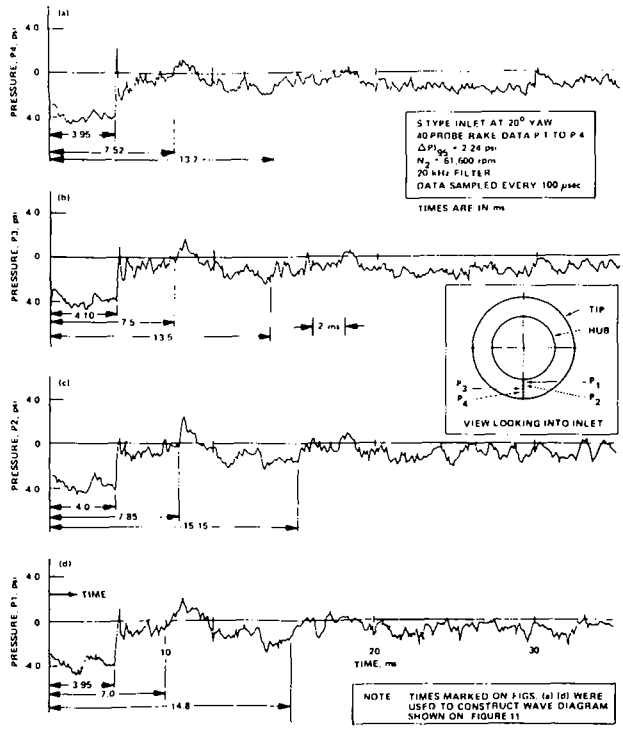

Fig. 9 Typical pressure-data history from 40-probe rake in S-type inlet at 20 deg yaw

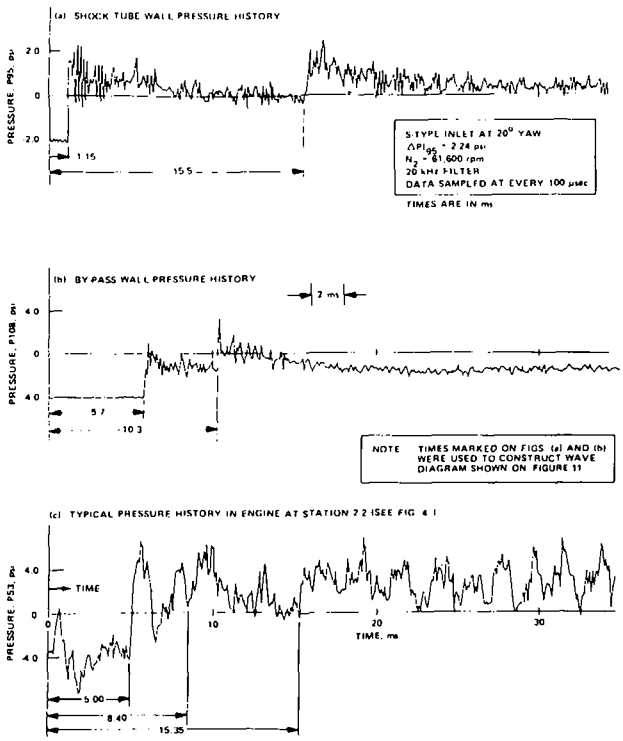

Fig. 10 Typical pressure-history data for shock tube, bypass, and internal to engine for 20 deg yaw

shortened and the time base has been expanded by comparison with Fig. 3. The magnitude of the noise on the pre-shock baseline records for the 40-probe rake and engine transducers increased with increasing engine speed as can be seen by comparing Figs. 3 and 9.

The arrival of the shock wave at the rake is clearly seen on the pressure records. The disturbance occurring between 7 and 8 ms is consistent with the previous results at 0 deg yaw angle and the discussion given earlier. The disturbance noted be-

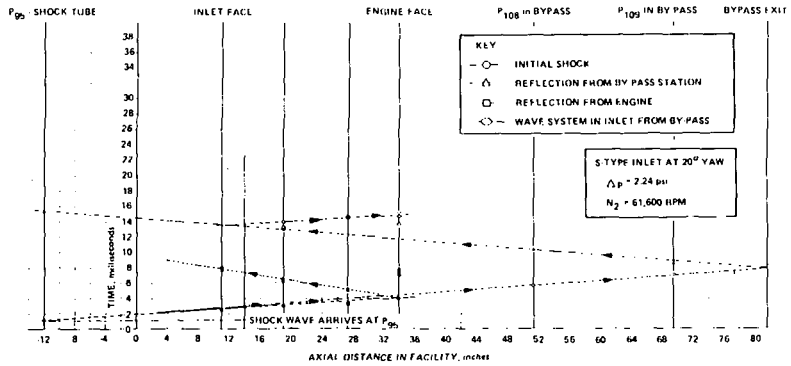

Fig. 11 X-τ diagram with S-type inlet at 20 deg yaw

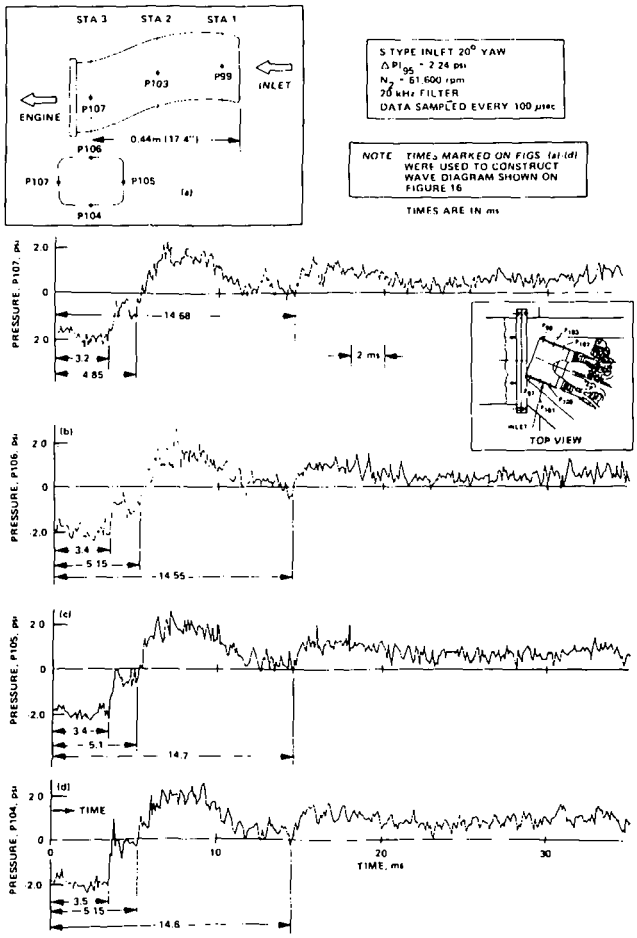

Fig. 12 Typical pressure-data history for station #3 in S-type inlet at 20 deg yaw

tween 14 and 15 ms can be traced to the reflection from the perforated plate.

Pressure histories for the shock-tube sidewall, the bypass sidewall and in the engine core flow just ahead of the centrifugal compressor are shown in Fig. 10. The times noted on Figs. 10(*a*) and 10(*b*) were used to aid in the construction of the wave diagram shown on Fig. 11. Comparison of Figs. 5 and 11 suggests that the yaw angle has essentially no influence on the external wave diagram. The 0 rpm wave diagram is given in [2] and it is essentially the same as that of Figs. 5 and 11.

It is, however, interesting to look at the influence of yaw angle on typical inlet pressure records shown on Fig. 12 for station #3. Figure 12 presents the pressure histories for the four transducers nearest the fan face. A comparison between Figs. 8 and 12 (note the different time scales) does not indicate any dramatic influence of yaw angle on the flow characteristics obtained at station #3 within the inlet. This result suggests that the inlet is well designed and that it is of sufficient length for flow disturbances associated with the yaw angle to dampen by the time that the flow reaches the fan entrance. At inlet locations nearer the inlet entrance, the influence of yaw angle is pronounced.

3.3 Steady-State Inlet/Engine Response to Overpressure. The steady-state portion of the test period is illustrated on Fig. 2. The pressure change measured by the transducer during the steady-state engine response time period was obtained by using the DDAS to arithmetically average the sampled pressure level (either 100 μs or 250 μs sampling rate) for each pressure record over the steady-state time period and then subtracting the baseline level (also arithmetically averaged) prior to shock-wave arrival. All of the pressure results discussed in this section were obtained using the technique just described.

3.4 Steady-State Response to Shock Wave. One of the principal objectives of this measurement program was to investigate the response of a turbofan engine to an overpressure imposed at the inlet face. Specifically, the question to be answered was: if an overpressure of ΔP were imposed on the fan face, then would this overpressure be increased by the appropriate pressure ratio for the respective stages of the machine? That is to say, if we assume that

$$P_{i+1} + \Delta P_{i+1} = \left[\frac{P_{i+1}}{P_i}\right]_{ss} (P_i + \Delta P_i)$$

where $(\ )_{ss}$ means steady state and where i and $i+1$ denote upstream and downstream of a stage, then the increments should satisfy

$$\Delta P_{i+1} = \left[\frac{P_{i+1}}{P_i}\right]_{ss} \Delta P_i$$

since

$$P_{i+1} = \left[\frac{P_{i+1}}{P_i}\right]_{ss} P_i$$

One must also consider the question of how much the unloading of the fan and compressor due to the shock-wave passage changes the relative position on the operating map. The performance maps necessary for this determination were supplied to us by Williams International for this machine.

To illustrate the result, the steady-state increase in pressure for a given stage, ΔP_i, normalized by the averaged increase of the 40-probe rake, ΔP_2, as a function of machine stages has been plotted and is given in Fig. 13. This plot includes the theoretical performance value for the engine in the absence of a shock wave. This theoretical value was experimentally verified during the course of the measurement program as was noted earlier in the paper.

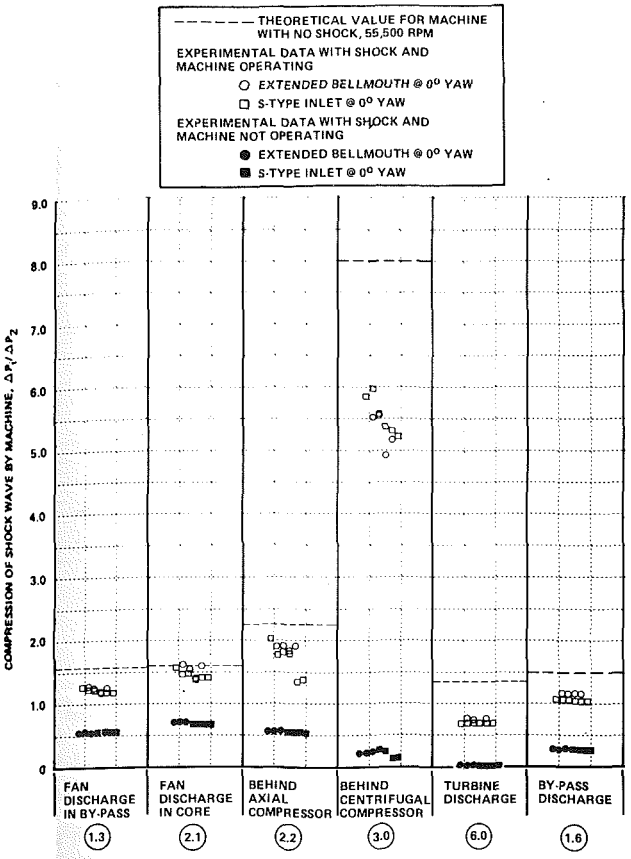

Fig. 13 Engine pressure results for core speed of 55,500 rpm

The engine results obtained with the extended bellmouth and with the S-type inlet at 0 deg yaw angle for engine speeds of 0 rpm and 55,500 rpm are presented in Fig. 13. The multiple data points indicate different runs and not different measurement positions within a given component. The results shown in Fig. 13 are generally independent of the inlet type. However, the bypass fan discharge and the core fan discharge appear to be influenced differently by the shock-wave system. The core fan-discharge results are in reasonably good agreement with the predicted response, but the fan bypass discharge result is less than anticipated. The measurements obtained downstream of the axial compressor and downstream of the compressor were both below the theoretical value with the most noticeable difference occurring after the centrifugal compressor. The turbine discharge and bypass discharge results are also low, but they are influenced by the upstream compressor and fan discharge, respectively.

As noted above, it was necessary to consider the question of whether or not a change of location on the performance map could explain the observed result. When the shock wave passed through the engine, the fan speed was observed to increase by about 4 or 5 percent while the core speed increased by about 0.2 or 0.3 percent. The performance maps were used to conclude that the observed results could not be explained on the basis of a temporary change in operating point. A more detailed calculation procedure than the simple quasi-steady one-dimensional approach attempted here is required to explain the observations. At the present time, the authors are not aware of a code that can stisfactorily treat the physical problem encountered here, though there are codes that have attempted portions of the solution [6–10].

3.5 Influence of Overpressure on Engine Vibrations. This engine was equipped with several accelerometers located at strategic engine positions in order to monitor the acceleration values and the linear displacements. These measurements were of particular interest because of a large linear displacement measured for the turbojet engine experiments reported in [1]. Typical accelerometer histories are given in [2] for the rear bearing housing. The results shown in that report were obtained for an overpressure of approximately 2.5 psi at an engine speed of 61,605 rpm. This particular bearing has a limit of ±20 g's. The influence of the shock-wave system on the engine accelerometer history resulted in very limited excursions outside of the 40 g boundaries and no resultant damage on the engine. Acclerometers located at other places on the engine noted the passage of the shock-wave system but nothing more.

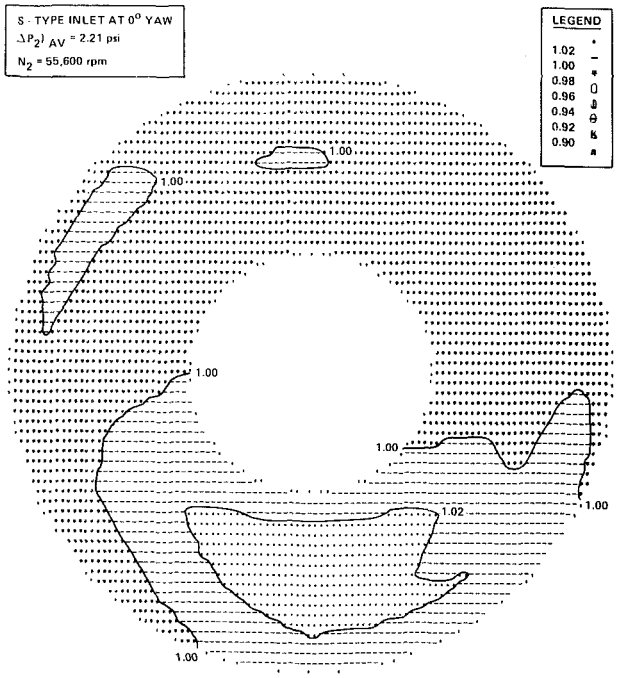

Fig. 14 Distortion index for S-type inlet at 0 deg yaw

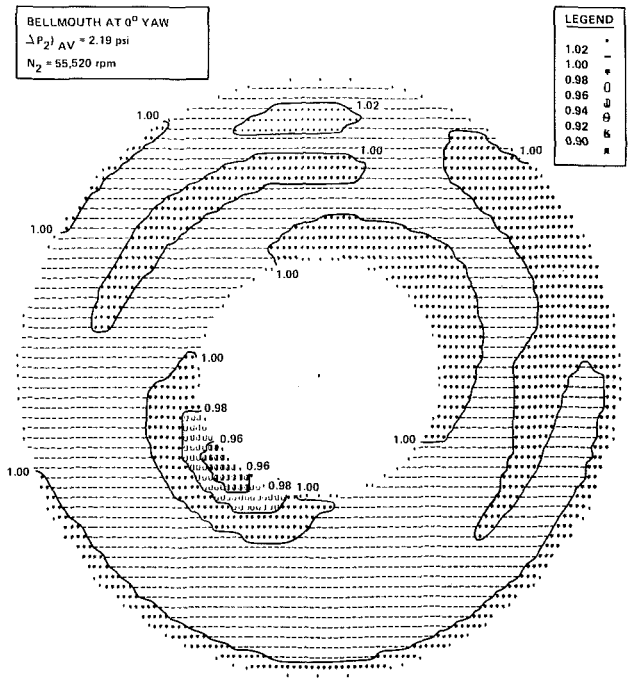

Fig. 15 Distortion index for bellmouth at 0 deg yaw

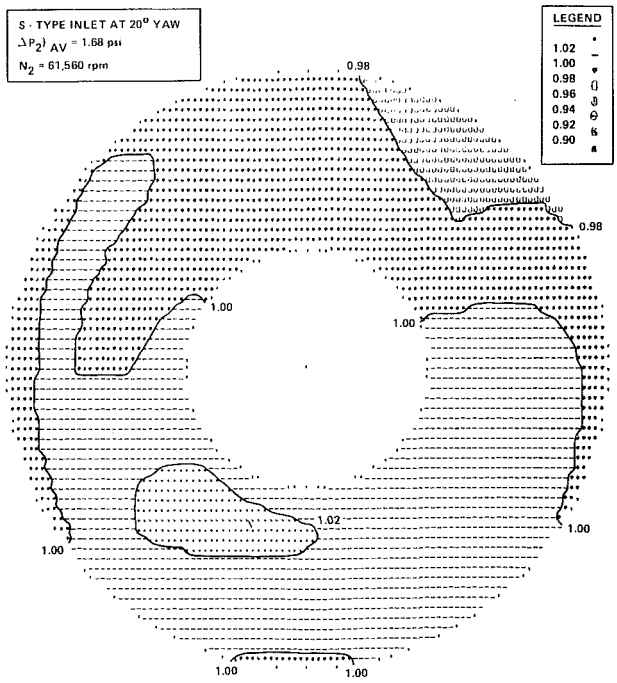

Fig. 16 Distortion index for S-type inlet at 20 deg yaw

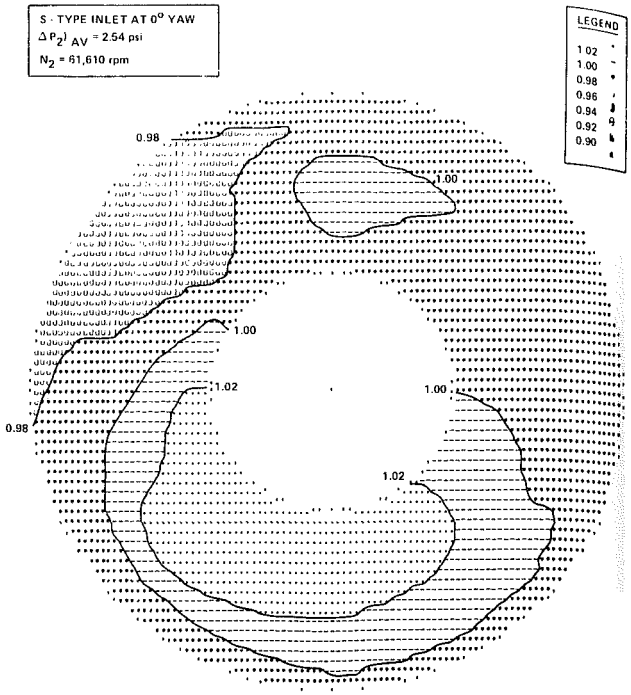

Fig. 17 Distortion index for S-type inlet at 0 deg yaw

3.6 Distortion Index Calculated from 40-Probe Rake Data. For many of the measurement conditions discussed herein, the fan face distortion index was calculated[2] from the 40-probe rake pressure data and typical results of these calculations are presented in Figs. 14–16. Isobars are drawn on the plots in order to better visualize the results. The 1.00 isobar is defined as

$$\sum_{i=1}^{i=40} \left(\frac{\Delta P_i + 14.7}{40}\right) = 1.00.$$

The influence of engine speed on the distortion index is illustrated in [2] by comparing distortion plots obtained at the same overpressure and the same inlet configuration but with the engine speed at 0 rpm in one case and at 61,610 rpm in the other. For the engine-off case, the fan-face pressure distribution is relatively uniform. However, when the main core was operating at 61,610 rpm, a higher pressure region appears in the lower part of the fan face and a lower pressure region appears in the upper left quadrant.

It is also of interest to compare the S-type inlet and bellmouth results as is done on Figs. 14 and 15. These data were obtained for a 0 deg yaw angle, a main core speed of approximately 55,500 rpm, and approximately the same average overpressure. The bellmouth resulted in a small higher-pressure zone near the top in the bypass region and a small lower-pressure zone in the lower left quadrant near the hub. By comparison, the S-type inlet had a significant high-pressure region in the lower 90 deg quadrant that was large in extent.

Figure 16 is a similar distortion plot calculated from pressure data obtained for the S-type inlet at 20 deg yaw angle with a main core speed of 61,560 rpm. The 0 rpm results for this orientation were similar to those obtained at 0 deg yaw angle suggesting that in the absence of core speed, the flow pattern at the fan face is not significantly influenced by yaw angle. This result was also noted earlier when describing the pressure data and thus will not be shown. However, an indication of the influence of yaw angle on the distortion pattern with the engine operating can be seen by comparing the results shown in Fig. 16 with those shown in Fig. 17. The overpressure value applicable to the measurement reported in Fig. 17 was somewhat larger than that of Fig. 16, but for a given inlet configuration, the yaw angle appears to have a more significant influence on the distortion index than the overpressure values does for small to moderate overpressures.

Uncertainty: The uncertainty of the measurement is estimated to be on the order of ± 0.005 psi.

Conclusions

This paper describes the results of a technology development program for which extensive measurements have been obtained for the response of a turbofan engine subjected to a simulated blast-wave environment. At the present time, it is possible to conclude the following:

(1) A facility has been developed that can be used to obtain controlled laboratory data for the study of the influence of overpressure pulses on air breathing propulsion systems.

(2) The flow field near the leading edge of an S-type inlet is the dimensional for both 0 deg and 20 deg yaw angle.

(3) For the S-type inlet, a significant radial pressure grasient exists at the engine face as a result of communication between the engine and the inlet.

(4) The turbofan stage-by-stage compression of the imposed pressure pulse is significantly less than the stage compression ratios. A quasi-steady state one-dimensional calculation does not satisfactorily explain the results.

(5) Potential engine vibrations as a result of the overpressure pulse are not a problem area for this particular turbofan engine.

References

1 Dunn, M. G., and Rafferty, J. M., "Nuclear Blast Response of Air-breathing Propulsion Systems: Laboratory Measurements with an Operational J-85-5 Turbojet Engine," ASME *Journal of Engineering for Power*, Vol. 104, July 1982, pp. 624–632.

[2]The authors would like to thank Mr. John Lueke of the Air Force Wright Aeronautical Laboratories for performing these calculations and for generating the computer graphics plots of the results.

2 Dunn, M. G., and Padova, C., "Response of an Operational Turbofan Engine to a Simulated Nuclear Blast," Calspan Report No. 6840-A-1, Final Report for period 31 January 1981 to 31 January 1982, Jan. 1986.

3 Muirhead, J. C., Naylor, R., and Felt, G. D., "The Transmission of Blast Waves Through an Orenda 8 Engine," Suffield TN No. 219, DRES, Alberta, Canada.

4 Muirhead, J. C., "A Review of DRES Studies on the Effect of Blast on Gas Turbine Engines," Suffield Report No. 267, DRES, Alberta, Canada.

5 Wittliff, C. E., Pflueger, P. C., and Donovan, P. J., "A High-Speed Digital Data Acquisition System for Short-Duration Test Facilities," International Congress on Instrumentation in Aerospace Simulation Facilities, ICIASF Record-97, September 1979, Monterey, CA.

6 Sugiyama, Y., Hamed, A., and Tabakoff, W., "A Study of Compressor Surge Due to Inlet Pressure Disturbances," AIAA Paper 78-246, Jan. 1978.

7 Jansen, W., Swarden, M. C., and Carlson, A. W., "Compressor Sensitivity to Transient and Distorted Transient Flows, Volume II—Mathematical Details and Computer Programs," Northern Research and Engineering Corporation, Cambridge, MA, Jan. 1971, AD728024.

8 Peacock, R. E., Das, D. K., and Erlap, O. C., "Compressor Response to Pulsed Transients," AIAA-80-1080, June 30–July 2, 1980, Hartford, CT.

9 Tesch, W. A., and Steenken, W. G., "Blade Row Dynamic Digital Compressor Program," NASA CR134978, March 1976.

10 Reynolds, G. G., and Steenken, W. G., "Dynamic Digital Blade Row Compression Component Stability Model," AFAPL-TR-76-76, May 1976.

Pressure Fluctuations on the Surface of a Hemisphere Immersed in a Thick Turbulent Boundary Layer

Y. Suzuki

M. Kiya

T. Sampo

Y. Naka

Department of Mechanical Engineering,
Hokkaido University,
Sapporo, 060, Japan

Statistical properties of pressure fluctuations on the surface of a hemisphere immersed in a thick turbulent boundary layer are described. The height of the hemisphere tested was 0.275 thicknesses of the boundary layer. Reynolds number based on the model diameter D and the time-mean approaching flow velocity at the level of the top U_r was 3.0×10^5. Time-mean and root-mean-square (rms) values, probability density and power spectra of the pressure fluctuations are presented and discussed. The pressure fluctuations are related to the fluctuating approaching-flow velocity in terms of the pressure-velocity admittance and the cross correlation. Main results are that the time-mean and rms pressures attained a primary maximum at the front stagnation point; that the pressure-velocity admittance near the front stagnation point was approximately unity at frequencies less than about 0.4 U_r/D; that the pressure fluctuation in front of the hemisphere is positively correlated with that in the rear side and negatively correlated with that in the middle.

1 Introduction

Hemispherical structures are economical in that a maximum volume is enclosed within minimum surface area. This design is frequently air-supported and is well suited for underwater structures. It is important to obtain statistical properties of surface pressures imposed on hemispherical bodies since terrestrial and underwater structures are potentially exposed to strong winds and tidal currents. This paper presents results of an experimental study on the time-mean and surface pressures of a hemisphere immersed in a thick turbulent boundary layer.

Maher [1], Taniguchi et al. [2], and Toy et al. [3] have studied the time-averaged surface pressure of the hemispherical bodies immersed in turbulent boundary layers. Properties of the surface-pressure fluctuations, however, have not yet been presented within the authors' knowledge. Terrestrial hemispherical structures are often constructed with thin materials; knowledge of fluctuating surface pressures is useful in estimating unsteady surface loads. Power spectra and probability density of the surface-pressure fluctuations can be deduced from wind tunnel experiments and provide useful information on vibrations, fatigue of the structural materials and aerodynamic noise.

In wind tunnel tests, models of such structures are immersed in a thick turbulent boundary layer simulating the atmospheric boundary layer during strong winds. These tests require that Reynolds number is equal to that of the full-scale structures (of the order 10^7–10^8). This requirement has not been met in most experiments of this type for round structures and has been simulated by addition of roughnesses to the surface to induce transition from laminar to the turbulent boundary layer [3]. It is uncertain, however, whether this method works well for fluctuating surface pressures. Since the main objective of the present study is to obtain fundamental properties of the fluctuating pressures, no attempt was made to simulate a Reynolds-number in excess of 3.0×10^5, the maximum attainable in the apparatus used.

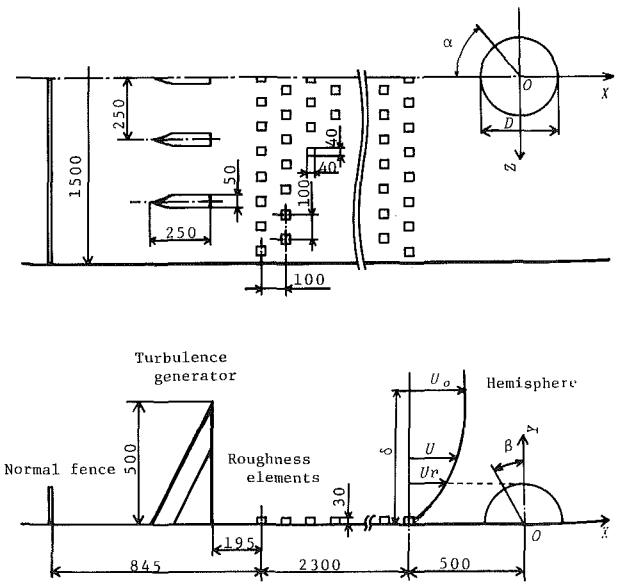

Fig. 1 Turbulence generator, roughness elements and definition of symbols. Dimensions in mm.

Contributed by the Fluids Engineering Division for publication in the JOURNAL OF FLUIDS ENGINEERING. Manuscript received by the Fluids Engineering Division December 18, 1984.

Table 1 Characteristic values of the turbulent boundary layer at a position $X/D = 0$. U_0, free-stream velocity; δ, boundary layer thickness; δ^*, displacement thickness; θ, momentum thickness; u_τ, friction velocity; n, exponent of power law; L_x, integral scale of velocity fluctuation.

U_0(m/s)	δ(mm)	δ^*(mm)	θ(mm)	u_τ/U_0	$1/n$	L_x(mm)
19.5 ± 0.2	600 ± 30	100 ± 5	70 ± 3	0.074 ± 0.005	0.251 ± 0.005	150 ± 10

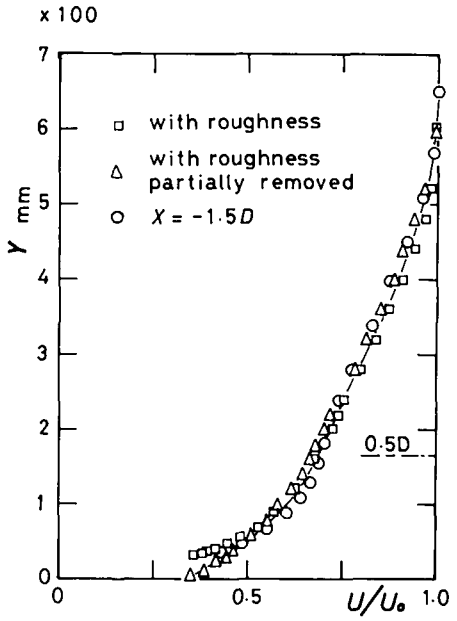

Fig. 2(a)

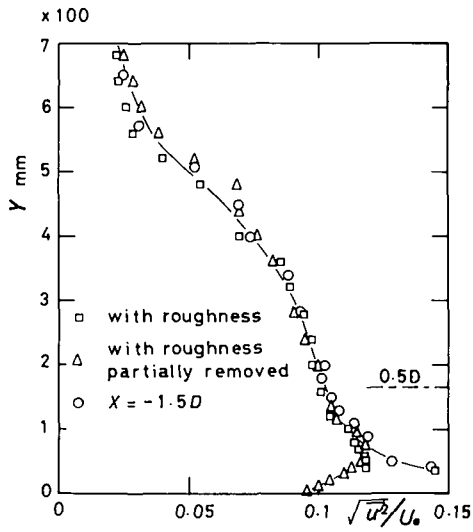

Fig. 2(b)

Fig. 2 Distribution of (a) time-mean and (b) rms values of velocity fluctuation in artificially generated turbulent boundary layer at X/D = 0 and −1.5. Uncertainties of (a) and (b) are within ±4 percent and ±8 percent (odds of 20 to 1).

2 Experimental Apparatus and Method

Experiments were performed in a low-speed, closed-return wind tunnel with a 1.2 m high, 1.5 m wide, and 6.0 m long working section. The free-stream turbulence was 0.3 percent at a speed of 19.5 m/s. A flexible ceiling of the working section allowed adjustment of the zero pressure gradient in the longitudinal direction.

A thick turbulent boundary layer was produced along the floor of the working section by employing a technique similar to that of Counihan [4]. A normal fence and a series of turbulence generators were installed immediately downstream of the entrance of the working section whose floor was distributed by three-dimensional roughnesses (blocks with the dimensions 4 cm × 4 cm × 3 cm), see Fig. 1.

The coordinate system (X, Y, Z) and main symbols are defined in Fig. 1. The X-axis is taken in the longitudinal direction along the mid span, the Y-axis normal to and measured from the floor and the z-axis normal to the X- and Y-axes so as to form a right-handed system. The origin is at the center of the hemisphere. The time-mean and fluctuating components of the longitudinal velocity are denoted by U and u'. The free-stream velocity is U_0 and the velocity in the boundary layer at the level of top of the hemisphere is U_r. The diameter of the hemisphere is denoted by D; the azimuthal and zenithal angles are denoted α and β. Other symbols will be defined in the text when they first appear.

A model hemisphere was manufactured from plastic, having the outer diameter of 33 cm and the thickness of 0.3 cm. Pressure taps of 0.8 mm diameter were drilled onto the surface at properly distributed 19 locations. Some of the pressure taps were separately connected to a semi-conductor strain-gauged pressure transducer (TOYODA PD-104K) with a small cavity between the pressure tap and the diaphragm of the transducer. The transducer was calibrated in situ against a standard condenser microphone by means of sound waves of various frequencies generated by a loud speaker. The gain factor was found to be close to unity (1 ± 0.05) up to 120 Hz, with negligibly small phase shift.

The model was mounted flush with the tunnel floor on a turn table in such a manner that their centres were coincident. Pressure distributions on the surface of the model were measured by rotating the turn table from the outside of the tunnel. The distance from the turbulence generator to the model center was about 3.0 m and the roughnesses were removed from the floor in a region -0.5 m $< X < 0.7$ m when the model was installed in the tunnel.

The velocity fluctuation u' was measured by a constant-temperature hot-wire anemometer (KANOMAX 2100) with a single I-probe of 5 μm tungsten wire and 1 mm in working length. These data were analyzed by a digital signal processor (SANEI 7T08) to obtain various statistical properties.

3 Results and Discussion

3.1 Characteristics of the Turbulent Boundary Layer. The time-mean velocity U and rms values of the fluctuating velocities in the three directions were measured at many points in the boundary layer. The measurements showed that the boundary layer was tolerably two-dimensional and its thickness δ ($\fallingdotseq$ 0.6m) remained almost constant downstream of the turbulence generators. Profiles of U and rms velocity $(\overline{u'^2})^{1/2}$ at the position $X/D = 0$ are shown in Fig. 2 for two cases with and without the roughnesses in the region $-1.52 < X/D < 2.12$. No significant changes are observed between the profiles in the two cases except a narrow region below the roughnesses ($Y < 3$ cm or $Y/D < 0.09$) which is excluded from consideration in tests of this nature. Characteristic values of the boundary layer at the position $X/D = 0$ are summarized in Table 1 and following features should be noted: (*i*) the model hemisphere was fully immersed in the boundary layer since $(D/2)/\delta = 0.275$; (*ii*) the longitudinal integral

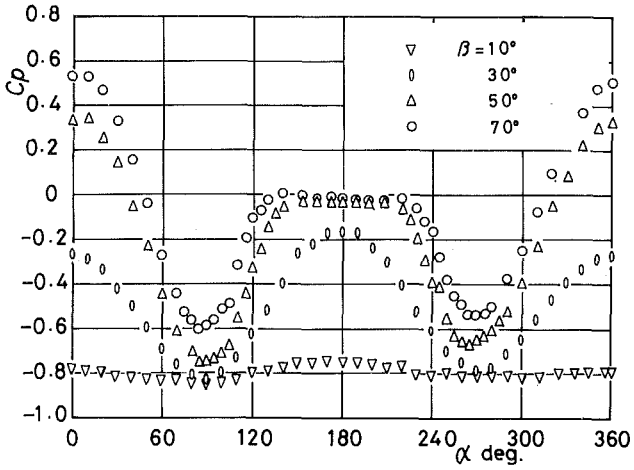

Fig. 3(a)

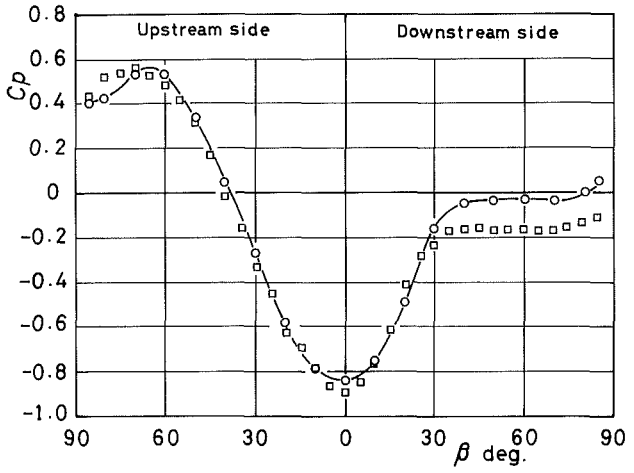

Fig. 3(b)

Fig. 3 Time-mean surface-pressure distribution (*a*) at various angles β and (*b*) along longitudinal centerline. ○, present result; □, results of Toy et al. [3]. Solid line for visual aid only. Uncertainty of C_p is within ±4 percent (odds of 20 to 1).

length scale L_x at the height $Y = D/2$ was about $0.45D$; (*iii*) if the velocity profile is represented by a power law $U/U_0 = (Y/\delta)^{1/n}$, the exponent n is approximately 4.0. This value of the exponent is found in the suburbs of cities (Cermak [5]).

In Fig. 2 profiles of U and $(\overline{u'^2})^{1/2}$ at an upstream section $X/D = -1.5$ are included. The position ($X/D = -1.5$, $Y/D = 0.5$) was chosen arbitrarily as a reference position whose longitudinal velocity was correlated with the fluctuating pressures on the surface of the model. This correlation perhaps explains the fluctuating surface pressure in terms of the fluctuating velocities of the approaching flow.

3.2 Time-Averaged Surface Pressure. Distributions of the time-averaged pressure p on the surface of the model are presented in Fig. 3 in the form of pressure coefficient C_p defined by

$$C_p = (p - p_0)/\frac{1}{2}\rho U_r^2$$

where $U_r (= 13.5$ m/s) and p_0 are the longitudinal velocity and static pressure at the reference position and ρ denotes the density of fluid. In Fig. 3(*a*), C_p is plotted against the azimuthal angle α for several zenithal angles β whereas in Fig. 3(*b*) its distribution on the longitudinal centerline is compared with the results of Toy et al. [3].

Toy et al.'s experimental conditions are similar to those of

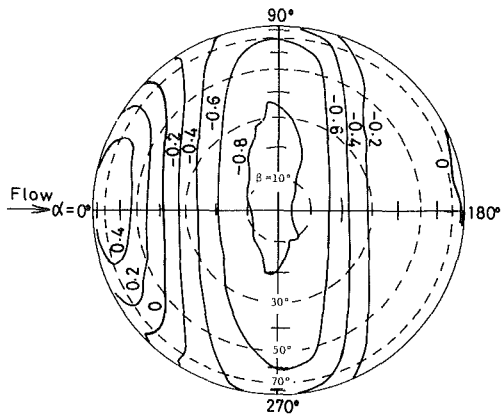

Fig. 4 Isobars of time-mean surface pressure. Broken circles indicate constant zenithal angle β; radius is equal to cos β. Uncertainty of isobars is within ±6 percent (odds of 20 to 1).

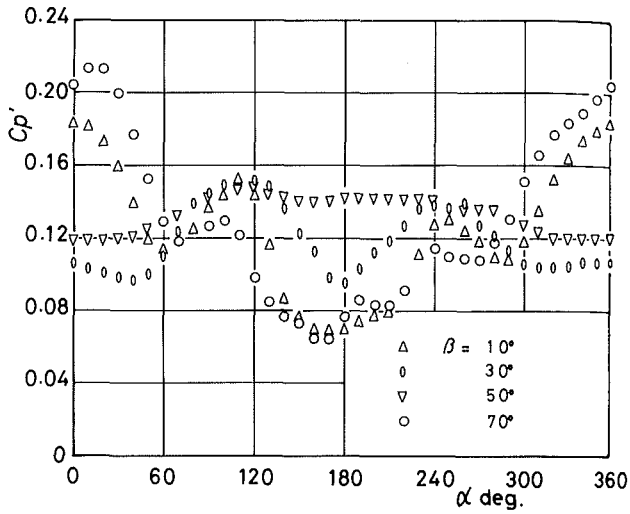

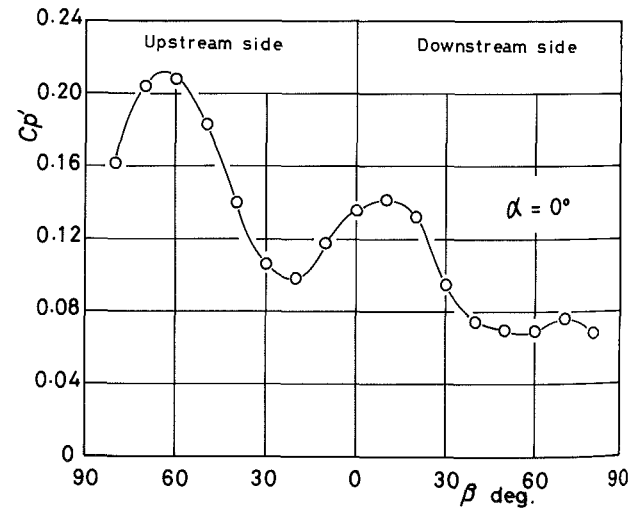

Fig. 5 Rms surface pressure (*a*) at various angles β and (*b*) along longitudinal centerline. Solid line for visual aid only. Uncertainty of C_p' is within ±8 percent (odds of 20 to 1).

this experiment except that in their case the surface of the model was artificially roughened by sand to simulate the high Reynolds-number flow over the full-scale structure. Accordingly the difference between the two pressure distributions shown in Fig. 3(*b*) probably demonstrates the simulated high Reynolds-number effect. This effect is clearly manifested by the difference in the base pressure (in the range $\beta > 30$ deg) which is somewhat higher in this experiment than in that of

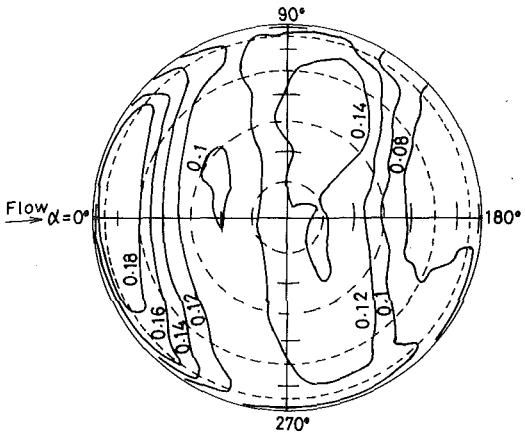

Fig. 6 Isobars of rms surface pressure. Broken circles as in Fig. 4. Uncertainty of isobars is within ±10 percent (odds of 20 to 1).

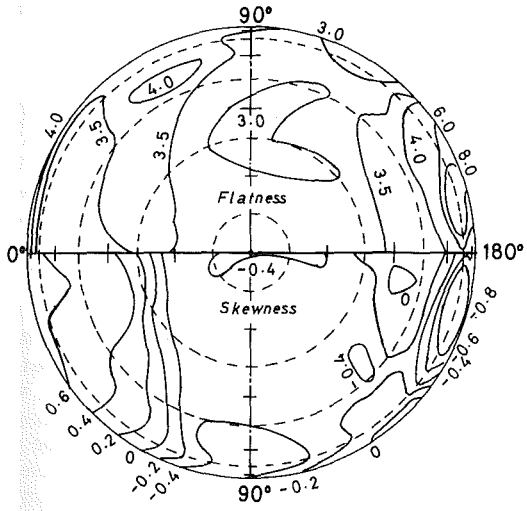

Fig. 7 Isobars of skewness S and flatness factor F of surface-pressure fluctuations. Broken circles as in Fig. 4. Uncertainty of S and F is within ±10 percent (odds of 20 to 1).

Toy et al. Over the remaining surface, however, the two experiments yield nearly the same pressure profile. This is reasonable because the flow near the surface facing upstream is primarily governed by the horse-shoe vortex and the turbulence in the approaching boundary layer, thus being relatively insensitive to the surface roughness of the model. In Fig. 4, the time-mean surface pressure is summarized by means of isobars. It is worth noting that the isobars are approximately normal to the longitudinal direction.

Finally, the pressure drag and lift normalized by $(1/2)\rho U_r^2(\pi D^2/8)$ are respectively 0.155 and 0.322.

3.3 Rms Surface Pressure. The rms value of the fluctuating surface pressure p' is plotted in Fig. 5 in the form of the pressure coefficient

$$C_p' = (\overline{p'^2})^{1/2} \Big/ \frac{1}{2}\rho U_r^2$$

The rms pressure distribution on the longitudinal centerline will be discussed since this is most informative, see Fig. 5(b). A maximum at $\beta \fallingdotseq 65$ deg on the upstream side is probably produced by the turbulence approaching the front stagnation point, because this position coincides with the first maximum of the time-mean pressure (see Fig. 3(a)). Another maximum at $\beta \fallingdotseq 20$ deg on the downstream side is probably associated with an oscillation of the separation position on the model surface. A summary of the rms surface pressure is given in Fig. 6 in terms of isobars. The symmetry of the isobars is much less in this case than in the time-mean pressure. This probably suggests that the fluctuating pressure is more sensitive to the spanwise nonuniformity of the approaching boundary layer than is the time-mean pressure. The nonuniformity of the rms longitudinal velocity along the line passing the reference position ($X/D = -1.5$, $Y/D = 0.5$) was approximately ±2 percent of the average value in the range $|Z| < D/2$.

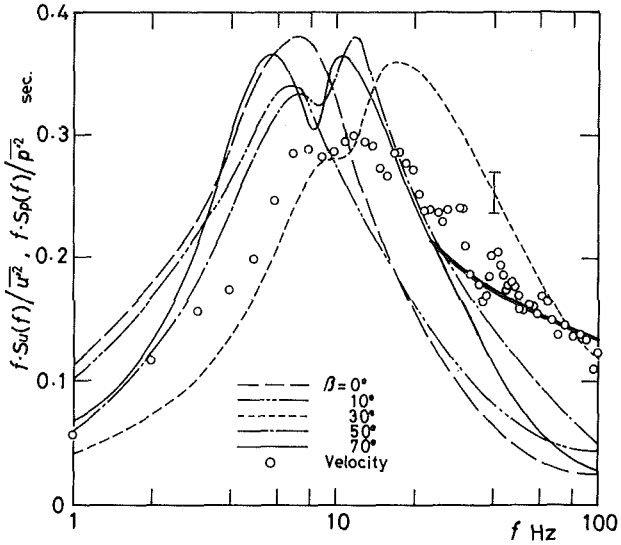

Fig. 8 Power spectra of fluctuating pressure on the upstream side of longitudinal centerline and power spectrum of fluctuating velocity at reference position ($X = -1.5D$, $Y = 0.5D$). Thick solid line shows the $-5/3$ power law. Uncertainty is shown by I (odds of 10 to 1).

3.4 Probability Density of Fluctuating Surface Pressure. The probability density distribution of the fluctuating pressure p' is useful for estimating the instantaneous local stress exerted on the material forming the surface of the structure. The skewness S and the flatness F of p' are presented in Fig. 7. The skewness and the flatness are generally close to those of Gaussian distributions ($S = 0$ and $F = 3.0$) except the upstream stagnant region and the base-flow region. The skewness is positive in the former and negative in the latter, so that the pressure fluctuation in these regions has, respectively, negative and positive spikes. That the flatness is larger than 3.0 is another indication of such spikes. A large magnitude of negative skewness at $(\alpha, \beta) \fallingdotseq (165 \text{ deg}, 70 \text{ deg})$ in the base-flow region suggests a frequent appearance of significant positive spikes. The ratio of maximum amplitudes of p' to its rms value was measured at this position during a sufficiently long time $1350\, D/U_r$ and was found to be approximately 7.0. Accordingly a high pressure can instantaneously occur at this position although the time-mean and rms pressures are generally low in the base region.

3.5 Power Spectra and Pressure-Velocity Admittance. The power spectra of the surface-pressure fluctuations are useful for estimating the vibration and fatigue of the structural materials and the aerodynamic noise associated with the flow over the structure. Figure 8 shows the pressure spectra S_p on the upstream side of the longitudinal centerline ($\alpha = 0$ deg) of the model, together with the u' spectrum S_u at the reference position ($X/D = -1.5$, $Y/D = 0.5$). In Fig. 8, data points for the pressure spectra are not included for clarity, the scatter of experimental uncertainty being almost the same as that for the velocity spectrum. A large part of energy of the pressure fluctuation is included in a frequency range $f < 30$ Hz or $fD/U_r < 0.73$. The energy of the pressure fluctuations is generally higher in this low-frequency range and lower in the higher-

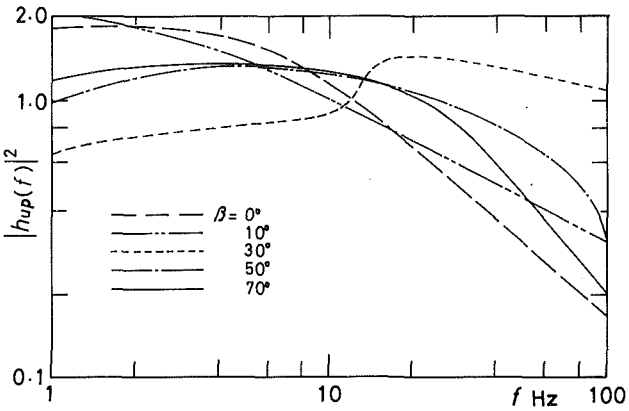

Fig. 9 Pressure-velocity admittance at several angles β. Uncertainty of the admittance is ±20 percent (odds of 20 to 1).

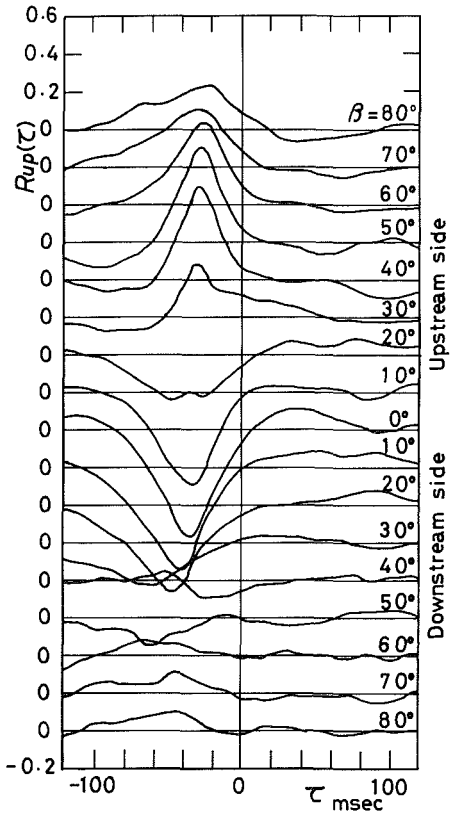

Fig. 10 Cross correlation coefficient of surface-pressure fluctuation on longitudinal centerline and velocity fluctuation at reference position ($X = -1.5D$, $Y = 0.5D$). Uncertainty of the correlation is ±10 percent (odds of 20 to 1).

frequency range than that of the velocity fluctuations. As suggested by the theory of Durbin and Hunt [6], the surface-pressure spectra decay much faster in the high-frequency range than the velocity spectrum of an approaching stream.

From the practical standpoint it is useful to estimate the surface-pressure spectra in terms of the velocity spectrum at the reference position. The pressure-velocity admittance is used for this purpose. This is essentially the pressure spectrum divided by the velocity spectrum. The admittance $|h(f)|^2$ was defined by

$$|h_{up}(f)|^2 = [S_p(f)/\overline{p'^2}]/[S_u(f)/\overline{u'^2}]$$

where S_u and $\overline{u'^2}$ were measured at the reference position. The result is shown in Fig. 9 for the upstream side of the longitudinal centerline. The admittance at positions $\beta \fallingdotseq 50$ and 70 deg is fairly constant (approximately unity) in a low frequency range $f < 20$ Hz or $fD/U_r < 0.48$. These positions are close to the front stagnation point $\beta \fallingdotseq 65$ deg. At positions far from the front stagnation point the admittance changes markedly with the frequency. This is probably due to an increasingly large distortion of turbulent eddies in the approaching stream as they travel along the surface of the model.

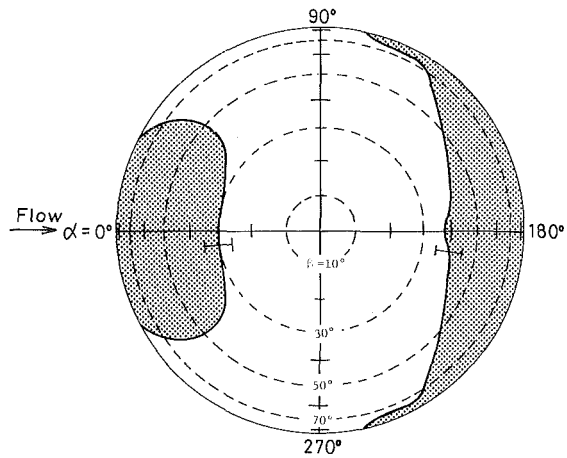

Fig. 11 Spatial extent to which instantaneous pressure fluctuations are correlated. Shaded and unshaded areas experience pressure fluctuations of opposite sign at the same instant. Broken circles as in Fig. 4. Uncertainty of boundary is shown by I (Odds of 10 to 1).

3.6 Cross Correlation Between Pressure and Velocity Fluctuations. The surface-pressure fluctuation will further be discussed in terms of its cross correlation with the velocity fluctuation at the reference position. As a typical example, the cross correlation coefficient $R_{up}(\tau)$, τ being the time lag, on the upstream side of the longitudinal centerline is presented in Fig. 10. The cross correlation shows an entirely opposite trend in two regions of β; that is, in an upper region $\beta < 20$ deg the cross correlation takes a negative minimum while in a lower region $\beta > 30$ deg it attains a positive maximum. The minima and maxima appear at a negative time lag and their magnitude decreases with an increasing angle β. This time lag, together with the longitudinal distance ΔX between the reference position and the pressure taps, yields the convection velocity of disturbances contributing to the pressure fluctuation. The convection velocity was approximately 13.0 m/s, which is close to the longitudinal velocity at the reference position. Accordingly it appears that a large part of the pressure fluctuation on the upstream side is associated with turbulent eddies of the approaching boundary layer except for their distortion near the model.

As is seen in Fig. 10, the cross correlation takes negative or positive values over a wide range of the time lag. This provides information on the instantaneous spatial distribution of the pressure fluctuation. For example, when u' is positive at the reference position, the pressure fluctuation p' is generally negative in a region $\beta < 20$ deg and positive in another region $\beta > 30$ deg. On the other hand, if $u' < 0$ at the reference position, then $p' > 0$ for $\beta < 20$ deg and $p' < 0$ for $\beta > 30$ deg.

The cross correlation was measured at many points on one side of the longitudinal centerline to find the loci on which the correlation at $\tau = -30$ ms was zero. The result is summarized in Fig. 11, in which shaded areas experience the pressure fluctuations of the same sign at an instant whereas in an unshaded area the pressure fluctuation has the opposite sign at the same instant. A large spatial extent of these areas suggests that the pressure fluctuations are mostly produced by energy-containing eddies of the approaching boundary layer where

the longitudinal length scale L_x is approximately equal to the model height.

4 Conclusion

The present paper has presented statistical properties of the pressure fluctuation on the surface of a smooth hemisphere immersed in a thick turbulent boundary layer. Main results may be summarized as follows:

(1) The time-mean surface-pressure profile is similar to that on a hemisphere artificially roughened to simulate high Reynolds-number flows, except that the base pressure is higher in this study than in the latter.

(2) The time-mean and rms pressures attain a primary maximum at the same position on the upstream side. This position is the front stagnation point.

(3) A large part of energy of the pressure fluctuation on the upstream side is contained in frequencies less than about 0.7 U_r/D.

(4) The pressure-velocity admittance near the front stagnation point is fairly constant at frequencies less than about 0.4 U_r/D. This allows one to estimate the pressure spectrum near the stagnation point in terms of the velocity spectrum at an upstream reference position.

(5) The pressure fluctuation in front of the hemisphere is positively correlated with that in a wide range of the rear side and negatively correlated with that in the middle.

Acknowledgments

The authors are grateful to Mr. H. Tamura for his advice on the experimental apparatus and to Mr. T. Yamazaki for his help in the construction of the model hemisphere.

References

1 Maher, F. J., "Wind Loads on Basic Dome Shapes," *J. Structure Division*, Proc. A.S.C.E., Vol. 91, No. 3, 1965, pp. 219–228.

2 Taniguchi, S., Sakamoto, H., Kiya, M., and Arie, M., "Time-Averaged Aerodynamic Forces Acting of a Hemisphere Immersed in a Turbulent Boundary Layer," *J. Wind Engng. and Indust. Aerodyn.*, Vol. 9, 1982, pp. 257–273.

3 Toy, N., Moss, W. D., and Savory, E., "Wind Tunnel Studies on a Dome in Turbulent Boundary Layers," *J. Wind Engng. and Indust. Aerodyn.*, Vol. 11, 1983, pp. 201–212.

4 Counihan, J., "An Improved Method of Simulating an Atmospheric Boundary Layer in a Wind Tunnel," *Atmos. Environ.*, Vol. 3, 1969, pp. 197–214.

5 Cermak, J. E., "Aerodynamics of Buildings," *Ann. Rev. Fluid Mech.*, Vol. 8, 1976, pp. 75–106.

6 Durbin, P. A., and Hunt, J. C. R., "On Surface Pressure Fluctuations Beneath Turbulent Flow Round Bluff Bodies," *J. Fluid Mech.*, Vol. 100, 1980, pp. 161–184.

Local Force Measurements on Finite-Span Cylinders in a Cross-Flow

V. K. Sin

Ronald M. C. So

Mechanical and Aerospace Engineering Department, Arizona State University, Tempe, Ariz. 85287

A technique employing a three-axis piezoelectric load cell is developed to measure local unsteady forces induced on cylinders placed in a cross flow. Verification of the technique is carried out with a two-dimensional circular cylinder. All measurements are made at a Reynolds number of $\sim 4.8 \times 10^4$ *and a free-stream turbulence of* ~ 1.5 *percent. The local two-dimensional unsteady lift measurement is found to be in excellent agreement with spanwise-averaged data reported in the literature, thereby validating the feasibility of the present technique. Steady and unsteady force measurements on finite-span circular cylinders are reported and compared with available data in the literature.*

1 Introduction

When a large two-dimensional structure is exposed to a cross-flow, vortex shedding occurs around the structure. As a result, the structure will oscillate at the shedding frequency. An undesirable effect of major importance will occur if the vortex shedding frequency is at or near the natural frequency of the structure. This will result in amplification of the motions of the structure to near resonant levels and possible structural damage. The existence of turbulence in the on-coming stream and edge effects due to finite-span structure complicates the vortex shedding phenomenon along the structure. These effects would lead to the presence of discrete cells whose relative frequencies and phasing can significantly affect the dynamics of the structure.

Examples of finite-span structures exposed to highly turbulent cross flows are many. Among them are cooling towers and other large structures exposed to the atmosphere, fuel rods, control guide-rods, etc. in nuclear reactors, cold water pipes in an ocean thermal energy conversion plant, and turbomachinery components. The collapse of the Tacoma Bridge in Seattle, Washington was perhaps the most famous example of a structural design in which the fluid-structure interaction phenomenon was not adequately accounted for. Therefore, an understanding of this phenomenon is of great importance to many branches of engineering.

Another area where finite-span bodies are placed in a cross flow can be found in the study of missiles in flight. When a missile is inclined to an air stream, it experiences components of forces both in the plane in which the inclination occurs and normal to that plane. The force normal to the plane of inclination, or commonly known as side force, is primarily responsible for missile instability and its distribution along the length of the missile is an important parameter to know in the study of missile dynamics. Since the time-averaged side force distribution along the length of the missile is periodic [1,2], it is expected that a similar behaviour would also persist for the fluctuating side force. In view of this, it is of great importance to the study of missile dynamics if the time-averaged and fluctuating side forces on missiles in flight could be measured.

Present knowledge of fluid-structure interactions is rather incomplete, especially our understanding of the dynamic response of finite-span structures exposed to turbulent cross flows. Substantial amount of data have been accumulated by past researchers on the two-dimensional flow around infinite cylinders and the steady and unsteady response of the cylinders [3,4]. However, the bulk of the observations were restricted to uniform flow approaching the cylinders. The effects of turbulence in the on-coming stream was investigated by numerous researchers [5–13]. With the exception of Savkar and So [10], none of the prior studies appears to have measured the unsteady forces directly. The bulk of the measurements is limited to unsteady pressure around the cylinder. Therefore, it is very difficult to interpret the dynamic force response of the cylinder from these data. The first reported direct measurements of unsteady forces were presented by So and Savkar [14] using the novel force measurement technique developed in [10]. However, this study was limited to two-dimensional bodies only, and the dynamic response of finite-span structures remains unexplored.

The flow around and behind finite-span structures has been extensively studied by various investigators. However, the emphasis of these studies is placed on the disturbances in the flow created by the presence of the structure. Little or no attention is paid to the dynamic response of the structure and its effect on the flow downstream. An attempt to study the unsteady pressure distributions around finite-span cylinders has been made by Farivar [15] and a more recent attempt to measure the spanwise-averaged unsteady forces directly has been reported by Sakamoto and Oiwake [16]. These studies, therefore, represent the first effort to systematically investigate the dynamic response of finite-span cylinders in a

Contributed by the Fluids Engineering Division for publication in the JOURNAL OF FLUIDS ENGINEERING. Manuscript received by the Fluids Engineering Division January 25, 1985.

cross flow. According to these studies, the mean drag coefficient decreases as the L/d ratio of the cylinder is decreased. Also, the unsteady forces and the Stronhal frequency are observed to decrease from the two-dimensional cylinder values. These changes can be attributed to the influence of the separated flow originating from the top of the cylinder. In spite of these new findings, the local dynamic response of finite-span cylinder in a cross flow remains unavailable.

The purpose of this paper is to report on the development of a technique used to measure local fluctuating forces acting on finite-span cylinders placed in a turbulent cross-flow. Verification of the technique is carried out with a two-dimensinal circular cylinder where numerous literature data are available for comparison. In addition, local steady drag measurements on finite-span cylinders are reported.

2 The Local Force Measurement Technique

So and Savkar [14] made use of three-axis piezoelectric load cells to measure the spanwise-averaged fluctuating forces acting on a two-dimensional circular cylinder placed in a turbulent cross flow. The load cells are placed at the support ends of the cylinder and are preloaded along the axis of the cylinder. This preload also holds the test cylinder in place. Since the cylinder spans the tunnel cross-section, the measurements obtained from the load cells represent spanwise-averaged values over the active span of the cylinder. In principle, the active span can be made very small, and in the process, the local fluctuating forces can be measured. A study of the effects of span on the fluctuating forces is given in [17] and shows that the fluctuating forces increase with decreasing active span. This increase in fluctuating forces is a direct consequence of the perfect correlation of the forces as the active span is decreased. In view of this, the technique is also capable of local force measurements in two-dimensional circular cylinders.

The present technique is a direct extension of So and Savkar's [14] method to finite-span cylinders. In their method, the test cylinder and the preloading device are attached to the tunnel walls, hence, making the technique unsuitable for finite-span cylinders. To remedy this drawback, the test cylinder and the preloading device are designed as one integral model as shown in Fig. 1. The active element rests on a support strut which is connected to the base of the test cylinder. Since So and Savkar [14] have shown that each load cell measures one half of the forces acting on the active element, it is not necessary to use two load cells as they have. Instead, a dummy load cell of the same dimensions is installed at one support end as shown (Fig. 1). A preload is applied along the cylinder axis to hold the active element in place and this is done through the bolt and nut arrangement shown in Fig. 1. Depending on the force to be measured, a preload as high as 1000 times the measured load can be achieved by applying a suitable torque to the lock nuts at the base of the test cylinder. The active element is separated from the top and bottom dummy sleeves by two rubber rings as suggested by so and Savkar's

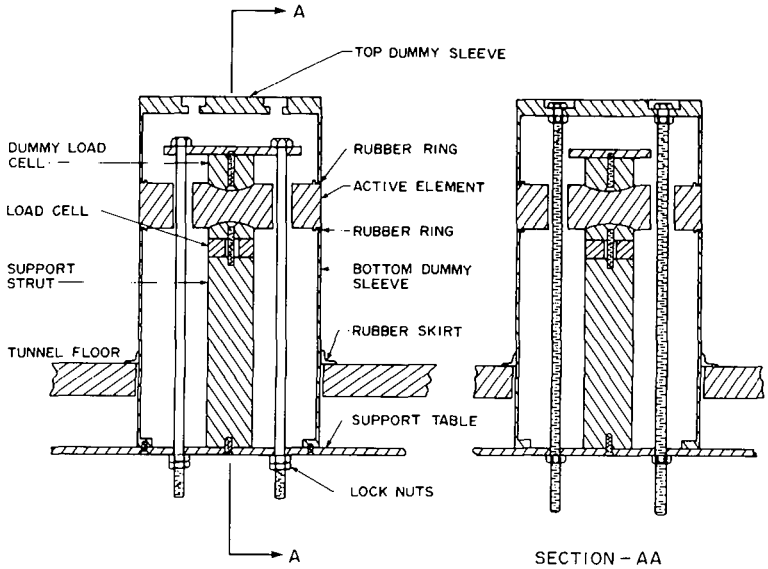

Fig. 1 Schmatic of cylinder model for local force measurement

Nomenclature

$C_D = D/[\frac{1}{2}\rho U^2 d(1)]$ = local drag coefficient

$\bar{C}_D = 1/L\int_0^L C_D dy$ = mean drag coefficient

$(C_D)_{2\cdot D}$ = local drag coefficient for two-dimensional cylinder

$C_p = \Delta p/(\frac{1}{2}\rho U_\infty^2)$ = pressure coefficient

$-(C_p)_b$ = average base pressure coefficient

$C_D' = D'/(\frac{1}{2}\rho U_\infty^2 dS_a)$ = local RMS drag coefficient

$C_L' = L'/(\frac{1}{2}\rho U_\infty^2 dS_a)$ = local RMS lift coefficient

D = local steady drag

D' = local RMS fluctuating drag

d = cylinder diameter

$E(f)$ = auto-power spectrum in (volt)^2

f = frequency

f_s = Stronhal frequency

H = tunnel height

$k = [1-(C_p)_b]^2$ = base pressure parameter

L = cylinder span

L' = local RMS fluctuating lift

$\mathrm{Re} = U_\infty d/\nu$ = Reynolds number

$S = fd/U_\infty$ = normalized frequency

$\mathrm{St} = f_s d/U_\infty$ = Stronhal number

S_a = active span

U_∞ = tunnel centreline velocity

y = coordinate measured from tunnel floor

$\Phi = \dfrac{(U_\infty/d)E(fd/U_\infty)}{(\frac{1}{2}\rho U_\infty^2 dS_a)^2}$ = normalized spectrum

[14] design (Fig. 1). A nut and bolt arrangement is used to assemble the test cylinder together and to prevent the top dummy sleeve from motion when the test cylinder is placed in a cross flow.

This design allows the active element to be placed at any spanwise location of the cylinder. Since the active element length can be made as short as possible (the controlling factors are the magnitude of the measured forces and the accuracy of the load cells), true local measurements of the fluctuating forces can be achieved. For the present experiment, an active element length of 25.4 mm is chosen for a cylinder diameter of 101.6 mm. A Kistler Model 9251A three-axis piezoelectric load cell is used to measure the fluctuating forces acting on the active element. One axis measured the preload and the other two axes measure the fluctuating lift and drag. The load cell outputs are converted to voltage readings by Kristal Model 5001 charge amplifiers. From these voltage outputs, the RMS lift and drag can be determined by passing the signals through true RMS meter. Also, auto-power spectra of the signals are obtained from a HP Model 3582A Spectrum Analyser.

Static calibrations similar to those carried out by So and Savkar [14] are performed on the load cell as indicated in the assembly shown in Fig. 1. In order to verify that the load cell indeed measures one half of the applied load, the locations of the load cell and dummy load cell are interchanged and the calibrations repeated. These results are shown in Fig. 2. It can be seen that the calibration curves are identical. The curves show that the end effects of the support are also identical. In view of this, all subsequent measurements are carried out with the load cell located as shown in Fig. 1.

The test cylinder, made of aluminum, is introduced into the tunnel test section through a hole in the tunnel floor. In order to prevent tunnel vibrations from contaminating the load cell signals, it is desirable to completely isolate the test cylinder from the tunnel walls. This is accomplished by making the hole in the tunnel floor to be slightly larger than the cylinder diameter and by mounting the test cylinder on a separate support that is not connected to the tunnel walls or support. Blower vibrations transmitted through the laboratory floor are isolated by rubber pads attached to the legs of the test cylinder support table. Air leakage through the hole is prevented by a rubber skirt attached to the tunnel floor around the hole. The thickness of the rubber skirt is chosen to be $\sim 1/20$ of the floor boundary-layer thickness. Hence, its effect on the flow outside the boundary layer is minimal. When the test cylinder spans the tunnel height to give the two-dimensional cylinder case, the top of the test cylinder is positioned at ~ 1.5 mm away from the tunnel ceiling. Again, a rubber skirt is used to seal up the gap between the top of the cylinder and the tunnel ceiling. This way, the test cylinder is completely isolated from any tunnel vibrations.

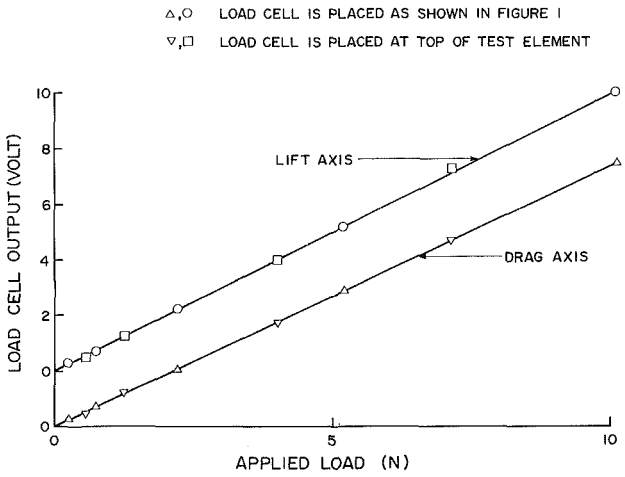

Fig. 2 Calibration curves for piezoelectric load cell

Fig. 2 Uncertainty in Load Cell Output = ± 0.04 (Volt), in Applied Load = ± 0.01 (N) at 20:1 odds

3 The Experiments

The experiments are carried out in an open-jet wind tunnel with a cross-section that measures 55.9 cm wide by 25.4 cm high. Location of the test cylinder is selected at 66 cm downstream of the entrance to the tunnel test section. This choice is decided by the desire to create a fairly uniform mean flow approaching the test cylinder and thin boundary layers on the tunnel walls. Since the tunnel was not well designed, the resultant free-stream turbulence level is quite high. A plot of the mean velocity and turbulence intensity distributions across the tunnel height at 66 cm downstream of the test section entrance is shown in Fig. 3. It can be seen that the mean flow is essentially uniform over 80 percent of the tunnel height, the floor and ceiling boundary-layer thickness is ~ 25.4 mm and the free-stream turbulence intensity is ~ 1.5 percent and again uniform over 80 percent of the tunnel height. The tunnel centerline velocity, U_∞, is measured at 6.96 m/s, and this is used to normalize the plots shown in Fig. 3. All experiments are carried out with $U_\infty = 6.96$ m/s and a freestream turbulence level of 1.5 percent. The Reynolds number based on U_∞ and the cylinder diameter, $d = 101.6$ mm, is $\sim 4.8 \times 10^4$. Further details about the tunnel and the velocity measurements are given in [18].

In order to verify the local force measurement technique, an experiment on two-dimensional cylinder is required. In addition, experiments on two other finite-span cylinders are carried out. These configurations have $L/d = 2$ and 1.5, respectively. All three experiments are carried out with the centre of the active element positions at $y/d = .875$. Since the boundary layer on the tunnel floor extends to $y/d \simeq .3$ only (Fig. 3), the fluctuating force measurements are made at a location where the mean velocity is uniform and the turbulence level is 1.5 percent. Later local steady drag measurements show that the local drag coefficient, C_D, is also uniform at this location for

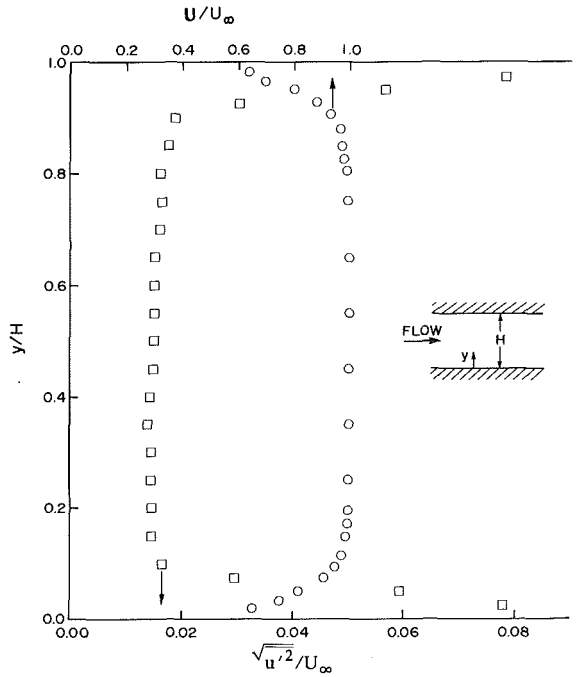

Fig. 3 Mean velocity and turbulence intensity distributions across tunnel test location

Fig. 3 Uncertainty in $y/H = \pm 0.02$, in $U/U_\infty = \pm 0.02$, in $\sqrt{u'^2}/U_\infty = \pm 0.001$ at 20:1 odds

the two-dimensional cylinder configuration. Therefore, this allows the fluctuating force measurements for this case to be compared with other literature data. The blockage for the present experiments is ~18 percent, similar to that of [14].

Local mean pressure distributions around the cylinder are measured using a model made of aluminum sections. These sections could be interchanged to give $L/d = 2$, 1.5, 1, and .5. Pressure taps are provided along a generator of the model. The taps are spaced closely near the top of the model and the spacing is increased as the base of the cylinder is approached. This arrangement allows 7 taps to be exposed to the flow when the cylinder is reduced to $L/d = .5$. The model is mounted on a turntable and is then introduced into the tunnel in the same manner as before. Rubber skirt is again used to seal up the opening at the tunnel floor. This way, the cylinder could be rotated to measure the pressure along the desired generator. Pressure taps are connected via vinyl tubing to a 24-port scanivalve, one end of which is connected to a pressure transducer with a pressure range of ±15 cm of water. The pressure difference between the upstream flow and the pressure taps are measured. For the two-dimensional cylinder case, $L/d = 2.5$, the cylinder spans the tunnel height. Again, the top of the cylinder is positioned at ~1.5 mm away from the tunnel ceiling and a rubber skirt is used to seal up the opening. These experiments are carried out with the same free-stream conditions as before.

4 Discussion of Results

4.1 Steady Drag. The pressure coefficient, C_p, is calculated from the pressure tap measurements and U_∞. From these distributions, the local drag coefficient, C_D, again normalized with U_∞, can be evaluated. The mean drag coefficient of the cylinder, $\bar{C}_D$, can be obtained by integrating C_D over the span of the cylinder. In the following discussion, only C_D will be presented and it denotes the local drag coefficient.

Sample plots of C_p distribution around the cylinders at two different y locations are shown in Figs. 4 and 5. One location is at $y/H = .15$ (Fig. 4) and another at the same spanwise distance measured from the top of the cylinder (Fig. 5). These are chosen to illustrate the local behavior of C_p just outside the boundary layer and near the top of the cylinder for different L/d ratios. Figures 6 and 7 show the spanwise distributions of $-(C_p)_b$ and C_D, respectively. In evaluating $-(C_p)_b$, the average over the angular range 150 to 210 deg is taken. The C_D plots are normalized by the average C_D determined from the two-dimensional cylinder case. This average is evaluated over the y/H range in which C_D is fairly uniform, i.e., $.1 \le y/H \le .9$, and the value obtained is 1.37. Denoting this value by $(C_D)_{2-D} = 1.37$, the plots shown in Fig. 7 are all normalized by this value.

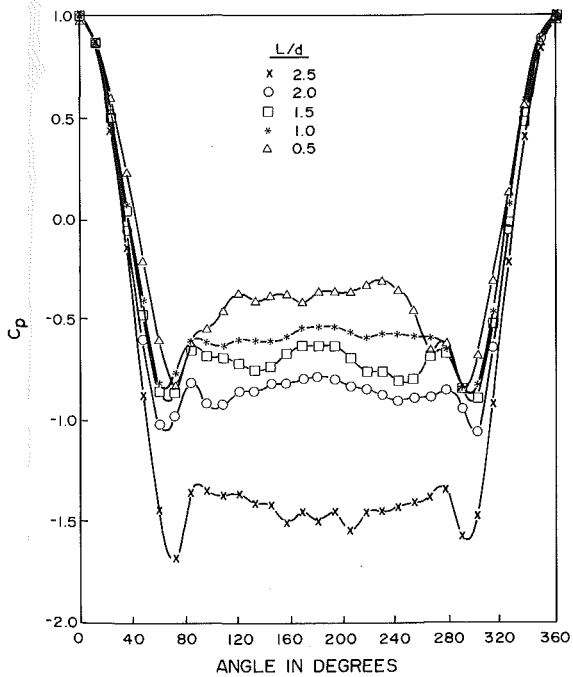

Fig. 4 C_p distributions at $y/H = .15$ for all L/d ratio cylinders

The following observations can be made about these results. First and foremost, the C_p distributions for the two-dimensional case in the range $.1 \le y/H \le .9$ are essentially identical, resulting in a fairly uniform spanwise distribution for $-(C_p)_b$ and C_D outside of the wall boundary layers. This shows that the flow around this region is quite two-dimensional and that C_D is essentially the same as $\bar{C}_D$. Therefore, $(C_D)_{2-D}$ evaluated above gives $\bar{C}_D$ for the two-dimensional case. This compares with a value of 1.29 given in [14] and a value of 1.15 given in [15] for about the same Reynolds number. Since C_D is known to increase with blockage at a fixed Reynolds number, the present value is consistent with those reported in [14,15] where the blockage is ~16 percent in [14] and ~0 percent in [15]. The results further show that the vortex shedding along the span and away from the boundary layers is perfectly correlated for the two-dimensional case. Therefore, any constant C_D distribution along the span can be interpreted as a region of local two-dimensional flow.

The base pressure is practically constant over the angular range 80 to 280 deg for all spanwise locations and all L/d ratio finite-span cylinders (Figs. 4 and 5). Contrary to the observations of Farivar [15], a spanwise region in which the base pressure is constant is not observed for the finite-span cylinders. This is, perhaps, due to the shortness of the span tested. In other words, flow separation from the top of the cylinder affects the wake flow behind the whole cylinder and manages to destroy the perfect correlation of the vortex shedding along the cylinder span. When L/d increases to 5 or more as in the experiments of [15], the penetration of the separated flow cannot cover the whole span and a suppressed two-

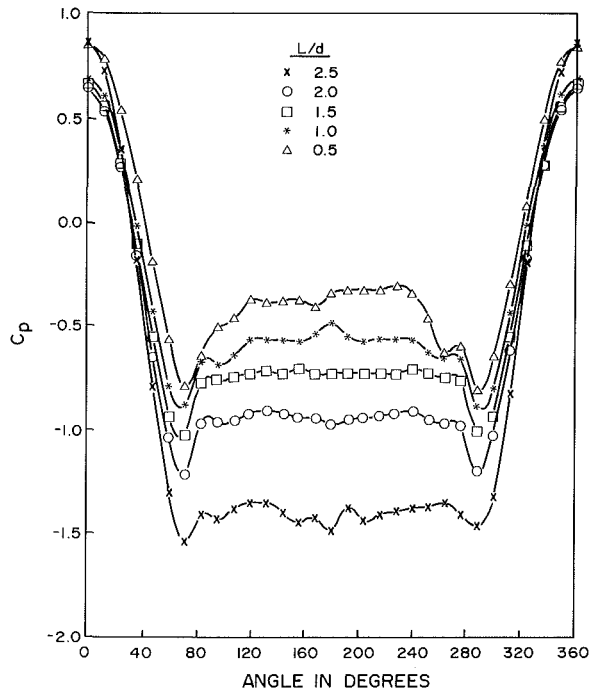

Fig. 5 C_p distributions at the same spanwise distance from cylinder top for all L/d ratio cylinders

Figs. 4 and 5 Uncertainty in C_p = ±0.05, in Angle in Degree = ±0.2 (Degree) at 20:1 odds

dimensional region on the lower part of the cylinder is observed.

At the same y/H, the base pressure is observed to increase as L/d decreases (Fig. 4). The same phenomenon is also observed near the top of the cylinder (Fig. 5). This increase in base pressure is the cause for the observed decrease in C_D (Fig. 7), and is a direct consequence of the effect of the separated flow on the wake. In spite of this, the spanwise distributions of $-(C_p)_b$ bear a striking resemblance to those of C_D (Figs. 6 and 7). This, therefore, suggests that the wake still dominates the response of the cylinder. More will be said about this behaviour when the fluctuating force results are analysed.

Finally, it should be noted that the spanwise distributions of C_D for all finite-span cylinders are essentially similar. As the span of the cylinder is traversed from the top to the base, C_D increases to a maximum and then decreases towards the base. For the three finite-span cylinders with $L/d=2$, 1.5 and 1, the maximum C_D is located at approximately the same distance $d/3$ away from the top of the cylinder. This indicates that the seprated flow has a maximum effect on the wake at this location. As long as the cylinder span that protrudes out of the boundary layer is longer than $d/3$, the maximum C_D occurs at the same location irrespective of the L/d ratio. Once the span decreases to less than $d/3$, as in the case of $L/d=.5$, the separated flow starts to interact with the boundary-layer flow to produce a different maximum C_D location (Fig. 7). Therefore, this suggests that the extent of the separated flow effect is limited to the first $d/3$ away from the top of the cylinder.

4.2 Unsteady Forces. Since the C_D measured at $y/H=.35$ for the two-dimensional cylinder case is essentially equal to $\bar{C}_D$, it is expected that the fluctuating forces measured at this same location would also be the two-dimensional values. The RMS fluctuating lift and drag coefficients, C_L' and C_D', respectively, are calculated from the load cell outputs and normalized by U_∞ and the frontal area of the active element.

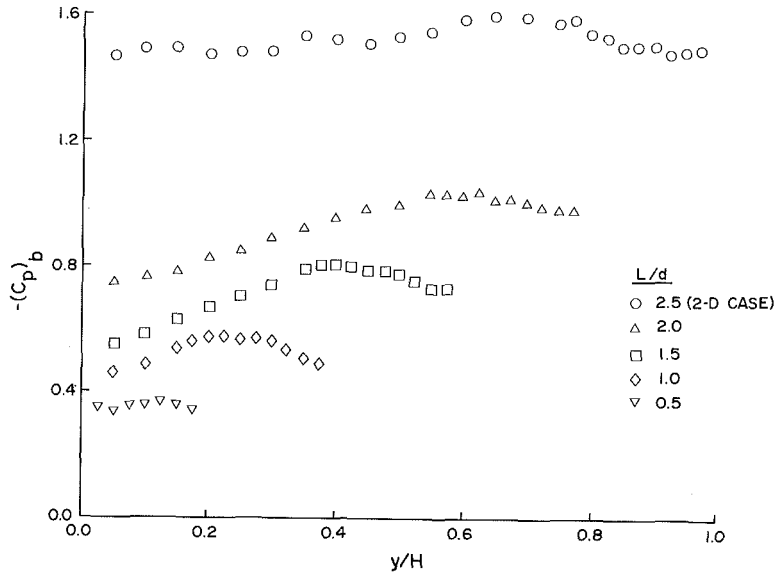

Fig. 6 Distributions of $-(C_p)_b$ along cylinder span

Fig. 6 Uncertainty in $-(Cp)_b = \pm 0.02$, in $y/H = \pm 0.02$ at 20:1 odds

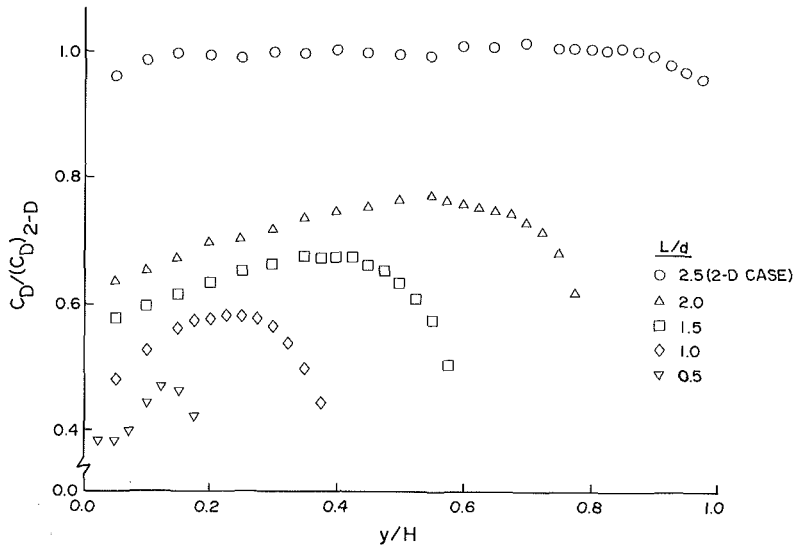

Fig. 7 Distributions of C_D along cylinder span

Fig. 7 Uncertainty in $C_D/(C_D)_{2-D} = \pm 0.02$, in $y/H = \pm 0.02$ at 20:1 odds

These are plotted in Figs. 8 and 9 for comparison with data from [4, 14, 17].

At a Reynolds number of 4.8×10^4, the dynamic response of the cylinder is expected to be Stronhal-like. Therefore, the fluctuating lift force signal should be periodic with little high frequency fluctuations superimposed over the basic periodic response. The spectrum of the lift signal is expected to be delta-function like with very narrow frequency band around the Stronhal frequency. Indeed, these characteristics are observed in the lift force signal and the spectrum shown in Fig. 10 resembles that of a delta function. Here, the normalized spectrum of Φ versus S is shown. The Stronhal frequency, f_s, determined from this spectrum gives a Stronhal number, St, of ~.2, which agrees with the two-dimensional results reported in [4, 14] at the same Re. This is the first piece of evidence to show that the local force measurement technique is capable of resolving the local dynamic response of the cylinder correctly.

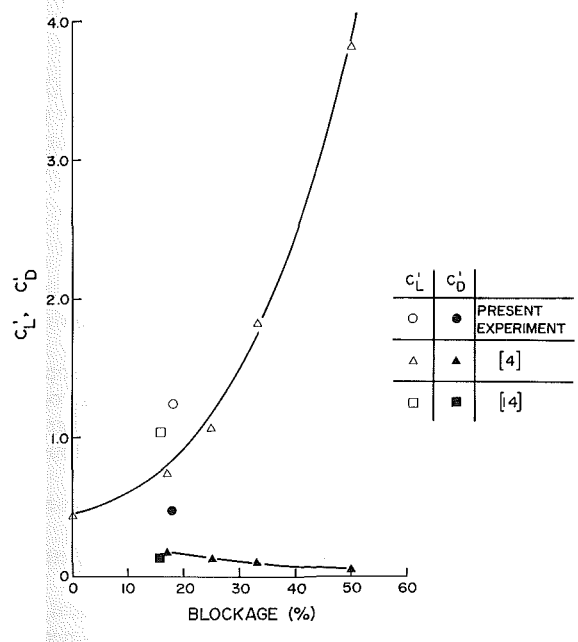

Fig. 8 Variations of C_L' and C_D' with blockage

Fig. 8 Uncertainty in $C_L' = \pm 0.01$, in $C_D' = \pm 0.01$, in Blockage $= \pm 0.2$ (percent) at 20:1 odds

Other evidence in support of this validation can be found in the measurement of the RMS lift coefficient, C_L'. From [4–6, 9–11, 17], it is known that C_L' measurements at a fixed Reynolds number are very much influenced by blockage, active span-to-diameter ratio, S_a/d, and free-stream turbulence. While blockage and S_a/d ratio tend to increase C_L' [4, 17], free-stream turbulence tends to decrease it [5, 6, 10]. Since C_L' measurements with the same blockage, S_a/d and free-stream turbulence are not available, the present C_L' data has to be compared with literature data in the following manner. The data of [4] are extracted to show the effect of blockage (Fig. 8), while the measurements of [17] are used to illustrate the influence of S_a/d on C_L' (Fig. 9). In Fig. 8, the free-stream turbulence level of the present measurement is 1.5 percent while that of [4] is ~.5 percent. Also, the S_a/d for [4] is 6.8. This compares with a $S_a/d = 1/4$ for the present data. For the comparison shown in Fig. 9, the blockage of the two set of data is about the same, 16 percent for [17] and 18 percent for the present data; however, the free-stream turbulence level is different, ~10 percent for [17] compared to 1.5% for the present data. Although free-stream turbulence level is known to decrease C_L', a great portion of the decrease occurs in the free-stream turbulence range of 0 – 1.5 percent [10]. Thereafter, the decrease in C_L' is rather mild. In view of this, Fig. 9 shows that the present C_L' is essentially correct. The same can also be said about the comparison shown in Fig. 8, even though the present C_L' is higher than the curve shown for C_L' variation with blockage. The higher value is most likely due to the fact that S_a/d is 1/4 compared to 6.8 for the data of [4].

The measured C_D' is greater than the measurements of [4] by about a factor of 2 (Fig. 8). Since there are few data to indicate the variation of C_D' with S_a/d, it may indeed be possible that C_D' increases faster with decrease in S_a/d compared to that of C_L' and hence contributes to a much higher C_D' value when

Table 1 Force coefficients measured at $y/H = 0.55$ for the three cylinder models at a fixed Re of ~ 4.8×10^4

	(2 – D Case)		
L/d	2.5 ± 0.02	2 ± 0.02	1.5 ± 0.02
C_D	1.37 ± 0.02	1.01 ± 0.02	0.93 ± 0.02
C_L'	1.24 ± 0.01	0.25 ± 0.01	0.24 ± 0.01
C_D'	0.48 ± 0.01	0.31 ± 0.01	0.30 ± 0.01
St	0.21 ± 0.01	0.18 ± 0.01	0.16 ± 0.01

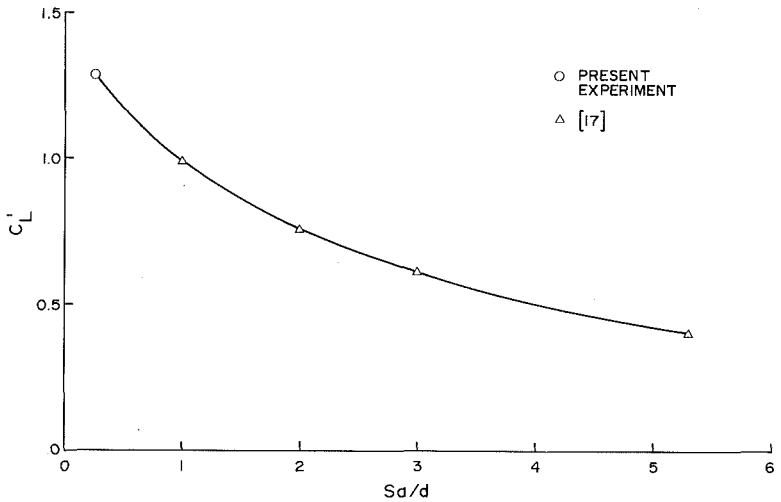

Fig. 9 Variations of C_L' with active span

Fig. 9 Uncertainty in $C_L' = \pm 0.01$, in $Sa/d = \pm 0.02$ at 20:1 odds

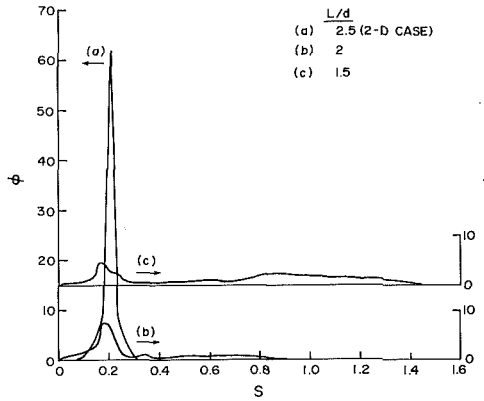

Fig. 10 Normalized spectra of C_L'

Fig. 10 Uncertainty in $\Phi = \pm 0.1$, in $S = \pm 0.01$ at 20:1 odds

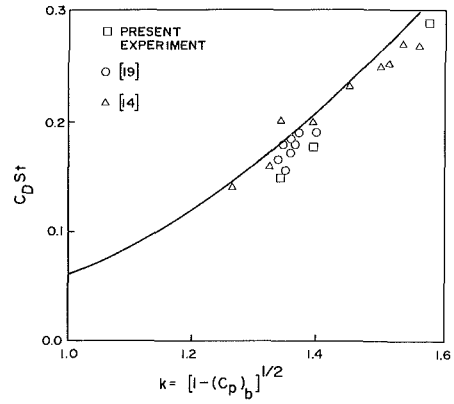

Fig. 11 A plot to illustrate the applicability of Roshko's postulate for finite-span cylinders

Fig. 11 Uncertainty in $C_D St = \pm 0.014$, in $K = 0.009$ at 20:1 odds

measured locally. This expectation is consistent with the observation that the fluctuating drag force is less correlated along the span than the lift. Therefore, when the active span is shortened, the increase in C_D' could be greater than that of C_L'. Considering the scatter in reported C_D' measurements, the measured C_D' falls within that scatter. In conclusion, it can be said that the local force measurement technique developed in this work is capable of resolving the local dynamic response of the cylinder correctly.

The measured St, C_L' and C_D' for the two finite-span cylinders are listed in Table 1 together with the C_D at the same y/H location. Shown also for comparison are the corresponding measurements for the two-dimensional cylinder. It can be seen that even though $C_L'/C_D' \sim 2.5$ for the two-dimensional cylinder case, this ratio is ~ 1 for finite-span cylinders. The measurements of [16] at about the same Re show that $C_L'/C_D' \sim 2$ for $L/d = 2$ and 1.5. However, in that case, the measurements represent spanwise-averaged values and the effective blockage is at least one-order-of-magnitude less than the present measurements. These factors could contribute the lower values reported in [16] for C_L' and C_D'. Sakamoto and Oiwake [16] reported C_L' values of .2 and .16, respectively, for $L/d = 2$ and 1.5. Considering the fact that theirs are spanwise-averaged values, they compare favorably with the present measurements. As for St, the present measurements give an approximate value of $\sim .17$ for both $L/d = 2$ and 1.5 which is also in agreement with the value of .14 reported in [16]. Furthermore, away from the suppressed two-dimensional region of the finite-span cylinder of [15], a constant St of $\sim .16$ is also measured for all L/d ratios investigated. Therefore, the present measurements for finite-span cylinders can be considered to be in good agreement with known data in the literature and further validates the local force measurement technique developed here.

The lift spectra for $L/d = 2$ and 1.5 are shown in Fig. 10. In spite of the separated flow effect on the wake behind the cylinder, the spectra still display a characteristic similar to the Stronhal lift spectrum. A dominant frequency can still be identified. However, the frequency band width becomes wider and is a result of the interaction of the separated flow with the wake flow which in turn modulate the vortex shedding from the cylinder. The lift signals which give rise to these spectra do indeed display a periodic behaviour but with high frequency fluctuations superimposed over the basic oscillations. These spectra resembles those given in [14] for cylinder response in transitional Re range.

Since the base pressure is closely related to C_D as pointed out in Section 4.1, Roshko's [19] postulate that the wake dominates the response of the cylinder could be tested for finite-span cylinder. A plot of C_D St versus k is given in Fig. 11. Shown also are the theoretical curve of Bearman [20] and some data from the literature. It can be seen that the present data for finite-span cylinders fall within the experimental scatter shown and tend to support Roshko's postulate, even for finite-span cylinders.

5 Conclusions

From the results presented in Section 4, the following conclusions can be drawn. These are:

(1) The local force measurement technique developed can indeed resolve the dynamic response of the cylinder correctly.

(2) Measured dynamic responses are in good agreement with known data, both for two-dimensional and finite-span cylinders.

(3) A suppressed two-dimensional region is not observed in finite-span cylinders of small L/d ratios.

(4) The maximum effect of the separated flow is detected at $d/3$ from the top of the cylinder.

(5) For a two-dimensional cylinder, C_D is identical to $\bar{C}_D$, indicating that vortex shedding is perfectly correlated along the span of the cylinder.

Acknowledgment

This work was partially supported by ONR Grant No. N00014-81-K-0428 and by the MAE Department of Arizona State University. These supports are gratefully acknowledged.

References

1 Lamont, P. J., and Hunt, B. L., "Pressure and Force Distributions on a Sharp-Nosed Circular Cylinder at Large angles of Inclination to a Uniform Subsonic Stream," J. Fluid Mech., Vo. 76, 1976, pp. 519-559.

2 Yanta, W. J., and Wardlaw, Jr., A. B., "Flowfield About and Forces on Slender Bodies at High Angles of Attack," *AIAA* J., Vol. 19, 1981, pp. 296-302.

3 Jones, G. W., Cincotta, J. J., and Walker, R. W., "Aero-dynamic Forces on a Stationary and Oscillating Circular Cylinder at Higher Reynolds Number," NASA TR-R300, 1968.

4 Richter, A., and Naudascher, E., "Fluctuating Forces on a Rigid Circular Cylinder in Confined Flow," *J. Fluid Mech.*, Vol. 78, 1976, pp. 561-576.

5 Vickery, B. J., "Fluctuating Lift and Drag on a Long Cylinder of Square Cross Section in a Smooth and in a Turbulent Stream," *J. Fluid Mech.*, Vol. 25, 1966, pp. 481-494.

6 Surry, D., "Some Effects of Intense Turbulence on the Aerodynamics of a Circular Cylinder at Subcritical Reynolds Number," *J. Fluid Mech.*, Vol. 52, 1972, pp. 543-563.

7 Batham, J. P., "Pressure Distributions on Circular Cylinders at Critical Reynolds Number," *J. Fluid Mech.*, Vol. 57, 1973, pp. 209-228.

8 Lee, B. E., "Some Effects on Turbulence Scale on the Mean Forces on a Bluff Body," *J. Ind. Aerody.*, Vol. 1, 1976, pp. 361-370.
9 Brunn, H. A., and Davis, P. O. A. L., "An Experimental Investigation of the Unsteady Pressure Forces on a Circular Cylinder in a Turbulent Crossflow," *J. Sound Vib.*, Vol. 40, 1975, pp. 535-559.
10 Savkar, S. D., and So, R. M. C., "On the Buffeting Response of a Cylinder in a Turbulent Crossflow," BNES Conf.-Vibration in Nuclear Plant, Keswick, U. K., Paper 2.1, 1978.
11 Petty, D. G., "The Effects of Turbulence Intensity and Scale on the Flow Past Square Prisms," *J. Ind. Aerody.*, Vol. 4, 1979, pp. 247-252.
12 Kiya, M., Suzuki, Y., Aric, M., and Hagino, M., "A Contribution to the Free-Stream Turbulence Effect on the Flow Past a Circular Cylinder," *J. Fluid Mech.*, Vol. 115, 1982, pp. 151-164.
13 Norberg, C., and Sunden, B., "Influence of Stream Turbulence Intensity and Eddy Size on the Fluctuating Pressure Forces on a Single Tube," ASME Publication, *Symposium on Flow-Induced Vibrations*, Vol. 1, 1984, pp. 43-56.
14 So, R. M. C., and Savkar, S. D., "Buffeting Forces on Rigid Circular Cylinders in Cross Flows," *J. Fluid Mech.*, Vol. 105, 1981, pp. 397-425.
15 Farivar, D. J., "Turbulent Uniform Flow Around Cylinders of Finite Length," *AIAA J.*, Vol. 19, 1981, pp. 275-281.
16 Sakamoto, H., and Oiwake, S., "Fluctuating Forces on a Rectangular Prism and a Circular Cylinder Placed Vertically in a Turbulent Boundary Layer," ASME JOURNAL OF FLUID ENGINEERING, Vol. 106, 1984, pp. 160-166.
17 Savkar, S. D., So, R. M. C., and Listzinger, T. A., "Fluctuating Lift and Drag Forces Induced on Large Span Bluff Bodies in a Turbulent Crossflow," ASME Publication HTD-9, 1980, pp. 19-26.
18 Sin, V. K., "Dynamic Response of Finite-Span Cylinders in Cross Flows," M.S. thesis, Arizona State University, 1985.
19 Roshko, A., "Experiments on The Flow Past a Circular Cylinder at Very High Reynolds Number," *J. Fluid Mech.*, Vol. 10, 1961, pp. 345-356.
20 Bearman, P. W., "On Vortex Street Wakes," *J. Fluid Mech.*, Vol. 28, 1967, pp. 625-641.

R. G. Teyssandier

Z. D. Husain*

Corporate Research and Development,
Daniel Industries, Inc.
Houston, Texas 77055

Experimental Investigation of an Orifice Meter Pressure Gradient

Wall and plate pressure gradients were investigated in a 3.5 in. (89 mm) air flow orifice meter facility for 3 orifice plates covering a pipe Reynolds number range of 21,000 to 160,000. The influence of the orifice plate on the upstream wall pressure gradient extended to 0.62D location. It was also found that the pressure gradient is a weak function of the orifice plate β ratio. The downstream location of the minimum pressure point located at about 3.3 dam heights. The pressure gradient on the face of the orifice plate shows that the deflection calculation based on any differential pressure taps is conservative.

Introduction

Improvement in the accuracy of flow measurement with orifice meters is dependent upon the accumulation of new data not only on such general parameters such as the discharge coefficient, but also on more specific parameters such as the pressure field in the vicinity of the orifice. For the general parameters new data will soon be available. These data are currently being generated by three extensive studies, conducted under the auspices of the Gas Research Institute, the American Petroleum Institute and Gas Processors Association, and by the European Economic Community. While these data will presumably form the basis for a globally accepted coefficient equation, the development of that equation will require information regarding the pressure gradients in the near field of the orifice. This pressure gradient detail which was first recognized and used by Stolz [1, 2] to develop a rational form of the orifice coefficient equation will most probably be used as part of any new equation development as opposed to any other generalized curve fitting scheme.

In addition to the gradient along the wall of the pipe on both the upstream and downstream side of the plate, the pressure gradient on the plate itself is also of great practical importance. Excessive pressure drop across an orifice will cause the plate to bend [3, 4]. Depending upon the degree of bending this can cause significant deviation from the predicted coefficient. All of the present analyses [5, 6], however, assume that the wall static differential pressure is constant over the entire face of the plate.

The solution to potential flow through an orifice plate shows a pressure gradient along the upstream face of the orifice plate [7, 8], but the gradient on the plate for a viscous fluid has not been published to date. Based on the potential flow solution, it is expected that the gradient for the viscous fluid will be such that the wall differential pressure will always produce a conservative answer when calculating plate deflection. Pressure must decrease along the plate since the flow is under a continuous radial acceleration causing the fluid to pass through the orifice.

On a much less practical level the data on pressure gradients can be of use to those who at sometime in the future will attempt to mathematically model orifice flows. Currently, there is an extremely limited data set on orifice details which can be used for verification of any model. A much more extensive data set that that presented herein will of course be necessary prior to any acceptance of these models.

Experimental Facility

A suction type 3.5 in. (89 mm) diameter plexiglass air-flow facility at Daniel Industries, Air Laboratory was used to obtain data for this orifice plate experimental study. A schematic of the flow facility and instrumentation is shown in Fig. 1. The inlet to the pipe was fitted with a smooth toroidal shape profile as described in the reference [9], and 21-D upstream and 20-D downstream straight sections were adequate for a fully developed flow profile at the test section [9]. An 8-blade centrifugal pressure blower was belt-driven by a 3 hp DC motor whose speed could be adjusted by a DC-motor controller and the speed could be held to ±0.25 percent of any set speed. The upstream section of the pipe had 17 pressure taps at 1/2 in. spacings over a length of 8 ins. There were 32 downstream pressure taps over a length of 24 in.; taps were 1/2 in. apart near the orifice plate and an inch apart from 8 in. downstream. Three 1/4 in. thick square-edged orifice plates of 0.697, 0.498, and 0.299 β ratios were used to obtain the ex-

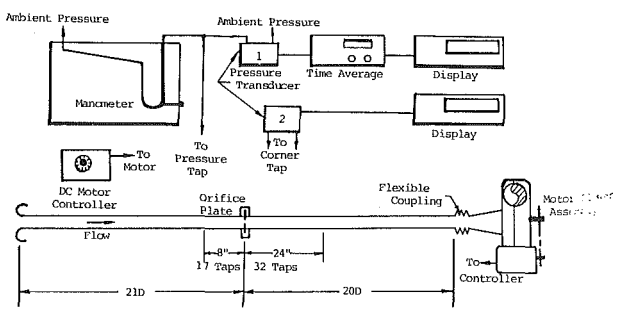

Fig. 1 Schematic of flow facility and instrumentation

*Currently, Chief Engineer, McCrometer, Hemet, CA 92343.

Contributed by the Fluids Engineering Division for publication in the JOURNAL OF FLUIDS ENGINEERING. Manuscript received by the Fluids Engineering Division April 29, 1985.

perimental data. In order to maintain the concentricity of the plate two dowel pins were placed on the flange and those pins passed through the orifice plate, thereby, fixed the orifice plate orientation also. A number of pressure tap holes were made on both the upstream and downstream face of the plate. Figure 2 shows a view of the orifice plate with the pressure tap and tube connections. All pressure taps were 1/32 in. diameter. Pressure at each tap was measured with respect to the atmospheric pressure with at least a 10 second averaging time.

A differential pressure transducer and an inclined manometer was simultaneously monitored to cross check the result. The time averaged pressure-transducer reading were used for the data presented here. For each plate, data were obtained for two dfferential pressures – one was approximately twice that of the other. A second pressure transducer continually monitored the differential pressure at the corner taps ΔP_o, and the pressure was maintained to within ± 0.05 percent of the set differential pressure over the entire test run. This experimental study of 6 test runs covered a pipe Reynolds number range of 21,000 to 160,000. The differential pressures at the pair of corner taps were between 9 and 15 in. of water for all β ratios. Ambient temperature and pressures were also monitored and proper corrections were made on test results.

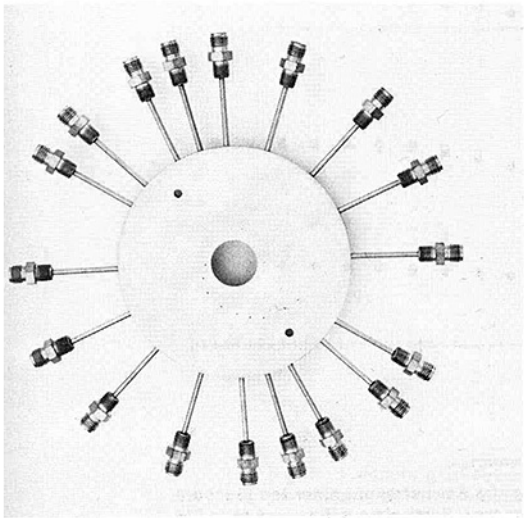

Fig. 2 Orifice plate with tap holes

Experimental Results

Data presented here are compared with previously published data. These data, however, are for the wall pressure gradient only. Experimental studies of Bean et al. [10] and Witte [11] were published in 1931 and results of Herning and Bellenberg [12] were published in 1960. Data presented here were obtained with improved resolution in instrumentation and would possibly provide a better documentation of pressure gradients in the meter tube. The axial flow direction is the increasing x measured from the upstream face of the orifice plate. The y-location is measured radially inward from the inside pipe wall. The upstream tap pressure ΔP_{uc}, is the differential pressure with respect to the upstream corner tap pressure. The downstream tap pressure ΔP_{dc}, is the differential pressure reading with respect to downstream corner tap pressure.

Wall Gradient. As has been previously stated the wall pressure gradients on both the upstream and downstream side of the orifice plate are those of most importance to the development of an orifice coefficient equation. Not surprisingly the results obtained in this part of the overall study did not qualitatively differ from those obtained by previous investigators [10-12], however, some quantitative differences were found. For the upstream side the results are presented in Figs. 3 and 4. The upstream pressure is measured as a differential with respect to upstream corner tap. Figure 3 shows the gradient as a percent of corner tap differential and its change with β follows the function $\beta^4/(1-\beta^4)$ used by Stolz in his equation [1]. Figure 4 shows the same data normalized by the minimum upstream pressure of each data set. This plot shows two aspects of the upstream gradient which differ from the current Stolz equation [2]. First, the pressure gradient upstream extends up to about $x/D = 0.62$ whereas Stolz's equation limits the upstream gradient to $x/D = 0.43$ for the tap locator function. Published data of Bean et al. [10] and Herning and Bellenberg [12] in the similar coordinate showed minimum pressure to be at about 0.6 also. Therefore, a value of about 0.62 as a cut off of the upstream pressure gradient should be used. This location of 0.6 was previously suggested by one of the co-authors in an earlier paper [13]. A change in this value will have implications on the discharge coefficient

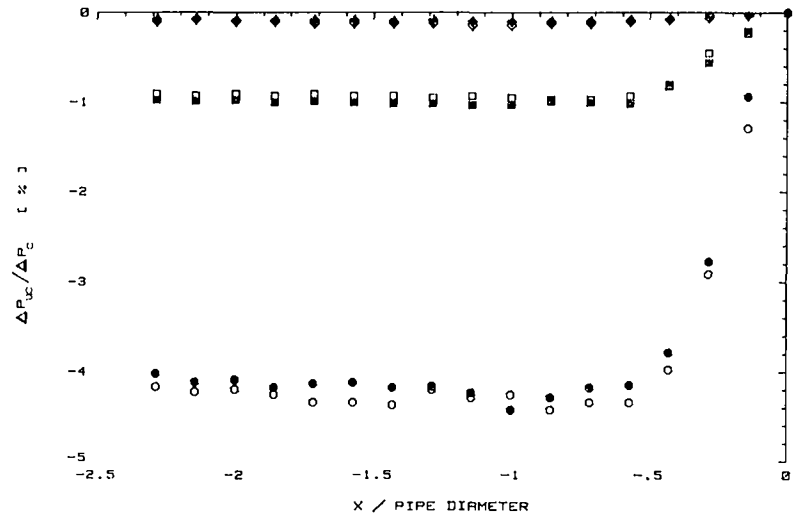

Fig. 3 Normalized upstream pressure with respect to upstream corner tap pressure. Symbols for β ratios of 0.697, 0.498 and 0.299 are ○, □, and ◇, respectively. For the same orifice plate, the solid symbol is at a higher flow rate than that of the open symbol.

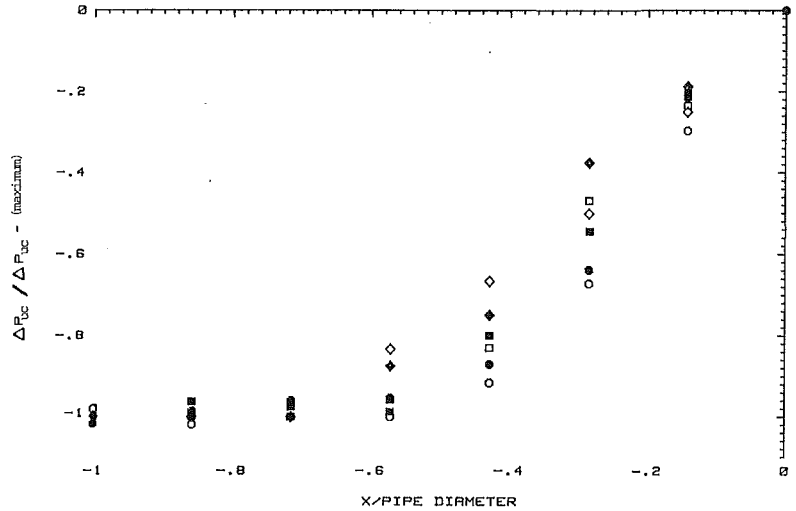

Fig. 4 Upstream pressure normalized by the maximum upstream differential pressure. Symbols are the same as in Fig. 3.

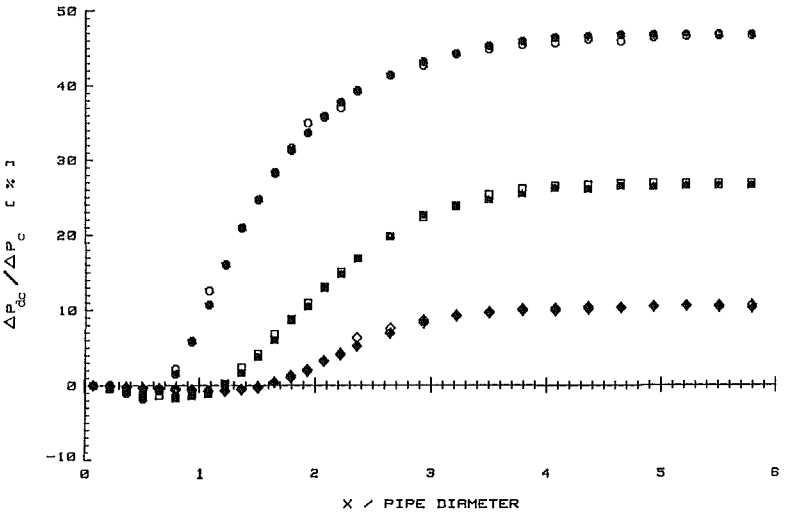

Fig. 5 Downstream wall pressure with respect to the downstream corner tap pressure, normalized by the differential pressure at the corner taps. Symbols are the same as in Fig. 3.

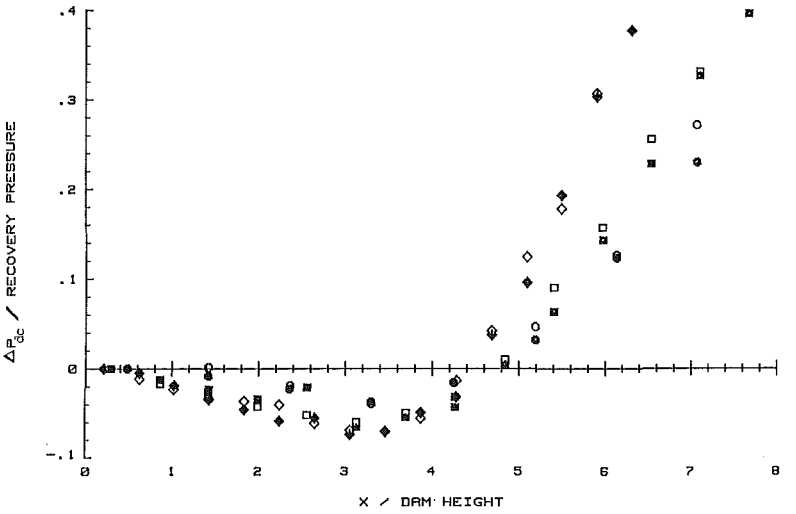

Fig. 6 Near field downstream pressure gradient normalized by the recovery pressure (differential pressure with respect to downstream corner tap at $x/D > 4.5$). Symbols are same as in Fig. 3.

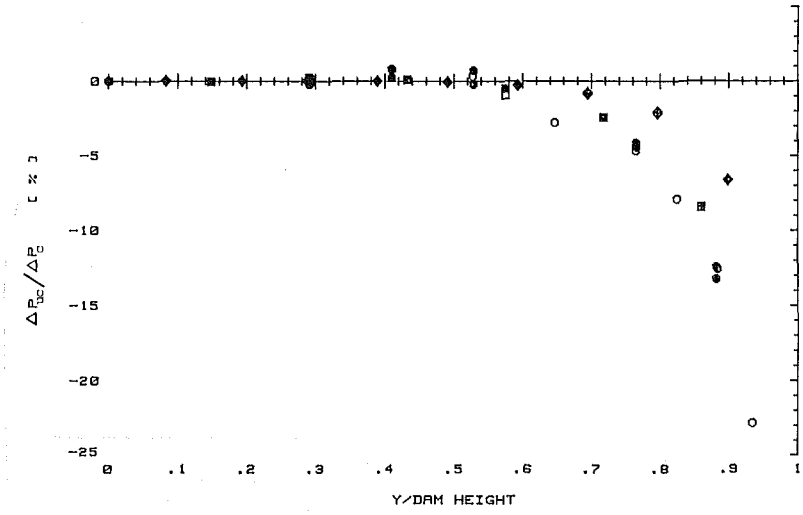

Fig. 7 Pressure gradient on the upstream face of the orifice plate normalized by the differential pressure at the corner tap. Symbols are same as in Fig. 3.

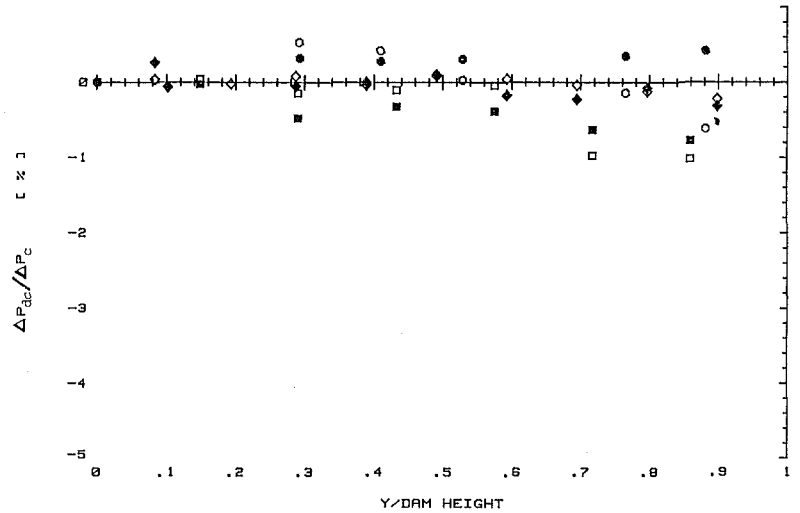

Fig. 8 Pressure gradient on the downstream face of the orifice plate normalized by the differential pressure at the corner taps. Symbols are same as in Fig. 3.

equation of the flange taps. Second, the shape of the pressure gradient is β dependent. The data shows that as β increases the pressure at a given point is relatively lower than at the lower β. This effect can also be observed in the published data of Bean et al. [10] and Herning and Bellenberg [12]. It should be noted that the effect is quite small and will have negligible effect on the orifice coefficient.

The downstream pressure gradient is shown in Figs. 5 and 6. The location of minimum downstream pressure is a function of the β ratio and the pressure recovery is complete at a downstream location of 4.5D from the upstream face of the plate (Fig. 5). Near field data of the downstream pressure gradient is presented in Fig. 6. In this case the dam height and the recovery pressure (i.e., downstream corner to downstream maximum) were used to normalize the data. For equation development it appears that the minimum pressure point occurs at a value of 3.3 dam heights when this coordinate is used. Corresponding values for the published data of Bean et al. [10] and Herning and Bellenberg [12] were 3.65 and 3.24, respectively.

Plate Gradients. Unique to this study was the measurement of the pressure gradient on both the upstream and downstream faces of the plate. Figure 7 shows these results on the upstream side and Fig. 8 shows those on the downstream side. On the upstream side the pressure starts to decrease significantly at about 50 percent of dam height. This pressure continuously decreases along the face of the plate to a point where there is no differential across the plate (at the edge of the throat). Data taken on the land in the throat of the plate in fact showed a pressure below that of the downstream corner tap. These results qualitatively follow the potential flow solution of Rouse and Abul-Fetouh [7] and Hunt [8]. In general this data indicates that calculations on plate deflection [5, 6] are somewhat conservative in nature since the forces (or moment) decrease significantly at the most cantilevered location. Downstream data also shows a similar trend in that the pressure decreases toward the bore. This would increase the forces on the plate, however, these deviations from the corner tap pressure value are negligibly small and are in the order of the data uncertainty, hence, this effect can basically be ignored.

Conclusions

From the investigation of pressure gradients along the boundaries of three different β ratio orifices it can be concluded that

1. The upstream tap locator correction of any coefficient equation should extend to $x/D = 0.62$.
2. The relative value of the upstream pressure does follow $\beta^4/(1-\beta^4)$.
3. The upstream gradient is weakly dependent on the β ratio of the orifice plate.
4. The downstream location of the minimum pressure point is at about 3.3 of dam height of the orifice plate.
5. Deflection calculations based on any wall differential pressure (corner, flange, or D, $D/2$) are conservative.

References

1 Stolz, J., "An Approach Towards a General Correlation of Discharge Coefficients of Orifice Plate Meters," Conference on Fluid Flow Measurement in the Mid 1970s, National Engineering Laboratory, East Kilbride, Glasgow, U.K., Apr. 1975.

2 ISO-5167, "Measurement of Fluid Flow by Means of Orifice Plates, Nozzles and Venturi Tubes Inserted in Circular Cross-Section Conduits Running Full," 1980 (E).

3 Jepson, J., and Chipchase, R., "Effect of Plate Buckling on Orifice Meter Accuracy," *J. Mechanical Engineering Science*, Vol. 17, No. 16, 1975.

4 Mason, D., Wilson, M. P., Jr., and Birkhead, W. G., "Measurement Error Due to Bending of Orifice Plates," ASME Paper No. 75-WA/FM-6, 1975.

5 Norman, B., Rawat, M. S., and Jepson, P., "Buckling and Eccentricity Effects on Orifice Metering Agency," International Gas Research Conference, 1983, IGRC/A 22-83.

6 Trumpler, W. E., Jr., "Design Data of Flat Circular Plates with Central Holes," ASME *Journal of Applied Mechanics*, Vol. 65, Sept. 1943.

7 Rouse, H., and Abul-Fetouh, A., "Characteristics of Irrotational Flow Through Axially Symmetric Orifices," ASME *Journal of Applied Mechanics*, Vol. 17, No. 4, 1950.

8 Hunt, B. W., "Numerical Solution of an Integral Equation for Flow from a Circular Orifice," *J. Fluid Mechanics*, Vol. 31, Part 2, 1968.

9 Ower, E., and Pankhurst, R. C., *The Measurement of Airflow*, Pergammon Press, New York, 5th Edition, 1977.

10 Bean, H. S., Benesh, M. E., and Buckingham, E., "Experiments on the Metering of Large Volumes of Air," *Bureau of Standards Journal of Research*, Vol. 7, Washington, July 1931.

11 Witte, Von R., "Die Stromung durch Dusen und Blender," Forschung 2, Bd./Heft 7, July 1931.

12 Herning, Von F., and Bellenberg, H., "Neue Versuche mit Normblenden," Brennstoff, Warme-Kraft, Vol. 12, 1960.

13 Teyssandier, R. G., and Miller, R. W., "A New Coefficient Equation for Concentric Sharp-Edged Orifice: Part 1 – Fundamental Considerations," ASME Paper No. 79-WA/FM-3, Nov. 1979.

T. Ota
Professor,
Department of Mechanical Engineering,
Faculty of Engineering,
Tohoku University,
Sendai 980, Japan

H. Nishiyama
Lecturer,
Department of Mechanical and Production Engineering,
Akita University,
Akita 010, Japan

Y. Taoka
Engineer,
Nippon Kokan KK,
Yokohama 230, Japan

Flow Around an Elliptic Cylinder in the Critical Reynolds Number Regime

Flow around an elliptic cylinder of axis ratio 1:3 has been investigated experimentally in the critical Reynolds number regime on the basis of mean static pressure measurements along the cylinder surface and of hot-wire velocity measurements in the near wake. The critical Reynold number has been found to vary with the angle of attack α and attains a minimum around α = 5 to 10 deg. At the critical Reynolds number, the drag, lift, and moment coefficients change discontinuously, and the Strouhal number based on the upstream uniform flow velocity and the major axis length of the cylinder reaches a maximum of about 1.0 to 1.5 depending on α. It is found, however, that the universal Strouhal number based on the velocity along the separated shear layer and the wake width is nearly equal to 0.19, on average, even in the critical Reynolds number regime. The pressure distribution along with the surface oil flow pattern revealed the existence of a small separation bubble near the leading edge accompanying a turbulent boundary layer.

Introduction

Flow around an elliptic cylinder at moderate and high Reynolds numbers has been investigated by many authors for a long time. Many of the drag coefficient obtained have been cited in references [1, 2]. It can be found that many of the drag coefficients referred by Goldstein [1] decrease steadily with increasing Reynolds number. It suggests that those data were obtained in the critical flow state. Further the lift and moment coefficients of an elliptic cylinder of axis ratio 1:6 [3] have a strong dependency upon Reynolds number. In addition, experimental and theoretical studies have been reported for the flow at low and moderate Reynolds numbers [4–9]. In these previous works, very little description of the flow behavior in the critical Reynolds number regime is given.

The velocity and turbulence in the boundary layer around an elliptic cylinder having an axis ratio 1:2.96 at α = 0 deg were measured by Schubauer [10, 11], where α denotes the angle of attack. He found that there exists the critical Reynolds number regime, which extends from about Re = 85,000 to 312,000, Re being the Reynolds number based on the major axis of the cylinder. He also observed a so-called separation bubble upstream of the turbulent boundary layer at the critical Reynolds number. His main purpose, however, seems to have been investigation of the boundary layer characteristics. The drag coefficient and the Strouhal number were measured for an elliptic cylinder of axis ratio 1:2 at α = 0 and 90 deg by Delay and Sorensen [12]. All the results at α = 90 deg seem to be characteristic of the subcritical flow but the data at α = 0 deg extend from the subcritical flow to the supercritical one. The Strouhal number was found to vary discontinuously at the critical Reynolds number. Details of the flow around the cylinder, however, have not been described in their paper.

A series of experimental studies upon steady and unsteady flow behaviors of elliptic cylinders have been reported by Modi and his colleagues [13–16]. The mean and fluctuating pressure distributions, the drag, lift, and moment coefficients, the Strouhal number and also the near wake features were clarified at the subcritical Reynolds number. They described that the Reynolds number range examined was included in the subcritical flow regime and that the aerodynamic characteristics exhibited no dependency upon the Reynolds number. In spite of their descriptions, the lift and moment coefficients for an elliptic cylinder of axis ratio 2:5 indicate a large variation with the Reynolds number especially at angles of attack smaller than 20 deg [14].

In consideration of these previous works, it may be concluded that very little is known of details of the flow around the elliptic cylinder in the critical Reynolds number regime. In general, the drag coefficient of the elliptic cylinder at small angle of attack is quite lower than that of a circular cylinder. On the other hand, the mean heat transfer coefficient of elliptic cylinders has been found to be nearly equal to or a little higher than that of a circular cylinder by the present authors [17, 18]. These characteristics of the elliptic cylinder may be very useful for exploiting a high performance heat exchanger in order to save the energy and make its effective use [19, 20]. For such a purpose, details of the flow characteristics of the elliptic cylinder should be clarified in a wide range of the Reynolds number including the critical one. The present paper represents some experimental results on the flow around an elliptic cylinder of axis ratio 1:3 in the critical Reynolds number regime.

Contributed by the Fluids Engineering Division for publication in the JOURNAL OF FLUIDS ENGINEERING. Manuscript received by the Fluids Engineering Division December 17, 1985.

Experimental Apparatus and Technique

The experiments were carried out using a low speed open circuit wind tunnel. Its closed test section is 150 mm wide, 500 mm high, and 800 mm long. The free-stream velocity was varied from about 7 m/s to 38 m/s with the corresponding Reynolds number, Re = $U_\infty c/\nu$, extending from about 35,000 to 125,000. The free-stream turbulence intensity ranged from 0.2 to 0.8 percent [21].

The elliptic cylinder examined has an axis ratio of 1:3, the major axis being 50 mm and the spanwise length 150 mm, which gives an aspect ratio 3. The cylinder was the same as in our previous work [19]. Accordingly, only the main points will be described. The cylinder was made of F.R.P. and thirty pressure holes of 0.3 mm diameter were arranged spirally on the surface. The pressure distribution was measured with a water multimanometer. The drag, lift, and moment coefficients, C_D, C_L, C_M, based on the major axis of the elliptic cylinder were evaluated from the pressure distribution by numerical integrations. The moment coefficient around the cylinder center is defined positive in the counterclockwise direction. The drag coefficient includes no contribution from the surface skin friction, then C_D representing the pressure drag coefficient. The surface skin friction may increase its contribution to the total drag at small angles of attack. In the present Reynolds number range, it was estimated to be at most an order of 0.01 in the form of the drag coefficient. The position of zero angle of attack was carefully determined by comparing the pressure distributions on two sides of the cylinder. The angle of attack α ranged from 0 to 90 deg. However, the greater part of the present paper concerns with the data at small angles of attack, $\alpha \leqq 17$ deg, since the critical flow state was reached only in that range of α in the Reynolds number range examined. The flow around the cylinder was visualized with the surface oil flow pattern especially in the critical flow state in order to clarify the correlation between the pressure distribution on the cylinder surface and the flow field.

The streamwise time-averaged and fluctuating velocities, U and u, in the near wake of the cylinder were measured with a linearized constant temperature hot-wire anemometer. The single wire probe used was made of 0.005 mm tungsten wire. The output of the anemometer was put into a FFT spectral analyzer, then the power spectrum of the turbulent fluctuating velocity and the vortex shedding frequency f were obtained. It cannot be expected to measure the mean and turbulent fluctuating velocities in the highly turbulent and reversing flow region with high reliability by the hot-wire anemometer. However, it may be useful to obtain some important features of the wake flow variation occurring in the critical Reynolds number regime.

Uncertainty of the present data depends upon several factors: manufacturing accuracy of the elliptic cylinder, reading error of the manometer, accuracy of the hot-wire anemometer among others. The accuracy of C_p is estimated to be about ±3 to ±5 percent with the corresponding uncertainty of C_D, C_L, and C_M at about ±5 to ±8 percent by repeating measurements and examining carefully the pressure distribution. These uncertainties may exceed ±10 percent in the critical Reynolds number regime, where the flow around the cylinder is very unstable. The uncertainty of U and u is estimated to be about ±2 and ±8 percent, respectively, outside the wake region. However it may exceed ±10 percent in the separated shear layer and further ±30 percent in the reverse flow region of the wake, because of the high turbulence intensity and also of the severe fluctuation of flow therein.

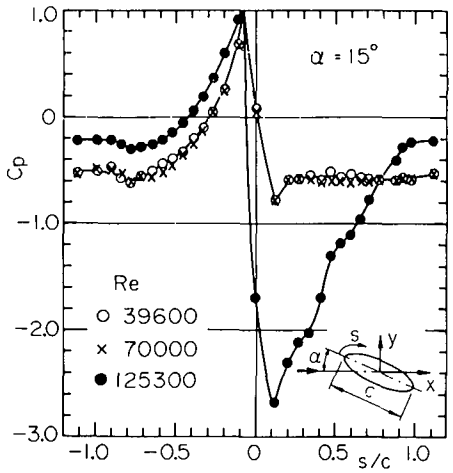

Fig. 1 Pressure distribution, α = 15 deg

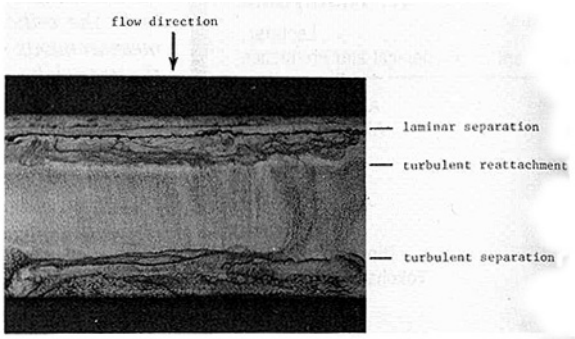

Fig. 2 Surface oil flow pattern on suction side, α = 15 deg and Re = 119,000

Nomenclature

c = major axis of elliptic cylinder

C_D, C_L, C_M = drag, lift and moment coefficients $= D/\frac{1}{2}\rho U_\infty^2 c,\ L/\frac{1}{2}\rho U_\infty^2 c,\ M/\frac{1}{2}\rho U_\infty^2 c^2$

C_p = pressure coefficient $= (P - P_\infty)/\frac{1}{2}\rho U_\infty^2$

C_{pb} = base pressure coefficient

D, L, M = drag, lift and moment

f = vortex shedding frequency

P_∞, U_∞ = static pressure and velocity of upstream uniform flow

Re = Reynolds number = $U_\infty c/\nu$

Rec = critical Reynolds number

s = surface distance from leading edge

St = Strouhal number = fc/U_∞

St* = universal Strouhal number = fw/U_s

U, u = streamwise time-averaged and fluctuating velocities

U_s = velocity along separated shear layer

w = wake width

x, y = coordinates

α = angle of attack

ρ, ν = density and kinematic viscosity of fluid

There have been several correction rules for blockage effects upon fluid-dynamic characteristics of bluff bodies. However many of them assume, for example, that the separation points are unaffected by the Reynolds number. In the critical Reynolds number regime, the pressure distribution around the cylinder changes severely with the Reynolds number as shown in the following. Therefore it may not be expected that the existing correction rules be applicable with high reliability. In accordance with such a situation, the present data have not been corrected for the tunnel wall effects.

The aspect ratio of the present elliptic cylinder is 3.0 as previously noted. The boundary layers developing on two side walls of the test section may have some influences upon the flow around the cylinder, especially in the critical Reynolds number regime. In order to examine such effects, some preliminary experiments were made by visualizing the surface flow pattern with oil film. It revealed that the laminar separation line near the leading edge was almost straight over 80 percent of the cylinder. In the critical Reynolds number regime, a small separation bubble was formed in the neighborhood of the leading edge. As illustrated later in the paper, both the laminar separation line and also the turbulent reattachment one were found to be almost straight over 80 percent of the cylinder. The turbulent separation line located near the trailing edge was detected to be, in general, straight over two-thirds of the cylinder. These results support a reasonable two-dimensionality of the flow around the present elliptic cylinder.

Experimental Results and Discussion

Figure 1 shows a representative example of variations of the pressure distribution with Re. The results at $\alpha = 15$ deg are illustrated in the figure, which includes the main physical parameters and the coordinates. That is, the surface distance s is measured from the leading edge of the cylinder and its positive direction is taken along the suction side. Further the origin of x-y coordinates is located at the cylinder center. At relatively low Reynolds numbers of 39,600 and 70,000, the boundary layer separates laminarly at about $s/c = 0.2$ to 0.3 on the suction surface and about -0.9 on the pressure one, respectively. A large wake is formed behind the cylinder and the pressure in the separated flow region is nearly constant, say about $C_p = -0.5$ to -0.6. The pressure distribution is characteristic of the subcritical flow.

On the other hand, an increase of Re beyond 80,000 produces a great change of the pressure distribution as found in Fig. 1. The flow on the suction side separates in laminar state at about $s/c = 0.3$ and the separated shear layer transits to the turbulent one, which reattaches onto the cylinder surface at about $s/c = 0.5$ forming a small separation bubble. Subsequently, a turbulent boundary layer develops downstream and finally separates at about $s/c = 1.0$. Such a flow feature is demonstrated clearly by a surface oil flow pattern for $\alpha = 15$ deg and Re = 119,000 shown in Fig. 2. As included in the figure, the laminar separation line, the turbulent reattachment one and also the turbulent separation one are definitely detected. The corresponding pressure distribution is represented in Fig. 1. The flow is accelerated very rapidly around the leading edge, producing a very steep decrease of C_p and an extremely low value of about -2.7 is reached at $s/c = 0.1$. Subsequently C_p increases severely to the downstream. On the other hand, C_p on the pressure side is qualitatively similar to that at Re = 39,600 and 70,000, though its value is higher than the latter. The flow separates laminarly at about $s/c = -0.9$, whose location is almost the same as at the subcritical Reynolds number. Consequently a very narrow wake is formed and the entrainment rate of fluid from the main flow outside the wake into the separated region may increase, resulting in the high pressure in the separated flow region and also on the pressure side of the cylinder compared to that at

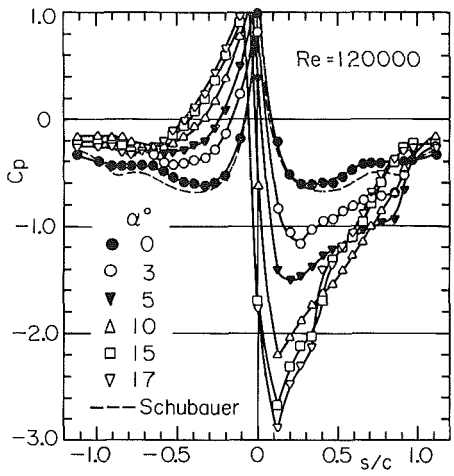

Fig. 3 Effect of α upon pressure distribution, Re = 120,000

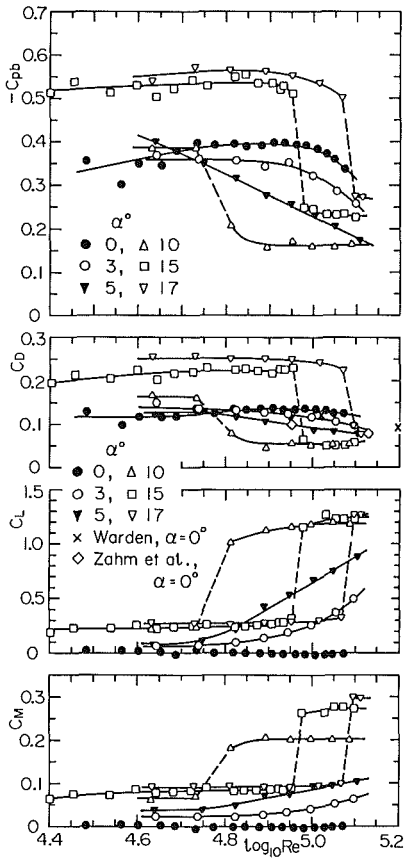

Fig. 4 Variation of C_{pb}, C_D, C_L, and C_M with Re

low Reynolds numbers. These results say that the flow around the cylinder becomes the critical state at Re = 125,300. In the present paper, the critical Reynolds number Rec producing such a great change of the flow is defined as the Reynolds number, at which the Strouhal number varies discontinuously as shown later.

It has been well established that the flow around the elliptic cylinder depends upon its axis ratio and also its angle of attack along with the Reynolds number. It suggests that Rec may be a function of α. Figure 3 shows a comparison of the pressure distribution at various values of α for Re = 120,000, which is higher than Rec. In the Reynolds number range examined in the present experiment, the critical flow state is reached only

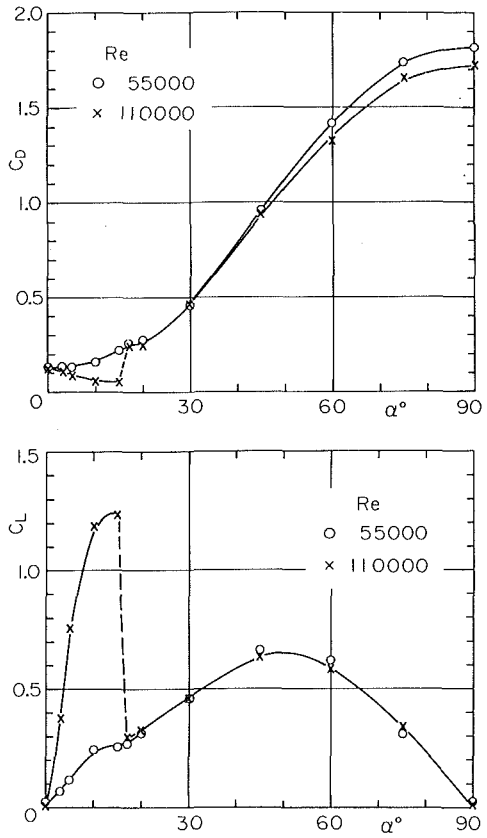

Fig. 5 Variation of C_D and C_L with α

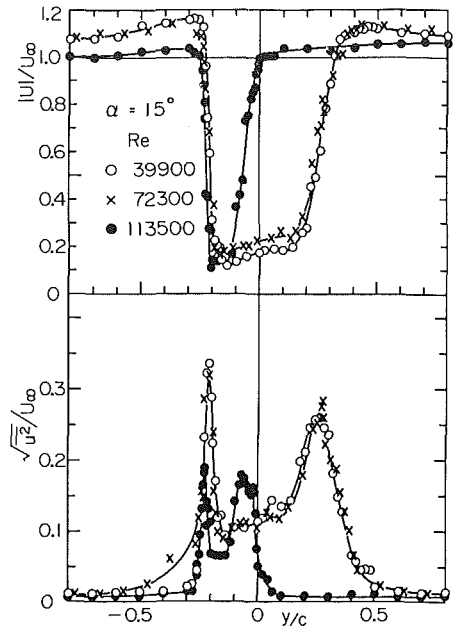

Fig. 6 Streamwise time-averaged and fluctuating velocity distributions, α = 15 deg

at α = 0 to 17 deg. In accordance with such a situation, only the pressure distributions in the same range of α are shown in Fig. 4. Previous data on an elliptic cylinder of axis ratio 1:2.96 for α = 0 deg and Re = 113,000 measured by Schubauer [11] are included in the figure for comparison. He described that the critical flow state extended from about Re = 85,000 to 312,000. Therefore the present flow for α = 0 deg and Re = 120,000 is considered as an initial state of the critical flow. A gradual increase of C_p toward the trailing edge may support such an inference.

It is clear that the pressure distribution depends strongly upon α, though their general trend is almost the same. On the suction side ($s/c > 0$), C_p decreases steeply and reaches a minimum, whose location moves upstream with increasing α. Subsequently C_p increases to the downstream. These pressure distributions represent that on the suction side, the turbulent boundary layer downstream of the small separation bubble separates just upstream of the trailing edge. On the other hand, the minimum value of C_p on the pressure side moves downstream with an increase of α suggesting a downstream shift of the laminar separation point.

Shown in Fig. 4 are variations of C_{pb}, C_D, C_L, and C_M with Re at α = 0 to 17 deg. The base pressure coefficient C_{pb} is defined as a value of C_p at the trailing edge of the cylinder. Inserted in the figure for comparison are previous data for an elliptic cylinder of axis ratio 1:3 [22, 23]. The present data of C_D agree well with those by Warden [23] but are somewhat larger than those by Zahm et al. [22]. At α = 0, 3, and 5 deg, $-C_{pb}$ decreases steadily with Re at higher Reynolds numbers accompanying a gradual decrease of C_D. On the contrary, C_L and C_M increases in the same range of Re. At α = 10, 15, and 17 deg, all of C_{pb}, C_D, C_L, and C_M vary discontinuously at the critical Reynolds number. That is, as Re increases beyond Rec, $-C_{pb}$, and C_D decrease suddenly, and C_L and C_M increase. It is interesting that at higher Reynolds number than Rec, both C_D and C_L show no essential dependency upon α at α = 10 to 17 deg.

Figure 5 shows variations of C_D and C_L with α at Re = 55,000 and 110,000. The former Reynolds number is the subcritical one in the whole range of α and the latter is the critical one at $\alpha \leqq$ 15 deg. At the subcritical Reynolds number, C_D increases monotonically with α from 0.12 at α = 0 deg to 1.7 at α = 90 deg. However, at Re = 110,000, C_D decreases first from 0.12 at α = 0 deg to a minimum of 0.05 at α = 10 to 15 deg, then increases suddenly to 0.15 at α = 17 deg and subsequently becomes nearly equal to that at Re = 55,000. On the other hand, C_L at Re = 55,000 increases with an increase of α reaching a maximum of 0.65 around α = 45 deg, then decreases. At Re = 110,000, as α increases, C_L first increases very rapidly attaining a maximum of about 1.2 at α = 10 to 15 deg, then decreases suddenly to about 0.3 at α = 17 deg. Subsequently it becomes almost equal to that at Re = 55,000. The projected height of the inclined elliptic cylinder to a plane normal to the upstream uniform flow may be more suitable as the reference length for C_D, C_L, and C_M. In the critical flow regime, however, the flow around the cylinder varies very severely with Re and α. Therefore, the major axis of the elliptic cylinder is chosen as the reference length in the present study.

The severe variation of the flow around the cylinder at the critical Reynolds number brings about a great variation of the near wake structure. Represented in Fig. 6 are typical examples of the streamwise time-averaged and fluctuating velocities in the near wake for α = 15 deg and x/c = 0.6. The flow may reverse its direction in the central part of the wake. Then the absolute value of U is shown in the figure, though a region of the reverse flow was examined in y-direction with a tuft probe. Profiles of U and u for Re = 39,900 and 72,300 are almost equal. Those for Re = 113,500, however, become quite different. The separation point on the suction side of the cylinder shifts greatly downstream and the wake width becomes much narrow compared to that at lower Reynolds numbers, as described previously. In addition to it, the maximum of $\sqrt{u^2}/U_\infty$ decreases by about 50 percent, as found in the figure. Such a difference may be due to a following reason. That is, at the subcritical Reynolds number, the laminar boundary layer separates near the leading edge. The separated

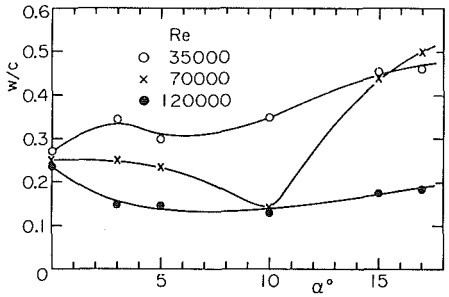

Fig. 7 Variation of w with α

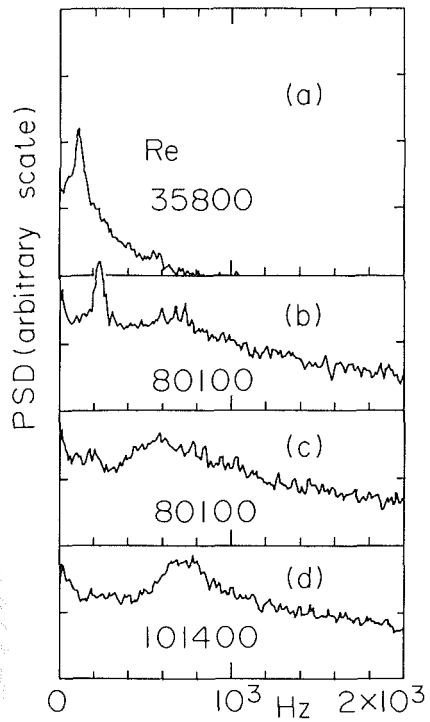

Fig. 8 Power spectral density, α = 15 deg

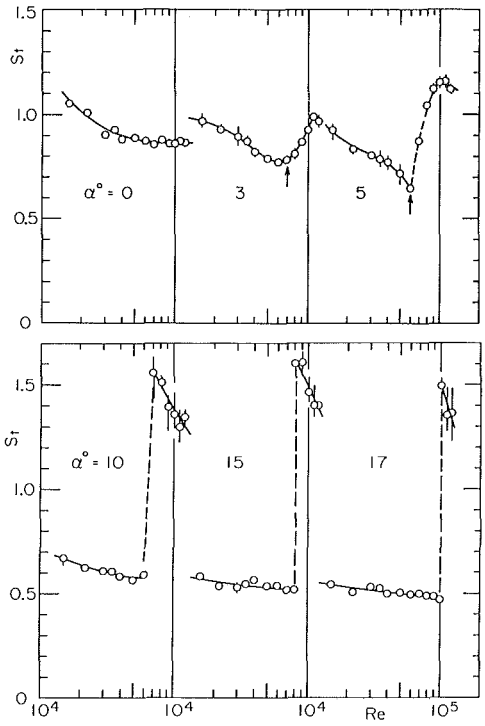

Fig. 9 Variation of St with Re

shear layer is very unstable and may increase its turbulence intensity with the streamwise distance in the near wake of the cylinder. On the other hand, at the critical flow state, say Re = 113,500, the turbulent boundary layer downstream of the small separation bubble flows along the cylinder surface for a long distance until it separates in the neighborhood of the trailing edge. Viscosity of the fluid has a great influence upon the flow in the wall boundary layer and suppresses a growth of the turbulence.

A variation of the wake width w with α is shown in Fig. 7. w was determined as a distance between two maxima of the turbulent fluctuating velocity profile at x/c = 0.6, as exemplified in Fig. 6. It is clear that w depends strongly upon α and also Re. At Re = 35,000, w increases generally with an increase of α, though a small hump exists around α = 3 deg. Such a variation may be common to the subcritical flow. However, at Re = 70,000, w decreases very slightly between α = 0 to 5 deg, and attains a minimum at α = 10 deg. As α increases beyond 10 deg, w increases largely and becomes nearly equal to that at Re = 35,000. At the highest Reynolds number, Re = 120,000, as α increases from 0 deg, w decreases first, shows no essential variation between α = 3 to 10 deg, and subsequently increases gradually. These say that the flow at Re = 70,000 may be an initial state of the critical flow for α = 3 and 5 deg and be the critical one for α = 10 deg. Furthermore, it is clear that the flow at Re = 120,000 is the critical one in a range of 0 deg < α ≦ 17 deg.

Typical examples of the power spectral density of the velocity fluctuation are represented for α = 15 deg in Fig. 8. At the subcritical Reynolds number, Re = 35,800, a very high peak at the vortex shedding frequency is found in Fig. 8(a). However, in the critical Reynolds number regime, Re = 80,100, two spectra were observed at different times. One of them shows a narrow peak at 220 Hz as found in Fig. 8(b) and another shows a weak vortex shedding at 580 Hz in Fig. 8(c). The flow around the cylinder was observed to fluctuate intermittently with time from the former to the latter. That is, the flow is very unstable and exhibits the subcritical one at one moment but changes into the critical one at other time. Such a fluctuation of the flow may be originated from the formation of the separation bubble and its burst. At Re = 101,400 beyond the critical Reynolds number, the flow around the cylinder becomes relatively stable, though the peak frequency of the spectrum fluctuates from 760 Hz to 890 Hz, and the power spectral density extends in a very wide range of frequency, as shown in Fig. 8(d).

Figure 9 represents a variation of the Strouhal number St = fc/U_∞ with Re at α = 0 to 17 deg, in which f denotes the vortex shedding frequency determined as a predominant frequency of the power spectrum of the velocity fluctuation, as exemplified in Fig. 8. In the subcritical flow regime examined in the present study, St gradually decreases with increasing Re at all the angles of attack from 0 to 17 deg. St reaches a minimum at some Reynolds number, which depends on α, then increases discontinuously as attaining a very high value of an order of 1.0 to 1.6, though the case of α = 0 deg is excluded. Its increasing rate is moderate at α = 3 and 5 deg, but is great at α = 10 to 17 deg. It may be reasonable to define the critical Reynolds number Rec as the Reynolds number at which St changes suddenly, as described previously. At α = 3 deg, Rec is evaluated as Re reaching a minimum of St, which is shown by an arrow in the figure. At the critical Reynolds number, two Strouhal numbers are shown, since two predominant frequencies were observed as detected in Fig. 8. Similar

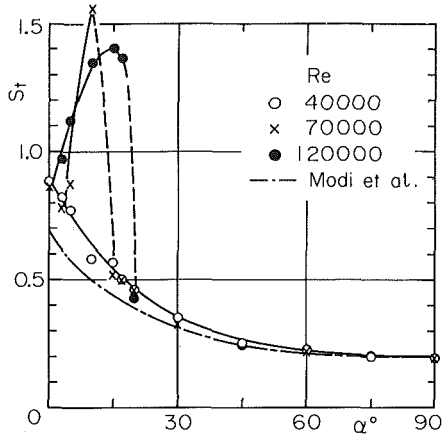

Fig. 10 Variation of St with α

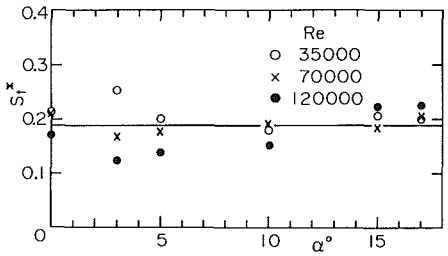

Fig. 11 Universal Strouhal number

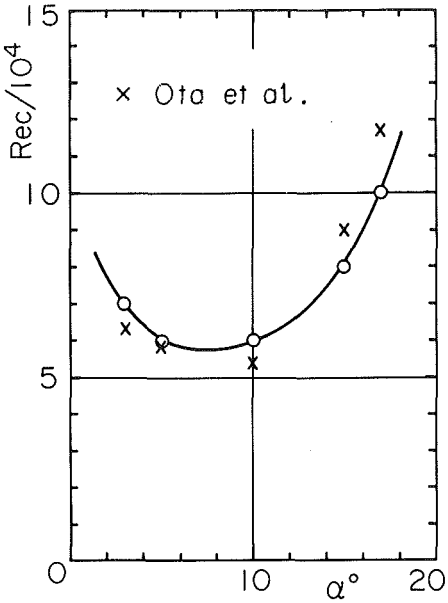

Fig. 12 Variation of Rec with α

situation was also reported for a circular cylinder [24]. As Re increases furthermore beyond Rec, St rather decreases in the present study. The power spectrum extends in a very wide range of frequency and the spectral peak becomes weak. It results in a scatter of St as found in Fig. 9.

Very large values of St at the Reynolds numbers higher than Rec may be due to a very narrow wake. That is, at the critical flow state, the turbulent separation point on the suction side of the cylinder shifts very close to the trailing edge. Accordingly two shear layers separated from the upper and lower sides exist very closely with each other and their mutual interaction is severe. It brings about a very large value of the Strouhal number.

Figure 10 shows a correlation of St with α in the subcritical and the critical flow regimes. Previous data for an elliptic cylinder having an axis ratio 2:5 at the subcritical Reynolds number [16] are included for comparison. The present results at Re = 40,000 show a very similar behavior to the previous ones and their agreement is very good at $\alpha \geqq 45$ deg, in spite of the difference of the axis ratio. At Re = 70,000, however, the flow attains the critical one for $\alpha = 10$ deg as previously noted and St becomes a very high value of 1.55 there. Furthermore at Re = 120,000, the flow around the cylinder is critical for $\alpha = 3$ to 17 deg. When α increases from 0 deg, St increases very rapidly, reaches 1.4 at $\alpha = 17$ deg and decreases discontinuously to a value in the subcritical flow state at $\alpha = 20$ deg. Accordingly the vortex shedding process from the elliptic cylinder, in general, depends strongly upon its axis ratio, the angle of attack, and also the Reynolds number.

An attempt was made to explore whether the concept of the universal Strouhal number [25] be effective or not in the critical flow regime. The results obtained are shown in Fig. 11. That is defined as $St^* = fw/U_s$. w denotes the wake width and U_s being the velocity of the separated shear layer ($U_s = U_\infty\sqrt{1-C_{pb}}$). In spite of large variations of St and w, the present universal Strouhal number may be regarded constant, in essence, its average value being 0.19, though the data scatter is not small. The present average value of 0.19 is a little higher than 0.16 by Roshko [25]. Such a difference may partly be due to the definition of w, which was determined at $x/c = 0.6$ in the present study. An additional attempt was made by using w at $x/c = 1.5$ but the results of St* were much scattered compared to the present ones. The more appropriate determination of w may reduce the scatter of St*.

It has been clarified from previous data that the critical Reynolds number Rec exists for the present elliptic cylinder of axis ratio 1:3 and it depends on the angle of attack. Figure 12 shows a variation of Rec with α. In the present study, Rec is defined as the Reynolds number at which St changes discontinuously, as described previously. Included in the figure for comparison is Rec, which was estimated from the correlation curve between C_L and Re shown in Fig. 4 [26]. The agreement between them is reasonably good. It is clear in Fig. 12 that as α increases, Rec first decreases, attains a minimum at $\alpha = 5$ to 10 deg and subsequently increases rapidly. The value of Rec at $\alpha = 17$ is an order of 10^5. Further increase of α shows no critical flow state in the present range of Re. Such a peculiar behavior of Rec may be presumed as follows. At small angles of attack, the pressure gradient on the suction side of the cylinder is quite small. Then the transition of the laminar boundary layer to the turbulent one is delayed. On the other hand, at larger angles of attack than 17 deg, the positive pressure gradient near the leading edge becomes extremely large. Accordingly the fluid may not be able to flow along the cylinder surface, especially near the leading edge, unless the boundary layer transits to the turbulent one immediately after the upstream stagnation point. These flow characteristics may bring about an increase of Rec at smaller and higher angles of attack.

The critical Reynolds number for the circular cylinder has been determined as the Reynolds number attaining a minimum of the drag coefficient. In the present study, C_D does not necessarily reach the minimum at Rec. The present data of Rec may be tentative since the critical flow around the bluff body with a smooth contour (it means that the separation point can not be fixed) is very sensitive to many factors. Examples include the blockage ratio, the aspect ratio, the surface roughness (its configuration and also its distribution), and the free stream turbulence intensity. Effects of the blockage ratio, the free stream turbulence, and the surface roughness upon Rec have been investigated. However, there is no systematic

investigation on the effect of the cylinder aspect ratio upon Rec. This is an important problem to be solved.

Concluding Remarks

The two-dimensional flow around an elliptic cylinder of axis ratio 1:3 has been investigated in the critical Reynolds number regime. The Reynolds number Re ranged from about 35,000 to 125,000. It has been found that the critical Reynolds number Rec is a function of the angle of attack α. Rec attains a minimum at $\alpha = 5$ to 10 deg and it increases both at smaller and larger angles of attack. The critical flow state, however, was not attained at $\alpha > 17$ deg in the present range of Re. The flow around the cylinder at Rec is very unstable. The subcritical flow state and the critical one appear alternately and two Strouhal numbers exist. The characteristics of the wake vary greatly at Rec. The wake width decreases and the maximum of the turbulent fluctuating velocity becomes smaller by about 50 percent than in the subcritical flow regime. Even under such a situation, the concept of the universal Strouhal number holds good and its value is, on average, about 0.19 though the data scatter is not small. The flow at higher Reynolds number beyond Rec becomes relatively stable and the small separation bubble was observed on the suction side of the cylinder.

Acknowledgments

The present authors wish to thank Messrs. N. Kon, K. Miyoshi, T. Toba, S. Suzuki, and M. Nagayama for their assistance in the experiments.

References

1 Goldstein, S., Ed., *Modern Developments in Fluid Dynamics*, Vol. II, Oxford Univ. Press, 1938.

2 Hoerner, S. F., *Fluid-Dynamic Drag*, published by the author, 1958.

3 Williams, D. H., and Brown, A. F., "Experiments on an Elliptic Cylinder in the Compressed Air Tunnel," ARC R&M, No. 1817, 1937.

4 Taneda, S., "Visual Study of Unsteady Separated Flows Around Bodies," *Prog. in Serospace Sci.*, Vol. 17, 1977, pp. 287–348.

5 Tatsuno, M., "Secondary Flow Around an Oscillating Elliptic Cylinder," Rept. Res. Inst. Appl. Mech., Kyushu Univ., Vol. 27, 1979, pp. 99–110.

6 Stapountzis, H., and Graham, J. M. R., "The Unsteady Lift on Bluff Cylindrical Bodies in Unsteady Flow," *Aeron. Quart.*, Vol. 33, 1982, pp. 219–236.

7 Parkinson, G. V., and Jandali, T., "A Wake Source Model for Bluff Body Potential Flow," *J. Fluid Mech.*, Vol. 40, 1970, pp. 577–594.

8 Nees, N., "Laminar Separated Flow Over Nonlifting Ellipses," *AIAA J.*, Vol. 13, 1975, pp. 688–690.

9 Shintani, K., Umemura, A., and Takano, A., "Low-Reynolds-Number Flow Past an Elliptic Cylinder," *J. Fluid Mech.*, Vol. 136, 1983, pp. 277–289.

10 Schubauer, G. B., "Air Flow in a Separating Laminar Boundary Layer," NACA Tech. Rep., No. 527, 1935.

11 Schubauer, G. B., "Air Flow in the Boundary Layer of an Elliptic Cylinder," NACA Tech. Rep., No. 652, 1939.

12 Delay, N. K., and Sorensen, N. E., "Low-Speed Drag of Cylinders of Various Shapes," NACA Tech. Note, No. 3038, 1953.

13 Modi, V. J., and Wiland, E., "Unsteady Aerodynamics of Stationally Elliptic Cylinders in Subcritical Flow," *AIAA J.*, Vol. 8, 1970, pp. 1814–1821.

14 Modi, V. J., and Dikshit, A. K., "Mean Aerodynamics of Stationally Elliptic Cylinders in Subcritical Flow," *Proc. Third Int. Conf. on Wind Effects on Buildings and Structures*, Tokyo, 1971, pp. 345–355.

15 Modi, V. J., and Dikshit, A. K., "Near-Wakes of Elliptic Cylinders in Subcritical Flow," *AIAA J.*, Vol. 13, 1975, pp. 490–497.

16 Modi, V. J., and Ieong, L., "On Some Aspects of Unsteady Aerodynamics and Vortex Induced Oscillations of Elliptic Cylinders at Subcritical Reynolds Number," ASME *Journal of Mechanical Design*, Vol. 100, 1978, pp. 354–362.

17 Ota, T., Aiba, S., Tsuruta, T., and Kaga, M., "Forced Convection Heat Transfer from an Elliptic Cylinder of Axis Ratio 1:2," *Bull. JSME*, Vol. 26, 1983, pp. 262–267.

18 Ota, T., Nishiyama, H., and Taoka, Y., "Heat Transfer and Flow around an Elliptic Cylinder," *Int. J. Heat Mass Transfer*, Vol. 27, 1984, pp. 1771–1779.

19 Ota, T., and Nishiyama, H., "Flow Around Two Elliptic Cylinders in Tandem Arrangement," ASME JOURNAL OF FLUIDS ENGINEERING, Vol. 108, 1986, pp. 98–103.

20 Ota, T., Nishiyama, H., Kominami, J., and Sato, K., "Heat Transfer from Two Elliptic Cylinders in Tandem Arrangement," ASME *Journal of Heat Transfer*, Vol. 108, 1986, pp. 525–531.

21 Ota, T., and Itasaka, M., "A Separated and Reattached Flow on a Blunt Flat Plate," ASME JOURNAL OF FLUIDS ENGINEERING, Vol. 98, 1976, pp. 79–86.

22 Zahm, A. F., Smith, R. H., and Louden, F. A., "Forces on Elliptic Cylinders in Uniform Air Stream," NACA Tech. Rep., No. 289, 1928.

23 Warden, R., "Resistance of Certain Strut Form," ARC R&M, No. 1599, 1934.

24 Bearman, P. W., "On Vortex Shedding from a Circular Cylinder in the Critical Reynolds Number Regime," *J. Fluid Mechanics*, Vol. 37, 1969, pp. 577–585.

25 Roshko, A., "On the Wake and Drag of Bluff Bodies," *J. Aeron. Sci.*, Vol. 22, 1955, pp. 124–132.

26 Ota, T., and Taoka, Y., "Flow around Two Elliptic Cylinders in Tandem Arrangement," Preprint of JSME Meeting, No. 820-10, 1982, pp. 1–3 (in Japanese).

Improved Form of the k-ϵ Model for Wall Turbulent Shear Flows

Y. Nagano
Professor.
Mem. ASME

M. Hishida
Professor.

Department of Mechanical Engineering,
Nagoya Institute of Technology,
Gokiso-cho, Showa-ku,
Nagoya 466, Japan

An improved k-ϵ turbulence model for predicting wall turbulence is presented. The model was developed in conjunction with an accurate calculation of near-wall and low-Reynolds-number flows to meet the requirements of the Evaluation Committee report of the 1980-1981 Stanford Conference on Complex Turbulent Flows. The proposed model was tested by application to turbulent pipe and channel flows, a flat plate boundary layer, a relaminarizing flow, and a diffuser flow. In all cases, the predicted values of turbulent quantities agreed almost completely with measurements, which many previously proposed models failed to predict correctly, over a wide range of the Reynolds number.

1 Introduction

Turbulence models are still the only economically feasible approach to the analytical studies of turbulent flow problems encountered in engineering applications (e.g., see review articles of Rodi [1] and Lumley [2]). In 1980-1981 an important competition was held at Stanford to judge various existing turbulence models for calculating complex turbulent flows [3]. At this conference thirty-five different computor groups used 67 different methods to compare the results of calculations with experimental data. The most important conclusion of the Evaluation Committee is that the range of satisfactory performance of the models is rather narrow, and that all models are well worthy of further study and refinement.

The k-ϵ model of turbulence to be considered here was one of the most extensively used methods at the 1980-1981 Stanford Conference. For wall flows, this model is normally used in conjunction with empirical so-called wall functions, by which surface boundary conditions are transferred to points in the fluid removed from the boundaries. However, as pointed out by the Evaluation Committee [3], universal wall functions are not well established in many situations, and thus the methods which include an integration to the wall are better than those assuming the wall functions.

Jones and Launder [4, 5] were the first to extend the original k-ϵ model to the low-Reynolds-number form which allowed calculations right up to a solid wall. Later, improvements of the k-ϵ model were made successively for the same purpose, and their performance was well assessed at the Stanford Conference. A primary defect of all existing k-ϵ model is that they do not reproduce the "law of the wall" which has been observed over a range of pressure gradients [3, 6]. A corollary effect of this defect is the insufficient prediction of the wall shear stress which is of prime importance in practice.

The present study presents the development of an improved form of the k-ϵ model which permits the above problems to be solved. Predictions with the proposed model are then compared with a set of basic test cases covering a broad range of wall flows of engineering interest.

2 The Model Equations

2.1 The Existing k-ϵ Models. The governing equations for the k-ϵ model of turbulence may be written [7] as:

$$\frac{\partial k}{\partial \tau}+\bar{U}_j\frac{\partial k}{\partial x_j}=\frac{\partial}{\partial x_j}\left\{\left(\nu+\frac{\nu_t}{\sigma_k}\right)\frac{\partial k}{\partial x_j}\right\}-\overline{u_iu_j}\frac{\partial U_i}{\partial x_j}-\epsilon+D \tag{1}$$

$$\frac{\partial \epsilon}{\partial \tau}+\bar{U}_j\frac{\partial \epsilon}{\partial x_j}=\frac{\partial}{\partial x_j}\left\{\left(\nu+\frac{\nu_t}{\sigma_\epsilon}\right)\frac{\partial \epsilon}{\partial x_j}\right\}-C_{\epsilon 1}f_1\frac{\epsilon}{k}\overline{u_iu_j}\frac{\partial \bar{U}_i}{\partial x_j}-C_{\epsilon 2}f_2\frac{\epsilon^2}{k}+E \tag{2}$$

Here ν_t is the eddy viscosity defined as:

$$-\overline{u_iu_j}=\nu_t\left(\frac{\partial \bar{U}_i}{\partial x_j}+\frac{\partial \bar{U}_j}{\partial x_i}\right)-\frac{2}{3}\delta_{ij}k \tag{3}$$

The eddy viscosity ν_t is related to k and ϵ through the Kolmogorov-Prandtl relation as:

$$\nu_t=C_\mu f_\mu\sqrt{k}L_\epsilon=C_\mu f_\mu k^2/\epsilon \tag{4}$$

where $L_\epsilon=k^{3/2}/\epsilon$, is the eddy length scale.

The turbulence quantities can be obtained from equations (1)-(4), together with the following continuity and momentum equations:

$$\partial \bar{U}_i/\partial x_i=0 \tag{5}$$

$$\frac{\partial \bar{U}_i}{\partial \tau}+\bar{U}_j\frac{\partial \bar{U}_i}{\partial x_j}=-\frac{1}{\rho}\frac{\partial \bar{P}}{\partial x_i}+\frac{\partial}{\partial x_j}\left(\nu\frac{\partial \bar{U}_i}{\partial x_j}-\overline{u_iu_j}\right) \tag{6}$$

Table 1 summarizes the values of the constants in the k-ϵ model, model functions which account for low-Reynolds-number and/or wall-proximity effects, and additional terms denoted by D and E which mainly improve predictions in the wall region, recommended by the various authors [6]. The up-

Contributed by the Fluids Engineering Division for publications in the JOURNAL OF FLUIDS ENGINEERING. Manuscript received by the Fluids Engineering Division January 16, 1986.

Table 1 Constants and functions in the k-ε models

Model	ϵ_w-BC	C_μ	$C_{\epsilon 1}$	$C_{\epsilon 2}$	σ_k	σ_ϵ	f_μ	f_1	f_2	D	E
Basic High-Re	WF	0.09	1.44	1.92	1.0	1.3	1.0	1.0	1.0	0	0
Jones-Launder	$\epsilon=0$	0.09	1.45	2.0	1.0	1.3	$\exp\left(\frac{-2.5}{1+R_t/50}\right)$	1.0	$1-0.3\exp(-R_t^2)$	$-2\nu\left(\frac{\partial\sqrt{k}}{\partial y}\right)^2$	$2\nu\nu_t\left(\frac{\partial^2 U}{\partial y^2}\right)^2$
Hassid-Poreh	$\epsilon=0$	0.09	1.45	2.0	1.0	1.3	$1-\exp(-0.006R_t)$	1.0	$1-0.3\exp(-R_t^2)$	$-2\nu\frac{k}{y^2}$	$-2\nu\left(\frac{\partial\sqrt{\epsilon}}{\partial y}\right)^2$
Hoffmann	$\epsilon=0$	0.09	1.81	2.0	2.0	3.0	$\exp\left(\frac{-1.75}{1+R_t/50}\right)$	1.0	$1-0.3\exp(-R_t^2)$	$\frac{\nu}{y}\frac{\partial k}{\partial y}$	0
Dutoya	$\epsilon=0$	0.09	1.35	2.0	0.9	0.95	$1-0.86\exp\left\{-\left(\frac{R_t}{600}\right)^2\right\}$	$1-0.04\exp\{-(R_t/50)^2\}$ $-0.25(\lambda/y)^2$	$1-0.3\exp\{-(R_t/50)^2\}$ $-0.08(\lambda/y)^2$	$-2\nu\left(\frac{\partial\sqrt{k}}{\partial y}\right)^2$	$-C_{\epsilon 2}f_2\frac{\epsilon}{k}\epsilon$
Chien	$\epsilon=0$	0.09	1.35	1.8	1.0	1.3	$1-\exp(-0.0115R_t)$	1.0	$1-0.22\exp\{-(R_t/6)^2\}$	$-2\nu\frac{k}{y^2}$	$-2\nu\frac{\epsilon}{y^2}\exp(-0.5R_t)$
Reynolds	$\epsilon=\nu\frac{\partial^2 k}{\partial y^2}$	0.084	1.0	1.83	1.69	1.3	$1-\exp(-0.0198R_k)$	1.0	$\{1-0.3\exp\{-(R_t/3)^2\}\}f_\mu$	0	0
Lam-Bremhorst	$\epsilon=\nu\frac{\partial^2 k}{\partial y^2}$	0.09	1.44	1.92	1.0	1.3	$\{1-\exp(-0.0165R_k)\}^2\left(1+\frac{20.5}{R_t}\right)$	$1+(0.05/f_\mu)^2$	$1-\exp(-R_t^2)$	0	0
Present Model	$\epsilon=0$	0.09	1.45	1.9	1.0	1.3	$\left\{1-\exp\left(-\frac{R_\tau}{26.5}\right)\right\}^2$	1.0	$1-0.3\exp(-R_t^2)$	$-2\nu\left(\frac{\partial\sqrt{k}}{\partial y}\right)^2$	$\nu\nu_t(1-f_\mu)\left(\frac{\partial^2 U}{\partial y^2}\right)^2$

permost model in Table 1 is the basic version of the k-ϵ model for high-Reynolds-number flows. In the basic model, viscous diffusions in equations (1) and (2) are neglected and empirical wall function formulas are used in order to bridge the viscous sublayer. All modifications to the basic k-ϵ model listed in Table 1 have been already assessed systematically, and the model of Lam and Bremhorst [8] is found to perform considerably better than the others though it still needs further refinement [3, 6]. The next section describes a present proposed model along with a discussion on two previously proposed models, one devised by Jones and Launder (JL) [4, 5] and the other by Lam and Bremhorst (LB) [8], since these are regarded as representative turbulence models for near-wall and low-Reynolds-number flows.

2.2 The Proposed Model. In order to develop a new form of the k-ϵ model for predicting near-wall turbulence, it is necessary to give full consideration to two physically distinct effects: the influence of low Reynolds number and the influence of wall proximity. The former is due to the predominant effect of molecular viscosity on the flow structures in the immediate neighborhood of the wall. The latter concerns the preferential damping of velocity fluctuations in the direction normal to the wall. As is obvious from equations (1) and (3), the production of turbulent kinetic energy is so dependent upon the eddy viscosity ν_t that the correct modelling of ν_t is critical in obtaining correct turbulence values near the wall. This in turn suggests that the function f_μ modifying the Kolmogorov-Prandtl relation in equation (4) must be modelled so as to account for the two separate effects mentioned previously. The function f_μ of the JL model, given in Table 1, is apparently a unique function of turbulence Reynolds number R_t, and thus the direct influence of the presence of a wall on ν_t is not taken into consideration. On the other hand, the formula f_μ of the LB model, as seen in Table 1, is now dependent upon the turbulence Reynolds number R_t and the nondimensional distance from the wall R_k. Thus, the aforementioned two effects are considered in this formulation. We may, however, point out that this formula still conflicts with the following physical requirement: as R_t decreases, f_μ should decrease accordingly. The function f_μ consistent with physical arguments should tend to unity as the turbulence Reynolds number and the nondimensional distance from the wall increase and should become much smaller than unity with a decrease of these parameters. The integrated form of equation (6), i.e., momentum-integral equation, suggests that the wall shear stress τ_w is directly dependent upon the streamwise pressure gradient $\partial\bar{P}/\partial x$. Also, it is known that τ_w is a function of the Reynolds number. Thus, the wall shear stress τ_w is an appropriate flow parameter indicative of Reynolds number and/or pressure gradient effects. On the other hand, turbulent velocities near the wall are usually the same order of magnitude as the friction velocity u_*. Therefore, the local Reynolds number R_τ $(=u_*y/\nu)$ has a function similar to the local turbulence Reynolds number $R_k(=\sqrt{k}y/\nu)$ in the wall region. The utmost difference is that R_τ is much more directly sensitive to flow conditions than R_k, since u_* changes with the state of a velocity field via τ_w as $u_*=\sqrt{\tau_w/\rho}$.

In view of the above factors, we propose the following formula for f_μ:

$$f_\mu = \{1-\exp(-R_\tau/26.5)\}^2 = \{1-\exp(-y^+/26.5)\}^2 \quad (7)$$

In this formulation, the influence of wall proximity is directly counted via the local Reynolds number, i.e., nondimensional distance from the wall, R_τ. When the Reynolds number decreases, the sublayer thickness generally becomes thicker. Hence, the apparent wall-dominating region expands. The proposed formula for f_μ (7) satisfies this relation, because f_μ is a unique function of R_τ $(=u_*y/\nu)$, and thus the actual wall distance y giving the same value of f_μ becomes larger with

Nomenclature

C_f = skin-friction coefficient $= \tau_w/(\rho\bar{U}_e^2/2)$
C_μ, $C_{\epsilon 1}$, $C_{\epsilon 2}$ = turbulence model constants
d = pipe diameter or channel width
f_μ, f_1, f_2 = turbulence model functions
h = channel half-width
k = turbulent kinetic energy $= \overline{u_iu_i}/2$
$\bar{P}$ = mean pressure
R_c = Reynolds number $= \bar{U}_m d/\nu$
R_t = turbulence Reynolds number $= k^2/\nu\epsilon$
R_k = dimensionless distance $= \sqrt{k}y/\nu$
R_τ = dimensionless distance $= u_*y/\nu = y^+$
$\bar{U}$, $\bar{U}_e$, $\bar{U}_m$ = time mean streamwise velocity, velocity external to boundary layer, and bulk velocity
$\bar{U}^+$ = dimensionless velocity $= \bar{U}/u_*$
$\bar{U}_i$ = mean velocity component in x_i direction (tensor notation)
u, v = fluctuating velocity components in x and y directions
u_i = fluctuating velocity component in x_i direction (tensor notation)
u_* = friction velocity $= \sqrt{\tau_w/\rho}$
x = streamwise coordinate
x_i = coordinates in tensor notation
y = distance from wall
y^+ = dimensionless distance $= u_*y/\nu$
ϵ = dissipation rate of turbulence energy $= \nu\overline{(\partial u_i/\partial x_j)(\partial u_i/\partial x_j)}$
ν, ν_t = molecular and eddy viscosities
ρ = density
σ_k, σ_ϵ = turbulent Prandtl numbers for diffusion of k and ϵ
τ = time
τ_w = wall shear stress
$\overline{(\ )}$ = time mean value

decreasing u_* (or decreasing Reynolds numbers). The influence of turbulence Reynolds number R_t is not included in the present f_μ, since the eddy viscosity ν_t is already modelled as a function of R_t. This may be readily realized by rewriting equation (4) as:

$$\nu_t/\nu = C_\mu f_\mu R_t \tag{8}$$

Further inclusion of R_τ dependence in f_μ may be possible. However, the simplest formulation is adopted here. It should be noted that the proposed f_μ is equivalent to the Van Driest damping function for the mixing length [9]:

$$\nu_t = (\kappa y)^2 \{1 - \exp(-y^+/A^+)\}^2 |\partial \bar{U}/\partial y| \tag{9}$$

where κ is Von Kármán's universal constant and A^+ (=26-27) is a damping-length constant.

At the wall, ϵ is finite. However, we make ϵ zero at the wall for computational expediency, as suggested by Jones and Launder [4, 5]. Since this makes the k-equation inconsistent at the wall, we add the same term D in equation (1).

The extra term E in equation (2) is necessary to improve near-wall behaviour. The basic high-Reynolds-number form of the k-ϵ model suggests that E must tend to zero in fully turbulent regions remote from the wall. Hence, we propose:

$$E = \nu\nu_t(1 - f_\mu)(\partial^2 \bar{U}/\partial y^2)^2 \tag{10}$$

The substantial difference from the JL model is an inclusion of $(1 - f_\mu)$.

The model functions and constants proposed in the present study are included in Table 1. Values of the constants are the same as those recommended by Bradshaw et al. [7].

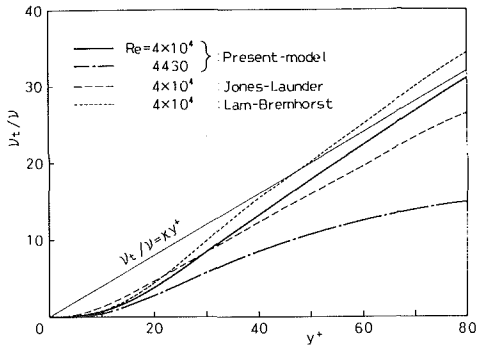

Fig. 1 Comparison of models for eddy viscosity near the wall

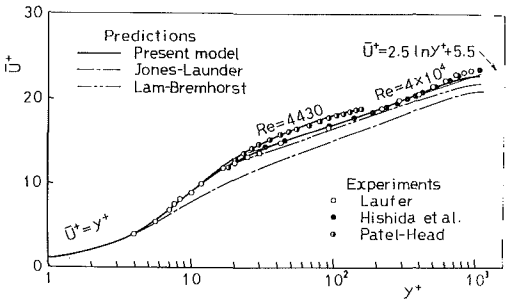

Fig. 2 Mean velocity profiles in a pipe

3 Numerical Method of Solution

The numerics affect the results of the turbulence models both in the algorithm chosen and the number and distribution of nodal points [3]. Therefore special attention was paid to the numerics in order to make model comparisons more meaningful. The numerical technique used is a well-tested Keller's Box method [7, 10]. It is known that this method is unconditionally stable and the accuracy of a solution is high. The coordinate for regions of very large gradients should be expanded near the wall. Thus, for internal flows, a transformation is introduced so that $\eta = (y/r_0)^{1/2}$ or $(y/h)^{1/2}$. For external flows, the following nonuniform grid [7] across the layer is employed:

$$y_j = \Delta y_1 (K^j - 1)/(K - 1) \tag{11}$$

where Δy_1, the length of the first step, and K, the ratio of two successive steps, are chosen as 10^{-5} and 1.03, respectively. For both internal and external flow cases, 201 cross-stream grid points were used to obtain grid-independent solutions. The first grid point was normally located well into the viscous sublayer: e.g., less than $y^+ = 0.03$ in the case of internal flows. In order to resolve the streamwise changes in the viscous sublayer sufficiently, the maximum streamwise step-size was restricted to a sublayer thickness, i.e., $\Delta x < \nu/u_*$.

The boundary conditions for equations (1), (2), (5), and (6) are as follows:

$$\bar{U} = k = \partial k/\partial y = \epsilon = 0 \text{ at } y = 0 \tag{12}$$

$$\partial \bar{U}/\partial y = \partial k/\partial y = \partial \epsilon/\partial y = 0 \text{ at the axis for internal flows} \tag{13}$$

$$\bar{U} = \bar{U}_e, \text{ and } k = \epsilon = 0 \text{ at the free stream for external flows} \tag{14}$$

where $\bar{U}_e$ or $d\bar{P}/dx$ is prescribed from experiments.

The criteria for convergence are:

$$\text{Max} |Y^{(i+1)} - Y^{(i)}| / \text{Max} |Y^{(i)}| < 10^{-5} \tag{15}$$

where $Y = \partial X/\partial y$ (X: $\bar{U}$, k, and ϵ),

and

$$|U_*^{(i+1)} - U_*^{(i)}| < 10^{-5} \tag{16}$$

where $U_* = u_*/\bar{U}_m$ or $u_*/\bar{U}_e$, and $u_* = \sqrt{\tau_w/\rho}$ with $\tau_w/\rho = \nu (\partial \bar{U}/\partial y)_{y=0}$. Calculations stop when both criteria are satisfied. The computations were performed on a FACOM M-382 computer.

4 Discussion of Predictions With the Proposed Model

To assess the performance of the model, the following five test cases are calculated.

4.1 Pipe Flows. The first criterion by which success or failure is to be judged is that the model should reproduce the well-known Prandtl-Nikuradse wall function for high-Reynolds-number flows. As mentioned previously, the correct modelling of the eddy viscosity ν_t holds the key to success. The profiles of ν_t calculated with the proposed model are compared in Fig. 1 with those of the JL and LB models. In the turbulent part of the wall region, ν_t may be expressed as:

$$\nu_t/\nu = \kappa y^+ \tag{17}$$

where κ is Von Kármán's universal constant: $\kappa = 0.4$ for pipe flow. It can be seen from Fig. 1 that the proposed model tends to reproduce equation (17) asymptotically, while both JL and LB models ended in failure. Also observed is the present prediction of degeneration of eddy viscosity with a decrease of Reynolds number, which is quite realistic.

This reflects mean velocity profiles in a pipe, as shown in Fig. 2 where measurements of Laufer [11], Hishida et al. [12], and Patel and Head [13] are included so as to evaluate the performance of the models. The proposed model predicts exactly the universal velocity profile given by the Prandtl-Nikuradse equation:

$$\bar{U}^+ = 2.5 \ln y^+ + 5.5 \tag{18}$$

and progressive deviation from this equation with decreasing Reynolds numbers. The JL model gives an underprediction for equation (18). The LB model yields a comparatively good prediction for equation (18) although this is not yet perfect.

To verify the effectiveness of the proposed model for calculating turbulent quantities, the prediction of turbulent

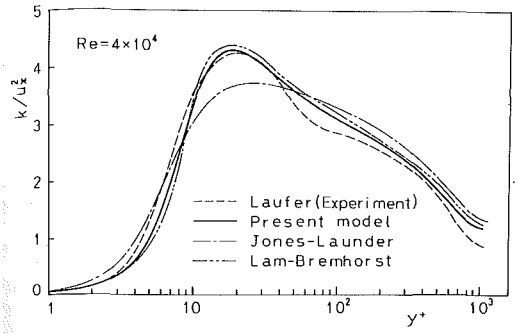

Fig. 3 Turbulent energy profiles in a pipe

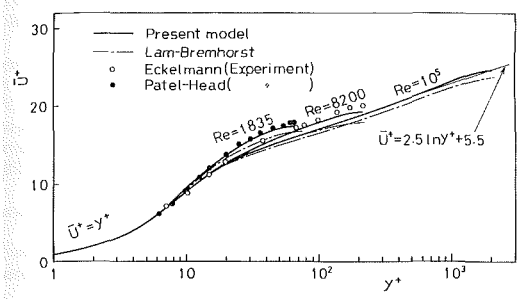

Fig. 4 Mean velocity profiles in plane channel flow

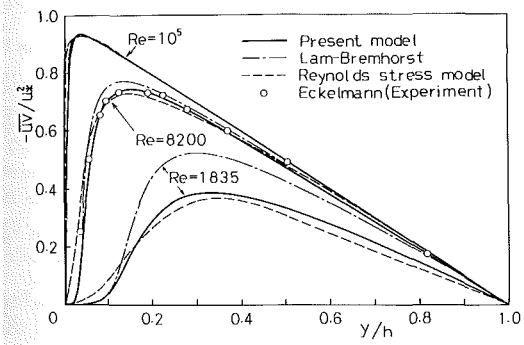

Fig. 5 Turbulent shear stress profiles in a plane channel

kinetic energy k is compared in Fig. 3 with the models of JL and LB, and with Laufer's measurements. The results with the proposed model and LB show excellent agreement with measurements. The underprediction of the large peak k value with the JL model is found to originate in not only the formula for f_μ in equation (4) but the proposal for an added term E in ϵ-equation (2).

4.2 Channel Flows. The results for the second test case, namely channel flows, are shown in Figs. 4 and 5. In Fig. 4, predictions of mean velocity profiles are presented, compared with the experimental data of Patel and Head [13], and Eckelmann [14]. The present predictions again correctly display the shift of the velocity profiles progressively above the universal "law of the wall" given by equation (18) as the Reynolds number is reduced. The LB model, however, gives an underprediction for the measured velocity profiles, especially at low Reynolds numbers.

Figure 5 shows the results of calculated turbulent shear stress profiles. Also included here are the calculations for the Reynolds-stress model of Hanjalić and Launder [15] in which the turbulent shear stress is obtained from a transport equation for the turbulent shear stress itself. Agreement between the present prediction and Eckelmann's data is seen to be virtually complete. The difference in $\overline{uv}$ predictions between the LB and present models is as remarkable as that observed in

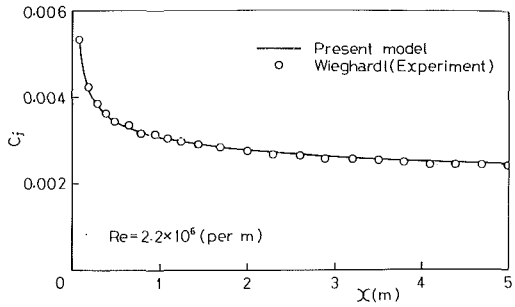

Fig. 6 Measured and calculated skin-friction coefficient for a flat plate boundary layer

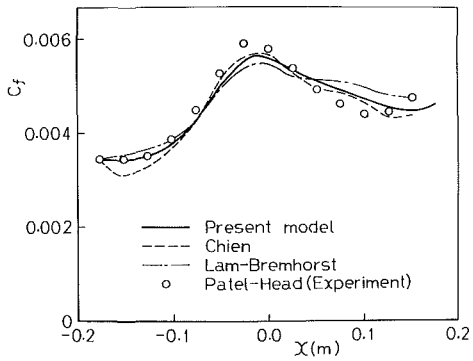

Fig. 7 Comparison of model results for relaminarizing flow

mean velocity profiles shown in Fig. 4. It may be well worth noting that the present less sophisticated approach functions as well as the Reynolds-stress model.

4.3 Flat Plate Boundary Layer. The foregoing test cases are concerned with internal flows. The following present the results of predictions for external flows so as to identify the wide-ranging performance of the proposed model. In the interest of brevity, the comparisons are limited to the skin-friction coefficient C_f, since there is a strong correlation between the ability of a model near the wall and the prediction of the wall shear stress. Note that C_f has been determined from the slope of the velocity profile at the wall.

The flat plate boundary layer is the most fundamental test case for external flows. This test case corresponds to Flow Case 0612 of the Stanford Conference and was used to assure that simple shear layers were modelled adequately. It can be seen from Fig. 6 that the present prediction is in almost complete agreement with the carefully reviewed experimental data. The LB model was found to give an over-estimation of C_f [6].

4.4 Relaminarizing Flow. Relaminarization or retransition occurs when a turbulent boundary layer is subjected to a sustained steep, streamwise acceleration accompanied by a strong favorable pressure gradient $d\bar{P}/dx<0$. As shown in Fig. 7, the calculations with the proposed model reproduce accurately the succession of stages [16] that occur in a relaminarizing flow: the initial increase in C_f, and the subsequent decrease associated with relaminarization. It is also obvious from the figure that the proposed model works better than the LB model.

4.5 Diffuser Flow. The last test case for which calculations have been performed is a diffuser flow with an adverse pressure gradient $d\bar{P}/dx>0$. This test case is identical to Flow Case 0141 of the Stanford Conference. The flow has an adverse pressure gradient so strong that it appears to be approaching separation at the end of the working region, but no separation is present. From Fig. 8 it is evident that the perfor-

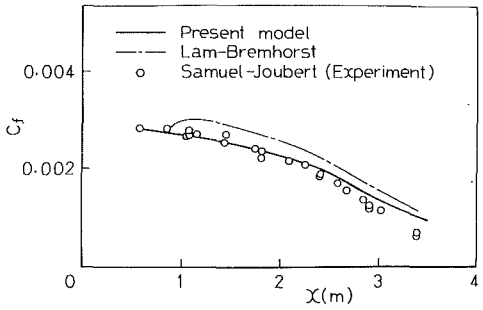

Fig. 8 Comparison of model results for diffuser flow

mance of the proposed model is practically acceptable, or at least much better than that of LB.

5 Conclusions

A newly improved form of the k-ϵ model has been developed with reference to the conclusions and suggestions of the Evaluation Committee report of the Stanford Conference on Complex Turbulent Flows. The proposed model is partly similar to (though with important differences from) that devised by Jones and Launder. However, it is established that the performance of the proposed model is far better than the existing k-ϵ models for a wide range of wall-turbulent shear flows encountered in practice. The correct modelling of the eddy viscosity for near-wall and low-Reynolds-number flows holds the key to success in the prediction of an entire flow zone over a range of pressure gradients.

Finally, a cautionary note needs to be sounded. One of the conclusions of the Stanford Conference on Complex Turbulent Flows was that the effects of adverse pressure gradients on shear layers were predicted insufficiently by most turbulence models. As pointed out by Rodi and Scheuerer [17], the differences between the prediction and existing data manifested themselves mostly in consistently overpredicted skin-friction coefficients and a tendency of the calculated flow to remain attached where experiments indicated separation. As seen from Fig. 8, the present model, on the whole, has made a considerable improvement. Near separation, however, the present prediction is not yet perfect. We must leave this for a future study.

Acknowledgment

The authors are grateful to Mr. T. Asano for his help in setting up an initial version of the computer program.

References

1 Rodi, W., *Turbulence Models and Their Application in Hydraulics—a State of the Art Review*, (2nd ed.), International Association for Hydraulic Research-Publication, Delft, 1984.

2 Lumley, J. L., "Turbulence Modeling," ASME *Journal of Applied Mechanics*, Vol. 50, 1983, pp. 1097–1103.

3 Kline, S. J., Cantwell, B. J., and Lilley, G. M., The 1980-81 AFOSR-HTTM-Stanford Conference on Complex Turbulent Flow: Comparison of Computation and Experiment I, II and III, Thermosciences Division, Mechanical Engineering Department, Stanford University, Stanford, Calif., 1981.

4 Jones, W. P., and Launder, B. E., "The Prediction of Laminarization with a Two-Equation Model of Turbulence," *International Journal of Heat and Mass Transfer*, Vol. 15, 1972, pp. 301–314.

5 Jones, W. P., and Launder, B. E., "The Calculation of Low-Reynolds Number Phenomena with a Two-Equation Model of Turbulence," *International Journal of Heat and Mass Transfer*, Vol. 16, 1973, pp. 1119–1130.

6 Patel, V. C., Rodi, W., and Scheuerer, G., "Evaluation of Turbulence Models for Near-Wall and Low-Reynolds Number Flows," Third Symposium on Turbulent Shear Flows, University of California, Davis, Calif., 1981, pp. 1.1–1.8.

7 Bradshaw, P., Cebeci, T., and Whitelaw, J. H., *Engineering Calculation Methods for Turbulent Flow*, Academic Press, 1981.

8 Lam, C. K. G., and Bremhorst, K., "A Modified Form of the k-ϵ Model for Predicting Wall Turbulence," ASME JOURNAL OF FLUIDS ENGINEERING, Vol. 103, 1981, pp. 456–460.

9 Van Driest, E. R., "On Turbulent Flow Near a Wall," *Journal of the Aeronautical Sciences*, Vol. 23, 1956, pp. 1007–1011.

10 Cebeci, T., and Bradshaw, P., *Momentum Transfer in Boundary Layers*, Hemisphere, 1977, pp. 213–280.

11 Laufer, J., "The Structure of Turbulence in Fully Developed Pipe Flow," NACA Report 1174, 1954.

12 Hishida, M., Nagano, Y., and Morimoto, Y., "Structure of Pipe Flow Turbulence. 1st Report, Characteristics of Velocity Fluctuations and Reynolds Shear Stress," *Trans. Japan Soc. Mech. Engrs.*, Ser. B, Vol. 46, 1980, pp. 1455–1466.

13 Patel, V. C., and Head, M. R., "Some Observations on Skin Friction and Velocity Profiles in Fully Developed Pipe and Channel Flows," *Journal of Fluid Mechanics*, Vol. 38, 1969, pp. 181–201.

14 Eckelmann, H., "The Structure of the Viscous Sublayer and the Adjacent Wall Region in a Turbulent Channel Flow," *Journal of Fluid Mechanics*, Vol. 65, 1974, pp. 439–459.

15 Hanjalić, K., and Launder, B. E., "Contribution Towards a Reynolds-Stress Closure for Low-Reynolds-Number Turbulence," *Journal of Fluid Mechanics*, Vol. 74, 1976, pp. 593–610.

16 Patel, V. C., and Head, M. R., "Reversion of Turbulent to Laminar Flow," *Journal of Fluid Mechanics*, Vol. 34, 1968, pp. 371–392.

17 Rodi, W., and Scheuerer, G., "Scrutinizing the k-ϵ Turbulence Model Under Adverse Pressure Gradient Conditions," ASME JOURNAL OF FLUIDS ENGINEERING, Vol. 108, 1986, pp. 174–179.

D. C. Wiggert

F. J. Hatfield

Department of Civil and Environmental Engineering, Michigan State University, East Lansing, MI 48824-1212

S. Stuckenbruck

Department of Mechanical Engineering, Catholic University of Rio de Janeiro, Rio de Janeiro, Brazil

Analysis of Liquid and Structural Transients in Piping by the Method of Characteristics

Since liquid-filled piping systems are composed of slender elements, their transient behavior can be described as one-dimensional wave phenomena. Seven wave components are identified: coupled axial compression of liquid and pipe material; coupled transverse shear and bending of the pipe elements in two principal directions; and torsion of the pipe wall. Utilizing the method of characteristics, the combined system of difference equations for pipe elements and the pipe junction boundary conditions comprise a general mathematical tool for predicting the liquid pressure and pipe stress responses to transient excitation of either liquid or piping. The complexity of fluid-structure interaction that can take place is demonstrated.

Introduction

The analytical procedures usually employed for design of piping systems are approximate, in part since they neglect the effects of structural mass, stiffness and damping on transient pressures in the contained liquid. Although a number of studies addressing this issue have appeared in the recent literature, and although significant gains have been realized, there remains a need to rigorously investigate all of the mechanisms by which properties of the pipe structure influence liquid transients and vice versa.

In their attempts to more accurately couple fluid-structure interaction in piping systems, investigators have utilized several different methodologies. The conventional and most common means to represent the structural motion of the piping has been to employ finite element techniques, and the coupled liquid motion has been modeled either by finite elements or by the method of characteristics. Complete modeling has not yet been achieved from the viewpoint of correctly coupling the significant motions in both the piping and the liquid. This paper presents wave equations which account for the coupled motion of piping and contained liquid. A technique based on acoustic wave analysis allows explicit solution of the system of equations.

Wave Equations for Fluid-Structure Interaction

The primary coupling mechanisms for fluid-structure interaction in liquid-filled piping are: Poisson coupling, by which dynamic pressure and the resulting circumferential strain induce axial strain in the pipe wall; and junction coupling, by which dynamic pressure exerts an axial resultant on piping and, conversely, pipe motion generates changes in dynamic pressure. The former mechanism occurs throughout the length of a pipe and the latter is associated with junctions where flow area or direction changes.

A number of investigators [1–5] have identified axial stress waves in the pipe wall which are generated by the Poisson effect. In addition, a few others [6–8] have introduced shear, bending and torsion waves in the structural elements. Most notably, Wilkinson [6, 7] clearly shows the interaction between liquid and structure at pipe fittings and the manner in which the various waves are generated. His analytical techniques were based on a frequency-domain formulation [6] or on a simplified wave approach [7], which impose limitations on the excitation function and complexity of the piping system.

Fundamental Equations. Since liquid-filled piping systems are composed of slender components, their transient behavior can be described as one-dimensional wave phenomena. Consider the prismatic liquid-filled pipe element shown in Fig. 1. It can transmit torsional waves in the pipe wall, transverse shear and bending waves in the pipe wall, and axial compression waves in both the pipe wall and the liquid. The equations to describe such motion are given below.

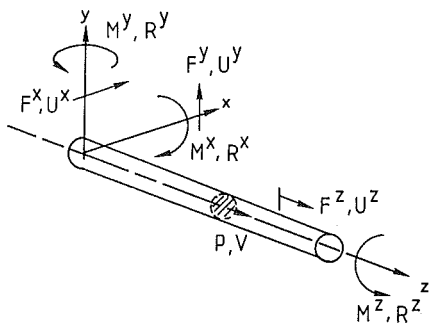

Fig. 1 Pipe element

Contributed by the Fluids Engineering Division for publication in the JOURNAL OF FLUIDS ENGINEERING. Manuscript received by the Fluids Engineering Division October 1, 1985.

1) Torsion in the pipe wall:

$$M_z^z - \rho_p J R_t^z = 0 \tag{1}$$

$$M_t^z - GJ R_z^z = 0 \tag{2}$$

2) Shear and bending in the y-z plane [9]:

$$M_z^x - (\rho_p I_p + \rho_f I_f) R_t^x - F^y = 0 \tag{3}$$

$$M_t^x - EI_p R_z^x = 0 \tag{4}$$

$$F_z^y - (\rho_p A_p + \rho_f A_f) U_t^y = 0 \tag{5}$$

$$F_t^y - GA_p (U_z^y + R^x) = 0 \tag{6}$$

3) Shear and bending in the x-z plane [9]:

$$M_z^y - (\rho_p I_p + \rho_f I_f) R_t^y + F^x = 0 \tag{7}$$

$$M_t^y - EI_p R_z^y = 0 \tag{8}$$

$$F_z^x - (\rho_p A_p + \rho_f A_f) U_t^x = 0 \tag{9}$$

$$F_t^x - GA_p (U_z^x - R^y) = 0 \tag{10}$$

4) Axial stress, pressure and velocities [1]:

$$P_z + \rho_f V_t = 0 \tag{11}$$

$$P_t + K^* V_z - 2\nu K^* U_z^z = 0; \quad K^* = \frac{\mathrm{K}}{1 + \dfrac{2rK}{eE}(1-\nu^2)} \tag{12}$$

$$F_z^z - A_p \rho_p U_t^z = 0 \tag{13}$$

$$F_t^z - A_p E U_z^z - \frac{r\nu A_p}{e} P_t = 0 \tag{14}$$

The formulations are based on assumptions of linear elasticity, no buckling, cylindrical pipes, negligible radial inertia, and low Mach number, i.e., small liquid velocity relative to acoustic velocity. Furthermore, it is understood that instantaneous pressures will remain above vapor pressure, so that no cavitation will occur, and that high-frequency lobar modes of the pipe are not excited by the dynamic interaction of the fluid and structure.

Numerical Model

Characteristic Equations. Equations (1)–(14) are hyperbolic partial differential equations and can be converted to ordinary differential equations by the method of characteristics transformation [10]. The method has been applied to Timoshenko beam theory by Leonard and Budiansky [11], and to axial coupled behavior for liquid-filled pipe by Otwell, Wiggert and Hatfield [1]. The complete set of characteristic and compatibility equations corresponding to equations (1)–(14) is given below. Equations 20 and 21 have been simplified by assuming that

$$\nu^2 << \frac{e}{2r}\left(\frac{E}{K^*} + \frac{\rho_p}{\rho_f}\right).$$

$$\frac{dM^z}{dt} - a\rho_p J \frac{dR^z}{dt} = 0 \tag{15a}$$

$$\frac{dz}{dt} = a = \pm\sqrt{G/\rho_p} \tag{15b}$$

$$\frac{dM^x}{dt} - a(\rho_p I_p + \rho_f I_f)\frac{dR^x}{dt} - aF^y = 0 \tag{16a}$$

$$\frac{dz}{dt} = a = \pm\sqrt{\frac{EI_p}{\rho_p I_p + \rho_f I_f}} \tag{16b}$$

$$\frac{dF^y}{dt} - a(\rho_p A_p + \rho_f A_f)\frac{dU^y}{dt} - GA_p R^x = 0 \tag{17a}$$

$$\frac{dz}{dt} = a = \pm\sqrt{\frac{GA_p}{\rho_p A_p + \rho_f A_f}} \tag{17b}$$

$$\frac{dM^y}{dt} - a(\rho_p I_p + \rho_f I_f)\frac{dR^y}{dt} + aF^x = 0 \tag{18a}$$

$$\frac{dz}{dt} = a = \pm\sqrt{\frac{EI_p}{\rho_p I_p + \rho_f I_f}} \tag{18b}$$

$$\frac{dF^x}{dt} - a(\rho_p A_p + \rho_f A_f)\frac{dU^x}{dt} + GA_p R^y = 0 \tag{19a}$$

$$\frac{dz}{dt} = a = \pm\sqrt{\frac{GA_p}{\rho_p A_p + \rho_f A_f}} \tag{19b}$$

$$\frac{dF^z}{dt} - a\rho_p A_p \frac{dU^z}{dt} - 2\nu A_f \frac{dP}{dt} = 0 \tag{20a}$$

$$\frac{dz}{dt} = a = \pm\sqrt{E/\rho_p} \tag{20b}$$

$$\frac{dV}{dt} + \frac{a}{K^*}\frac{dP}{dt} + \frac{2\rho_p \nu}{\rho_f\left(\dfrac{E}{K^*} - \dfrac{\rho_p}{\rho_f}\right)}\frac{dU^z}{dt} - \frac{2a\nu}{K^* A_p\left(\dfrac{E}{K^*} - \dfrac{\rho_p}{\rho_f}\right)}\frac{dF^z}{dt} = 0 \tag{21a}$$

$$\frac{dz}{dt} = a = \pm\sqrt{K^*/\rho_f} \tag{21b}$$

Nomenclature

A = cross-sectional area
a = wave speed
B = coefficients for equation (22)
E = modulus of elasticity
e = thickness of pipe wall
F = force
G = shear modulus of rigidity
H = constant terms for equation (22)
I = moment of inertia
J = polar moment of inertia
K = bulk modulus of elasticity
M = moment
n = number of pipes meeting at junction
P = pressure
R = rotational velocity
r = radius of pipe cross-section
T = direction cosines
U = velocity of pipe
V = velocity of liquid
ρ = mass density
ν = Poisson's ratio

Superscripts

x,y,z = principal directions
T = matrix transposition

Subscripts

f = fluid
j = junction quantities in global coordinates
p = pipe
t = partial derivative with respect to time
z = partial derivative with respect to axial direction.

Note that distributed coupling takes place between shear and bending parameters in the compatibility relations equations (16*a*) and (17*a*), and equations (18*a*) and (19*a*). An additional coupling occurs between the axial pipe stress and velocity and the liquid pressure in Equations (20*a*) and (21*a*).

Boundary Conditions and Solution of System Equations. At the end of a given pipe element only one compatibility equation for a companion pair of variables is available for each adjoining pipe element. An additional equation in the form of a boundary condition is required. For example, in Fig. 2, equation (15) is available along the positive characteristic for computation of the torque M^z and the rotational velocity R^z. If the end of the element is fixed against twist, the boundary condition will be $R^z = 0$.

A junction is a point where several pipe ends are connected so that flow, forces and moments can be transmitted from pipe to pipe; the junction has no length or mass. At the junction of n prismatic pipes, $7(2n+1)$ equations can be formed which relate the continuity and equilibrium of the various displacements, pressures, forces and moments in the connecting pipes at the junction. These relations are combined with the finite difference approximations derived from equations (15)-(21), and by successive substitution a matrix equation with seven unknowns is developed:

$$\begin{Bmatrix} V_j \\ \{F_j\} \\ \{M_j\} \end{Bmatrix} = \sum_n \pm [T]^T [B][T] \begin{Bmatrix} P_j \\ \{U_j\} \\ \{R_j\} \end{Bmatrix} + \sum_n \pm [T]^T \{H\} \tag{22}$$

The vector $\{H\}$ contains known quantities, including forces, moments, pressures and velocities for previous times. The contents of $[B]$ are material properties and geometrical information that are time invariant. At a junction, either velocity V_j or pressure P_j will be known and the other quantity unknown. Similarly, unknown external forces F_j and moments M_j, that is reactions, will correspond to known translation and rotational velocities. Equation (22) may be partitioned and solved by inverting a portion of $\Sigma[T]^T[B][T]$. Inversion is performed only once for each junction, and is not required at each time step.

The method of characteristics formulation provides three useful features: 1) the Poisson coupling (of equations (20) and (21)) is represented; 2) nonlinearities such as fluid friction and material damping can be represented by additional terms in the compatibility equations; and 3) nonlinear boundary conditions such as pump trip, column separation, and external viscous or viscoelastic damping of pipe supports can be incorporated.

In the developed numerical scheme, pipe segments may be subdivided into smaller reaches if necessary. Equation (22) is applied at every junction and boundary location. The five characteristic lines identified with each pipe reach are projected back in time to an opposite junction, and time-line interpolations are utilized to obtain numerical values of the required parameters. With this scheme, two sources of error have been identified: numerical attenuation and phase changes due to the time-line interpolations [12], and inexact integration of the nondifferential shear and bending terms in the compatibility relations, Equations (16)-(19).

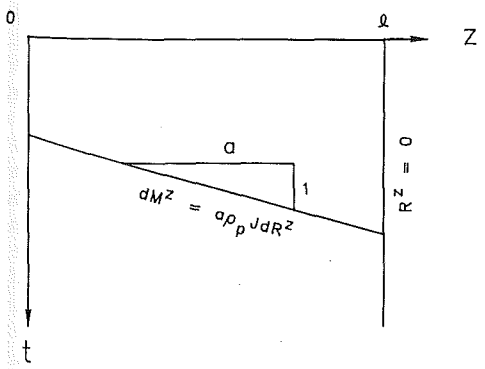

Fig. 2 Boundary condition with characteristics grid

Application

The formulation is demonstrated for a system of three pipes directed orthogonally and connected in series as shown in Fig. 3. The piping is made of copper with mitered bends and an inside diameter of 25 mm; each reach is 2 m long. The conveyed liquid is water, and damping is neglected in the fluid as well as in the pipe structure. The upstream end of the piping (location A) is restrained from motion and connects to a reservoir with static pressure. The piping is constrained at the downstream end (location D) by connection to a valve. The system is excited by closure of the valve; initially the velocity is 1.0 m/s and subsequently the velocity decreases linearly to zero in approximately 2.2 ms. It is assumed that the static pressure is of sufficient magnitude that dynamic pressures will not reach vapor pressure.

Figures 4 through 6 are calculated responses to the valve closure excitation. In the figures, only the dynamic components are shown; total pressures, forces and moments may be computed as the sum of steady-state – that is, static – and dynamic components. The maximum permissible time incre-

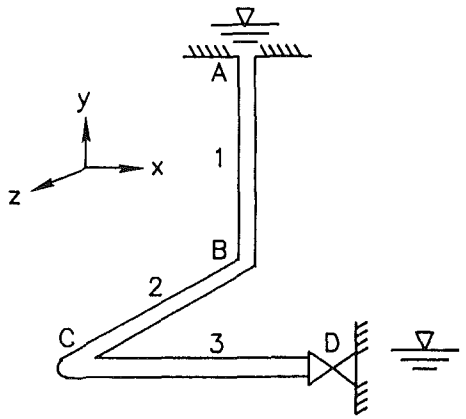

Fig. 3 Example piping

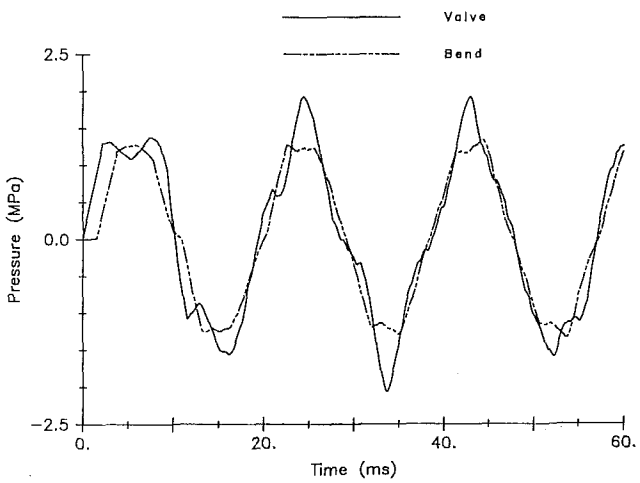

Fig. 4 Fluid pressures at bend (location C) and valve (location D)

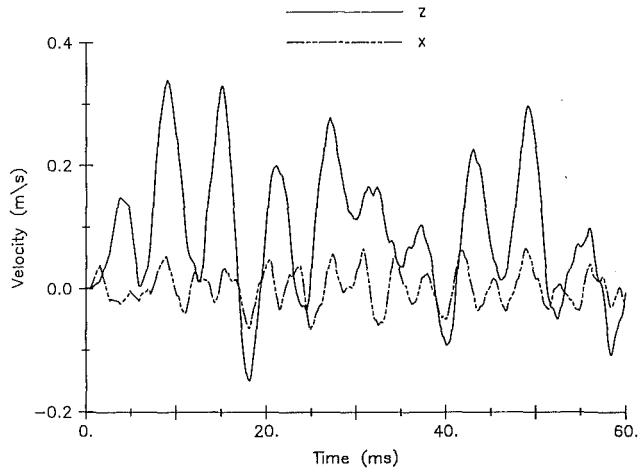

Fig. 5 Pipe velocities in x and z directions at bend (location C)

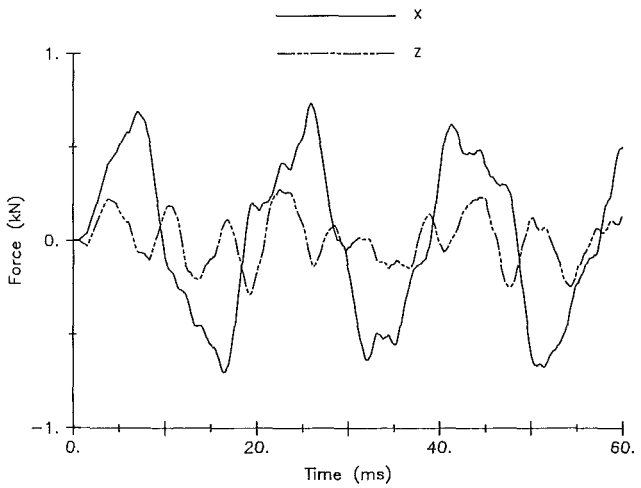

Fig. 6 Forces in x and z directions in pipe 3 at bend (location C)

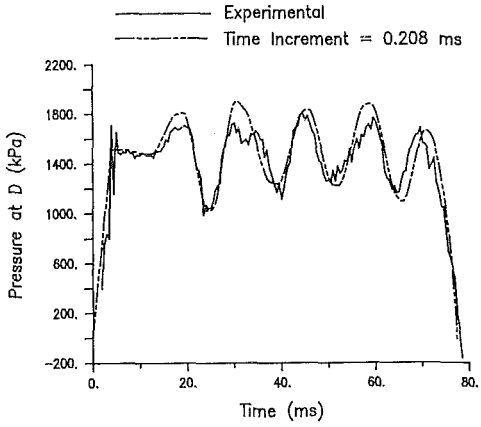

Fig. 7 Predicted and experimental fluid pressure at valve (location D)

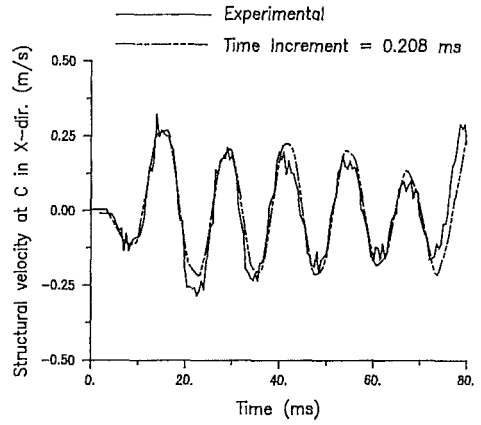

Fig. 8 Predicted and experimental structural velocity at bend (location C)

ment is computed as the pipe element length divided by the largest wave speed, i.e., 0.55 ms.

The effects of Poisson and junction coupling are apparent in Figs. 4 and 5. When the valve begins to close, the pressure at D increases causing the pipe to dilate. Because of the Poisson effect, the dilation generates an axial force. This force propagates through the pipe wall and reaches the bend at location C at the end of the first time interval, causing the bend to accelerate in the positive x-direction. Because of junction coupling, this motion causes as pressure rise at C, as well as motion in the positive z-direction. Pressure waves travel 2 m in three time intervals. In response to the primary pressure pulse, the motion of C in the x-direction reverses at the end of the third time interval. At the end of the fourth interval, the secondary pressure induced by the motion of bend C reaches location D, causing the pressure there to continue to rise after the valve is completely closed. Figure 6 illustrates the axial force and transverse shear force in the z-direction for the end of pipe 3 at junction C.

A second configuration of the piping shown in Fig. 3 is used to simulate the laboratory experiment described in Wiggert et al. [1]. Elbow B is constrained from motion and elbow C is free to move in the x-z plane. Pipe segments 1, 2 and 3 are respectively 28.0 m, 7.6 m, and 12.3 m in length. Significant structural motion is to be expected in segments 2 and 3. Predicted pressure at location D and predicted structural velocity in the x-direction at location C are presented along with experimental data in Figs. 7 and 8, respectively. For the computation, the piping was divided into seven links: five for segment 1, one each for segments 2 and 3. A time increment of 0.2081 ms was employed.

The numerical model can be seen to predict the motion and pressure in an acceptable fashion. However, no significant shear and bending moments were developed in the experiment, so that the numerical model is not severely taxed with regard to accurately predicting those parameters.

Summary and Conclusions

Because piping systems are composed primarily of slender components, transient responses may be represented by one-dimensional wave phenomena. Seven wave components must be considered: pressure in the liquid; and in the pipe material, axial compression, torsional shear, transverse shear in two orthogonal directions, and bending about the two transverse axes. For linearly elastic pipe material, torsion and transverse shear are not coupled, nor are bending and axial compression. The phenomenon of axial compression of liquid and pipe material consists of two distinct but coupled waves. Timoshenko beam theory [9] describes the interaction of transverse shear and bending of the pipe elements. The various independent wave mechanisms are coupled at pipe junctions.

Propagation of the waves along a straight pipe may be described by finite difference equations derived from the method of characteristics. The combined system of difference equations for pipe elements and the junction boundary conditions comprise a general mathematical tool for predicting the liquid pressure and pipe stress responses to transient excitation

of either liquid or piping. Two possible sources of error in the numerical solution scheme have been identified; additional development is necessary before the model can be used for application to practical piping systems. Numerical examples are presented which do not predict significant shear and bending, and hence pose no problem numerically, but otherwise demonstrate relevant structural motion along with transient pressures and velocities in the contained liquid. Experimental data is used to partially verify the wave model.

Acknowledgment

This work has been supported in part by the National Science Foundation through Grant MEA-8401339. Mr. Marlio Lesmez helped with computations and graphics.

References

1 Wiggert, D. C., Otwell, R. S., and Hatfield, F. J., "The Effect of Elbow Restraints on Pressure Transients," ASME JOURNAL OF FLUIDS ENGINEERING, Vol. 107, No. 3, Sept. 1985.

2 Skalak, R., "An Extension of the Theory of Water Hammer," *Trans. ASME*, Vol. 78, No. 1, 1956.

3 Thorley, A. R. D., "Pressure Transients in Hydraulic Pipelines," ASME *Journal of Basic Engineering*, Vol. 91, Sept. 1969.

4 Williams, D. J., "Waterhammer in Non-Rigid Pipes: Precursor Waves and Mechanical Damping," *Journal of Mechanical Engineering Science*, Vol. 19, No. 6, Institute of Mechanical Engineers, 1977.

5 Walker, J. S., and Phillips, J. W., "Pulse Propagation in Fluid Filled Tubes," ASME *Journal of Applied Mechanics*, Mar. 1977.

6 Wilkinson, D. H., "Acoustic and Mechanical Vibrations in Liquid Filled Pipework Systems," *Proceedings of the Vibration in Nuclear Plant Conference*, British Nuclear Engineering Society, May 1978.

7 Wilkinson, D. H., and Curtis, E. M., "Water Hammer in a Thin-Walled Pipe," *Proceedings 3rd International Conference on Pressure Surges*, Vol. 1, British Hydromechanics Research Association, Mar. 1980.

8 Ellis, J., "A Study of Pipe-Liquid Interaction Following Pump Trip and Check-Valve Closure in a Pumping Station," *Proceedings 3rd International Conference on Pressure Surges*, Vol. 1, British Hydromechanics Research Association, Mar. 1980.

9 Timoshenko, S., and Young, D. H., *Vibration Problems in Engineering*, 3rd ed., D. Van Nostrand Company, New York.

10 Forsythe, G. E., and Wasow, W. R., *Finite-Difference Methods for Partial Differential Equations*, Wiley, New York, 1960.

11 Leonard, R. W., and Budiansky, B., "On Traveling Waves in Beams," National Advisory Committee for Aeronautics, Report 1173, 1955.

12 Goldberg, D. E., and Wylie, E. B., "Characteristics Method Using Time-Line Interpolations," *Journal of Hydraulic Engineering*, Vol. 109, No. 5, American Society of Civil Engineers, May, 1983.

Incompressible Laminar Flow Past a Transversely Vibrating Cylinder

R. Chilukuri
Senior Scientist,
JAYCOR,
San Diego, Calif. 92121

An implicit finite difference scheme in primitive variables is used for analysis of unsteady, laminar flow past transversely vibrating cylinders. Predictions of flow past an impulsively started cylinder and of vortex shedding from a stationary cylinder agree well with experimental data. Calculations of flow past a transversely vibrating cylinder were within the range of experimental scatter only for small vibration amplitudes. Several experimentally observed phenomena such as drag amplification and reduction in excitation lift coefficient at large vibration amplitudes were numerically predicted.

1 Introduction

Vortex shedding in flow past an isolated cylinder undergoing forced vibrations has been extensively studied as a first step towards understanding the behavior of more complex systems. The influence of cylinder vibration amplitude and frequency on the wake and on the forces experienced by the cylinder has been experimentally established [1, 2].

A computer program for prediction of flow past vibrating structures would be invaluable in engineering design. Accordingly, earlier investigators [3–7] have developed numerical models for laminar flow past a vibrating cylinder. Earlier studies used the vorticity-stream function formulation [except [3,7]] and have generally been confined to small amplitude cylinder vibration.

This paper presents finite difference predictions of flow past a vibrating cylinder. Primitive variables were used to permit future study of turbulent flows. The computer program was validated against experiments on flow past an impulsively started cylinder and flow past a stationary cylinder. Calculations of lift and drag forces experienced by a vibrating cylinder were made for several Reynolds numbers and for large vibration amplitudes.

2 Problem Formulation

Incompressible laminar flow past a cylinder undergoing transverse harmonic vibrations is considered as shown in Fig. 1. The governing Navier-Stokes equations are transformed to an accelerating frame of reference that is fixed relative to the vibrating cylinder. In the interest of brevity, only the transformed radial momentum equation is presented below. An analogous equation may be derived for angular velocity.

Radial Momentum Equation

$$\frac{\partial u}{\partial t}+\frac{1}{r}\frac{\partial (ru^2)}{\partial r}+\frac{1}{r}\frac{\partial (uv)}{\partial \theta}=-\frac{\partial \phi}{\partial r}+\frac{v^2}{r}$$

$$+\frac{1}{\mathrm{Re}}\left\{\frac{1}{r^2}\frac{\partial}{\partial r}\left[r\frac{\partial (ru)}{\partial r}\right]+\frac{1}{r^2}\frac{\partial^2 u}{\partial \theta^2}\right\}+R \qquad (1)$$

R is an acceleration term arising from the noninertial transformation from a stationary frame of reference to a frame that moves with the vibrating cylinder. For the case of transverse, harmonic cylinder vibrations, we have

$$y=A\sin(2\pi \text{ ft}) \text{ and } R=-\frac{d^2y}{dt^2}\sin\theta. \qquad (2)$$

3 Numerical Method

The overall solution scheme closely follows the well known Simplified Marker And Cell (SMAC) method [8]. The particular finite difference approximations used in the present study minimize artificial diffusion and allow large time steps (implicit scheme). Centered space differences were employed to approximate spatial derivatives. The trapezoidal rule was employed for advancing the solution in time. This scheme will hereafter be referred to as "Time-Averaged Central-Space" (TACS). For the case of a simple, one-dimensional, unsteady advection-diffusion equation, TACS differencing is stable at all Courant numbers, is second order accurate, and introduces no artificial diffusion. Though Von Neumann stability

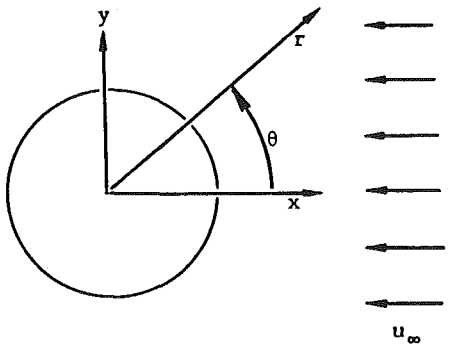

Fig. 1 Coordinate system and flow geometry

Contributed by the Fluids Engineering Division and presented at the Winter Annual Meeting, Anaheim, Calif., December 7–12, 1986 of The American Society of Mechanical Engineers. Manuscript received by the Fluids Engineering Division March 26, 1986. Paper No. 86-WA/FE-8.

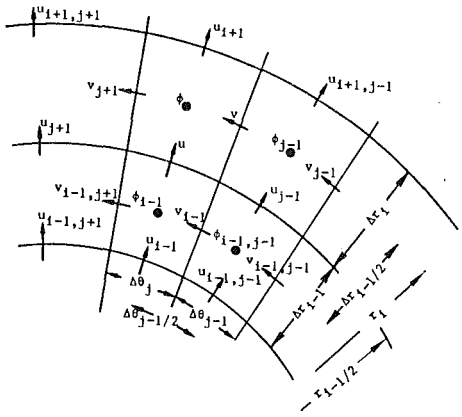

Fig. 2 Staggered mesh notation. Subscripts i and j are not explicitly specified. Thus $u_{j-1} = u_{i,j-1}$ and $\phi_{i-1} = \phi_{i-1,j}$

analysis indicates unconditional stability, loss of diagonal dominance for large Courant numbers $[(u_0\Delta t)/\Delta x > 2]$ will prevent accurate solution of the algebraic equations.

The finite difference approximation to the radial momentum equation is presented below [9]. An analogous equation can be derived for angular velocity. Figure 2 shows the staggered placement of dependent variables on the mesh.

Radial Momentum Equation

$$\frac{\tilde{u}^{n+1}-u^n}{\Delta t} + \frac{(r_{i+1/2}u_{i+1}+r_{i-1/2}u)^a(u_{i+1}+u)^{n+1/2}-(r_{i-1/2}u+r_{i-3/2}u_{i-1})^a(u+u_{i-1})^{n+1/2}}{4r_{i-1/2}\Delta r_{i-1/2}}$$

$$+\frac{(v_{j+1}+v_{i-1,j+1})^a(u_{j+1}+u)^{n+1/2}-(v+v_{i-1})^a(u+u_{j-1})^{n+1/2}}{4r_{i-1/2}\Delta\theta_j}$$

$$=-\frac{\phi^n-\phi^n_{i-1}}{\Delta r_{i-1/2}}+\frac{1}{4\Delta r_{i-1/2}}\left\{\frac{\Delta r_i}{r_i}[v^2+v^2_{j+1}]^a+\frac{\Delta r_{i-1}}{r_{i-1}}[v^2_{i-1,j+1}+v^2_{i-1}]^a\right\} \qquad (3)$$

$$+\frac{1}{\mathrm{Re}}\left\{\frac{1}{r^2_{i-1/2}\Delta r_{i-1/2}}\left[\frac{r_i(r_{i+1/2}u_{i+1}-r_{i-1/2}u)}{\Delta r_i}-\frac{r_{i-1}(r_{i-1/2}u-r_{i-3/2}u_{i-1})}{\Delta r_{i-1}}\right]^{n+1/2}\right.$$

$$\left.+\frac{1}{r^2_{i-1/2}\Delta\theta_j}\left[\frac{u_{i,j+1}-u}{\Delta\theta_{j+1/2}}-\frac{u-u_{j-1}}{\Delta\theta_{j-1/2}}\right]^{n+1/2}\right\}-[\ddot{y}\sin(\theta_j)]^{n+1/2}$$

The superscript "$n+1/2$" in the above equation refers to the average between known values at time n and unknown values at time $n+1$. Thus each of the momentum equations yields algebraic equations for the unknowns $\tilde{u}^{n+1}$ and $\tilde{v}^{n+1}$. The resulting two equation sets were sequentially solved using a standard ADI scheme.

Nonlinear advection terms were linearized by using the best available estimates for the coefficients. Thus, the superscript "a" in the finite different momentum equations refers to the average of the value at time n and the best available estimate for the value at $n+1$. Iteration within a time step is required to update the nonlinear advection term coefficients. Upon convergence of iterations within a time step, $u^a = u^{n+1/2} = 0.5*(u^n + u^{n+1})$, etc. Iteration was not required in the present study because of the small time steps used (Courant number <2).

The solution procedure consists of solving the finite difference momentum equations for tentative velocities $\tilde{u}^{n+1}$ and $\tilde{v}^{n+1}$. Then the tentative velocities and pressure are corrected using the SMAC procedure [8]. The algebraic equations that approximate the Poisson equation for pressure correction were solved using Cholesky's scheme for symmetric, positive definite matrices.

4 Boundary Conditions and Mesh Details

Noninertial transformation of the governing equations to a reference frame that is fixed relative to the vibrating cylinder

Nomenclature (asterisks indicate dimensional quantities)

A = nondimensional vibration amplitude; A^*/D
C_D = drag coefficient; drag force per unit length of cylinder nondimensionalized by $1/2(\rho u_0^2 D)$. Depending on the context, C_D may be instantaneous or time averaged
C_{D0} = time averaged drag coefficient for a stationary cylinder
C_L = lift coefficient; lift force per unit length of cylinder nondimensionalized by $1/2\ (\rho u_0^2 D)$
C_{LE} = excitation lift coefficient; see equation (5)
D = cylinder diameter; m
E = nondimensional energy transferred to cylinder; see equation (4)
f = nondimensional frequency of cylinder vibration; f^*D/u_0
f_s = nondimensional frequency of vortex shedding from a stationary cylinder; f_s^*D/u_0
p = pressure; N/m^2
P = nondimensional power transmitted to cylinder; $C_L\dot{y}$
r = nondimensional radial coordinate; r^*/D
Re = Reynolds number; u_0D/ν
St = Strouhal number; same as f_s
t = nondimensional time; t^*u_0/D
u = nondimensional radial velocity; u^*/u_0
u_∞, u_0 = freestream velocity; m/s
v = nondimensional angular velocity; v^*/u_0
V = nondimensional cylinder velocity; same as $\dot{y}$
V_r = reduced velocity; $1/f$
W_r = wake response parameter; $[1+2(A^*/D)]/(\mathrm{St}\,V_r)$
$y, \dot{y}, \ddot{y}$ = nondimensional cylinder displacement, velocity and acceleration, respectively; $y = y^*/D$

Special Symbols

ν = kinematic viscosity; m^2/s
ϕ = nondimensional reduced pressure; $p/\rho u_0^2$
ρ = density; kg/m^3
θ = angular coordinate; radians

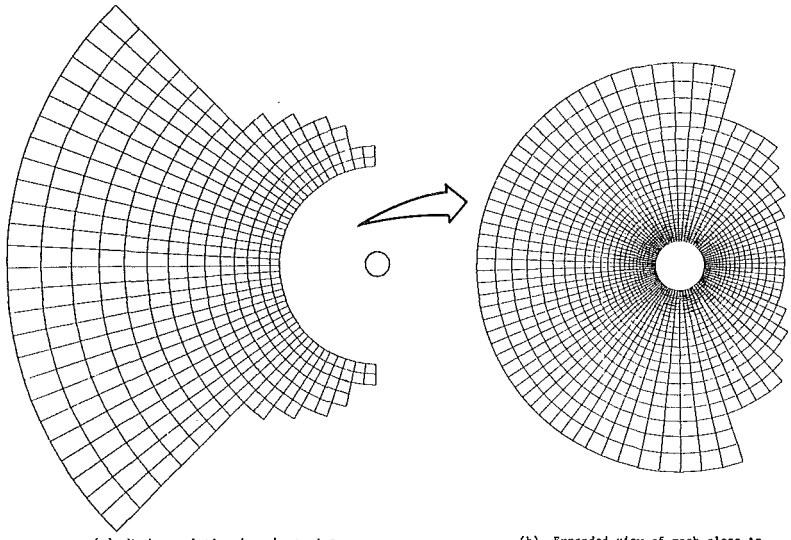

Fig. 3 Discretization of flow field grid #1. Computational costs were reduced by curtailing mesh in upstream and transverse directions. See text for description of grid #2.

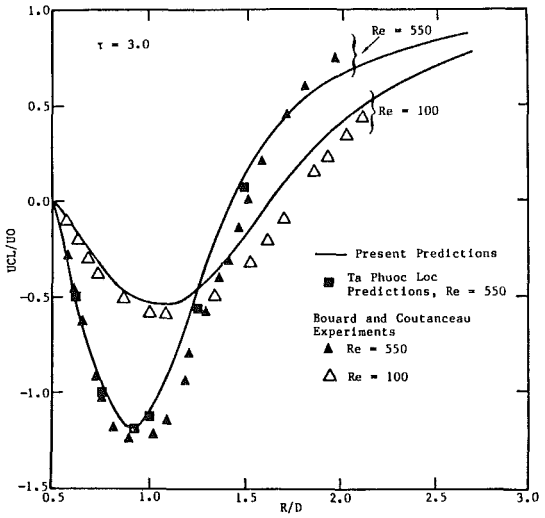

Fig. 4 Streamwise velocity along wake centerline at $t = 3.0$, impulsively started cylinder, grid #1

simplifies specification of boundary conditions at the cylinder surface. No-slip, no-blowing conditions are enforced at the cylinder surface by setting normal and tangential (transformed) velocities to zero.

Far from the cylinder (upstream and in transverse direction), the analytical solution for potential flow past a cylinder is enforced. The potential-flow, far-field velocity boundary conditions are time dependent when specified in a reference frame that moves with the vibrating cylinder. The location of the outer boundaries is an important part of the boundary condition specification and is discussed below.

Downstream boundary conditions are always difficult to specify. In the present study, pressure and radial gradients of transformed velocities at the downstream boundary were set to zero. The weak influence of downstream boundary conditions on the flow field was verified by changing the location of the downstream boundary relative to the cylinder.

Four finite difference grids were employed in the present study. Grids #1 and #2 were used in most of the calculations. Grid #3 and #4 were used for mesh refinement tests.

Grid #1 (Fig. 3) has 80 circumferential cells and 40 radial cells. The minimum radial size was 0.025 * D. The outer boundaries form an approximate rectangle with all "active" mesh cells located close to the cylinder surface and in the wake. Thus, regions of near-uniform flow are eliminated from the computation, with the intention of minimizing computational costs. As discussed in the results section, vortex shedding calculations made using grid #1 were found to suffer from significant lateral confinement errors.

Grid #2 has outer boundaries that are located much further away from the cylinder than in grid #1. Grid #2 has 80 circumferential cells and 53 radial cells. Constant mesh spacing is used in the circumferential direction. Variable spacing is employed in the radial direction, with minimum mesh size of 0.0375 * D just adjacent to the cylinder. The radial distance from the cylinder surface to the outer boundary is about 50 * D.

Grid #3 differs from Grid #2 in radial cell spacing. Grid #3 has 80 radial cells, with a minimum radial mesh size of 0.0335 * D and a radial distance of 90 * D between the cylinder surface and the outer boundary. Grid #4 has identical radial mesh spacings as grid #2, but has 100 equispaced cells in the circumferential direction.

5 Results

5.1 Impulsively Started Cylinder. Transient flow past a cylinder moving with constant speed in a direction perpendicular to its generators following an impulsive start from rest was chosen to test the computer program. This classic problem has recently been revisited by Bouard and Coutanceau [10] and Ta Phuoc Loc [11].

Bouard and Coutanceau visualized the flow and measured wake velocity development for Reynolds numbers ranging from 40 to 10,000. They differentiate three regimes according to whether Re is below 60, between 60 and 500, or above 500. For $Re < 60$ and at early times, the wake consists of twin (primary) eddies. For $Re > 60$, they discovered several secondary phenomena, including the formation of secondary eddies encapsulated within the primary eddies. At large enough time, and for $Re > 40$, the wake becomes unstable and vortices are shed from the cylinder.

Figure 4 shows present predictions, obtained using grid #1, for wake-centerline velocity profiles at Reynolds numbers of

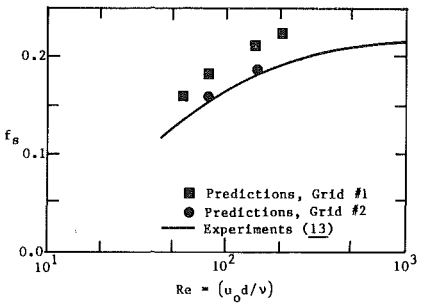

Fig. 5(a) Strouhal number

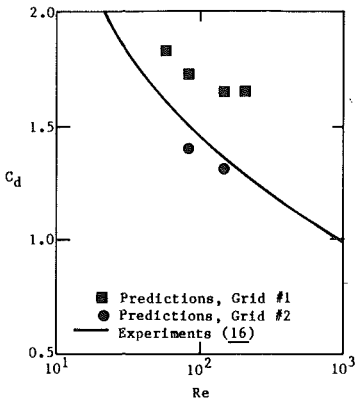

Fig. 5(b) Drag coefficient

Fig. 5 Strouhal number and drag coefficient as a function of Reynolds number for flow past a stationary cylinder. The large discrepancies observed with grid #1 calculations are attributed to lateral confinement errors.

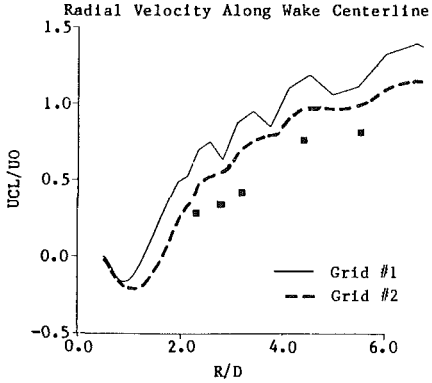

Fig. 6 Comparison of predicted mean streamwise velocity along wake centerline with experimental data (12); Re = 144; stationary cylinder

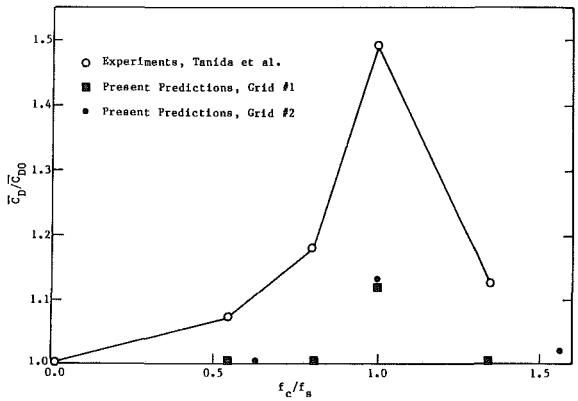

Fig. 7 Amplification of mean drag during "lock-in," Re = 80, A = 0.14

100 and 550 and at nondimensional time $t = 3$. The present predictions of wake centerline velocity profile appear to be shifted upstream relative to experimental measurements. The maximum shift is about 0.08 D at Re = 550 and about 0.11 D at Re = 100. Similar agreement was also obtained at Re = 60, 200, and 1000, but these additional results will not be displayed here in the interest of brevity.

Ta Phuoc Loc's [11, 12] numerical predictions used the vorticity-stream function approach and fourth order accurate compact differences. The excellent agreement obtained between Ta Phuoc Loc's results and the present predictions establishes the accuracy and computer implementation of the present second order accurate primitive variables approach. In addition, the mesh resolution and distance of boundaries from the cylinder (grid #1) appears to be adequate, at least for early times after cylinder startup.

5.2 Vortex Shedding From an Isolated, Stationary Cylinder. Vortex shedding from a stationary cylinder was examined at four Reynolds numbers (Re = 60, 80, 144, and 200) as a precursor to studying cylinder vibration. Figure 5 shows the predicted Stouhal number and drag as a function of Reynolds number.

Calculations made with grid #1 predict Strouhal numbers that are about 19 percent higher than Kovasnay's data [13] and drag coefficients that are about 16 percent higher than Wieselberger's data as presented by Roshko [14]. Increased Strouhal numbers and drag coefficients are generally attributed to lateral confinement errors [15]. Hence vortex shedding calculations were repeated at Re = 80 and 144 using grid #2 and good agreement was obtained with experimental data.

Figure 6 compares present predictions of time-averaged streamwise velocities along the wake centerline against the measurements of Griffin and Votaw [16] for Re = 144. Again, much better agreement with experiments is observed with grid #2 than with grid #1.

5.3 Vortex Shedding From a Transversely Vibrating Cylinder. Several earlier studies have established that as the frequency of vibration of the cylinder approaches the natural vortex shedding frequency, a phenomenon known as "lock-in" occurs. During lock-in, vortices are forcibly shed at the cylinder vibration frequency. The conditions for lock-in and the existence of a minimum threshold vibration amplitude have been experimentally determined by Koopman [17].

Figure 7 shows the amplification of mean drag that occurs when the cylinder vibration frequency approaches the Strouhal frequency (i.e., during "lock-in"). The ratio of drag coefficient to stationary cylinder drag coefficient is used along the ordinate of Fig. 7 rather than the drag coefficient itself in order to remove a systematic error (due to confinement effects) in grid #1 calculations. Similar reasoning applies to the abscissa. The calculations at Re = 80 and $A = 0.14$ predict lower drag amplification than measured in the experiments of Tanida et al. [18]. Grids #1 and #2 yield almost identical results.

Figure 8 shows drag amplification as a function of vibration amplitude. The experimental data shown in Fig. 8 was compiled by Griffin [1] and includes both laminar and turbulent flow conditions. Again, present predictions using both grid #1 and grid #2 significantly underestimate the drag amplification. However, present results agree well with the calculations of Hurlbut and Spaulding [7].

Aeroelastic stability was investigated by examining nondimensional power transmission and cumulative energy transfer from the fluid to the cylinder. Power and energy transfer are defined as follows:

$$\text{Power} = P(t) = C_L(t)\dot{y}(t) \tag{4}$$

$$\text{Energy transfer} = E(t) = \int_{t_0}^{t} P(t)dt.$$

Figures 9 and 10 show the effect of vibration amplitude on cylinder stability for Re = 144. The frequency of vibration was chosen to match the Strouhal frequency predicted by the code for Re = 144, thus ensuring lock-in.

Figure 9 shows the lift, drag and cumulative energy transfer histories obtained using grid #2, for $A = 0.14$, 0.50, and 1.0. Lift histories are no longer sinusoidal at large vibration amplitudes. Both the mean and fluctuating drag increase with vibration amplitude. Examination of the cumulative energy transfer reveals that the cylinder vibration is unstable at $A = 0.14$, marginally unstable at $A = 0.50$ and stable for $A = 1.0$. Apparently, a critical amplitude exists above which the structural motion is damped by the flow. These results, when interpreted for the case of a spring-mounted cylinder whose natural frequency matches the natural vortex shedding frequency, indicate that the cylinder will extract energy from the flow and vibrate with increasing amplitude until the critical amplitude is reached.

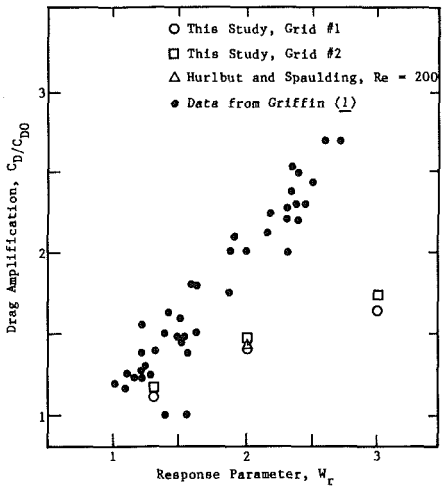

Fig. 8 The drag coefficient amplification, C_D/C_{D0}, plotted as a function of the wake response parameter, $w_r = (1 + 2A^*/D)(\text{St } V_r)^{-1}$, for the crossflow vibrations of a circular cylinder. Data are from Griffin [1]. Present predictions are under "lock-in" conditions with Re = 144 and $f = f_S$.

Figure 10 shows predicted and measured excitation lift coefficient as a function of vibration amplitude. The experimental data shown in Fig. 10 was compiled by Griffin [1] and includes both laminar and turbulent flow data. The predicted excitation lift coefficient was obtained from time averaged power transmission as follows:

$$C_{LE} = \frac{1}{\pi A f}\frac{1}{\tau}\int_{t_0}^{t_0+\tau} P(t)dt. \tag{5}$$

Figures 8-10 show that the predicted (Re = 144, $f = f_s$) effects of vibration amplitude on drag amplification and on excitation lift coefficient are qualitatively correct. However, among the cases studied, numerical calculations are within the range of experimental scatter only for $A = 0.14$.

Figure 11 presents calculated lift coefficient time histories at Re = 144 and $A = 0.5$. The effect of spatial and temporal mesh refinement as well as of increasing the distance between the cylinder and the outer boundary can be seen by comparing the four curves (see Section 4 for grid descriptions). The four lift histories of Fig. 11, when processed to estimate C_{LE}, yield indistinguishable points on Fig. 10.

6 Conclusions

A finite difference scheme in primitive variables for analysis

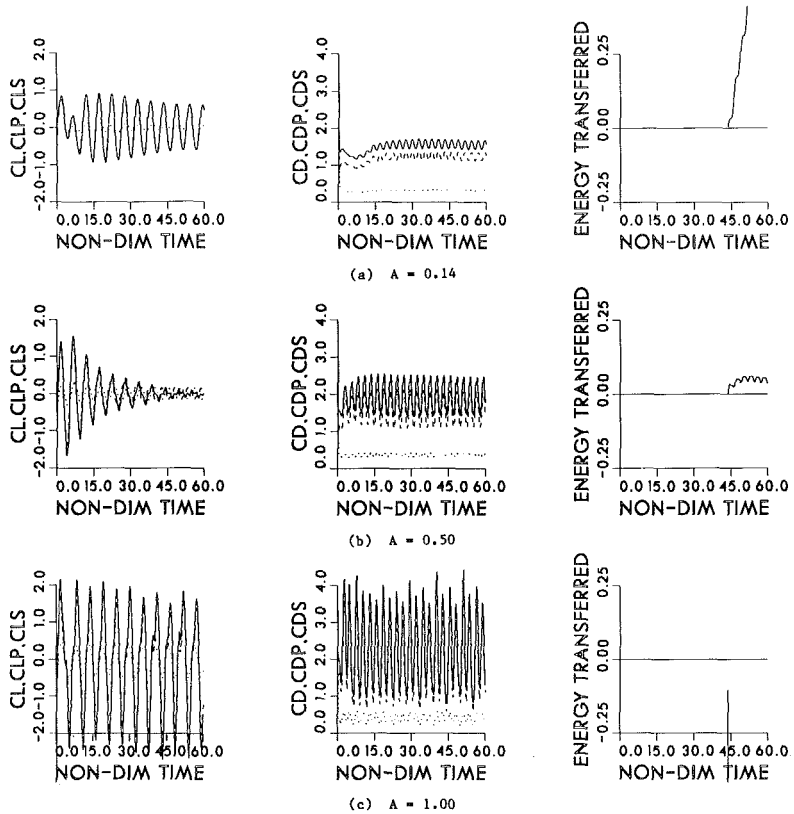

Fig. 9 Predicted lift coefficient, drag coefficient, and cumulative energy transfer to cylinder as a function of vibration amplitude under "lock-in" conditions, Re = 144, $f = 0.185$, grid #2

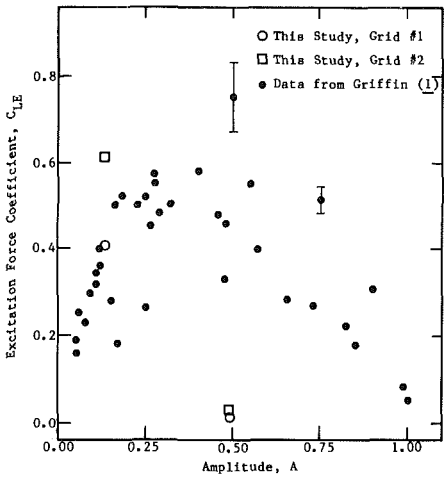

Fig. 10 Predicted and measured excitation lift coefficients as a function of displacement amplitude. Data are from Griffin [1]. Predictions are under "lock-in" conditions with Re = 144 and $f = f_S$.

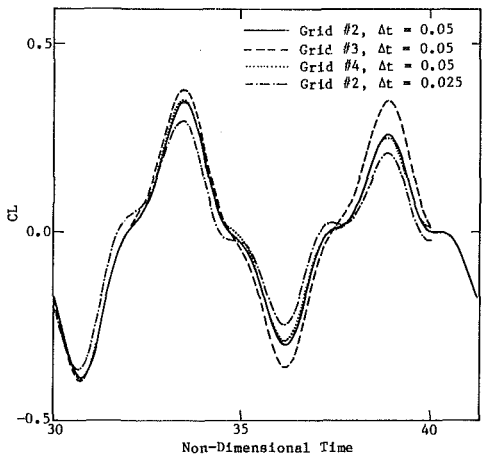

Fig. 11 Effect of spatial and temporal grid refinements on lift coefficient time history, Re = 144, $A = 0.5$. See Section 4 for grid description.

of laminar flow past vibrating cylinders is presented. The finite difference scheme is free of artificial (numerical) viscosity and is stable up to a Courant number of two.

The numerical scheme was applied to flow past an impulsively started cylinder and the predicted, instantaneous streamwise velocity in the wake was found to agree well with experimental data.

Calculations (grid #2) of vortex shedding from a stationary cylinder agreed well with experiments. Discrepancies observed with grid #1 calculations are attributed to lateral confinement errors.

Predictions of flow past a transversely vibrating cylinder agreed well with experimental data at small vibration amplitudes. Drag amplification and reduction in excitation lift coefficient at large vibration amplitudes were numerically predicted.

Acknowledgments

The author is grateful to Dr. James H. Stuhmiller for his encouragement and guidance through the course of this work, to Ms. Patricia Faller for fast and accurate typing in the face of impossible deadlines, and to JAYCOR for generously donating computer facilities. It is a pleasure to acknowledge a timely grant of computer resources by the San Diego Supercomputer Center.

References

1 Griffin, O. M., "Vibrations and Flow-Induced Forces Caused by Vortex Shedding," *Proceedings of the Symposium on Flow-Induced Vibrations*, Vol. 1, ASME Winter Annual Meeting, New Orleans, Dec. 9-14, 1984.

2 Bearman, P. W., "Vortex Shedding from Oscillating Bodies," *Ann. Rev. Fluid Mech.*, Vol. 16, 1984, pp. 195-222.

3 Hurlbut, S. E., Spaulding, M. L., and White, F. M., "Numerical Solution for Laminar Two Dimensional Flow About a Cylinder Oscillating in a Uniform Stream," ASME JOURNAL OF FLUIDS ENGINEERING, Vol. 104, 1982, p. 214.

4 Jordan, S. K., and Fromm, J. E., "Oscillatory Drag, Lift, and Torque on a Circular Cylinder in a Uniform Flow," *Phys. Fluids*, Vol. 15, No. 3, 1972, p. 371.

5 Lecointe, Y., and Piquet, J., "On the Use of Several Compact Methods for the Study of Unsteady Incompressible Viscous Flow Round a Circular Cylinder," *Computers & Fluids*, Vol. 12, No. 4, 1984, pp. 255-280.

6 Mehta, U., "Dynamic Stall of an Oscillating Airfoil," AGARD-CP227, Unsteady Aerodynamics Symposium held at Gov. Conf. Ctr., Ottawa, Canada, Paper No. 23, Sept. 1977.

7 Hurlbut, S. E., and Spaulding, M. L., "Simulation of a Linearly Sprung Rigid Cylinder in Vortex Shedding Flow," Univ. of Rhode Island, Dept. of Ocean Eng. report for Naval Research Laboratory, Dec. 1980.

8 Amsden, A. A., and Harlow, F. H., "The SMAC Method: A Numerical Technique for Calculating Incompressible Fluid Flows," Los Alamos Scientific Laboratory of the University of California, Report LA 4372, 1970.

9 Williams, G. P., "Numerical Integration of the Three-Dimensional Navier-Stokes Equations for Incompressible Flow," *J. Fluid Mech.*, Vol. 37, Part 4, 1969, pp. 727-750.

10 Bouard, R., and Coutanceau, M., "The Early Stage of Development of the Wake Behind an Impulsively Started Cylinder for $40 < Re < 10^4$," *J. Fluid Mech.*, Vol. 101, Part 3, 1980, pp. 583-607.

11 Loc, T. P., "Numerical Analysis of Unsteady Secondary Vortices Generated by an Impulsively Started Circular Cylinder," *J. Fluid Mech.*, Vol. 100, Part 1, 1980, pp. 111-128.

12 Loc, T. P., and Bouard, R., "Numerical Solution of the Early Stage of the Unsteady Viscous Flow Around a Circular Cylinder: A Comparison with Experimental Visualization and Measurements," *J. Fluid Mech.*, Vol. 160, 1985, pp. 93-117.

13 Kovasznay, L. S. G., "Hot-Wire Investigation of the Wake Behind Cylinders at Low Reynolds Numbers," *Proc. Roy. Soc.*, Series A, Vol. 198, 1949, pp. 174-190.

14 Roshko, A., "Experiments on the Flow Past a Circular Cylinder at Very High Reynolds Number," *J. Fluid Mech.*, Vol. 10, 1961, p. 345.

15 Richter, A., and Naudascher, E., "Fluctuating Forces on a Rigid Circular Cylinder in Confined Flow," *J. Fluid Mech.*, Vol. 78, Part 3, 1976, pp. 561-576.

16 Griffin, O. M., and Votaw, C. W., "The Vortex Street in the Wake of a Vibrating Cylinder," *J. Fluid Mech.*, Vol. 51, Part 1, 1972, pp. 31-48.

17 Koopman, G. H., "The Vortex Wakes of Vibrating Cylinders at Low Reynolds Numbers," *J. Fluid Mech.*, Vol. 28, Part 3, 1967, pp. 501-512.

18 Tanida, Y., Okajima, A., and Watanabe, Y., "Stability of a Circular Cylinder Oscillating in Uniform Flow or in a Wake," *J. Fluid Mech.*, Vol. 61, Part 4, 1973, pp. 769-784.

Motion of Particles in Gases: Average Velocity and Pressure Loss

E. E. Michaelides
Department of Mechanical and Aerospace Engineering, University of Delaware, Newark, Dela. 19716

A simplified physical model is developed for the motion of solid particles in gaseous streams confined by walls (channel or pipe flow). The equations of motion for the particle are solved and expressions for the average slip and pressure loss are developed. The pressure loss expression is supplemented with a statistically derived constant from a bank of approximately 1600 data. This pressure loss expression was compared with others, used by designers and was observed that it shows the lowest average error; the resulting standard deviation also compared favorably with that of other expressions used in the past.

1 Introduction

When one examines the field of air-solid flows in a channel he will soon become aware of many experimental projects that resulted to engineering correlations, such as the ones conducted by Rose and coworkers (1957, 1969), Dogin and Lebedev (1969), Pfeffer et al. (1966), Konchesky et al. (1975), Wirth and Molerus (1983). Others have resulted in tables of data (Hinkle, 1953). A few analytical approaches to the subject have appeared (Ozbelge, 1983, Choi and Chung, 1983) which mainly attempt to solve numerically the differential equations governing the flow of solid particles in air. A third type of approach to the subject is the "single-fluid" model advocated by Julian and Dukler (1965) and Michaelides (1984).

While all of the correlation methods have been valuable in the past to designers of pneumatic transport systems, it seems that none of them is universally applicable. Since all are based on a limited set of experimental data, they are pertinent only to a limited number of situations. Another drawback of the correlations is that the statistical analyses used to derive them were not based on any analytical model. Of the dimensionless groups analyzed in the correlations there are clearly some unimportant ones, which may have appeared only because of the statistical methods involved in the correlations. This observation is exemplified in a recent assessment of these correlations (Martin and Michaelides, 1983), where it is evident that even the best regarded correlations have a high standard error (up to 50 percent when compared with experimental data, other than the ones they are derived from).

As regards to the computational approaches to the subject it seems that they are based on adjustable (and still little known) parameters and they are too cumbersome to be used for design. The last observation may be also true for the "single-fluid" models, since the computer programs involved in them are not widely available.

It is believed that correlations will be used by designers for a long time. The correlations may also be improved if they are based on a physical model for the behavior of solid particles in air streams. This model would identify the pertinent parameters and subsequently yield useful expressions for desired design variables such as slip, pressure loss, etc. The results of such a model would have been more meaningful than the mere statistical analysis of a set of data.

The goal of this work is to derive meaningful expressions for the design variables in a pneumatic conveying system. In order to achieve this, a simplified model is developed for the solids flowing in air streams. This model will yield the average solid velocity, slip and other velocity related variables. A further development of it will subsequently yield the excess pressure loss due to the solid particles and ways to determine it. A bank of air-solids flow data will also be used to determine an adjustable constant of the model. Thus, the final expression derived will be the result of an analytical model supplemented with statistical analysis.

2 General Observations

(*a*) When one envisions the flow of a solid particle in an infinite flow field and at the absence of gravity he will come to the conclusion that the velocity of the particle must eventually become equal to the air velocity. This is because there is no other force to resist aerodynamic drag and, hence, the particle will accelerate or decelerate until its velocity is equal to the mainstream velocity. Therefore, no slip will be observed and the flow will reach a steady state.

(*b*) When the flow field is confined by straight walls (channel flow) the particle may collide with them. During each collision (which is necessarily inelastic) the particle loses some of its kinetic energy. As a result it will bounce with lower velocity and will be accelerated by the fluid until it collides again with the wall. In the absence of forces that will drive the particle to the wall (gravity, Magnus, concentration gradients etc.) it is possible for the particle to eventually reach a steady state; then the particle will acquire the same velocity as the gaseous stream and will move parallel to the walls.

(*c*) In the presence of gravity, Magnus forces, concentration gradients or turbulent diffusion forces, the particle will always

Contributed by the Fluids Engineering Division for publication in the JOURNAL OF FLUIDS ENGINEERING. Manuscript received by the Fluids Engineering Division February 27, 1985.

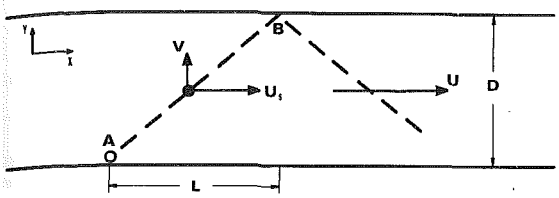

Fig. 1

collide with the confining walls. Its trajectory will be determined by a balance of these forces with aerodynamic forces, and this will lead to frequent collisions with the walls (Owens, 1969). After each collision the particle bounces with a deficit of kinetic energy and, hence, lower velocity in both the longitudinal and transverse direction. Between two collisions the particle will be accelerated by the airstreams in the longitudinal direction. This acceleration of the particle will retard the fluid locally and will manifest itself as an excess pressure loss. Thus, the particle will never attain a steady state but it will be continuously retarded by collisions and accelerated by aerodynamic forces.

One may easily conclude from the above that it is the collisions with the surrounding walls that are the main reason for the particles retardation, slip and excess pressure loss. The particles never attain a steady state and their longitudinal velocity changes between two collisions. The slip of particles experienced in the past (Govier and Aziz, 1969, Richardson and McLeman, 1960) which is an average quantity, may actually be defined as the gas velocity minus the average longitudinal velocity of solids between two collisions. The excess pressure loss experienced is actually the result of aerodynamic forces, which accelerate the particles between their collisions with the wall.

3 The Motion of a Particle in a Gas Stream Confined by Walls

Following the observations of the previous section a model is developed here for the flow of a single particle flowing in a channel. For simplicity it will be assumed that the air stream flows with a constant velocity U, and that the particle is spherical with diameter d. The channel width (diameter if it is circular) is D. This is depicted in Fig. 1 where the particle is shown with longitudinal and transverse velocities U_s and V_s (both of them functions of time). The particle is between two collisions with the confining walls (points A and B) and the longitudinal distance between these collisions is L. The trajectory of the particle between these collisions is not linear in general due to the action of several forces in the vertical direction.

The equation of motion of the particle in the longitudinal direction is:

$$m\frac{dU_s}{dt}=\frac{1}{2}A\rho C_D(U-U_s)|U-U_s|, \tag{1}$$

where ρ is the air density, m is the mass of the particle, A is the maximum cross-sectional area of the particle ($\pi d^2/4$) and C_D is the drag coefficient. If the particle density is ρ_s the above equation can be simplified as follows:

$$\frac{dU_s}{dt}=\frac{3}{4}\frac{\rho}{\rho_s}\frac{C_D}{d}(U-U_s)|U-U_s|. \tag{2}$$

The solution to equation (2) may be easily obtained if a closure equation for the drag coefficient is known. However, C_D is a function of many variables among which are the diameter of the particle and the relative velocity $U-U_s$. For very small particles moving with low relative velocity, C_D is given by the expression:

$$C_D=\frac{24\mu}{d|U-U_s|\rho}, \tag{3}$$

where μ is the dynamic viscosity of the gas. This equation is applicable if the Reynolds number for the particle, $\mathrm{Re}_p = d|U-U_s|\rho/\mu$, is less than 1 and yields the well-known Stokes' drag law:

$$F_D=3\pi\, d|U-U_s|. \tag{4}$$

If the Reynolds number of the particle is higher than 1 but less than 800 (most fine and medium sized particles are in this range) then C_D is better given by Allen's expression (Govier and Aziz, 1969):

$$C_D=30\left(\frac{d\rho|U-U_s|}{\mu}\right)^{-0.625}. \tag{5}$$

Coarse particles with Re_p higher than 800 exhibit constant drag coefficient according to Newton's law:

$$C_D=0.44, \tag{6}$$

if $800 < \mathrm{Re}_p < 2\times 10^5$, or

$$C_D=0.2 \tag{7}$$

if $\mathrm{Re}_p > 2\times 10^5$.

The last situation corresponds to very large particles and is very rarely met in practical applications.

Combination of equations (3), (5), (6), and (7) yields that the equation of motion for the particle (2) may be written in the following general form:

$$\frac{dU_s}{dt}=C(U-U_s)|U-U_s|^{n-1} \tag{8}$$

where C and n are determined by the form of the equation for C_D. Thus, if C_D is taken from equation (3) $n = 1$ and $C = 18\mu/(\rho_s d^2)$.

A glance at equation (8) proves that this equation is coupled with the vertical equation of motion for the particle which implicitly comes in the $|U-U_s|$ term. Therefore, its solution would be obtained by simultaneously solving the two equations of motion of the particle. Only if $n-1=0$ the two equations are independent. A moment's reflection though will prove that the contribution of the transverse velocity is indeed small and, therefore, may be neglected for an approximate solution of that equation. Here we may a priori quote the result of sections 4 and 6 (equations (16), (27)) where it ap-

Nomenclature

C = constant
C_D = drag coefficient
c_f = friction coefficient
d = particle diameter
D = pipe diameter
g = gravitational acceleration
K = constant (equation (28))
m = mass of a particle
m^* = loading
$\dot{m}_s$ = mass flow rate of solids
n = exponent
N = number density of particles
t = time
t^* = time between collisions
U = air velocity
U_s = solids velocity
ΔE = difference in kinetic energy
ΔP = pressure drop
ϵ = pressure drop fractional deviation
μ = air viscosity
ξ = bounding coefficient
ρ = air density
ρ_s = solids density
σ = standard deviation

pears that the effect of the transverse velocity to the magnitude of the relative velocity is less than 2 percent. Given that this number is raised to a power, which is always less than 0.5, it is apparent that the total effect on the rhs of equation (8) is less than 1 percent and, hence, it may be neglected for the range of applications considered here.

Therefore equation (8) becomes:

$$\frac{dU_s}{dt} \approx C(U-U_s)^n \text{sign}(U-U_s) \tag{8a}$$

A particle when traveling in a confined stream of gas may reach a "pseudo-steady" state if its behavior between any two collisions is the same on the average. The characteristic of this state is that after a collision with a wall the particle emerges with longitudinal velocity U_{s1} and is subsequently accelerated to U_{s2}, just before its next collision with the wall. From the last collision the particle bounces again with velocity U_{s1} and the same process is repeated after every collision. The motion of this particle becomes periodic with the velocity varying from U_{s1} to U_{s2} between any two collisions. While the behavior of an individual particle may vary slightly from the above it is reasonable to assume that on the average, particles will adhere to this periodic type of motion when conveyed in a channel after they are "fully accelerated." Also successive collisions of particles may be with the same wall (instead of opposite walls as shown in the figure). This will be due to the action of gravity forces and the motion of the particles will be similar to free saltation.

For the "pseudo-steady" motion of the particles equation (8*a*) may be integrated to yield, for the velocitiy U_s between two collisions:

$$U-U_s \approx [(n-1)Ct+(U-U_{s1})^{1-n}]^{\frac{1}{1-n}}, \tag{9}$$

if $n \neq 1$ and,

$$U-U_s \approx (U-U_{s1})e^{-Ct}, \tag{10}$$

if $n = 1$.

In equations (9) and (10) $t = 0^+$ just after the collision. If the next collision with a wall occurs at $t = t^*$ the velocity U_{s2} will be given by the equations:

$$U_{s2} \approx U-[(n-1)Ct^*+(U-U_{s1})^{1-n}]^{\frac{1}{1-n}} \tag{11}$$

for $n \neq 1$ and

$$U_{s2} \approx U-(U-U_{s1})e^{-Ct^*} \tag{12}$$

for $n = 1$.

One may define for convenience a bouncing coefficient ξ to express the ratio of the two velocities U_{s1} and U_{s2}.

$$\xi = \frac{U_{s1}}{U_{s2}} \tag{13}$$

The bouncing coefficient ξ will depend largely on the type of collision between the particle and the wall. In this simplified model we may assume that ξ is independent of the incoming velocity U_{s2} and depends only on the material characteristics of the wall and particle. For the low particle velocities encountered in pneumatic conveying this is a reasonable assumption.

In terms of ξ the kinetic energy lost after each inelastic collision is:

$$\Delta E = \frac{1}{12}\pi d^3 \rho_s \left(\frac{1}{\xi^2}-1\right) U_{s1}^2. \tag{14}$$

4 The Average Velocity and Average Slip

According to the above the time-average velocity $\bar{U}_s$ of the solids will be equal to:

Table 1

n \ C	C	Equation used for C_D	Re_p
1	$18\mu/(\rho_s d^2)$	Stokes' law	$1 > \text{Re}_p$
1.375	$22.5\,\rho^{0.375}\mu^{0.625}/(\rho_s d^{1.625})$	Allen's expression	$1 < \text{Re}_p < 800$
2	$0.33\rho/(\rho_s d)$	Newton's law	$800 < \text{Re}_p$.

$$\bar{U}_s = \frac{1}{t^*}\int_0^{t^*} U_s dt, \tag{15}$$

which is very close numerically to the arithmetic average of U_{s1} and U_{s2}.

The integration of equation (15) depends on the exponent n in the expression of U_s. If $n = 1$, equation (10) is used to yield the following expression for $\bar{U}_s$:

$$\bar{U}_s \approx U-\frac{U-U_{s1}}{Ct^*}(1-e^{-Ct^*}). \tag{16a}$$

For $n = 2$ equation (9) is integrated to yield:

$$\bar{U}_s \approx U-\frac{1}{Ct^*}\ln[(U-U_{s1})Ct^*+1]. \tag{16b}$$

For all other values of n except $n = 1$ and $n = 2$ the integration of equation (15) will give the following expression for the average solid velocity.

$$U_s \approx U-\frac{1}{t^*(n-2)C}[[(n-1)Ct^* + (U-U_{s1})^{1-n}]^{\frac{n-2}{n-1}} - (U-U_{s1})^{2-n}] \tag{15c}$$

It must be emphasized that the value of C is different in each of the above three expressions. C depends only on the properties of the conveying gas and the particle characteristics. In most common cases the values for C and n are summarized in Table 1, as determined from equations (8) and (2).

The average slip of the particles is given as the difference between the gas velocity U and particle average velocity:

$$S = U-\bar{U}_s \tag{17}$$

and may be easily obtained from equations (16*a*) to (16*c*), if the time t^* is known.

It is observed that the time between collisions t^* is an important parameter for the determination of the average velocity and the slip. This average quantity may be deduced from the interaction of the forces acting on the particle in the transverse direction. A discussion for the estimation of t^* will follow in Section 6.

5 Pressure Gradient

When the flow of solid particles in a conveying system is "fully accelerated" the mixture is in a "pseudo-steady" state as explained above and the pressure drop is usually expressed by two terms: one term due to the passage of the gas alone and the other due to the excess pressure contributed by the solids:

$$\Delta P_t = \Delta P_0 + \Delta P_s. \tag{18}$$

ΔP_0 is usually given in terms of the friction coefficient f and the dynamic velocity head.

$$\frac{\Delta P_0}{L} = \frac{1}{2D} c_f \rho U^2. \tag{19}$$

ΔP_s may be determined from an average equation of motion of all the particles. This may be achieved if we assume that on the average particles behave as described in Section 3: they collide with a wall during time intervals t^* and after a collision their velocity is reduced from U_{s2} to U_{s1}. If the excess pressure

drop within an interval t^* is ΔP_s and during this time the particles move in the longitudinal direction an average distance L, momentum balance of the flow will yield:

$$\frac{\Delta P_s}{\rho_p} = U(U_{s2} - U_{s1}) \tag{20}$$

where ρ_p is the flow density of the particles defined as the mass m of the particles multiplied by their number density (particles per unit volume), N.

The excess pressure gradient then becomes:

$$\frac{\Delta P_s}{L} = \frac{mN\, U_{s2}(1-\xi)}{t^*}. \tag{21}$$

The mass flow rate of the particles is:

$$\dot{m}_s = mN\, \pi\, \frac{D^2}{4}\, U_s, \tag{22}$$

and, hence, the excess pressure gradient may be written as:

$$\frac{\Delta P_s}{L} = \frac{4\dot{m}_s U_{s2}(1-\xi)}{\pi\, D^2 \bar{U}_s t^*} \tag{23}$$

The ratio of the excess pressure loss to that due to the flow of air alone is given as follows:

$$\frac{\Delta P_s}{\Delta P_0} = \frac{8\dot{m}_s D\, U_{s2}(1-\xi)}{\pi D^2 \bar{U}_s t^* \rho\; U^2 c_f}, \tag{24}$$

and since the mass flow rate of air is: $\dot{m}_a = \pi D^2 \rho U/4$, it appears that the above ratio may be expressed as follows:

$$\frac{\Delta P_s}{\Delta P_0} = 2m^*\, \frac{D}{t^* U c_f}\, \frac{U_{s2}}{\bar{U}_s}(1-\xi), \tag{25}$$

where m^* is the loading $\dot{m}_s/\dot{m}_a$.

If we take into account that $\bar{U}_s$ is very close to the arithmetic average of U_{s1} and U_{s2} (section 4) the above equation yields:

$$\frac{\Delta P_s}{\Delta P_0} = 4m^*\, \frac{D}{t^* U c_f}\left(\frac{1-\xi}{1+\xi}\right). \tag{25a}$$

6 The Average Time t^* Beween Collisions

A moments reflection on the form of equations (21)–(25) will convince that the average time between collsions t^*, is a very important variable for the determination of total pressure drop. However, there are no experimental data for the estimation of t^*. One may only infer to values of t^* from a balance of vertical forces acting on the particle and thus arrive to an order of magnitude determination of t^*. Because of the lack of more precise information one may approximate t^* (or deduce its order of magnitude) with the relaxation (or response) time of the particles. However, there are many offers for the particles relaxation time, depending on the size of the particles considered:

(*a*) For very small particles where Stokes drag is the predominant force for particle acceleration, the particle response time may be written according to the well known formula (Chen and Crowe, 1984):

$$t^* \sim \frac{\rho_s d^2}{18\mu}, \tag{26}$$

and the excess pressure loss will be:

$$\frac{\Delta P_s}{\Delta P_0} \sim m^*\, \frac{D}{d}\, \frac{\mu}{\rho d U}\, \frac{\rho}{\rho_s}\, \frac{1}{c_f}\left(\frac{1-\xi}{1+\xi}\right) \tag{26a}$$

(*b*) When larger particles are concerned Owen (1969) stipulated that saltation will be the predominant mode of particle movement. In this case he suggests the value $t^* \sim v_0/g$ for the free saltation, with v_0 being the terminal velocity. It seems, however, that this expression does not take into account the constraint of the finite saltation height imposed by the pipe diameter. For this reason the following expression is suggested as being more appropriate for a "constrained saltation flow" where the time between particle collisions must certainly be related to the constraining channel width D (the pipe diameter in this case):

$$t^* \sim \sqrt{D/g}. \tag{27}$$

Here, in contrast to Owen (1969), the terminal velocity is considered of secondary importance, because the particles do not have sufficient time to attain the terminal velocity before they hit the walls. The consequence of this fact is that particle diameters do not appear explicitly in t^*. The particle size though is implicitly taken into account since it influences ξ.

According to the last expression the pressure drop ratio becomes:

$$\frac{\Delta P_s}{\Delta P_0} \sim 2\, m^*\, \frac{\sqrt{Dg}}{U}\, \frac{1}{c_f}\left(\frac{1-\xi}{1+\xi}\right). \tag{27a}$$

The fact that D appears as the only physical variable for t^* may look a bit odd. However, one must recall that large eddies of length scale D, contribute to the lift of particles in a saltation motion (Owen, 1969). In addition, D is the only parameter that constrains the lateral motion of each particle. Thus, the pipe diameter seems to be the predominant physical parameter for the time t^* between collisions.

It is evident from an inspection of equations (26*a*) and (27*a*) that the pressure drop is a function of several dimensionless groups: loading, Froude number, Reynolds number, (which enters either explicitly or implicitly through the friction factor) bouncing coefficient, diameter ratio, and density ratio. All the known correlations mentioned in the introduction employ two or more of these dimensionless groups. One may also observe that Reynolds number and loading are the only dimensionless variables common to all correlations. The same two variables (together with the bouncing coefficient) appear in both equations (26*a*) and (27*a*).

7 A Pressure Drop Expression

The form of equations (26*a*) and (27*a*) suggests that the total pressure loss $\Delta P_t = \Delta P_s + \Delta P_0$ may be determined with a constant, whose order of magnitude is 1. However, it is observed that ξ has not been determined experimentally. Furthermore, its value depends only on the nature of the solids and must be characteristic of the type of collision between solids and pipe. With little loss of generality one may combine the groups $(1-\xi)/(1+\xi)$ with the above constant to yield another quantity, which is characteristic of the particular solid conveyed. This quantity may be denoted by K and its order of magnitude should be approximately 10^{-1} (this figure arises from an expected bouncing coefficient $\xi \sim 0.9$).

Regarding the two expressions developed for the pressure loss it seems that the second (equation (27*a*)) is more appropriate to be used in an engineering expression. This is because it is applicable to particle Reynolds numbers Re_p greater than one. Equation (26*a*) derived from Stokes' drag law, is only applicable to ultra fine particles ($d < 1\ \mu$m). Furthermore, when an a priori analysis of the final expression was made for both equations it was found out that equation (27*b*) yields better results for the data sets at hand. Thus, the following final expression is adopted for the pressure loss in pneumatic conveying systems:

$$\Delta P_t = \Delta P_0\left[1 + Km^*\, \frac{\sqrt{Dg}}{U}\, \frac{1}{c_f}\right]. \tag{28}$$

The form of equation (28) appears to be similar to correlations derived in the past, and especially to that by Welschof (1962). However, it is different because it only has one adjustable constant and Reynolds number appears implicitly in the function for f. In addition, Welschof's correlation was

derived in a different manner and the term $\mathrm{Fr}^{-2} = U^2/gD$ appears in it to account for very low fluid velocities, where material forms dunes in the pipe. Equation (28) is derived from order of magnitude considerations and is not applicable in the case of dune formation or moving beds.

It is apparent that gravity plays an important role in equation (28) because it causes collisions with the wall in a horizontal pipe. In a vertical pipe g will play an important role but for a different reason: it would be the main cause for the presence of slip between the two phases, which contributes to the excess pressure loss. In vertical pipes collisions with the walls are caused by Magnus forces and turbulent diffusion.

The value of K was evaluated for several materials flowing in steel pipes. This task was accomplished with the use of a data bank at the University of Delaware. The bank contains data from the following experimental projects: Koncheski (1975), Rose and coworkers (1958, 1969), Hinkle (1953), Hariu and Mostad (1948), Uematu and Moricawa (1960), Voigt and White (1948), Welschof (1962) and Degliobizzi et al. (1963). Combined there are approximately 1600 data on the pressure drop through horizontal pipes of the following substances: coal, wheat, rape seed, polyethylene, lucite, mustard seed, clover seed, glass, sand and alundum. An average K was chosen for all these substances as the number that would minimize the mean absolute fractional difference $\bar{\epsilon}_{abs}$ between the observed and the predicted pressure losses. Thus, if the observed pressure loss under certain conditions is $\Delta P_{\exp}$ and that predicted by equation (28) under the same conditions is ΔP_{pred}, $\bar{\epsilon}_{abs}$ is defined as:

Table 2

Material	K	ξ	Source/reference
1. Alundum	0.131	0.936	[6]
2. Coal	0.058	0.971	[9, 15]
3. Clover	0.093	0.954	[20]
4. Glass	0.041	0.980	[7]
5. Lucite	0.104	0.949	[2]
6. Mustard Seed	0.076	0.962	[17]
7. Polyethylene	0.177	0.915	[6, 2]
8. Rape Seed	0.194	0.907	[6, 2]
9. Sand	0.188	0.910	[5, 20]
10. Wheat	0.069	0.966	[20, 21]

$$\bar{\epsilon}_{abs} = \frac{1}{r}\sum_{i=1}^{r} |\epsilon_i|, \tag{29}$$

where r is the number of data pertaining to a given material and ϵ_i is a fractional deviation of experiments and prediction:

$$\epsilon_i = \frac{\Delta P^{\,i}_{\exp} - \Delta P^{\,i}_{\text{pred}}}{\Delta P^{\,i}_{\exp}} \tag{30}$$

Table 2 gives the values of K as estimated from the above optimization procedure for the various substances examined. The Table also shows estimated values of ξ obtained by assuming that equation (27) is exact for the time t^*. The numbers in square brackets denote the sources of experimental data.

As can be seen in Table 2 the values of K are of order of magnitude 10^{-1} as expected. This fact enhances the validity of the method employed here. The apparent fluctuation in the values of K for the different materials may be due to fluctuations of the bouncing coefficients ξ for different materials.

8 Comparison With Other Expressions for Pressure Loss

This work is not intended to be an assessment of the various correlations used for the prediction of pressure loss in gas-solid systems. However, it is not possible to avoid comparison of correlations used in the past and the expression (equation (28)) proposed here. For this reason the ten sets of data shown on Table 2 were used to compare the predicted values for pressure loss from equation (28) to five other expressions used in engineering practice. These expressions are: Rose and Duckwork (1969), Rose and Barnacle (1957), Pfeffer et al. (1966), Dogin and Lebedev (1962) as suggested originally and Dogin and Lebedev as modified by Soo (1982).

For the comparison it seems that the most appropriate quantities to be used are the average error, $\bar{\epsilon}$, the average absolute error $\bar{\epsilon}_{abs}$ and the standard deviation of the error σ.

Table 3 $\bar{\epsilon}_{(\sigma)}, \epsilon_{\text{abs}}, (\sigma)$

Correlation material	Rose and Duckworth	Rose and Barnacle	Pfeffer et al.	Dogin and Lebedev	Dogin and Lebedev (Modif. by Soo)	Equation (28)
Alundum	0.19, 0.20 (0.11)	0.26, 0.26 (0.12)	−0.03, 0.09 (0.11)	−0.15, 0.16 (0.23)	0.24, 0.24 (0.12)	0.02, 0.04 (0.05)
Clover	0.25, 0.34 (0.30)	0.14, 0.25 (0.28)	−0.29, 0.33 (0.38)	0.07, 0.19 (0.26)	0.28, 0.38 (0.32)	−0.05, 0.11 (0.23)
Coal	0.26, 0.29 (0.24)	0.39, 0.40 (0.21)	0.12, 0.25 (0.27)	−1.01, 1.01 (0.73)	0.26, 0.29 (0.23)	0.04, 0.21 (0.25)
Glass	0.16, 0.24 (0.27)	0.28, 0.30 (0.23)	−0.07, 0.28 (0.33)	−1.25, 1.30 (0.83)	0.18, 0.25 (0.26)	0.10, 0.22 (0.28)
Lucite	0.38, 0.38 (0.14)	0.51, 0.52 (0.20)	0.35, 0.35 (0.15)	0.10, 0.15 (0.18)	0.48, 0.49 (0.18)	0.09, 0.14 (0.15)
Mustard	0.12, 0.12 (0.07)	0.19, 0.19 (0.09)	−0.13, 0.15 (0.12)	−0.00, 0.06 (0.09)	0.21, 0.21 (0.10)	0.02, 0.06 (0.08)
Plastics	0.17, 0.17 (0.11)	0.24, 0.24 (0.13)	0.05, 0.10 (0.12)	0.10, 0.13 (0.12)	0.24, 0.24 (0.13)	0.01, 0.09 (0.12)
Rape Seed	0.27, 0.27 (0.11)	0.29, 0.29 (0.11)	0.12, 0.12 (0.08)	0.22, 0.23 (0.09)	0.30, 0.30 (0.12)	−0.00, 0.06 (0.08)
Sand	0.48, 0.48 (0.17)	0.41, 0.41 (0.14)	0.24, 0.25 (0.18)	0.31, 0.31 (0.13)	0.50, 0.50 (0.18)	0.07, 0.18 (0.20)
Wheat	0.25, 0.26 (0.23)	0.32, 0.33 (0.25)	0.35, 0.21 (0.26)	−0.26, 0.27 (0.17)	0.30, 0.30 (0.23)	−0.01, 0.08 (0.11)

Table 4 All experimental data, $K = 0.072$

Expression	Rose-Duck	Rose-Barn	Pfeffer	Dogin-Leb original	Dogin-Leb modified	equation (28)
$\bar{\epsilon}$	0.28	0.38	0.18	−0.48	0.32	0.06
σ	0.22	0.22	0.27	0.78	0.23	0.24
$\bar{\epsilon}_{abs}$	0.30	0.38	0.24	0.62	0.34	0.22

Equation (29) gives the absolute average error. The two others are related to the deviation between experimental data and predictions ϵ_i as follows:

$$\bar{\epsilon}=\frac{1}{r}\sum_{i=1}^{r}\epsilon_i, \tag{31}$$

and

$$\sigma^2=\frac{1}{r-1}\sum_{i=1}^{r}(\epsilon_i-\bar{\epsilon})^2. \tag{32}$$

The average error indicates how well on the average a given correlation represents the experimental data and the standard deviation yields the spread of the data. Statistical experience indicates that if for a given correlation σ is low and $\bar{\epsilon}$ high, a scaling factor may be needed to improve the predictability of the correlation. On the other hand, if σ is high, regardless of $\bar{\epsilon}$, then most probably an important parameter or dimensionless number has not been included in the correlation.

The results of the comparison for all the expressions considered are shown in Table 3. Here, $\bar{\epsilon}$ and $\bar{\epsilon}_{abs}$ are in the first line and σ is shown in parenthesis underneath. It must be pointed out that the constant K was chosen so as to minimize $\bar{\epsilon}_{abs}$. Therefore, it should not be surprising if equation (28) gives lower $\bar{\epsilon}_{abs}$ than the other correlations.

Regarding average errors it is easy to observe that equation (28) is by far better than any other expression. The average error and the average absolute error obtained by equation (28) are always less than that of other expressions. This may not be surprising, since the choice of K is such as to minimize $\bar{\epsilon}_{abs}$ although all the other correlations were obtained from similar optimization principles. It is also apparent in Table 3 that the standard deviation resulting from equation (28) is comparable to the lowest deviations observed. Actually if one listed the six expression from lower to higher σ, again it will appear that equation (28) has overall lower standard deviations than any of the other expressions. This indicates that all important parameters have been accounted for in this expression and no other scaling is needed apart from the determination of constant K.

One may ask whether it is possible to use equation (28) with a "universal" constant applicable to all solid substances. This was attempted by combining all available experimental data into a single file and using the latter to estimate K. It was found in this case that the mean absolute fractional error is minimized when $K = 0.072$. Then the average error $\bar{\epsilon}$ and standard deviation σ are 0.06 and 0.24 correspondingly. However, one has to be cautious in the use of this value for K because the coal data constitute a disproportionate part (40 percent) of the total number of data. Therefore, K is biased toward the coal constant (0.058). The statistical variables of the other correlations when used with all experimental data are given in Table 4.

Again the average errors of equation (28) are by far smaller than all other expressions, while the standard deviation is comparable to the lowest deviations observed.

From the above it appears that equation (28) is advantageous to be used instead of other expressions for the pressure gradient in solid conveying systems, especially when the material is one of the ten in Table 1. For a different material a constant K of the order 0.1 will give a good estimate of the pressure loss.

9 Conclusions

All expressions used in the past for the prediction of the pressure losses in air-solid systems are basically statistical correlations of dimensionless groups. The correlations are not based on any physical model. When compared with experimental data all correlations show relatively high average errors and deviations.

It appears that the excess pressure loss encountered in solid suspensions is primarily due to the collisions of particles with the wall. This work models the motion of the particles between any two collisions and derives expressions, for the mean velocity and slip of particles in terms of the average time t^* between two collisions. A method for the estimation of pressure loss is derived with t^* being a parameter. It is reasonable to assume that t^* depends on the pipe diameter and the gravitational acceleration, since the particle's motion is a constrained form of saltation. Hence, an expression for the pressure loss is derived with one adjustable constant, estimated from the experimental data. A statistical analysis of all available expressions with an existing bank of air-solids data reveals, that the expression derived from this simplified model of solids motion always results to lower average discrepancies between experimental data and predictions.

Acknowledgments

The help of Mr. Jon Martin in gathering the experimental data is appreciated. The project was partially supported by grants from DuPont Company and the University of Delaware Research Foundation.

References

Chen, P. P., and Crowe, C. T., 1984, "On the Monte-Carlo Method for Modeling Particle Dispersion in Turbulence," in *Gas-Solid Flows*, ed. J. T. Jurewicz, ASME, pp. 37-42.

Choi, Y. D., and Chung, M. K., 1983, "Analysis of Turbulent Gas-Solid Suspension Flow in a Pipe," ASME JOURNAL OF FLUIDS ENGINEERING, Vol. 105, pp. 329.

Degliobizzi, M. A., Michaelides, E. E., and Thompson, F. M., 1983, "Experimental Studies on the Feeding of Solid Particles in a Pneumatic Conveying System," Univ. of Delaware, Report No. 251.

Dogin, M. E., and Lebedev, V. P., 1962, "Dependence of the resistance in pneumatic conveying pipelines on the fundamental parameter of the two-phase flow," *Ind. Eng. Chem.*, Vol. 2, pp. 64-69.

Govier, G. W., and Aziz, K., 1977, *The Flow of Complex Mixtures in Pipes*, R. Krieger Publ., Huntington, 1977.

Hariu, O. H., and Molstad, M. C., 1949, "Pressure drop in vertical tubes in transport of solids by gases," *Ind. Eng. Chem.*, Vol. 41, pp. 1148-1160.

Hinkle, B. L., 1953, "Acceleration of Particles and Pressure Drops Encountered in Horizontal Pneumatic Conveying," Ph.D. thesis, Georgia Inst. of Tech.

Hitchcock, J. A., and Jones, C., 1958, "The Pneumatic Conveying of Spheres Through Straight Pipes," *Br. J. Appl. Phys.*, Vol. 9, pp. 218-222.

Julian, F. M., and Dukler, A. E., 1965, "An eddy viscositiy model for friction in gas-solids flow," *A.I.Ch.E. Journal*, Vol. 11:5, pp. 853-858.

Konchesky, J. L., George, J. J., and Craig, J. G., 1975, "Air and power requirements for the pneumatic transport of crushed coal in horizontal pipelines," ASME *Journal of Engineering for Industry*, Vol. 97, pp. 94-100.

Martin, J., and Michaelides, E. E., 1983, "A Critical Review of Frictional

Pressure-Drop Correlations for Gas-Solid Flows," Proc. 3rd Multilphase Flow and Heat Transfer Symposium-Workshop, Miami.

Michaelides, E. E., 1984, "A Model for the Flow of Solid Particles in Gases," *Int. J. Mult. Flow*, Vol. 10, pp. 61-77.

Owen, P. R., 1969, "Pneumatic Transport," J. Fluid Mech., Vol. 39, No. 2, pp. 407-432.

Ozbelge, T. A., 1983, "An Algorithm for Hydrodynamics of Turbulent Upward Flowing Dilute Gas-Solid Suspensions," *Int. J. Mult. Flow*, Vol. 9, pp. 437-446.

Pfeffer, R., Rossetti, S., and Licklein, S., 1966, "Analysis and Correlation of Heat Transfer Coefficient and Heat Transfer Data for Dilute Gas-Solid Suspensions," NASA TN-D 3603.

Richardson, J. F., and McLeman, M., 1960, "Pneumatic Conveying, Part II: Solids Velocities and Pressure Gradients in a One-Inch Horizontal Pipe," *Trans. Chem. Eng.*, Vol. 38, pp. 257-266.

Rose, H. E., and Duckworth, R. A., 1969, "Transport of Solid Particles in Liquids and Gases," *The Engineer*, pp. 392, 430, 478.

Rose, H. E., and Barnacle, H. E., 1957, "Flow of Suspensions of Non-cohesive Spherical Particles in Pipes," *Engineer*, pp. 898-903.

Soo, S. L., 1982, Pneumatic Conveying, Ch. 7, in "*Handbook of Multiphase Systems*", ed. G. Hetsroni, Hemisphere.

Uematu, T., and Moricawa, Y., 1960, "Pressure Losses in Pneumatic Conveying Systems," *Bulletin of JSME*, Vol. 3, No. 12, pp. 444-448.

Voigt, E. G., and White, R. R., "Friction in the Flow of Suspensions," *Ind. Eng. Chem.*, Vol. 40, No. 9, pp. 1731-1738.

Welshof, R. M., 1962, "Pneumatic Conveying at High Particle Concentration," VDI Forschungenshaft, #492, pp. 12-42.

Wirth, K. E., and Molerus, O., 1983, "Prediction of Pressure Drop with Pneumatic Conveying of Solids in Horizontal Pipes," *J. Powder and Bulk Solids Techn.*, Vol. 7, pp. 17-20.

Numerical Simulation of Spray Cooling Pond Performance

N. Moussiopoulos
Lecturer,
Institut für Technische Thermodynamik,
Universität Karlsruhe,
Federal Republic of Germany

A mathematical model for predictions of the performance of spray cooling ponds is presented. In contrast to previous methods, the present model requires neither empirical information from field measurements nor an adaptation of model constants. The airflow is described by partial differential equations for the vorticity and the stream function. Turbulence is taken into account by a modified version of the k-ϵ model. Temperature and humidity of air are obtained by solving appropriate transport differential equations. The equation system is solved by means of a finite difference method. The utilized numerical algorithm has been proved to be reasonably accurate. Predicted distributions for the dependent variables are presented for a circular spray cooling pond and the case of zero wind velocity. Results for the thermal performance of this pond are in good agreement with observations.

1 Introduction

Spray cooling systems are an alternative to cooling towers for heat rejection into the atmosphere. While cooling towers use ducted airflow generated by either mechanical or natural draft, open spray systems have no such channeling and are characterized by rather low convective air velocities which restrict heat and mass transfer. As a consequence, spray systems have the disadvantage of a rather high land requirement. This aspect limits their use for heat rejection in Central Europe [1]. Figure 1 shows a spray cooling system with fixed pipes which has been proposed as ultimate heat sink in the Federal Republic of Germany. This spray cooling pond should ensure a heat rejection of 15 MW even in the case of adverse ambient conditions with the mass flow rate of water and the water temperature before spraying not exceeding 450 kg/s and 40°C, respectively.

Because of the complexity of the flow pattern, most published performance models for spray systems are of an empirical or semiempirical nature (e.g., [2–4]). Predictive methods proposed so far (e.g., [5, 6]) are based on crude assumptions for the turbulent transport and need appropriate calibration.

In this work the two-dimensional version of the numerical model ASCONA (Algorithm for Spray Cooling Numerical Analysis) is presented. The model allows predictions of the thermal performance of spray cooling systems by solving the governing differential equations. Thus, no empirical information from measurements of the thermal performance is required. After a brief description of the assumed configuration in Section 2, the model equations are presented in Section 3, and the applied numerical methods are described in Section 4. Obtained results are discussed in Section 5, and the conclusions are summarized in Section 6.

Contributed by the Fluids Engineering Division for publication in the JOURNAL OF FLUIDS ENGINEERING. Manuscript received by the Fluids Engineering Division December 17, 1985.

2 Modeled System Configuration

The two-dimensional version of the model ASCONA was devised to predict the performance of equivalent circular spray cooling ponds for the critical case of zero wind velocity. It can also describe the performance of spray canals for any wind velocity, provided that the wind direction is perpendicular to the canal.

The droplet size is modeled by means of the Sauter mean diameter

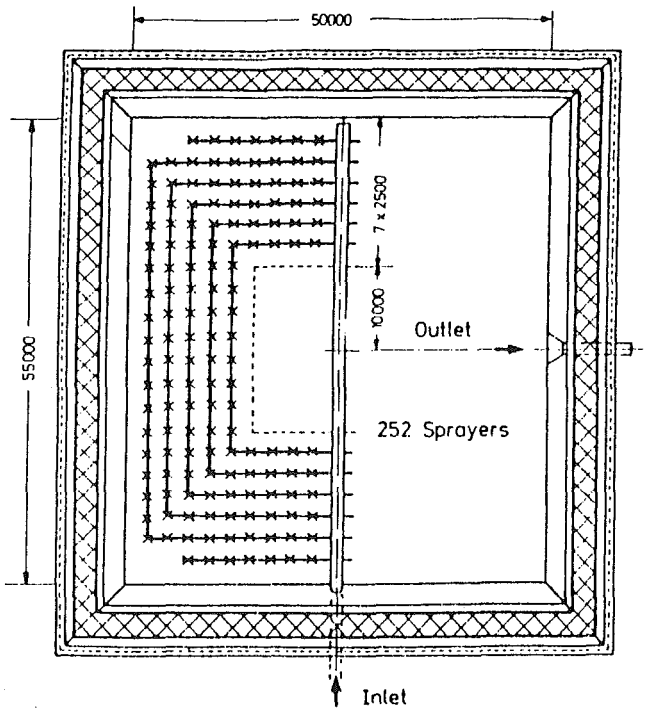

Fig. 1 Spray cooling pond with fixed pipes (measurement in mm)

$$d = \frac{\int_0^\infty f(D) D^3 dD}{\int_0^\infty f(D) D^2 dD} \tag{1}$$

where $f(D)$ is the droplet size distribution function. Apparently, the Sauter mean diameter is the ratio between total volume and total surface area of the spray droplets. According to simulation results achieved with the model ASCONA, the decrease of the droplet diameter because of evaporation is of the order of 1 percent [7].

In accordance with the proposal illustrated in Fig. 1, the spray nozzles are supposed to be located just above the (collecting) surface of the pond. The arrangement of the nozzles is assumed to provide a horizontally homogeneous droplet distribution in the spray region. The horizontal droplet velocity component is in general small compared to the vertical component and is neglected, as it has no influence on the momentum exchange between droplets and air (contributions of individual droplets cancel out). An estimate of the magnitude of individual terms in the equation of motion for droplets in moving air shows that the vertical component of the air velocity has only a minor influence on the vertical droplet motion. Therefore, the vertical droplet velocity component is calculated from the equation of motion for droplets in air at rest. With the appropriate expression for the force of friction

$$\mathbf{Fe}_y = -c_D \frac{\pi d^2}{4} \cdot \frac{1}{2} \rho_A |w| w \tag{2}$$

one gets the differential equation

$$w \frac{dw}{dy} + g \pm \frac{3}{4} c_D \frac{\rho_A}{\rho_W} \frac{1}{d} w^2 = 0 \tag{3}$$

The positive sign of the third term in this equation holds for upward droplet motion, the negative sign for downward motion. Introduction of the appropriate boundary conditions leads to the analytical solutions

$$w = \sqrt{g l_D} \cdot (\exp\{2(h_{sp} - y)/l_D\} - 1)^{0.5} \tag{4}$$

for the velocity of upward moving droplets and

$$w = -\sqrt{g l_D} \cdot (1 - \exp\{2(y - h_{sp})/l_D\})^{0.5} \tag{5}$$

for downward moving droplets, where the characteristic length l_D is defined as

$$l_D = \frac{4}{3} \frac{1}{c_D} \frac{\rho_W}{\rho_A} d \tag{6}$$

For the drag coefficient the constant value $c_D = 0.47$ is used. In the case of the spraying height $h_{sp} = 3.5$ m and the Sauter mean diameter $d = 2$ mm, equation (4) yields an initial droplet velocity of 12.4 m/s. According to equation (5), in this case the droplets hit on the pond surface with a velocity of 6.0 m/s (87 percent of the terminal velocity $|w_\infty| = \sqrt{g l_D} = 6.9$ m/s). Equations (4) and (5) further reveal that the velocity of upward moving droplets is, at the same height level, higher than the absolute value of the velocity of downward moving droplets. Thus, friction leads to a net upward momentum transfer from the droplets to the air.

An integration using equations (4) and (5) yields for the spray residence time

$$\tau_0 = \sqrt{l_D/g} \{\arctan(\exp(2h_{sp}/l_D) - 1)^{0.5} + \operatorname{arctanh}(1 - \exp(-2h_{sp}/l_D))^{0.5}\} \tag{7}$$

For $h_{sp} = 3.5$ m and $d = 2$ mm one gets $\tau_0 = 1.7$ s.

The mean droplet density in the spray region is given by

$$\bar{n} = \frac{6 \dot{M}_W \tau_0}{\rho_W \pi d^3} \frac{1}{h_{sp} A_{sp}} \tag{8}$$

Nomenclature

A, B = coefficients of the difference equation
A_{sp} = surface area of the spray region
a_T = eddy conductivity
$\mathbf{b}$ = force of buoyancy
c_D = drag coefficient
c_{pM} = specific heat of humid air
C_t, C_x = source terms
c_1, c_2, c_3, c_μ = constants of the k-ϵ model
D = diffusive part of A
d = Sauter mean diameter
$\mathbf{e}_y$ = unit vector in vertical direction
$\mathbf{F}, \mathbf{F}'$ = force of friction
$f(D)$ = droplet size distribution function
$\mathbf{f}_R$ = force of friction per unit mass of air
G = buoyancy production rate of k
g = gravity acceleration
h_{sp} = spraying height
K = convective part of A
k = turbulent kinetic energy
l_D = characteristic length
$\dot{M}$ = mass flow rate
n = droplet density
P = production rate of k
P_b = destruction rate of k due to friction
P_d = production rate of k due to local air flow field distortions
P_m = production rate of k due to mean velocity gradients
Pe = Péclet number
R = gas constant
r = radius
R_i = inner radius of spray region
R_0 = outer radius of spray region
T = thermodynamic temperature
t = air temperature
t_{CW} = cold water temperature
T_V = virtual temperature
t_{WW} = water temperature before spraying
$\mathbf{u}$ = air velocity
u, v = air velocity components
w = droplet velocity
w_{rel} = relative velocity
x = absolute humidity
y = height
β = thermal expansion coefficient
δ_T = eddy diffusivity
ϵ = dissipation rate of k
ϵ_{num} = relative deviation associated with numerical errors
ζ = vorticity
ν_T = eddy viscosity
ρ = density
$\sigma_k, \sigma_\epsilon$ = constants of the k-ϵ model
τ = time
τ_0 = spray residence time
ϕ = relative humidity
ψ = stream function

Subscripts

A = air
a = ambient
G = water vapor
r = partial derivative with respect to r
W = water
y = partial derivative with respect to y

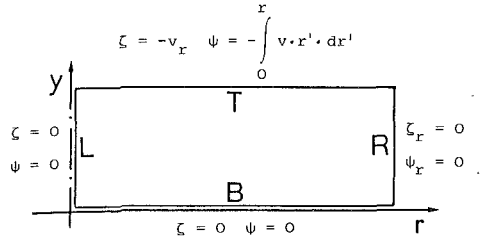

Fig. 2 Boundary conditions for ζ and ψ

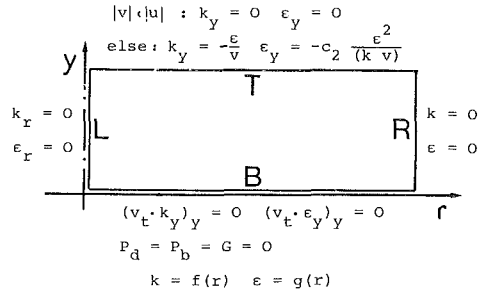

Fig. 3 Boundary conditions for k and ϵ

Consideration of mass conservation for the droplets leads to the local droplet density for upward or downward moving droplets

$$n(y) = \bar{n}\,\frac{h_{sp}}{\tau_0 |w(y)|} \tag{9}$$

with the vertical droplet velocity w from equations (4) and (5), respectively.

The above description of the modeled system configuration makes obvious that in the present version of the model spray interactions are not taken into account. Inclusion of interactions would require a far more sophisticated treatment of the droplet size distribution and would not comply with the simplifying neglects neither of the horizontal droplet velocity components nor of the horizontal variation of the droplet density. The additional effort required for the consideration of spray interactions would be beyond the scope of the present work.

3 Model Equations

In the following the model equations will be presented with respect to cylindrical coordinates. This formulation allows the simulation of the performance of equivalent circular spray cooling ponds for the critical case of zero wind velocity.

Airflow through the spray region is induced by buoyancy and by the momentum transfer between droplets and air due to friction forces. For the calculation of the air velocity, the vorticity transport equation

$$(u\zeta)_r + (v\zeta)_y = (\nu_T\zeta)_{rr} + (\nu_T\zeta)_{yy} + \left(\frac{\nu_T\zeta}{r}\right)_r + \nabla\times\mathbf{f}_R + \nabla\times\mathbf{b} - Z \tag{10}*$$

and the Poisson equation for the stream function

$$\psi_{rr} + \psi_{yy} = r\zeta + \frac{1}{r}\,\psi_r \tag{11}$$

are solved. The force of friction per unit mass of air

$$\mathbf{f}_R = -\left(\frac{n}{\rho_A}\,\mathbf{F}'\right)_{\text{up}} - \left(\frac{n}{\rho_A}\,\mathbf{F}'\right)_{\text{down}} \tag{12}$$

contains contributions of upward and downward moving droplets with the local droplet density given by equation (9). The force of friction $\mathbf{F}'$ is identical to the force $\mathbf{F}$ (equation (2)) except that the vertical droplet velocity $\mathbf{w}$ was replaced by the relative velocity between air and droplets

$$\mathbf{w}_{\text{rel}} = \mathbf{w} - \mathbf{u} \tag{13}$$

The force of buoyancy per unit mass of air

$$\mathbf{b} = \beta\mathbf{g}(T_{Va} - T_V) \tag{14}$$

is calculated using the virtual temperature

$$T_V = T\,\frac{1 + x_G R_G/R_A}{1 + x_G} \tag{15}$$

Thus, variations of the air density both due to heating and humidification are taken into account. The last term on the right-hand side of equation (10) is an additional term reflecting spatial variations of the eddy viscosity ν_T:

$$Z = 2\{(\nu_T)_{rr}u_y - (\nu_T)_{ry}(u_r - v_y) - (\nu_T)_{yy}v_r\} \tag{16}$$

A detailed derivation of the utilized form of the vorticity transport equation is given in [7]. Figure 2 shows a schematic representation of the computational domain and summarizes the boundary conditions used for the vorticity ζ and the stream function ψ.

Turbulent transport is described by means of a modified version of the k-ϵ model [8]. The eddy viscosity is calculated from the turbulent kinetic energy k and its dissipation rate ϵ:

$$\nu_T = c_\mu\,\frac{k^2}{\epsilon} \tag{17}$$

For k and ϵ transport differential equations are solved:

$$\nabla(\mathbf{u}k) = \frac{1}{\sigma_k}\,\nabla(\nu_T\nabla k) + P + G - \epsilon;$$
$$P = P_m + P_b + P_d \tag{18}$$

$$\nabla(\mathbf{u}\epsilon) = \frac{1}{\sigma_\epsilon}\,\nabla(\nu_T\nabla\epsilon) + c_1\,\frac{\epsilon}{k}\,\{P + (1-c_3)G\} - c_2\,\frac{\epsilon^2}{k} \tag{19}$$

The physical basis of the constants c_μ, c_1, c_2, c_3, σ_k, and σ_ϵ is discussed by Rodi [8]. The values of the constants used in the present work coincide with the ones recommended by Rodi [8]. Figure 3 illustrates the boundary conditions for k and ϵ.

The major modification of the "standard" k-ϵ model consists in the description of turbulent kinetic energy production: Apart from the production rates due to mean velocity gradients

$$P_m = 2\nu_T\{u_r^2 + v_y^2 + (u/r)^2\} + \nu_T(u_y + v_r)^2 \tag{20}$$

and due to buoyancy

$$G = -\beta g a_T\left\{(T_V)_y + \frac{g}{c_{pM}}\right\} \tag{21}$$

two additional terms appearing in the right-hand side of equation (18) reflect the mechanisms of kinetic energy exchange between droplets and air due to the droplet motion. The first additional term P_b is obtained by including the force of friction (equation (12)) in the derivation of the k-equation (equation (18)) [7, 8]. The final result is

$$P_b = -2c_D\,\frac{\dot{M}_W}{\rho_W dA_{sp}}\,k \tag{22}$$

This negative term can be interpreted as a reduction of turbulence due to the friction between droplets and air.

The second additional term P_d describes turbulent kinetic energy production attributed to local distortions of the airflow field: Droplet motion leads to small-scale air velocity gradients, i.e., to a shearing motion of air at a scale defined by the droplet size. For an accurate evaluation of P_d knowledge of the flow past water droplets is required. In spite of the fact

*r and y as subscripts denote partial derivatives.

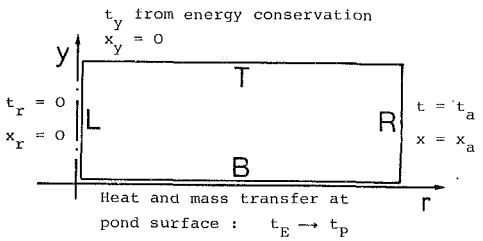

Fig. 4 Boundary conditions for t and x

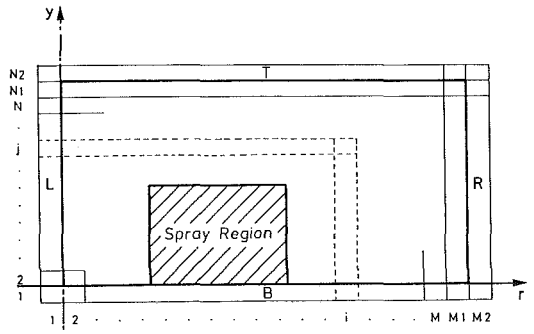

Fig. 5 Numerical grid

that for droplet diameters up to $d \cong 2$ mm deviations from the spherical shape are rather small and, therefore, the difference between the drag on the droplets and that on rigid spheres is negligible [9], a description of the flow past the droplets would require considerable effort: As the Reynolds number varies between 0 and 1650 (for $d = 2$ mm and w from equation (4) with $h_{sp} = 3.5$ m), different flow regimes would have to be distinguished (an excellent source for more details on this material is Pruppacher and Klett [10]) and additional effects would have to be considered (as for example partial slip at the air-water interface, unsteadiness of the flow at intermediate Reynolds numbers, effects of oscillation and internal circulation of the droplets etc.). Such an effort, however, would be far beyond the scope of the present work. Therefore, a far simpler approach has been adopted: It has been assumed that a droplet leads to a distortion of the air flow field within an equivalent spherical volume $4/3\ \pi\ r_d^3$ and that the corresponding air shearing motion is characterized by the gradient

$$|\nabla w_{\text{rel}}| \cong \frac{w_{\text{rel}}}{r_d} \tag{23}$$

Hence, the production rate of turbulent kinetic energy for one droplet is evaluated using the mixing length expression

$$P'_d = d^2 \cdot \left|\frac{w_{\text{rel}}}{r_d}\right| \cdot \left(\frac{w_{\text{rel}}}{r_d}\right)^2 \cdot \frac{4}{3}\pi r_d^3 \tag{24}$$

With the approximation $|w_{\text{rel}}| \cong w$, the production rate P_d is obtained by multiplying P'_d by the droplet density for upward and downward moving droplets (equation (9)). The final result is

$$P_d = \frac{8\dot{M}_W}{\rho_W d A_{sp}} \cdot (w_{\text{up}}^2 + w_{\text{down}}^2) \tag{25}$$

Comparison with equation (22) shows that this term strongly dominates in the lower part of the spray region where the droplets move fast. When the droplets have nearly reached the spraying height, P_d diminishes and P_b causes a damping of turbulence.

Temperature and absolute humidity of air are obtained by solving the transport differential equations

$$\nabla(\mathbf{u}t) = \nabla(a_T \nabla t) + C_t \tag{26}$$

$$\nabla(\mathbf{u}x) = \nabla(\delta_T \nabla x) + C_x \tag{27}$$

The eddy conductivity a_T and the eddy diffusivity δ_T are calculated from the eddy viscosity assuming $\text{Pr}_T = \text{Sc}_T = 1$. The source terms C_t and C_x correspond to the rates of heat and water vapor transfer between droplets and air. Different procedures are used for the calculation of these source terms in the cases of non-saturated and saturated air. Heat and mass transfer coefficients result from appropriate expressions for the Nusselt number and the Sherwood number.

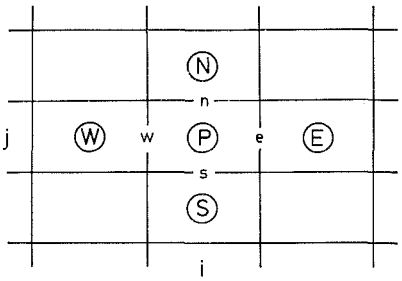

Fig. 6 Cell and interface notation

The initial droplet temperature is equal to the water temperature before spraying. The temperature variation of the droplets along their trajectory is obtained for any radial location in the spray region by integrating the energy balance equation for the droplets. Consideration of heat and mass transfer at the pond surface leads to the pond temperature, which is in general lower than the temperature of the droplets hitting on the pond. The cold water temperature t_{CW} is obtained by averaging the pond temperature over the pond surface.

Figure 4 summarizes the boundary conditions for the air temperature t and the absolute humidity x. A detailed description of the procedures adopted for the calculation of the source terms C_t and C_x and a complete list of the expressions used for the calculation of the heat and mass transfer coefficients are given in [11].

4 Numerical Solution

The presented system of differential equations was discretized and is solved by means of a finite difference algorithm on the grid shown in Fig. 5. The general form of the finite difference equation for the variable Φ in the cell (i, j) is

$$A^P \cdot \Phi^P + \sum_{(NB)} A^{NB} \cdot \Phi^{NB} = B, \quad NB \in \{W,N,E,S\} \tag{28}$$

The used cell notation is illustrated in Fig. 6. With the convective terms treated by means of an upwind scheme, the coefficients A^{NB} at the four neighboring grid points take the form

$$\begin{aligned} A^E &= D^e - \frac{1}{2}K^e + \alpha_0 \cdot \frac{1}{2}|K^e| \\ A^W &= D^w + \frac{1}{2}K^w + \alpha_0 \cdot \frac{1}{2}|K^w| \\ A^N &= D^n - \frac{1}{2}K^n + \alpha_0 \cdot \frac{1}{2}|K^n| \\ A^S &= D^s + \frac{1}{2}K^s + \alpha_0 \cdot \frac{1}{2}|K^s| \end{aligned} \tag{29}$$

$\alpha_0 = 0$ represents central differences, $\alpha_0 = 1$ full upwind. According to the "exponential scheme" (Patankar [12]), α_0 is a function of the cell Péclet number $\text{Pe} = K/D$. A comparison of computations using this function with results achieved with the arbitrarily chosen constant value $\alpha_0 = 0.95$ showed, however, no significant differences. Therefore, the value 0.95 is used for the simulations.

The Poisson equation for the stream function is directly solved with the fast elliptic routine POISSX based on cyclic reduction (Schumann and Sweet [13]). All other equations are

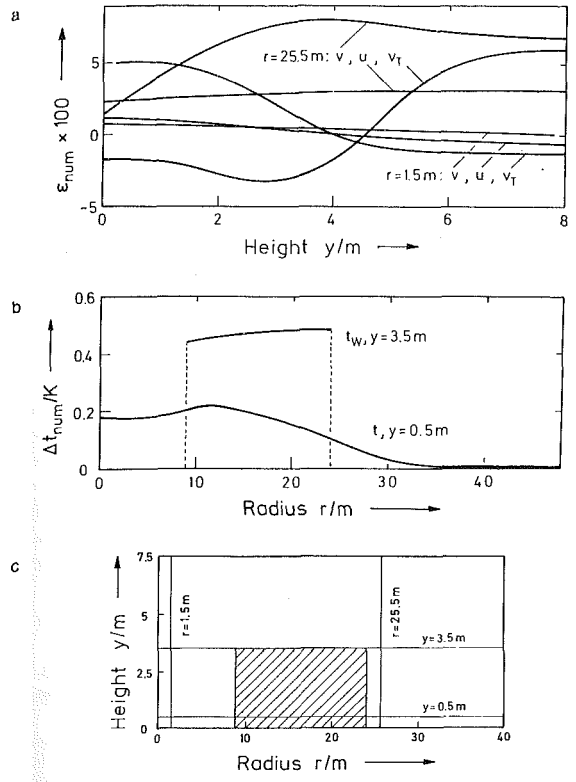

Fig. 7 Comparison of results obtained on a fine grid (30 x 30 points) with corresponding results on a coarse grid (16 x 16 points)
***a)* Relative deviations of the two air velocity components and the eddy viscosity at two radii**
***b)* Absolute deviations of the air and water temperatures at one height level each**
***c)* Location of the radii and the height levels in the domain**

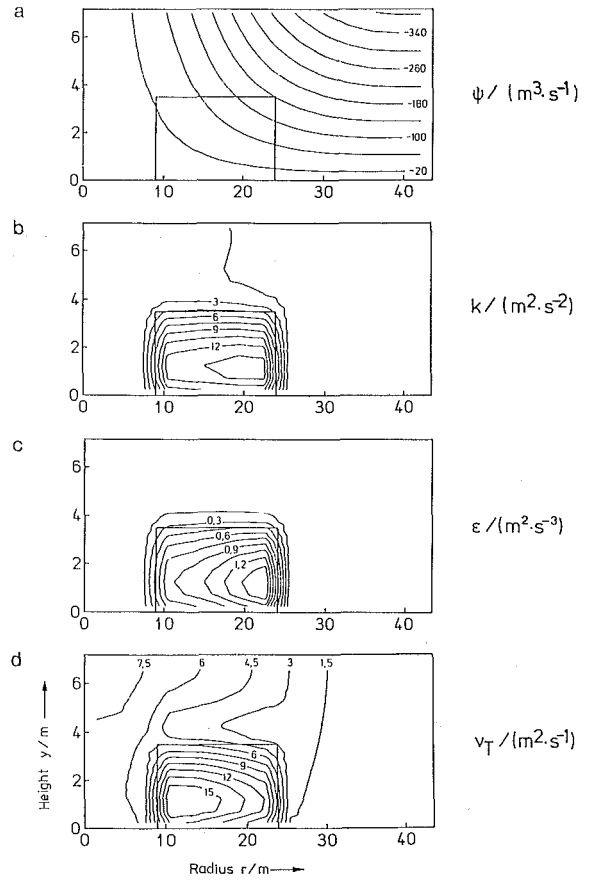

Fig. 8 Simulation results for the reference case (defined at the beginning of Section 5)
***a)* Streamlines of the air flow**
***b)* Turbulent kinetic energy**
***c)* Dissipation rate of turbulent kinetic energy**
***d)* Eddy viscosity**

solved using an ADI procedure with numerically optimized underrelaxation factors. Additional features of the numerical algorithm are the use of a staggered grid and the computation of interface diffusivities using the harmonic mean of the values for the adjacent cells [12].

The numerical accuracy of the model was proved by performing numerous calculations both on a fine grid (30×30 points) and on a coarse grid (16×16 points). The results were used to determine relative deviations

$$\epsilon_{\text{num}} = \frac{|\Phi|_{\text{fine}} - |\Phi|_{\text{coarse}}}{|\Phi|_{\text{fine}}} \tag{30}$$

for several variables (represented here by Φ) at different locations in the grid. Apparently, equation (30) is not applicable in the case of temperatures, as the result would depend on the thermometric scale. Therefore, absolute deviations of the air and water temperatures at different locations in the grid were compared with the total heating of air and the total cooling of water respectively.

As an example, Fig. 7 illustrates deviations originating from results for the reference case to be discussed in Section 5. Figure 7(*a*) shows the relative deviations of the two air velocity components and the eddy viscosity at two radii, Fig. 7(*b*) the absolute deviations of the air and water temperatures at one height level each (for comparison: total heating of the air ≅ 3.5 K, total cooling of the water ≅ 12 K). The locations of the two radii and the two height levels are indicated in Fig. 7(*c*).

In all calculations the maximum relative deviations from equation (30) were of the order of 5 percent and occurred only at few grid points, mainly at the inflow side of the spray region where the gradients of most of the variables are highest (cf. Section 5). Similarly, the maximum absolute temperature deviations amounted to approximately 5 percent of the appropriate heating (or cooling) ranges and also occurred at few grid points only. Deviations of this order of magnitude allow the conclusion that the numerical errors related to the grid are small.

As an additional estimate of the numerical accuracy, global budgets of energy and mass of water were evaluated from detailed results. For this purpose, first the net amounts of energy and mass of water transferred per unit time out of the computational domain were calculated by integrating the appropriate fluxes at the domain boundaries. The obtained values were subsequently compared with the total source terms summed up over the entire spray region. The resulting errors were in all calculations smaller than 2 percent of the corresponding total source terms on the coarse grid and even smaller than 1 percent on the fine grid. For practical applications, an accuracy of 1–2 percent in the calculation of the total rejected heat is more than satisfactory, especially if one considers the model simplifications outlined in Sections 2 and 3.

5 Results

Figure 8 illustrates simulation results for a reference case defined as follows:

outer radius of the spray region	R_0	= 24 m
inner radius of the spray region	R_i	= 9 m
spraying height	h_{sp}	= 3.5 m
Sauter mean diameter	d	= 2 mm
mass flow rate of water	$\dot{M}_W$	= 450 kg/s
water temperature before spraying	t_{WW}	= 40 °C
ambient conditions: air temperature	t_a	= 20 °C
relative humidity	ϕ_a	= 60 %

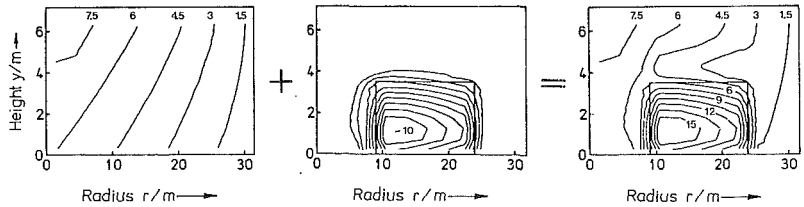

Fig. 9 Interpretation of the distribution of the eddy viscosity, Fig. 8(*d*), as the superposition of the distribution in an undistorted buoyant air flow and the distribution in the spray region

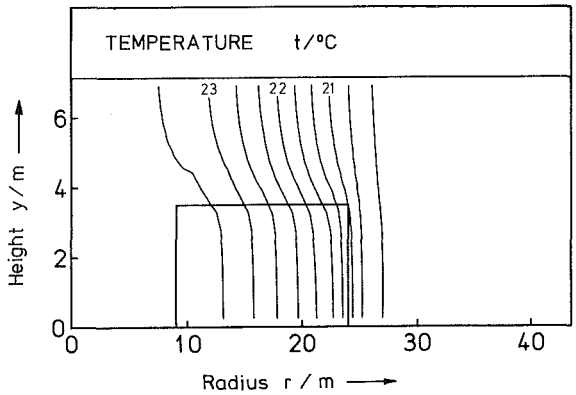

Fig. 10 Predicted air temperature for the reference case

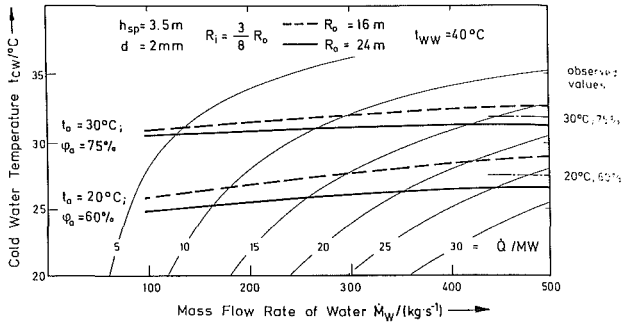

Fig. 11 Cold water temperature from ASCONA compared with summarized results from field measurements [14]. Isopleths for the total heat rejection are reproduced for convenience.

The considered pond geometry conforms with the geometry of the proposal shown in Fig. 1. A nozzle-free inner zone is recommended, as heat and mass transfer in this region would be ineffective due to vanishing air velocities ([7], cf. also Fig. 8(*a*)).

Predicted streamlines of the air flow are shown in Fig. 8(*a*). The location of the spray region corresponds to the plotted rectangle. Heating and humidification of air and vertical momentum transfer due to friction lead to an upward vertical component of the air velocity. This component varies between 0 and 0.5 m/s in the spray region and reaches 1.2 m/s at the top of the computational domain.

Figures 8(*b*) and 8(*c*) show simulation results for the turbulent kinetic energy k and its dissipation rate ϵ. The results indicate that the interaction of the droplet motion with the air flow leads to much higher values of k and ϵ in the spray region than in the surrounding air. Maximum values are reached in the lowest part of the spray region where the droplet velocities are high and the production rate due to small-scale velocity gradients dominates (cf. equation (25)).

The turbulent kinetic energy k only slightly depends on the radius r in the interior of the spray region. On the contrary, the dissipation rate ϵ clearly decreases with decreasing radius. This behavior can be explained by comparing the source terms in equations (18) and (19): In the case that the total production rate $P + G$ is equal to the dissipation rate ϵ, the source terms in the k-equation (equation (18)) cancel out; because of $c_3 > 0$ and $c_2 > c_1$ and as the buoyancy production rate G is positive in the spray region, however, the sum of the source terms in the ϵ-equation (equation (19)) is negative in this case. If $P + G < \epsilon$, the sum of the source terms in the ϵ-equation shifts further to the negative range. Hence, if both k and ϵ decrease, ϵ decreases more sharply than k.

The above outlined difference in the distribution of k and ϵ clearly influences the predicted distribution of the eddy viscosity (Fig. 8(*d*)): The eddy viscosity of air entering the spray region first increases with decreasing radius. Subsequently, however, the eddy viscosity falls down rapidly at the outflow of the spray region. On the contrary, above the spray region the eddy viscosity monotonically increases along the streamlines of the airflow. Figure 9 shows that the predicted distribution of the eddy viscosity can be interpreted as the superposition of two distributions: On the one hand, the typical distribution for the case of a buoyant air flow and no interaction with droplets, on the other hand, the distribution in the spray region. The considerable variations of the eddy viscosity illustrated in Figs. 8(*d*) and 9 reveal that turbulent transport in the air flow field induced by a spray cooling pond cannot be adequately described using oversimplified parameterizations.

Figure 10 illustrates the predicted distribution of the air temperature. Because of the analogy between equations (26) and (27), a similar distribution resulted also for the absolute humidity. The high gradients at the inflow side of the spray region reveal that the rates of heat and mass transfer are highest there.

Figure 11 summarizes predictions for the cold water temperature deduced from several simulations. Two different spray cooling ponds were assumed (outer radius of the spray region R_0 = 16 m and 24 m), both with a nozzle-free inner zone (R_i = 3/8 R_0). The larger spray cooling pond is comparable with the proposal illustrated in Fig. 1. Apart from typical ambient conditions for Central Europe (t_a = 20°C, ϕ_a = 60 percent), a case of hot and humid weather was considered (t_a = 30°C, ϕ_a = 75 percent; these conditions are rather rare in Central Europe). For all simulations, a spraying height of 3.5 m, a Sauter mean diameter of 2 mm and a water temperature before spraying of 40°C were prescribed. For convenience, isopleths for the total heat rejection are drawn in Fig. 11. The results prove that the heat rejected by the larger spray cooling pond exceeds 15 MW in the case $\dot{M}_W$ = 450 kg/s and t_{WW} = 40°C even at the adverse ambient conditions t_a = 30°C, ϕ_a = 75 percent.

The model predictions for the cold water temperature were compared with measured values reported by Hebden and Shah [14]. According to the authors, these values were obtained by averaging data received from both small and large ponds operating at different locations and are based on the low wind velocity of 2 m/s. Assuming that the reported values are representative for the case of zero wind velocity as well, Fig.

11 shows a good agreement between observation and prediction for the considered two ambient conditions. The model predictions reveal, however, that the achieved cold water temperature depends not only on the ambient conditions but also on the pond geometry and the mass flow rate of cooling water. This result led to the establishment of the mean droplet density (cf. equation (8)) as a characteristic quantity for the description of spray cooling performance [7].

A more detailed discussion of the predicted thermal performance of spray cooling ponds and a comparison with results from NTU-models are given in [11].

6 Conclusions

The model ASCONA predicts the performance of spray cooling ponds in good agreement with results of field measurements. By accurate modeling of all important physical processes involved (e.g., heat and mass transfer in the spray region, turbulent transport of momentum, energy and mass, production of turbulent kinetic energy) neither empirical information nor an adaptation of model constants is required. Thus, the model ASCONA might be useful for a check of assumptions made by simpler models.

References

1 Zimmermann, C., "Stand und Tendenzen in der Technik und der Anwendung der Kühlteich-/Sprühkühlteichtechnologie," *VGB Kraftwerkstechnik*, Vol. 62, No. 6, June 1982, pp. 512–519.

2 Chaturvedi, S., and Porter, R. W., "Air Vapor Dynamics in Large-Scale Atmospheric Spray Cooling Systems," ASME JOURNAL OF FLUIDS ENGINEERING, Vol. 100, No. 3, Mar. 1978, pp. 65–72.

3 Porter, R. W., Jain, M., and Chaturvedi, S. K., "Unit Thermal Performance of Atmospheric Spray Cooling Systems," ASME *Journal of Heat Transfer*, Vol. 102, No. 2, May 1980, pp. 210–214.

4 Chen, K. H., and Trezek, G. J., "Thermal Performance Models and Drift Loss Predictions for a Spray Cooling System," ASME *Journal of Heat Transfer*, Vol. 99, No. 2, May 1977, pp. 274–280.

5 Berger, M. H., and Taylor, R. E., "An Atmospheric Spray Cooling Model," Env. Effects of Atm. Heat/Moisture Releases, 2nd AIAA/ASME Thermophysics and Heat Transfer Conf., Palo Alto, Calif., May 1978, pp. 59–64.

6 Palaszewski, S. J., Jiji, L. M., and Weinbaum, S., "A Three-Dimensional Air-Vapor-Droplet Local Interaction Model for Spray Units," ASME *Journal of Heat Transfer*, Vol. 103, No. 3, Aug. 1981, pp. 514–521.

7 Moussiopoulos, N., *Mathematisches Modell zur Berechnung von Sprühkühlteichen*, Dissertation, Universität Karlsruhe, Fortschr.-Ber. VDI-Z., Reihe 6, No. 105, Düsseldorf, 1982.

8 Rodi, W., *Turbulence Models and Their Application in Hydraulics*, State-of-the-art paper, IAHR, Delft, The Netherlands, 1980.

9 Le Clair, B. P., Hamielec, A. E., Pruppacher, H. R., and Hall, W. D., "A Theoretical and Experimental Study of the Internal Circulation in Water Drops Falling at Terminal Velocity in Air," *Journal of the Atmospheric Sciences*, Vol. 29, pp. 728–740.

10 Pruppacher, H. R., and Klett, J. D., *Microphysics of Cloud and Precipitation*, D. Reidel, Dordrecht, The Netherlands, 1978.

11 Moussiopoulos, N., and Ernst, G., "Thermal Performance of Spray Cooling Ponds at Zero Wind Velocity," ASME *Journal of Heat Transfer*, Vol. 109, No. 1, Feb. 1987, pp. 212–217.

12 Patankar, S. V., *Numerical Heat Transfer and Fluid Flow*, Hemisphere, Washington, D.C., 1980.

13 Schumann, U., and Sweet, R. A., "A Direct Method for the Solution of Poisson's Equation with Neumann Boundary Conditions and a Staggered Grid of Arbitrary Size," *Journal of Computational Physics*, Vol. 20, No. 2, Feb. 1976, pp. 171–182.

14 Hebden, W. E., and Shah, A. M., "Effects of Nozzle Performance on Spray Ponds," *Proceedings of the American Power Conference*, Vol. 38, 1976, pp. 1449–1457.

A. M. Godon*
Research Assistant

J. H. Milgram
Professor,

Department of Ocean Engineering,
M.I.T., Cambridge, Mass. 02139

Mixing of Fluids in Tanks by Gas Bubble Plumes

The need to rapidly mix treating agent into the oil of a ruptured ship tank motivated scale model experiments of mixing in square-bottomed tanks by gas bubble plumes. The mixing time is primarily governed by the gas flow rate, the plume length and the tank base dimensions; and is quite insensitive to tank height. An empirical relationship between the degree of mixing and a single dimensionless variable is developed and an explanation of the relationship in terms of the fundamentals of the flow is provided.

Introduction

When a stream of gas bubbles is released at the bottom of a tank of fluid, the bubbles and entrained liquid form a rising plume. Such a plume mixes fluids effectively because of the turbulent mixing in the plume region coupled with the induced convection which circulates the fluid through the plume.

Here, we report on the mixing induced by gas bubbles released from perforated horizontal pipes in open-top rectangular tanks and how the mixing depends on the independent variables of the system. This leads to the formulation of a means of predicting the mixing in tanks of any size with any gas flow. Tests were conducted in a cubical tank measuring 1.22 meters along each edge and in a rectangular tank with 1.18 × 1.22 m base dimensions and 2.44 m high. Tests were done in the cubical tank both completely and half full so results were obtained for three fluid heights: 0.66, 1.22, and 2.44 meters.

The principal motivation for the work was the possibility of rapidily mixing treating agent into the oil in a large ship tank after damage to the tank, but before much of the oil escapes. Installation of a bubble plume mixer can offer significant economic and practical advantages over installation of a mechanical mixer when the tank is large or the need for mixing is extremely infrequent. Numerous applications involve one of these criteria. The ship tank involves both. Rapid mixing can materially reduce pollution damage through use of dispersant, sinking agent or gelling agent as the treating agent; the best choice being dependent on circumstances. Thus we consider mixing of an agent released from the same perforated pipe that releases the gas or from a perforated pipe directly above the gas pipe.

Because of the ship tank application, a gas release pipe was always along the bottom of a side wall. This wall would correspond to the wall along an exterior ship side that could be damaged so as to maximize the treatment of escaping oil. In some of our experiments a second release pipe leg was along an adjacent wall so the release pipe formed an "L," and in some experiments the second pipe leg was along a mid-line of the tank bottom so the release pipe formed a "T." For mixing without consideration of a damaged wall one would want to consider symmetric "+" and "×" pipe configurations as well as those we have tested.

The approach taken in the experiments was to release a small volume of fluorescent dye quickly and then to measure the dye concentration distribution as a function of time thereafter. The bubble plume was started either just after the dye release or before it.

Variables

The dimensionless segregation, S in the tank is defined in terms of the local concentration, $c(x, y, z)$ of dye by:

$$S=\sqrt{\frac{1}{\bar{c}^2}\iiint_{\text{vol}}[c(x,y,z)-\bar{c}\,]^2 dx\,dy\,dz} \tag{1}$$

The integral is to be taken over all the fluid. S, c, and $\bar{c}$ can depend on time.

In the experiments, samples to be analzyed were taken at the same time after the start of mixing from N discrete locations. S was approximated by U (the "unmixedness") defined as:

$$U=\sqrt{\frac{1}{\bar{c}^2}\sum_{i=1}^{N}[c_i-\bar{c}\,]^2 v_i} \tag{2}$$

where c_i is the concentration at the ith location and the mean concentration $\bar{c}$, was determined as the concentration after the tank was allowed to mix for a long time. v_i is a volume associated with the ith location such that,

$$\sum_{i=1}^{N} v_i = V \tag{3}$$

For example, locations and volume dimensions for the 1.22 m depth are shown in Fig. 1. U is the dependent variable that was measured in our experiments.

For a square based tank and a specific gas release geometry, and neglecting the influence of the viscosity and density of the gas because they are so small compared to those of the liquid, the independent dimensional variables are: h, L, g, P, Q, t, ρ, ν, and σ. We found that the results of several gas release

*Present address: Artec Canada, Ltd., Kanata, Ontario.

Contributed by the Fluids Engineering Division for publication in the JOURNAL OF FLUIDS ENGINEERING. Manuscript received by the Fluids Engineering Division March 25, 1986.

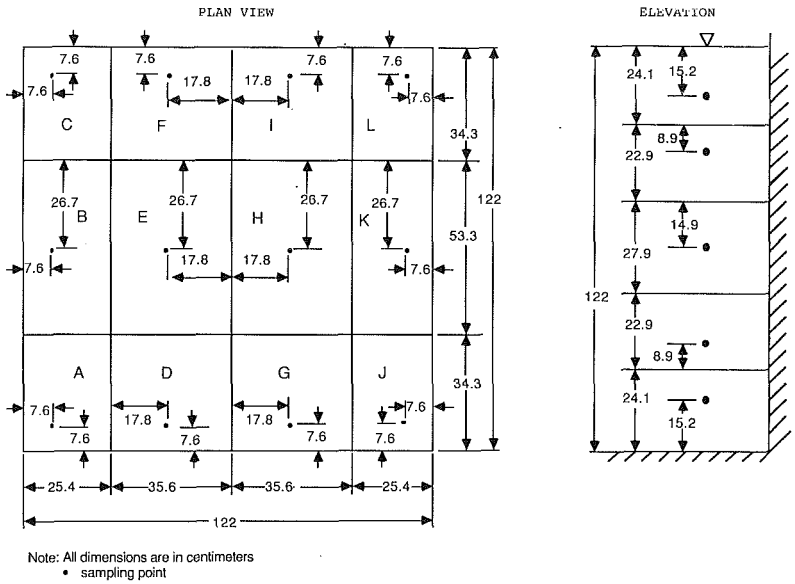

Fig. 1 Locations and dimensions of sampling points and associated volumes for a fluid depth of 1.22 m. Similar arrangements were used for the 0.66 and 2.44 m depths except they used four and six heights, respectively, instead of five.

geometries could be unified in terms of an effective horizontal length of gas release, L_{bp}, so we consider this as another independent variable. The seven independent dimensionless groups (variables) that can be formed from these 10 dimensional variables are: h', F_r, L', P_r, R_e, t', and W_e.

Dimensionless variables that significantly influence the mixing which we varied in the experiments are: the dimensionless time (t'), he height ratio (h'), the Froude number (F_r) and the plume length ratio (L'). Some comment on the other variables is in order.

The pressure ratio is the ratio of gas volume flux at the top of the tank to the volume flux at the bottom. Under ordinary laboratory conditions it cannot differ significantly from 1.0 unless experiments are done under vacuum which we did not do. Thus we have not determined the influence of pressure ratio on the mixing. For very large tanks, the pressure ratio can differ significantly from 1. In a large ship tank it is about 2. This opens the question as to how our results can be interpreted when the pressure ratio differs significantly from 1. For modest pressure ratios our results are best applied by using the gas volume flow rate at the mid-height in our formulations. Variations from this would be on the order of 35 percent for a pressure ratio of 2. As our results will show, 35 percent variations in gas flow affect U by just a few percent. On the other hand, our results cannot be applied to conditions where the pressure ratio is very large.

The Weber number influences the gas bubble diameters which are proportional to $\sigma^{1/2}$ (see Hu and Kinter, reference [1] and Milgram, reference [2]). To determine the influence of this to the extent practical in our laboratory, we did two experiments (Godon, reference [3]) that were identical except that one had a surfactant in the water which reduced the surface tension by a factor of 2. No significant differences were observed in results of U versus t so we will not consider the influence of the Weber number here.

The principal influences of the Reynolds number are on the

Nomenclature

a, b, e, f = numerical constants
B = buoyancy in plume
c = concentration (function of x, y, z, t)
$\bar{c}$ = mean concentration
c_i = concentration measured at the ith sampling location
$\bar{c}_s$ = spatially averaged concentration
F_r = $[Q/\sqrt{gL^5}]$ Froude number
g = acceleration of gravity
h = liquid depth
h' = $[h/L]$ height ratio
k = ratio of plume width (from its centerplane) to plume height
L = length or width of tank base
L_{bp} = effective length of plume [length of portion along wall plus twice length of portion not along wall]
L' = $[L_{bp}/L]$ plume length ratio
M_f = momentum flux in the plume
P = pressure
P_r = $[(P+\rho gh)/P]$ pressure ratio
Q = gas volume flow rate
Q_L = liquid volume flow rate through plume
R_e = $[\nu/\sqrt{gL^3}]$ Reynolds number
r = $[V_s/V_f]$ ratio of gas "slip" speed to liquid flow speed
S = theoretical concentration segregation
t = time since the start of mixing
t' = $[tQ/L^3]$ dimensionless time
t'' = $[t/T_m]$ time in units of characteristic mixing time
T_m = characteristic mixing time
U = experimental concentration segregation
v_i = volume associated with the ith sampling location
V_f = characteristic liquid flow speed
V_s = characteristic gas bubble "slip" speed
V = tank volume
W_e = $[\sigma/\rho gL^2]$ Weber number
x, y, z = cartesian coordinates
ν = fluid kinematic viscosity
ρ = fluid mass density
σ = gas-fluid surface tension

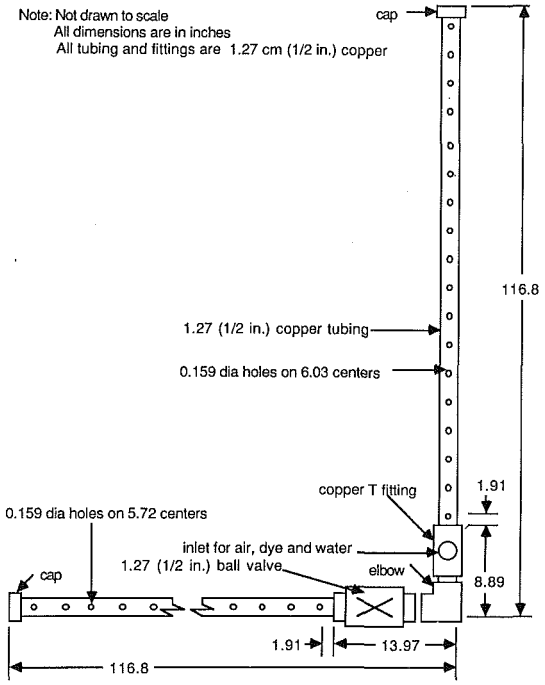

Fig. 2(*a*) Straight pipe (valve closed) and "*L*" (valve open)

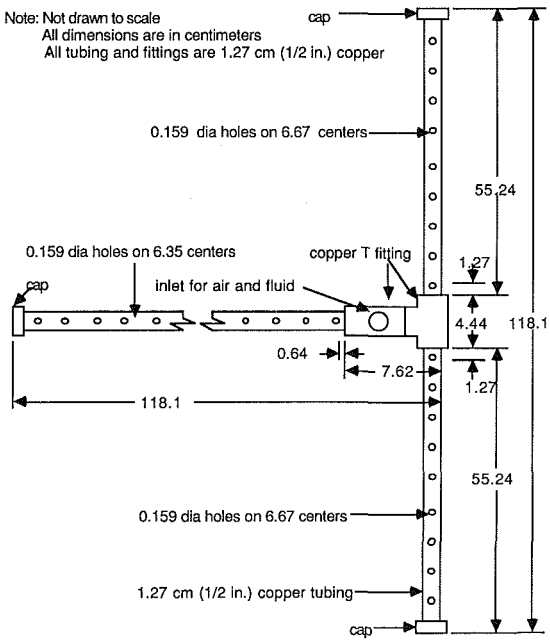

Fig. 2(*b*) "*T*" pipe

Fig. 2 The gas distribution pipes

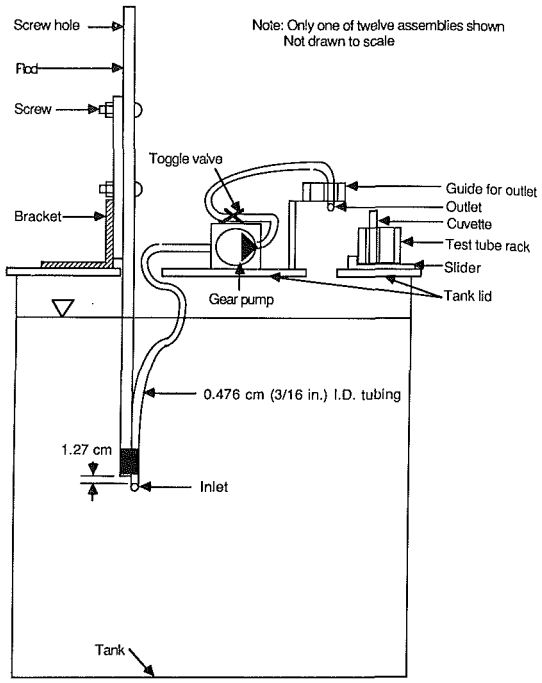

Fig. 3 Sampling pump and tubing arrangement

wall boundary layers, on the excess speed ("slip speed") of the bubbles over the mean liquid vertical speed, and on the size of the turbulence microscale. Details of the wall boundary layers are not important in the bubble plume mixing flow. Haberman and Morton [4] have shown that the rise speed of gas bubbles in liquid depends on liquid viscosity only for small bubbles. For viscosities varying by a factor of 100, rise speeds vary by less than 15 percent for bubble radii (radius of a sphere having the same volume as the bubble which is not spherical) greater than 0.4 cm. Our observations of bubble plumes in both water and in crude oil show most of the gas is in bubbles with radii greater than 0.4 cm when the gas is released from holes with diameters greater than 0.5 mm. Since our experiments and anticipated applications involve gas release hole diameters in excess of 0.5 mm the gas "slip speed" is expected to be independent of viscosity. Although the microscale size influences the mixing at very small scales, this is not detected in our experiments in which fluid elements larger than the microscale are sampled for analysis.

For the above reasons, we did not include the viscosity in our data analysis. However, it should be noted that our experiments in water have about the same Reynolds number as actual application in an oil-filled ship tank. For example, Reynolds number similitude with a ten-fold increase in length requires a kinematic viscosity 32 times greater than that of water: this being a typical viscosity for crude oil.

Apparatus and Experimental Procedures

Tap water was used for tank fluid and its temperature was between 15 and 20 C. The fluid to be mixed was tap water containing dissolved fluorescein dye. The fluorescein concentration in each sample of tank fluid taken was determined with a Model A-4 Farrand Fluorometer.

Air escaping through holes in a 12.7 mm ID perforated pipe at the bottom of the tank generated the bubble plume. Tests were done at air flows of 0.32, 0.48, 1.1 and 2.0 liters/s, referenced to standard conditions. Three different pipe configurations were tested:

1) A 1.17 m long straight pipe along one bottom edge,
2) A 1.17 × 1.17 m "*L*" configuration with a pipe along each of two adjacent edges,
3) A 1.18 × 1.18 m "*T*" configuration on the bottom.

Each of the "pipe legs" contained 18 gas release holes of 1.59 mm ID. The pipe configurations are shown in Fig. 2. A valve in the "*L*" configuration permitted it to be used for the single straight pipe tests as well.

For some of the tests, the dye was pumped out of the same pipe as was used for the gas. In other tests involving gas pipe configuration (1) (straight pipe), the dye was pumped out of a 1.17 m long straight pipe containing 16 3.18 mm diameter holes and located above the gas pipe at the mid-depth of the fluid.

Samples of the tank fluid were taken with twelve identical small gear pumps with individual inlet and outlet tubes as

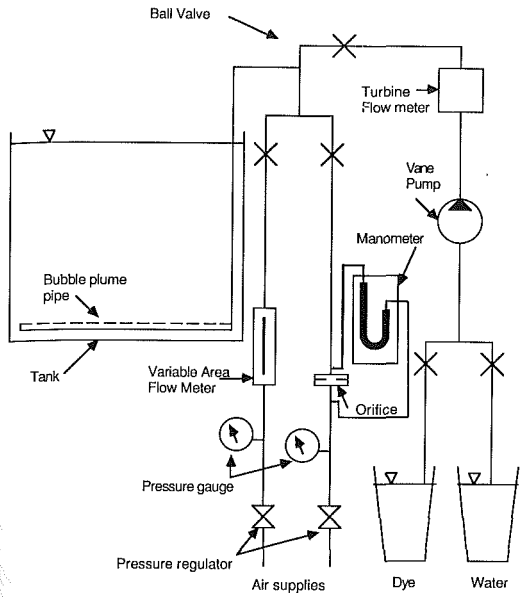

Fig. 4 General experimental arrangement. The orifice meter was used for gas flows of 1.1 and 2.0 *L/s* and the variable area flow meter was used for gas flows of 0.32 and 0.48 *L/s*. When a separate pipe was used to introduce the dye, the dye flow was attached to that pipe instead of the gas flow pipe as shown here.

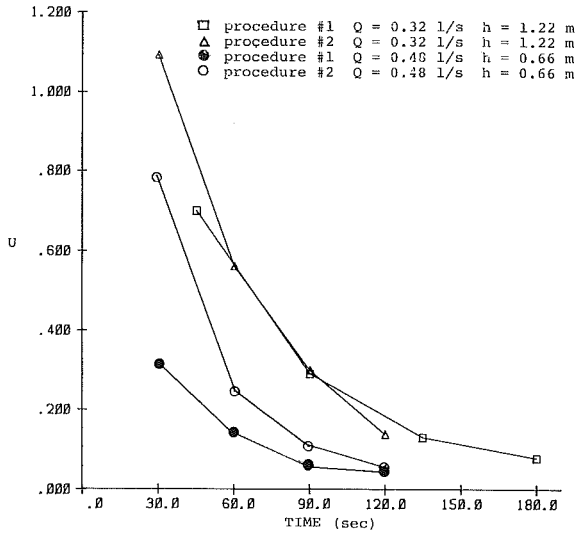

Fig. 5 Some comparative measurements for procedures 1 and 2

shown schematically in Fig. 3. Each sample pump delivered 18 *mL/s* and uncollected fluid was returned to the tank. To minimize mixing by the sampling pumps the volume moved by all 12 pumps in an experimental run was limited to 3 percent of the tank volume. Twelve samples were simultaneously taken at prescribed times with the twelve inlets located at the grid points on a horizontal plane. Samples were obtained at other depths by moving the inlets to a different horizontal plane and repeating the experiment.

Figure 4 shows a general schematic diagram of the experimental arrangement. Three different experimental procedures were used which are now explained.

Procedure #1—Used With Initial Tests of Straight Plume Pipe. The same perforated pipe was used to introduce the dye and the air. First, two samples were taken and the average of their concentrations was used as the background (relative zero) level of dye concentration. The dye pump was started and dye was pumped for 20 seconds. Without stopping the dye pump its inlet flow was switched from dye to water which was pumped for 15 seconds. Experiments showed that the dye was flushed from the system in 7 seconds of pump operation with water. At the end of the 15 second water pumping period, the dye pump was stopped, the timer was started and the air flow was started. The sampling pumps were started with their outlet flows going back into the tank. At a predetermined time, typically 30 seconds, a rack of 4 mL glass curvettes was moved under the sample streams. They filled in about 0.25 sec. and the rack was withdrawn. At predetermined regular time intervals additional racks of cuvettes were filled.

After the desired sets of samples were obtained, the tank was allowed to mix under the plume action for 10 to 15 minutes. Then four samples were taken and their mean concentration was used as the average dye concentration in analyzing the data.

Initial experiments showed that all measurements at the 0.66 m depth and those at the 1.22 m depth taken less than 60 seconds after the start of a run and with a low gas flow (0.32 l/s) were influenced not only by the gas plume mixing, but also by the initial mixing caused by the method of dye introduction. These data were eliminated from further consideration. Procedure #2 was found to cause only about half as much premixing as procedure #1.

Procedure #2—Used With Later Tests of Straight Plume Pipe. Separate distribution pipes were used for air and dye with the dye pipe at the mid-depth of the fluid. The gas flow was started and about 30 seconds later (to allow for establishment of the plume) two background-level samples were taken. Immediately thereafter the dye flow was started. Five seconds later the dye pump inlet was switched from dye to water which was pumped for 15 seconds after which the pump was stopped and its valves were closed. The sampling pumps were started with their outlet flows returning to the tank.

At the start of the dye pumping the dye pipes were filled with water. Experiments showed that dye reached the closest outlet hole five seconds after the start of pumping and it reached the furthest hole seven seconds after the start of pumping; the average being six seconds. The dye pumping persists for five seconds so the mid-time of dye introduction occurs 8.5 seconds after the start of pumping. The transit time for fluid in a sampling pump and its tubing is 3.5 seconds. The timer was started twelve seconds, the sum of these times, after the dye pump was started. Sets of twelve samples were taken at predetermined times as before. Fifteen minutes later the four average concentration samples were taken.

Figure 5 shows comparative measurements using procedures #1 and #2 with straight plume distribution pipes containing the procedure #1 data that was eliminated from consideration. The retained data, not all of which is contained in Fig. 5, has differences in U on the order of 0.06 between the two procedures, but without a clear trend. We believe that these are due to both pre-mixing differences and to our ability at making accurate fluorometer measurements which improved during the experimental program.

Procedure #3—Used With Tests of "*L*" and "*T*" Plume Pipes. This was identical with procedure #2 except here the same distribution pipe was used for gas and dye. Data were taken at a gas flow of 0.48 l/s with a fluid depth of 1.22 m. For these conditions with the straight distribution pipe results were little influenced by the choice of procedure.

Data

The raw data are sets of values of c_i for specific values of Q, h, and t. Each set contained 48, 60, or 72 values for depths of 0.66, 1.22, or 2.44 m, respectively.

The reduced data are comprised of all values of U versus t except for the aforementioned part of the procedure #1 data

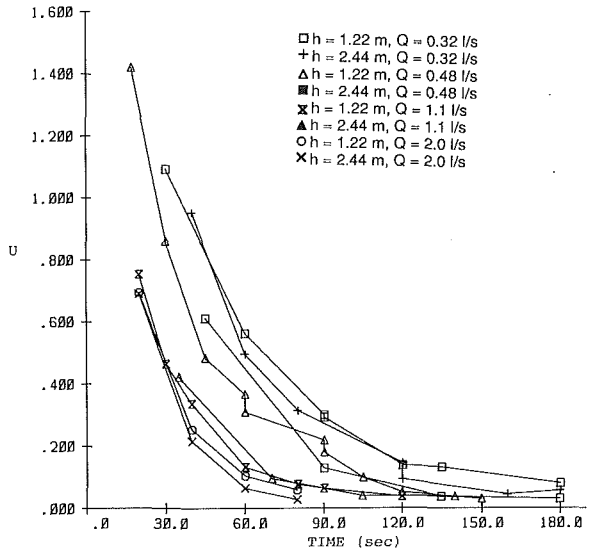

Fig. 6 Reduced data (U versus t) for the straight distribution pipe and fluids depths of 1.22 and 2.44 meters. Note that the influence of depth is small with the deeper fluid mixing slightly faster.

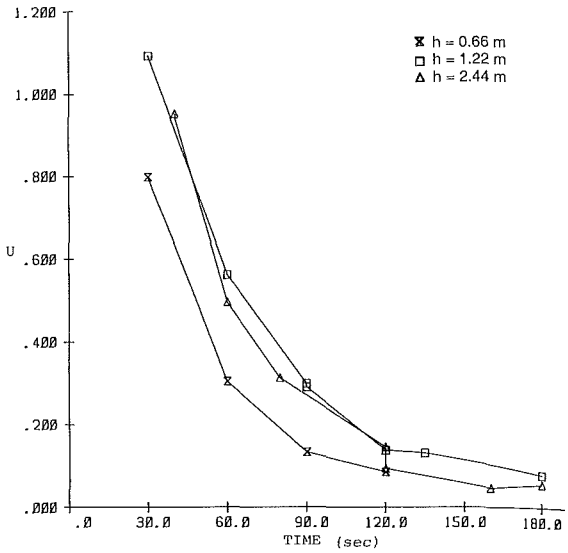

Fig. 8 Reduced data for the straight distribution pipe with a gas flow of 0.32 liters/second. Note that the 2.44 m depth case mixes very slightly faster than the 1.22 m depth case, but the 0.66 m depth case appears to mix considerably faster than the others.

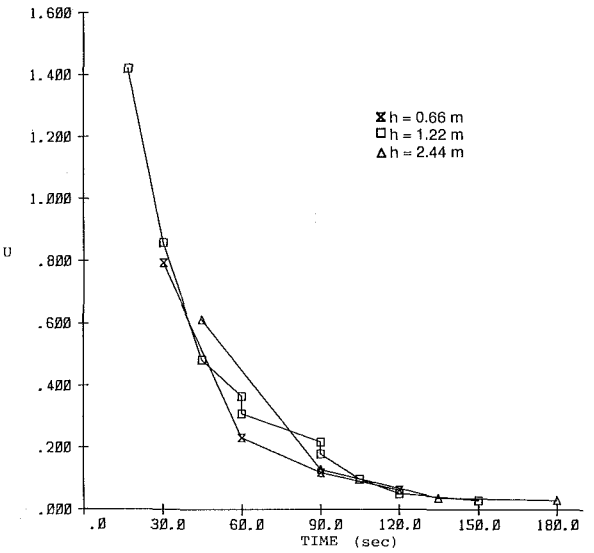

Fig. 7 Reduced data for the straight distribution pipe and a gas flow of 0.48 liters/second. Note that the influence of depth is small, but the 0.66 m depth case appears to mix slightly faster than the others.

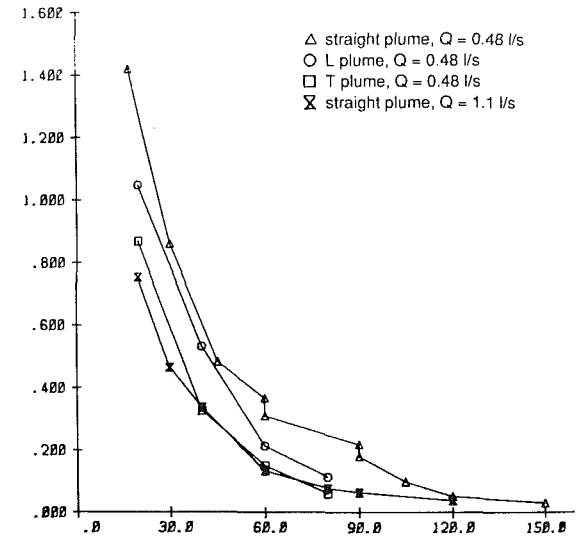

Fig. 9 Reduced data for a fluid depth of 1.22 m and a gas flow of 0.48 liters/second for three distribution pipe configurations. Data for the straight pipe at a gas flow of 1.1 l/s is included for comparison.

that was influenced by initial pre-mixing. Figure 6 shows the reduced data for a straight plume distribution pipe and fluid depths of 1.22 and 2.44 m. For each gas flow the results for the two different depths are very similar with the 2.44 m depth having values of U for any fixed time generally just a few percent smaller than the 1.22 m depth.

Figure 7 shows the reduced data for a gas flow of 0.48 L/s for fluid depths of 0.66, 1.22 and 2.44 m. With the exception of just one out of the 19 data points on the figure these results are only slightly influenced by fluid depth. However, here it is notable that for the 0.66 m depth the small depth influence is opposite in trend to the other data; the shallowest depth mixes fastest.

Figure 8 shows the reduced data for a gas flow of 0.32 L/s for fluid depth of 0.66, 1.22, and 2.44 m. Here the reverse-trend faster mixing for the 0.66 m depth is quite strong. For much of the time history, the 0.66 m depth has values of U that are about 0.15 less than that of the other depths.

We have identified three contributing causes for the apparent faster mixing at low gas flow for small fluid depth. One is the premixing due to introduction of the dye, even though procedure 2 was used. Since increased gas flow increases the mixing rate, a premixing error will be more apparent at low gas flow. The same amount of mixing energy is introduced with the dye flow, so its mixing will be more apparent when the total tank volume is small. Secondly, the cross-sectional shape of the bubble plume has an initial width near the bottom associated with initial bubble breakup followed by a linear increase in width with height. For the low depth case, the ratio of average plume width to fluid height is slightly higher than in the deeper fluid cases. Thirdly, the ratio of bubble diameter to average plume width is largest for the lowest height. The mixing due to individual bubbles at the outer part of the plume may be most influential for this condition.

Figure 9 shows reduced data at a fluid depth of 1.22 m and a gas flow of 0.48 L/s for all three plume distribution pipe configurations: straight pipe, "L" and "T". The "L" mixes considerably faster than the straight pipe and the "T" mixes considerably faster than the "L." Data for the straight distribu-

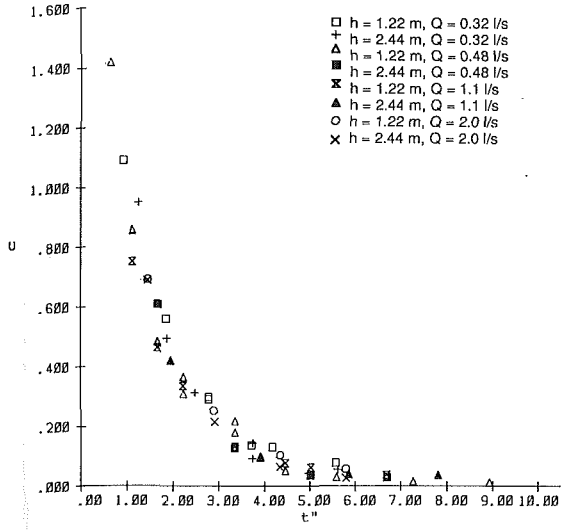

Fig. 10 U versus t″ (time measured in units of the mixing time T) for the straight distribution pipe data. $t'' = t' F_r^{-8/15}$

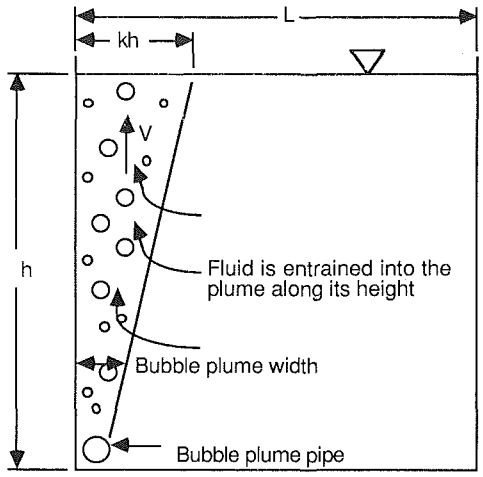

Note: not drawn to scale

Fig. 11 Schematic bubble plume cross section

tion pipe with a gas flow of 1.1 *L/s* are included in Fig 9. This shows that the "*T*" configuration at a gas flow of 0.48 *L/s* mixes as fast as the straight pipe at a gas flow of 1.1 *L/s*.

Data Accuracy

The measured data included values of the air flow rate, and c_i taken at time t. Assessing the accuracy of these quantities is straightforward. Low air flow rates were measured with a Fisher Scientific variable area flow meter and flow rates in excess of 1 liter/s were measured with a square-edge orifice meter [5]. We estimate that errors in determining gas flow rates with these instruments are less than 2 percent of measured values.

The method of estimating the time for fluid to pass through the sampling pumps and the procedure of taking samples made the sampling times accurate to within 2 seconds. Repeated fluorometer measurements on the same sample and on diluted portions of the sample yielded concentrations that never varied by more than 4 percent of the measured value so this error bound is valid with at least 95 percent confidence. 48 to 72 values of c_i^2 were averaged to determine U^2 so values of U, as defined by equation (2) were determined with errors less than 1 percent of their values with high confidence.

Since the measurement process determined values of U with high accuracy, the more important issue is how well U approximates the segregation S as given by equation (1). Due to the turbulent flow, c is a random variable. U is a functional on c so it is a random variable too and there is uncertainty in the approximation of S by U.

Three approaches were taken to provide some indication of the uncertainty. One was do the experiment twice for seven different sets of experimental conditions. The results can be seen in the plotted data as pairs of points, one above the other. The differences in pairs of values of U were 0.03, 0.05, 0.04, 0.03, 0.03, 0.01, and 0.05.

The second approach was to compare mean concentrations determined by a method similar to that for obtaining U with the concentration measured after the tank had been mixed for a long time. For any fixed time after the start of mixing, the spatially averaged sample mean concentration, c_s, is defined as:

$$c_s = \frac{1}{V} \sum_{i=1}^{N} c_i v_i \tag{4}$$

The extent to which c_s/c deviates from 1.0 is a measure of the uncertainty in sample values of statistics of c found by averaging through the tank. We calculated 98 values of c_s/c from the raw data used to determine 98 values of U. Each calculation has a value of N of 48, 60, or 72. These 98 values had a mean of 0.982 and a standard deviation of 0.051. Sixty of the 98 conditions were for times later than 45 seconds after the start of mixing. These 60 values of c_s/c had a mean of 0.988 and a standard deviation of 0.032.

The third approach was to approximate the uncertainty on the basis of theoretical statistics. $c/\bar{c}$ is a random variable and U^2 is its sample variance (of size 48, 60, or 72). For totally random samples of a random variable, the expectation and the variance of the sample variance are well known. Firstly, the expectation of the sample variance is $S^2(N-1)/N$. Secondly, the variance of the sample variance is $2S^4(N-1)/N^2$. These could indicate that our values of U systematically underestimate S by about 1 percent and they have a variability of about 1.5 percent (U^2 has a variability of about 3 percent). Our samples of c are not totally random in the sense that they are taken at specific locations. Thus the theoretical results for the expectation and variance of the sample variance are only approximate, but useful.

On the basis of the three approaches, we estimate the standard deviation in estimating S by U to be about 2 percent. This leads to 7.6 percent uncertainty for 95 percent confidence.

Data Analysis

The goal of the data analysis is to determine how the concentration segregation, U, depends on the dimensionless variables t' and F_r and L'. To find the most influential dimensionless variable we consider a new dimensionless independent variable t'' defined by:

$$t'' = (t'^a)(F_r^b)(h'^e)(L'^f) \tag{5}$$

We found that by defininig t' as we did, the best value for e was very nearly zero. Had we defined t' differently, say as tQ/L^2h, then e would not have been negligibly small. Thus equation (5) can be simplified as:

$$t'' = (t'^a)(F_r^b)(L'^f) \tag{6}$$

Then for all data points we seek the values of a, b, and f which most closely "collapse" the points to a single line on a plot of U versus t''. There is no loss in generality in choosing $a = 1$. The value of f is entirely dependent on the "L" plume and "T" plume data since $L' = 1$ for the straight plumes.

The best values of b and f were $-8/15$ and $-29/30$ (which we will consider to be -1). Thus,

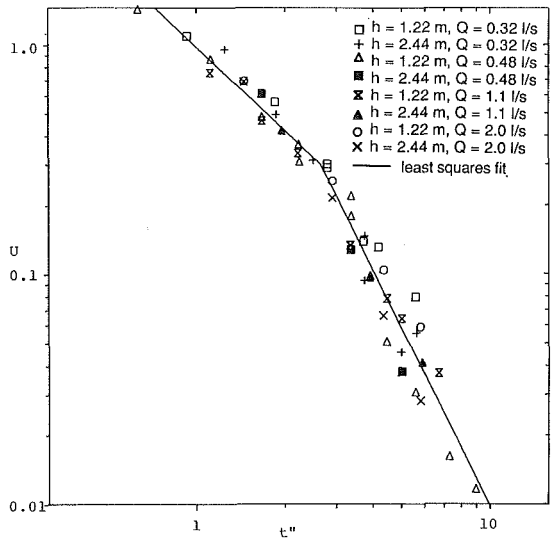

Fig. 12 Log-log plot of U versus t''

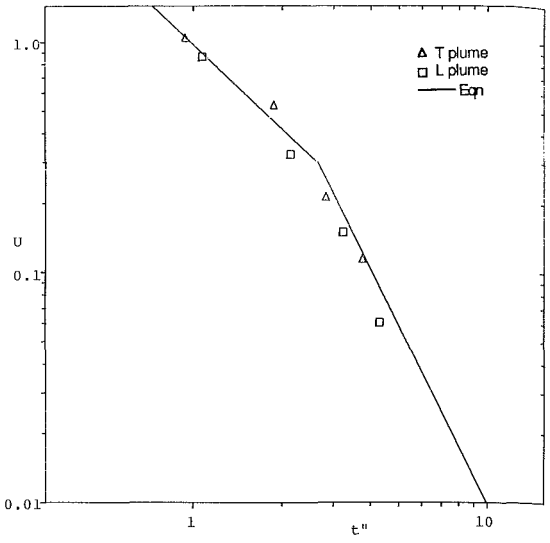

Fig. 13 Log-log plot U versus t'' for the "L" and "T" plume. Distribution pipes with a depth of 1.22 meters and a gas flow of 0.48 liters/second.

$$t'' = t' \mathrm{F}_r^{-8/15} L'^{-1} \tag{7}$$

Figure 10 is a graph of U versus t'' for the straight pipe data. To understand the meaning of t'' we write it as:

$$t'' = t/T_m \tag{8}$$

T_m is the characteristic mixing time and it can be expressed as;

$$T_m = (g^{1/15} Q^{-2/15} L_{bp}{}^{1/3}) T_s \tag{9}$$

where:

$$T_s = L^2/[L_{bp}{}^2 Qg]^{1/3} \tag{10}$$

T_m is most strongly dependent on T_s which is related to the "cycle time" it takes to circulate one tank volume of fluid through the bubble plume. This can be shown by the following "order of magnitude" analysis.

Figure 11 is a sketch of the bubble plume geometry. The flow in the plume is generally upward except very near the surface where it turns horizontal. Let V_f be the characteristic vertical liquid velocity just before it turns horizontal. k is the slope of the plume width versus height. The vertical momentum flux, M_f, is:

$$M_f = \rho V_f{}^2 L_{bp} k h \tag{11}$$

Neglecting the vertical momentum of any fluid entering the plume from the side, the vertical momentum flux equals the buoyancy, B, in the plume. If the characteristic time for a bubble to rise through the plume is t_b, then the buoyancy can be written as:

$$B = \rho g Q t_b \tag{12}$$

We can write t_b as:

$$t_b \sim h/(V_f + V_s) \tag{13}$$

where V_s is the "slip speed" of the gas with respect to the fluid. Equating the momentum flux and the buoyancy gives:

$$V_f{}^2 L_{bp}{}^k \sim Qg/(V_f + V_s) \tag{14}$$

The ratio of the slip speed to the liquid speed is called r. Solving equation (14) for the liquid speed;

$$V_f \sim [Qg/(L_{bp} k)]^{1/3} [1/(1+r)]^{1/3} \tag{15}$$

The liquid volume flux Q_L out of the plume is:

$$Q_L \sim k h V_f L_{bp} \tag{16}$$

and the cycle time, $L^3 h/Q_L$, for the tank fluid to pass through the plume once is:

$$\text{"cycle time"} \sim [(1+r)/k^2]^{1/3} T_s \tag{17}$$

The characteristic mixing time is expected to be very nearly proportional to the cycle time. However, it is not proportional to T_s because the factor $[(1-r)/k^2]^{1/3}$ is not a constant as neither r nor k is constant.

In the case of r, the slip speed, V_s, is nearly constant at 24 cm/s for bubble diameters of 0.3 to 1.2 cm (as shown in reference [4]). In our experiments the bubble diameters were about 1 cm and this size is anticipated for larger scale applications. The liquid speed, V_f, varies approximately as $Q^{1/3}$. In our experiments it varied roughly from 30 to 60 cm/s for which $1.12 < (1+r)^{1/3} < 1.22$. At ten times larger scale, $(1+r)^{1/3} \sim 1.05$.

The most comprehensive data on the variability of k is for round bubble plumes rather than the plane (linear) plumes we are considering here. The round plume data measured by several investigators shows [4] that k increases when gas flow is increased due to more entrainment of fluid when the number of bubbles increases. The same effect occurs in plane plumes when the ratio Q/L_{bp} increases. With a plane plume, Kobus [6] found k increased from 0.08 to 0.11 as Q/L_{bp} increased from 3 to 10 L/s per meter of plume length. The effect is weak, but significant.

Thus the quantity $[(1-r)/k^2]^{1/3}$, which multiplies T_s to yield the cycle time, is a weakly decreasing function of Q and a weakly increasing function of L_{bp}. Since this factor is a dependent variable, it cannot enter directly into the characteristic mixing time which we require to be an independent variable. However, the quantity $g^{1/15} Q^{-2/15} L_{bp}{}^{1/3}$ is an independent variable that is a weakly decreasing function of Q and a weakly increasing function of L_{bp}; and which influences the characteristic mixing time in the same way that $[(1-r)/k^2]^{1/3}$ influences the cycle time.

To obtain an approximating analytical relationship between U and t'' the data in Fig. 10 is plotted in log-log form in Fig. 12 where it is shown that the data is well approximated by:

$$U = \begin{cases} 0.98\,(t'')^{-1.21}, & t'' < 2.65 \\ 3.63\,(t'')^{-2.57}, & t'' > 2.65 \end{cases} \tag{18}$$

How well are the "L" plume and "T" plume distribution pipe data approximated by equation (18)? In seeking to answer this we note that for the "L" configuration $L_{bp} = 2L$.

In determining L_{bp} for the "T" configuration the derivation of T_2 is examined. In this regard, since the plume width above the center leg of the "T" is twice the width of the plume above a pipe along a wall, the correct value to use for L_{bp} in the case of the "T" pipe is $3L$. Using these values for L_{bp}, the results for the "L" and "T" configurations are shown in Fig. 13. Equation (18) is a good approximation to the data. The slight bias toward larger t'' shown in Fig. 13 results from choosing $f = -1$ instead of $f = -29/30$.

Acknowledgment

This study was supported, in part, by the Environmental Protection Service of the Government of Canada.

References

1 Hu, S., and Kinter, R. C., "The Fall of Single Drops Through Water," *AIChE. J.*, Vol. 1, 1955, pp. 42–48.

2 Milgram, J. H., "Mean Flow in Round Bubble Plumes," *J. Fluid Mech.*, Vol. 133, 1983, pp. 345–376.

3 Godon, A. M., "Mixing in Rectangular Tanks by Bubble Plumes," SM thesis, Mass. Inst. of Tech., 1986.

4 Haberman, W. L., and Morton, R. K., "An Experimental Study of Bubbles Moving in Liquids," *Proc. ASCE*, Vol. 80, Separate No. 387, 1954.

5 Leavy, Wm. A., and Tsai, D. H., "Metering of Gases by Means of The ASME Square Edge Orifice with Flange Taps," Sloan Automotive Laboratory for Automotive and Aircraft Engines, Massachusetts Institute of Technology, 1951.

6 Kobus, H. E., "Analysis of the Flow Induced by Air-Bubble Systems, *Proc. Coastal Engineering Conf.*, Vol. II, Chapter 65, London, 1968.

7 Chen, C. J., and Rodi, W., *Vertical Turbulent Buoyant Jets, A Review of Experimental Data*, Pergamon Press, Oxford, 1980.

Journal of Fluids Engineering

Technical Briefs

Numerical Model for Fluid Spin-Up From Rest in a Partially Filled Cylinder

G. F. Homicz[1] and N. Gerber[2]

A numerical investigation is presented for the axisymmetric spin-up of fluid in a partially filled cylindrical cavity. It is an extension of earlier analyses to those cases where the liquid free surface intersects one or both endwalls. Previous models of the laminar Ekman layer pumping are modified heuristically for situations where the layer(s) no longer covers the entire wall. Numerical results for a range of Reynolds number, Froude number, and fill ratio have been obtained. They clearly demonstrate that it is the bottom wall Ekman layer which is primarily responsible for spin-up.

Introduction

The transient spin-up of fluid in a cylindrical cavity plays an important role in determining the spin-decay of liquid-filled projectiles, as well as the eigenfrequencies of the interior fluid motion. These in turn impact the stability of the fluid-shell system [1]. Most previous investigators have assumed the fluid completely fills the cylinder, e.g., Wedemeyer [2]. Gerber [3] considered the partially filled cylinder in the steady limit of solid-body rotation, showing that the final shape of the free surface is a parabola. Goller and Ranov [4] extended the Wedemeyer [2] model to allow for free surface motion, and showed that it retards the spin-up process. Their analysis assumes the free surface does not intersect either of the endwalls, a rather restrictive assumption for large Froude numbers [3]. We summarize here an investigation which extends the Wedemeyer-Goller-Ranov model to situations where the free surface intersects one or both endwalls. Heuristic modifications are applied to the magnitude of the secondary flow, which is now driven by Ekman layers over a surface that may be only partially wetted. A more detailed exposition and literature review can be found in references [5, 6, 7].

Analysis

We wish to predict spin-up in a cylinder of radius R and height H (Fig. 1) which at $\bar{t} = 0$ begins to spin with constant angular velocity, Ω, about its axis. The flow is incompressible, axisymmetric, and characterized by its density, ρ, and kinematic viscosity, ν. Its initial level at rest is L. The velocity components in the $(\bar{r}, \theta, \bar{z})$ coordinates are $(\bar{u}, \bar{v}, \bar{w})$, respectively.

Following Wedemeyer [2], in the limit of large $\mathrm{Re} = \Omega R^2/\nu$ the flow can be conceptually divided into a relatively inviscid interior *core* flow, and the Ekman layers on the endwalls where viscous effects dominate. The ordering of terms in the core flow is such that a simplified model results, in which $\bar{u}$, $\bar{v}$ and the pressure $\bar{p}$ are functions of only $\bar{r}$ and $\bar{t}$, the so-called *columnar* flow approximation. In dimensionless form, the equation for $v(r, t)$ in the core flow reduces to,

$$\frac{\partial v}{\partial t} + u\left(\frac{\partial v}{\partial r} + \frac{v}{r}\right) = \mathrm{Re}^{-1}\left[\frac{\partial^2 v}{\partial r^2} + \frac{\partial}{\partial r}\left(\frac{v}{r}\right)\right] \quad (1)$$

where $r = \bar{r}/R$, $t = \Omega\bar{t}$, and (u, v, w) are normalized by ΩR. The initial and boundary conditions are $v(r, 0) = 0$, $v(0, t) = 0$, and $v(1, t) = 1$.

Equation (1) is solved using a Crank-Nicolson type finite difference scheme on a uniform grid in both space and time. Centered second-order accurate differences are used for the spatial derivatives. The presence of u, which depends on v, introduces a nonlinearity into equation (1) which is handled via iterative relaxation. It also requires that an additional equation relating u and v in the core be supplied to close the system.

Wedemeyer obtained the needed relation for a filled cylinder by arguing that the radial flux in the core flow must

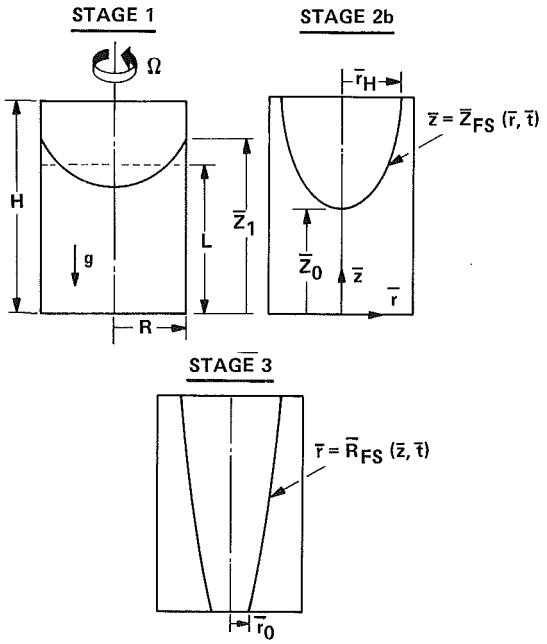

Fig. 1 Cylindrical geometry and possible fluid configurations for $L/H \geq 1/2$

[1]Physical Sciences Department, Calspan Advanced Technology Center, Buffalo, NY 14225; Presently Member of Technical Staff, Aerodynamics Department, Sandia National Laboratories, Albuquerque, NM 87115.

[2]Launch & Flight Division, U.S. Army Ballistics Research Laboratory, Aberdeen Proving Ground, MD 21005.

Contributed by the Fluids Engineering Division of The American Society of Mechanical Engineers. Manuscript received by the Fluids Engineering Division September 23, 1983.

be of equal magnitude, but opposite direction, to that within the Ekman layers. In the present case, these layers no longer necessarily cover the entire endwall. Furthermore, the drop in fluid level near the axis and the accompanying rise at the sidewall imply a radial outflux in opposition to the influx driven by the Ekman layers. Hence we imagine the total radial core velocity to be composed of contributions generated by the bottom and top Ekman layers and the free surface motion as follows,

$$u(v) = u_{BEL}(v) + u_{TEL}(v) + u_{FS}(v). \tag{2}$$

The form each of these contributions will take depends on whether the free surface intersects neither, the top, or both of the endwalls. Following reference [3] we shall refer to these successive configurations as Stages 1, 2b, and 3 (Fig. 1).

Stage 1. This is the case treated previously by Goller and Ranov [4], in which neither endwall is intersected. Neglecting surface tension and viscous effects, and summing to zero the remaining centrifugal and gravitational forces tangential to the surface, one obtains the following equation for the free surface contour, $z = Z_{FS}(r, t)$:

$$\frac{\partial Z_{FS}}{\partial r} = F\frac{v^2}{r} \tag{3}$$

where axial distances are normalized by the cylinder height, H, and $F = (\Omega R)^2/gH$ is the Froude number. This can be integrated to give

$$Z_{FS}(r,t) = Z_1 - F\int_r^1 \frac{v^2}{r'}\,dr' \tag{4}$$

$$Z_1(t) = \frac{L}{H} + F\int_0^1 v^2 r\,dr \tag{5}$$

where Z_1 is the fluid level at the sidewall.

The Ekman layers establish themselves within a few revolutions of the cylinder. The characteristic spin-up time is much longer, of order $(H/R)\mathrm{Re}^{1/2}\Omega^{-1}$ [8]. Hence Wedemeyer argued that the radial flux they generate could be treated in a quasi-steady manner: at each radial station, the flux responds instantaneously to the local difference in tangential velocity between the endwall and the core flow above it. The columnar nature of the flow dictates that the interior flux be spread uniformly in z, which leads to a simple expression for u [2]. In our case, during Stage 1 $u_{TEL} = 0$. The bottom layer flux is assumed equal to that for the filled case, but is now spread over a column of height Z_{FS}, yielding

$$u_{BEL} = -\mathrm{Re}^{-1/2}\frac{R}{H}\frac{r}{Z_{FS}}f(\omega). \tag{6}$$

This reduces to equation (10) of reference [2] upon setting $Z_{FS} = 1/2$. $f(\omega)$ is the dimensionless Ekman layer flux, expressed as a function of the local angular velocity, $\omega = v/r$. For this we have used the same expression as Goller and Renov, equation (9) of reference [4]. It has the property that $f(\omega)\to 0$ as $\omega\to 1$; i.e., pumping of the secondary flow is reduced as solid-body rotation is approached.

The free surface motion generates a flux across any radial surface, r = *constant*, equal to the rate of change of fluid volume between the axis and r. This gives

$$u_{FS} = \frac{-\int_0^r (\partial Z_{FS}/\partial t)r'\,dr'}{rZ_{FS}}. \tag{7}$$

Use of equations (6)–(7) in equation (2) completes the evaluation of u in terms of v needed in equation (1). These expressions are equivalent to those used by Goller and Ranov [4]. During Stage 1, the present model differs from theirs only in the use here of an *implicit*, as opposed to their *explicit*, differencing scheme. For $F > 4(1 - L/H)$ the flow eventually intersects the top endwall [5], and equation (5) yields $Z_1 > 1$. The flow is now in Stage 2b.

Stage 2b. The radius of intersection with the top wall is denoted by $r_H(t)$ (Fig. 1). Conservation of fluid volume requires that $F\int_0^{r_H} v^2 r\,dr = 1 - L/H$, from which r_H can be determined once $v(r, t)$ is specified [5]. Then $Z_{FS} = 1$ for $r \geq r_H$, while

$$Z_{FS}(r,t) = 1 - F\int_r^{r_H}\frac{v^2}{r'}\,dr' \qquad r < r_H. \tag{8}$$

Equation (7) is still used for u_{FS} for $r \leq r_H$, but now $u_{FS} = 0$ when $r > r_H$.

The contribution u_{BEL} from the bottom Ekman layer is still given by equation (6). However, the top wall is only partially wetted and the nature of the boundary layer is unknown. The authors are unaware of any published investigations for such flows, but one would expect the following behavior: (i) the outward flux in the layer should vanish at r_H since there is no fluid at $r \leq r_H$ to sustain it; (ii) the flux should reduce to that in the Wedemeyer model for $r_H = 0$. Thus we set $u_{TEL} = 0$ for $r \leq r_H$, while at other radial stations the mass flux $f(\omega)$, and hence u_{TEL}, is now multiplied by a factor $\mathcal{K}_T(1 - r_H/r)^{\gamma_T}$ giving,

$$u_{TEL} = -\mathrm{Re}^{-1/2}\frac{R}{H}r\mathcal{K}_T\left(1 - \frac{r_H}{r}\right)^{\gamma_T} f(\omega) \quad r_H \leq r \leq 1 \tag{9}$$

where $\mathcal{K}_T (>0)$ and γ_T are adjustable constants. Equation (9) has the following properties: the contribution from u_{TEL} vanishes at both $r = r_H$ and 1; the influence of the top endwall Ekman layer will increase as r_H decreases; and the columnar nature of the flow is maintained. Certainly other analytical forms suggest themselves, but without experimental data to serve as a guide, it was decided to use as simple a form as possible. If $F > (1 - L/H)^{-1}$ eventually the fluid displacement will expose a portion of the bottom endwall [5]. At some r, equation (8) then predicts that $Z_{FS} < 0$; the flow is now in Stage 3.

Stage 3. Once the bottom wall is intersected, the boundary condition $v(0, t) = 0$ is inapplicable, as there is no longer any fluid there. At the intersection point, $r = r_0(t)$ in Fig. 1, another condition on v can be derived from the fact that a particle on the free surface must remain there. The modification to the solution algorithm used in Stages 1 and 2b is straightforward [6, 7].

As for Z_{FS}, now both r_H and r_0 are changing with time. Moreover, the free surface in this stage is quite steep, so that the accuracy of the numerical quadratures on the radial grid is degraded. For these reasons, we now choose z as our independent variable and let $r = R_{FS}(z, t)$ represent the surface contour (Fig. 1). Now the contour always lies between $z = 0$ and 1, and also has a shallow slope, allowing the application of standard quadrature techniques. From reference [5], the free surface then evolves according to

$$R_{FS}^2(z,t) = r_0^2(t) + \frac{2}{F}\int_0^z \frac{R_{FS}^2(z',t)dz'}{v^2[R_{FS}(z',t),t]} \tag{10}$$

$$r_0^2(t) = 1 - \frac{L}{H} - \frac{2}{F}\int_0^1 \frac{R^2{}_{FS}(z,t)(1-z)dz}{v^2[R_{FS}(z,t),t]}. \tag{11}$$

Equation (10) is an integral equation for R_{FS}^2; it is also weakly nonlinear owing to the implicit dependence of $v(R_{FS}, t)$ on the solution. As a result, during Stage 3, in addition to the *outer* iteration on v used to solve equation (1), we will now have an *inner* iteration to determine the free surface contour consistent with v. Equation (10) is solved on a uniform axial grid using the method of successive approximation. The same physical reasoning as before now leads to $u_{FS} = 0$ for $r \geq r_H$, while

$$u_{FS} = \frac{\int_0^{Z_{FS}} (\partial R_{FS}/\partial t) R_{FS}\, dz'}{r Z_{FS}} \qquad r_0 \le r \le r_H. \tag{12}$$

u_{TEL} is still given by equation (9). But now u_{BEL} is similarly reduced by a multiplicative factor to reflect the fact that the bottom wall is only partially wetted:

$$u_{BEL} = -\mathrm{Re}^{-1/2} \frac{R}{H} \frac{r}{Z_{FS}} \mathcal{K}_B \left(1 - \frac{r_0}{r}\right)^{\gamma_B} f(\omega) \quad r_0 \le r \le 1 \tag{13}$$

where $\mathcal{K}_B\,(>0)$ and $\gamma_B\,(\ge 1)$ are adjustable constants. This expression statisfies constraints analogous to those cited following equation (9). Note that for a given r, u_{BEL} grows progressively smaller as more of the wall is exposed.

The model described above forms a rather simplified picture of a complex flowfield. The present equations are felt to adequately describe the gross features of the phenomena, and should thus provide a first step towards a better understanding. We are buoyed in this belief by the successful correlations with experiment of the earlier simplified models of Wedemeyer [2] and Goller and Ranov [4].

Numerical Results and Discussion

Numerical results for six cases are discussed in references [5]–[7]. These include flows whose final configurations lie in each of the three stages, as well as a comparison with Goller and Ranov's [4] experimental data for a Stage 1 flow; good agreement was exhibited. Here we present detailed results only for Case 3 from references [6, 7], which is representative of the others. The conditions are Re = 1.172×10^5, $F = 3.5$, $H/R = 3.0$, and $L/H = 0.6$. The empirical constants were given the values $\mathcal{K}_T = \mathcal{K}_B = 1.0$ and $\gamma_T = \gamma_B = 1.01$.

Figure 2 shows the azimuthal velocity profiles and free surface contours at equal increments of 400 in the dimensionless time. The last curve of each is at the spin-up time, $t_S = 4745$, defined as the instant at which the fluid has acquired 99 percent of its final angular momentum. The last five curves in Fig. 2(*a*) end at $r = r_0 > 0$ because there is no fluid to the left of this point. The progressively closer spacing of the curves indicates the asymptotic nature of the approach to solid-body rotation. There is unfortunately no experimental data against which to compare such predictions for flows in Stages 2b and 3.

For the linearized spin-up of fluid in a filled cylinder, the basic time dependence of v has been shown to be exponential [8]. Should one expect similar behavior here, where nonlinear convective terms are retained and a free surface is present? Consider the total angular momentum about the axis, L_z, which represents an integral of v over the whole flow. If the above were true, then a semi-logarithmic plot of the *angular momentum deficit*, $1 - L_z(t)/L_z(\infty)$, versus t should yield a straight line. Such a plot of the numerical data for Cases 3–5 is shown in Fig. 3. The conditions for Cases 4 and 5 are identical to those in Case 3, except that Re was decreased by a factor of 10 and 100, respectively.

The two flagged symbols for each case represent the instants just after the transition between stages, i.e., when the top and bottom walls are first intersected by the free surface. The numerical data do indeed lie on a straight line during the first two stages. However, after the transition to Stage 3, the results follow a line with a reduced slope, indicating a slower rate of spin-up. The fact that the fluid hitting the top wall apparently has little impact on the rate of spin-up can be explained by noting that the radial extent of the fluid layer there is relatively thin (Fig. 2(*b*)), and it has already acquired a significant fraction of its final angular velocity (Fig. 2(*a*)). Hence its contribution to the Ekman pumping remains small compared with that from the bottom layer, which still completely covers the wall.

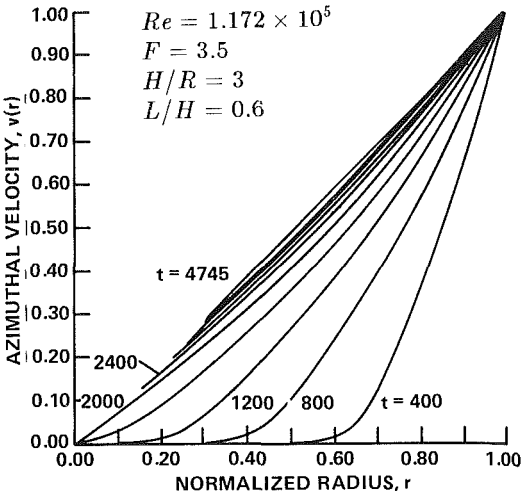

Fig. 2(*a*) Azimuthal velocity profiles for case 3

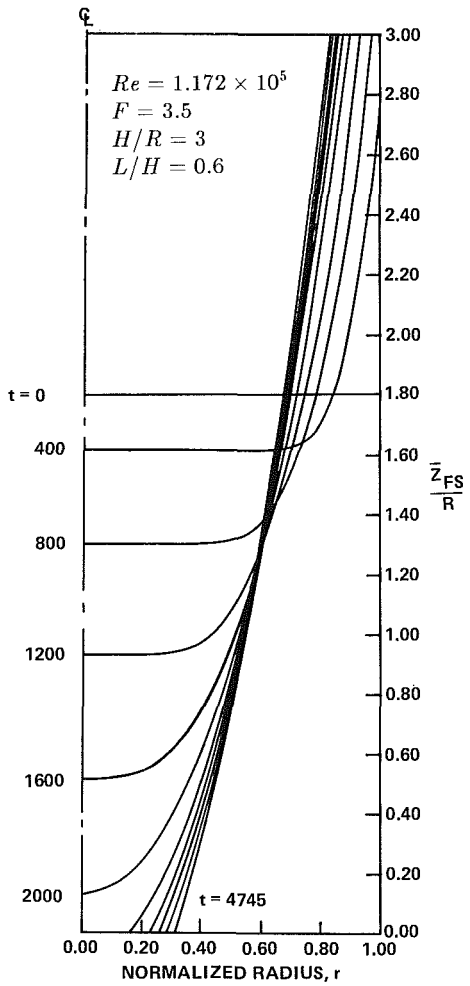

Fig. 2(*b*) Free surface contours for case 3

Upon making the transition to Stage 3, however, the strength of the bottom layer pumping is progressively reduced as the wall is exposed, and a slower spin-up rate results.

Conclusions

There are no quantitative data against which the analysis can be validated for cases where one or both endwalls are in-

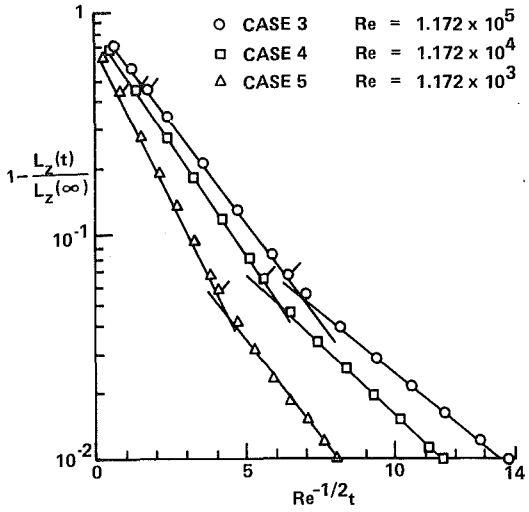

Fig. 3 Angular momentum deficit versus time for cases 3-5

tersected. Nevertheless, the following qualitative conclusions have been drawn. The angular momentum transfer follows a simple exponential behavior in time. For Re in the range 10^3-10^5, the growth rate appears uniform up to the time when the bottom endwall is intersected. After this, exponential behavior is still exhibited, but at a reduced rate. This reflects the diminishing influence of the bottom Ekman layer, which is primarily responsible for the secondary flow. The magnitude of the reduction in spin-up rate diminishes with decreasing Reynolds number. The model's predictions should be compared with laboratory experiments and more refined numerical calculations, e.g., solutions of the full axisymmetric Navier-Stokes equations. This would also provide guidelines for adjusting the empirical parameters in equations (9) and (13). The present model could then serve as an efficient means of predicting the gross characteristics of fluid spin-up in cases of practical interest.

Acknowledgments

This work was sponsored by the U.S. Army Research Office, Contract No. DAAG29-81-C-0007, under the technical supervision of Dr. Robert E. Singleton. The authors also wish to acknowledge numerous technical discussions with Drs. Raymond Sedney (U.S. Army Ballistic Research Laboratory) and William J. Rae (Calspan).

References

1 *Engineering Design Handbook: Liquid-filled Projectile Design*, AMC Pamphlet No. 706-165, U.S. Army Material Command, Washington, D.C., Apr. 1969.

2 Wedemeyer, E. H., "The Unsteady Flow Within a Spinning Cylinder," *Journal of Fluid Mechanics*, Vol. 20, Part 3, 1964, pp. 383-399.

3 Gerber, N., "Properties of Rigidly Rotating Liquids in Closed Partially Filled Cylinders," ASME *Journal of Applied Mechanics*, Vol. 97, 1975, pp. 734-735.

4 Goller, H., and Ranov, T., "Unsteady Rotating Flow in a Cylinder with a Free Surface," ASME *Journal of Basic Engineering*, Vol. 90, No. 4, 1968, pp. 445-454.

5 Homicz, G. F., *Numerical Model for Fluid Spin-Up in a Partially-Filled Cylinder*, Calspan Report No. 6856-A-1, Interim report prepared for U.S. Army Research Office, Durham, N.C., Contract DAAG29-81-C-0007, May 1982.

6 Homicz, G. F., *Numerical Studies of Fluid Spin-Up from Rest in a Partially-Filled Cylinder*, Calspan Report No. 6856-A-2, Final report prepared for U.S. Army Research Office, Durham, N.C., Contract DAAG29-81-C-0007, Nov. 1984.

7 Homicz, G. F., and Gerber, N., "Numerical Model for Fluid Spin-Up from Rest in a Partially-Filled Cylinder," AIAA Paper 86-1121, AIAA/ASME 4th Fluid Mechanics, Plasma Dynamics and Lasers Conference, Atlanta, GA, May 12-14, 1986.

8 Greenspan, H. P., *The Theory of Rotating Fluids*, Cambridge University Press, London, 1968.

Instability of Flow Through Tube Rows

P. M. Moretti[1] and M. Cheng[1]

The instability of the parallel plane jets emerging between the tubes of a tube row in crossflow, which results in a pairing of the jets, is well known (reference [1]). However, when the tube spacing is very close, we observe a more complex instability, which results in the joining of three or more jets.

The basic instability was investigated by von Bohl [2] and by Corrsin [3], using rows of noncircular rods. For round cylinders, the joining of pairs of jets may be expected downstream of transverse rows spaced at pitch-to-diameter ratios of less than 2.3 (reference [4]).

In exploratory flow visualizations using dye streaks in a closed water tunnel [5] we photographed more complex flow patterns behind single and double tube rows at pitch-to-diameter ratios of about 1.3; a typical example (Fig. 1) has been reproduced in color in a magazine [6]. Three or four jets could be seen to join together, while wide stagnant zones appeared between the combined jets. Some of the jets emerging between the tubes were deflected at severe angles (thirty degrees or more) before merging with others.

Our velocity measurements with Pitot tubes, Kiel probes, and hot-wire anemometers in a wind tunnel downstream of a single row of tubes at a pitch-to-diameter ratio of 1.3 [7] showed similarly irregular flow patterns, establishing that the phenomenon is not an artifact of a particular facility or test section. Figure 2 shows the result of a series of traverses at distances of 0.5 to 4.5 tube-diameters from the tubes; the immediate and continuing merging of jets is evident, and is not restricted to either the center or the walls of the test section. Sometimes, at irregular time intervals, the flow pattern changed to different groupings of merging jets, indicating a complex multi-stable condition rather than the consequences of irregularities in the tube row.

Careful reexamination of a smoke-tunnel photograph by Bradshaw at a pitch-to-diameter ratio of about 1.5 [8] confirmed the presence of a similar instability, though it is less prominent at this larger tube spacing. The jets are seen to pair off at first; then the combined jets coalesce for a second time, so that four of the initial jets ultimately group together. The

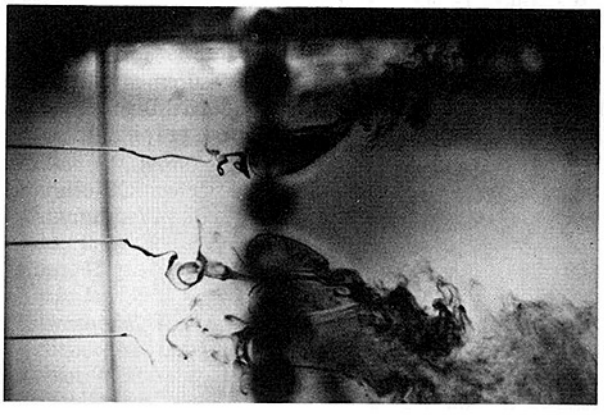

Fig. 1 Visualization of water flow through a tightly spaced row of tubes. The jets emerging between the tubes deflect sharply and join into groups at the top and bottom of the picture, leaving a stagnant zone in the center. Similar observations were made after double (in-line) tube rows.

[1] School of Mechanical and Aerospace Engineering, Oklahoma State University, Stillwater, Okla. 74078-0545

Contributed by the Fluids Engineering Division of THE AMERICAN SOCIETY OF MECHANICAL ENGINEERS. Manuscript received by the Fluids Engineering Division March 3, 1986.

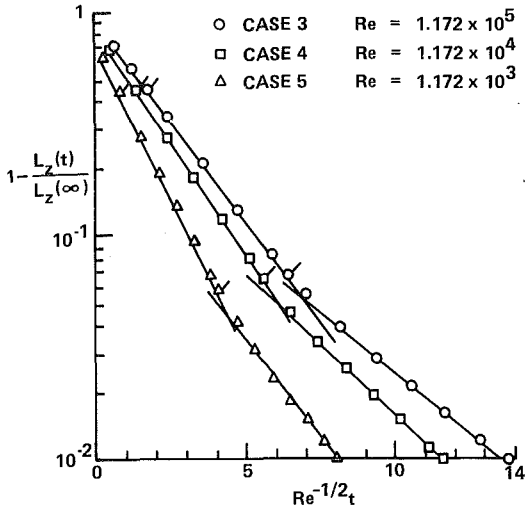

Fig. 3 Angular momentum deficit versus time for cases 3-5

tersected. Nevertheless, the following qualitative conclusions have been drawn. The angular momentum transfer follows a simple exponential behavior in time. For Re in the range 10^3-10^5, the growth rate appears uniform up to the time when the bottom endwall is intersected. After this, exponential behavior is still exhibited, but at a reduced rate. This reflects the diminishing influence of the bottom Ekman layer, which is primarily responsible for the secondary flow. The magnitude of the reduction in spin-up rate diminishes with decreasing Reynolds number. The model's predictions should be compared with laboratory experiments and more refined numerical calculations, e.g., solutions of the full axisymmetric Navier-Stokes equations. This would also provide guidelines for adjusting the empirical parameters in equations (9) and (13). The present model could then serve as an efficient means of predicting the gross characteristics of fluid spin-up in cases of practical interest.

Acknowledgments

This work was sponsored by the U.S. Army Research Office, Contract No. DAAG29-81-C-0007, under the technical supervision of Dr. Robert E. Singleton. The authors also wish to acknowledge numerous technical discussions with Drs. Raymond Sedney (U.S. Army Ballistic Research Laboratory) and William J. Rae (Calspan).

References

1 *Engineering Design Handbook: Liquid-filled Projectile Design*, AMC Pamphlet No. 706-165, U.S. Army Material Command, Washington, D.C., Apr. 1969.

2 Wedemeyer, E. H., "The Unsteady Flow Within a Spinning Cylinder," *Journal of Fluid Mechanics*, Vol. 20, Part 3, 1964, pp. 383-399.

3 Gerber, N., "Properties of Rigidly Rotating Liquids in Closed Partially Filled Cylinders," ASME *Journal of Applied Mechanics*, Vol. 97, 1975, pp. 734-735.

4 Goller, H., and Ranov, T., "Unsteady Rotating Flow in a Cylinder with a Free Surface," ASME *Journal of Basic Engineering*, Vol. 90, No. 4, 1968, pp. 445-454.

5 Homicz, G. F., *Numerical Model for Fluid Spin-Up in a Partially-Filled Cylinder*, Calspan Report No. 6856-A-1, Interim report prepared for U.S. Army Research Office, Durham, N.C., Contract DAAG29-81-C-0007, May 1982.

6 Homicz, G. F., *Numerical Studies of Fluid Spin-Up from Rest in a Partially-Filled Cylinder*, Calspan Report No. 6856-A-2, Final report prepared for U.S. Army Research Office, Durham, N.C., Contract DAAG29-81-C-0007, Nov. 1984.

7 Homicz, G. F., and Gerber, N., "Numerical Model for Fluid Spin-Up from Rest in a Partially-Filled Cylinder," AIAA Paper 86-1121, AIAA/ASME 4th Fluid Mechanics, Plasma Dynamics and Lasers Conference, Atlanta, GA, May 12-14, 1986.

8 Greenspan, H. P., *The Theory of Rotating Fluids*, Cambridge University Press, London, 1968.

Instability of Flow Through Tube Rows

P. M. Moretti[1] and M. Cheng[1]

The instability of the parallel plane jets emerging between the tubes of a tube row in crossflow, which results in a pairing of the jets, is well known (reference [1]). However, when the tube spacing is very close, we observe a more complex instability, which results in the joining of three or more jets.

The basic instability was investigated by von Bohl [2] and by Corrsin [3], using rows of noncircular rods. For round cylinders, the joining of pairs of jets may be expected downstream of transverse rows spaced at pitch-to-diameter ratios of less than 2.3 (reference [4]).

In exploratory flow visualizations using dye streaks in a closed water tunnel [5] we photographed more complex flow patterns behind single and double tube rows at pitch-to-diameter ratios of about 1.3; a typical example (Fig. 1) has been reproduced in color in a magazine [6]. Three or four jets could be seen to join together, while wide stagnant zones appeared between the combined jets. Some of the jets emerging between the tubes were deflected at severe angles (thirty degrees or more) before merging with others.

Our velocity measurements with Pitot tubes, Kiel probes, and hot-wire anemometers in a wind tunnel downstream of a single row of tubes at a pitch-to-diameter ratio of 1.3 [7] showed similarly irregular flow patterns, establishing that the phenomenon is not an artifact of a particular facility or test section. Figure 2 shows the result of a series of traverses at distances of 0.5 to 4.5 tube-diameters from the tubes; the immediate and continuing merging of jets is evident, and is not restricted to either the center or the walls of the test section. Sometimes, at irregular time intervals, the flow pattern changed to different groupings of merging jets, indicating a complex multi-stable condition rather than the consequences of irregularities in the tube row.

Careful reexamination of a smoke-tunnel photograph by Bradshaw at a pitch-to-diameter ratio of about 1.5 [8] confirmed the presence of a similar instability, though it is less prominent at this larger tube spacing. The jets are seen to pair off at first; then the combined jets coalesce for a second time, so that four of the initial jets ultimately group together. The

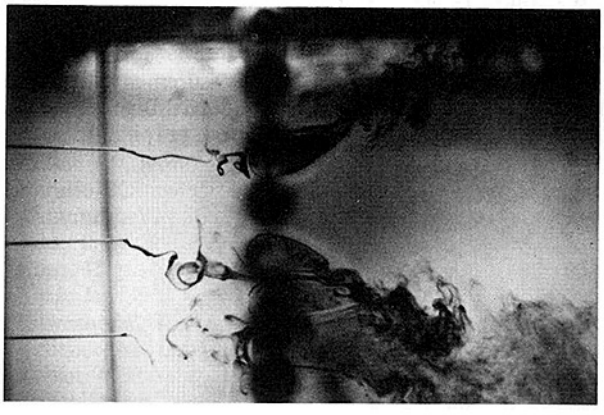

Fig. 1 Visualization of water flow through a tightly spaced row of tubes. The jets emerging between the tubes deflect sharply and join into groups at the top and bottom of the picture, leaving a stagnant zone in the center. Similar observations were made after double (in-line) tube rows.

[1]School of Mechanical and Aerospace Engineering, Oklahoma State University, Stillwater, Okla. 74078-0545

Contributed by the Fluids Engineering Division of THE AMERICAN SOCIETY OF MECHANICAL ENGINEERS. Manuscript received by the Fluids Engineering Division March 3, 1986.

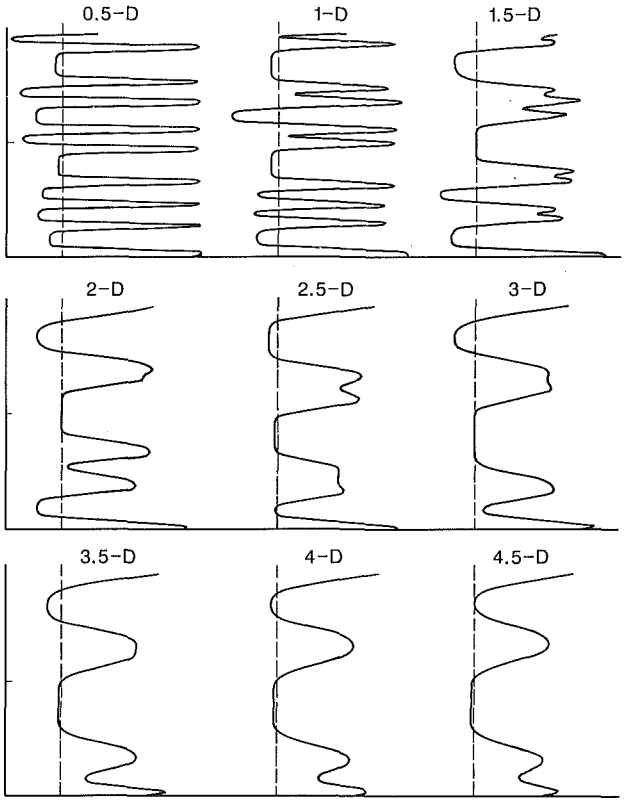

Fig. 2 Kiel-probe profiles at various distances downstream of a single tube row having a pitch-to-diameter ratio of 1.3, subjected to a cross flow at a tube-diameter Reynolds number of about 2500. The traverses are carried out at nine stations, from 0.5 to 4.5 tube-diameters distance from the tube row. The flow had started out as eight uniform, equally spaced and parallel two-dimensional jets. The jets can be seen to deflect and coalesce progressively.

flow deflections are less severe than at our closer tube spacings. The visualization also confirms that vortex shedding coexists with and is overlaid on the deflected flow as a relatively small perturbation.

We conclude that the threshold for the more complex instability is near a pitch-to-diameter ratio of 1.5, and that flow deflections are more abrupt as the tube spacing becomes smaller. This is confirmed by measurements of vortex-shedding frequencies by Ishigai and Nishikawa [9], which show two separate Strouhal numbers at pitch-to-diameter ratios of more than 1.5, but more than two at less than 1.4. This suggests that there are two different widths of tube wakes in the first case, but more than two at extremely close tube spacings.

The phenomenon affects the uniformity of the flow downstream of single and double tube rows, and probably also multi-row arrays. In addition to the implications for flow in heat exchangers, it is of interest in the same situations in which the previously known simple pairing instability has been shown to have an effect: settling screens in wind tunnels [2]; turning vanes in duct elbows [10]; multi-slotted airfoils [3]; and jet-switch-driven vibrations [11]. Similar flow patterns have recently been visualized also for the flow through ribbon parachutes [12].

References

1 Schlichting, Hermann, *Boundary-Layer Theory*, tr. J. Kestin, 7th Edition, McGraw-Hill, New York, 1979; Chapter XXIV, Part C, Section 4, p. 745.

2 von Bohl, J. G. Edler, "Das Verhalten paralleler Luftstrahlen," reported by L. Prandtl and A. Betz, *Ingenieur-Archiv*, Vol. 11, No. 4, 1940, pp. 295-314.

3 Corrsin, Stanley, "Investigation of the Behavior of Parallel Two-Dimensional Air Jets," N.A.C.A. Advanced Confidential Report 4H24, reprinted as Wartime Report W-90, 1944.

4 Morgan, P. G., "The Stability of Flow Through Porous Screens," Technical Note, *Journal of the Royal Aeronautical Society*, Vol. 64, June 1960, pp. 359-362.

5 Leuchter, Ruediger, unpublished graduate project, School of Mechanical and Aerospace Engineering, Oklahoma State University, Stillwater, OK 74078-0545, Dec. 1976.

6 Moretti, P. M., "Caught in a Cross Flow," *Mechanical Engineering*, Vol. 108, No. 12, Dec. 1986, p. 61, Fig. 6a.

7 Cheng, M., "Experimental Study of the Flow Field Downstream of a Single Tube-Row," M.S. Report, School of Mechanical and Aerospace Engineering, Oklahoma State University, Stillwater, OK 74078-0545, Nov. 1985.

8 Bradshaw, P., "The Effect of Wind-Tunnel Screens on Nominally Two-Dimensional Boundary Layers," *Journal of Fluid Mechanics*, Vol. 22, Part 4, pp. 679-688, 1965; see also "The Effect of Wind Tunnel Screens on 'Two-Dimensional' Boundary layers," Nat. Phys. Labs., Aero. Rep. no. 1085, 1963.

9 Ishigai, Seikan, and Nishikawa, Eiichi, "Experimental Study of Structure of Gas Flow in Tube Banks with Tube Axes Normal to Flow, Part II; On the Structure of Gas Flow in Single-Column, Single-Row, and Double-Row Tube Banks, *Bulletin of the JSME*, Vo. 18, No. 119, pp. 528-535, May 1975; see also Part I in *Bull. JSME*, Vol. 15, No. 86, p. 949.

10 MacPhail, D. C., "Experiments on Turning Vanes at an Expansion," communicated by G. I. Taylor, Reports & Memoranda No. 1876, (4015), A.R.U. Technical Report, British Aeronautical Research Committee, Apr. 1939, Figs. 11 to 14.

11 Roberts. B. W., "Low Frequency, Aeroelastic Vibrations in a Cascade of Circular Cylinders," *Mechanical Engineering Science Monograph*, No. 4, Institution of Mechanical Engineers, September 1966; see also "Low Frequency, Self-Excited Vibration in a Row of Circular Cylinders Mounted in an Air-Stream," Ph.D. dissertation, Cambridge University, 1962.

12 Higuchi, H., "An Experimental Investigation of the Flow Field Behind Grid Models," Paper AIAA-86-2460-CP, AIAA 9th Aerodynamic Decelerator & Balloon Technology Conference, Albuquerque, New Mexico, Oct. 7-9, 1986.